

EFFECT OF STRATIFICATION AND JOULE HEATING ON MHD DUSTY VISCOELASTIC FLUID FLOW THROUGH INCLINED CHANNELS IN POROUS MEDIUM IN PRESENCE OF MOLECULAR DIFFUSIVITY

 Saleem Javed Al Khayer^{a*},  Shyamanta Chakraborty^{b†}

^aDepartment of Mathematics, Gauhati University, Guwahati, Kamrup, 781014, Assam, India

^bUGC-HRDC, Gauhati University, Guwahati, Kamrup, 781014, Assam, India

*Corresponding Author e-mail: jabedsaleem155@gmail.com; †E-mail: schakrabortyhrdc@gauhati.ac.in

Received January 5, 2024; revised February 2, 2024; accepted February 21, 2024

An analysis is carried out to study laminar MHD convection flow of a second order dusty viscoelastic fluid in porous medium through an inclined parallel plate channel in the presence of molecular diffusivity. The plates are maintained at two different temperatures that decay with time. The study is done under the consideration that viscosity and density of the fluid are variable to the extent that it causes stratification and joule heating effect in the process of the flow. The purpose of the study is to examine how stratification and joule heating affect the flow in relation to the physical quantities namely, Stratification factor, Hartmann number, Viscoelastic coefficient, Joule heating parameter, Prandtl number, Eckert number, Schmidt number and Porosity of the medium etc. The non-dimensional governing equations are solved analytically by using regular perturbation technique, and the graphs are plotted using MATLAB programming language. The mathematical expressions for fluid and particle velocity, fluid temperature, fluid concentration, skin friction for fluid and particle, flow flux for fluid and particle, Nusselt number, Sherwood number at the plates are evaluated and their nature of variations for different numerical values of physical parameters are shown graphically, discussed and conclusions are drawn.

Keywords: Joule heating effect; Stratification effect; Inclined channel; Viscoelastic parameter; Mass diffusivity; Porous medium

PACS: 44.05.+e; 44.20.+b; 44.30.+v; 47.85.-g

INTRODUCTION

A non-Newtonian fluid embedded with symmetrically distributed uniform non-conducting solid spherical dust particles is commonly called ‘dusty viscoelastic fluid’. Study of viscoelastic flow has been receiving a great attention among the researchers in recent years because of its numerous applications in various fields of science and technology. The presence of dust particles in a fluid flow, has influences on fluid motion, for instance, situations arises in the movement of dust-laden air, in case of fluidization, use of dust in gas cooling systems, in power technology, in petroleum industry on purification of crude oil, solid fuel rocket nozzles used in guided missile system, flow of polymer solutions in industry, construction of wet-bulb thermometer, and in many kinds of fluid flow relating to engineering and industrial fields. Such flow simultaneously exhibits both viscous and elastic properties, normal stresses and relaxation effects. Various mathematical models have been designed to simulate such hydrodynamics behaviour of the fluid. When such a conducting fluid flows in presence of a magnetic field, the flow is influenced by the magnetic field. There are interactions between the conducting fluid and the applied magnetic field that in turn modifies the flow pattern with attendant effects on flow properties. Thus, it is possible to control effectively the flow by adjusting the magnitude and direction of the applied magnetic field. Moreover, the nature of interaction strongly depends upon the orientation of the magnetic field; as a result, working viscosity the flow system is under influence of the induced magnetic field. Understating the dynamics of such flow has relevant applications in the advent of technology that involves in various MHD devices such as MHD power generator, thermonuclear power devices etc. Moreover, engineers and scientists are interested on studies of flow of binary mixtures of viscous fluid and dust particles because of their wide range of real-world uses, including industrial, geophysical, astronomical, and many more.

Several authors have been carried out research on dusty viscoelastic fluid under various physical situations and conditions. Chakraborty and Sengupta [1] have studied the MHD flow of two immiscible viscoelastic Rivlin-Ericksen fluids in a rectangular channel. Datti et al. [2] had studied MHD viscoelastic fluid flow over a non-isothermal stretching sheet. Khan et al. [3] examined MHD transient flows in a porous medium with rectangular cross-section. Inverse solutions of a second-grade MHD fluid flow in porous medium was explored by Islam and Zhou [4]. Sivaraaj and Kumar [5] examined MHD heat and mass transfer in viscoelastic fluid flow over a vertical cone and flat plate. Akbar et al., [6] have investigated the MHD flow in a porous medium with prescribed vorticity. Sandeep and Sulochana [7] have examined the dual solutions of MHD micropolar fluid flow over a stretching/shrinking sheet. Verma and Singh [8] have studied MHD flow in a circular channel with porous medium. Reddy et al., [9] have studied the thermal radiation on MHD boundary layer flow over a stretching sheet with transpiration. Kiema and Wambua [10] have studied the steady and unsteady viscous incompressible MHD fluid flow. Ramadevi et. al., [11] have examined MHD Carreau fluid flow over a thickness melting surface with Cattaneo-Christov heat flux. Haq et. al., [12] have studied the MHD flow of Maxwell fluid in a channel with porous medium. Raghunath and Ravuri [13] have investigated the Hall effects, Soret effects and rotational

effect on unsteady MHD fluid flow through a porous medium. Hall effects on the MHD flow of the Rivlin-Ericksen fluid in porous plate was explored by Krishna and Vajravelu [14]. Heat transfer of MHD dusty fluid flow over an inclined irregular porous channel has been examined by Kalpana and S. Saleem [15]. Recently, Kodi et al. [16] have examined MHD mixed convection flow of Maxwell nanofluid through a vertical cone and Raghunath et al. [17] have explored radiation absorption on MHD fluid flow through porous medium over a vertical plate with heat source.

Joule heating in magnetodynamics system is a consequence of the electrical resistance of the conducting medium. The energy dissipated as heat due to the resistance of the fluid to the electric current is known as Joule heating. The Joule heating effect contribute to the overall energy balance in MHD systems. It is crucial to consider this heat generation when analysing the efficiency and performance of MHD devices. Researchers have considerable interest in this field and give noteworthy conclusion by using this phenomenon. Zhang et al. [18] studied the Joule heating effects on natural convection participating MHD under different levels of thermal radiation. Mousavi et al. [19] examined 2D-3D analysis of Joule and viscous heating effect on MHD. Jamalabadi and Park [20] have investigated on thermal radiation, joule heating, and viscous dissipation effects on MHD with uniform surface temperature. Bhatti and Rashidi [21] have studied heat and mass transfer with Joule heating on MHD peristaltic blood flow under influence of Hall effect. Hayat et al. [22] studied the Joule heating effects on MHD flow of Burgers' fluid. Recently, Kheder et al. [23] investigated the effect of Joule heating and MHD on periodical analysis of current density and amplitude of heat transfer.

In many of the above studies the physical properties of the ambient fluid were supposed to be non-variable. However, practically, the physical properties of the ambient fluid e.g. density, viscosity varies with temperature that in turn causes fluid stratification and thereby influences the fluid flow and heat transfer. The impact of Stratification effect on MHD have been discussed by several researchers, for example, Daniel et al. [24], Mutuku and Makinde [25], Khashi'ie et al. [26], Waqas et al. [27], Khan et al. [28]. Motivating with the works mentioned above and the idea of stratification of fluid due to the variation of fluid density and viscosity we have tried to investigate the flow and heat transfer on magnetohydrodynamics viscoelastic fluid flow through an inclined parallel plate channel in presence of uniform magnetic field. Such kind of problem often arises in many situations e.g. in the field of power generation using MHD fluid (MHD generator), MHD controlled forced and heat exchange flow such as in gas turbine etc. Besides these, the influence of dust particles is also utilized many industrial purposes such as in the production of rayon and nylon, pulp and paper industry, powder technology, production of plastic, textile industry, treating environment pollution, petroleum industry, purification of rain water, chemical processing, nuclear processing in the production of plastic sheet and electronics bundles etc. In such flows, stratification effect developed due to the variation of fluid density and viscosity.

The present study tries to examine an unsteady flow of dusty viscoelastic MHD fluid in a porous medium down an inclined parallel plate channel in presence of uniform magnetic field and molecular diffusivity. The issue is investigated in terms of the stratification and joule heating effect caused by varying fluid density and viscosity in a porous medium. Expressions for fluid and dust particle velocity, temperature distribution, concentration distribution, skin friction for fluid and particle, flux flow for fluid and particle, Nusselt number and Sherwood number at the plates are obtained under the assumption that the plates are positioned at different temperatures that decay exponentially over time. The effects of aforementioned expressions are analysed graphically for various values of the non-dimensional physical quantities Stratification factor, Hartmann number, Viscoelastic parameters, Joule heating parameter, Prandlt number, Eckert number, Schmidt number and Porosity of the medium.

FORMULATION OF THE PROBLEM

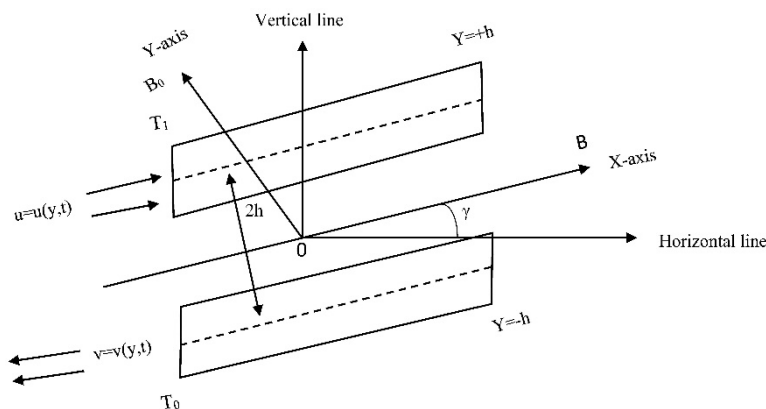


Figure 1. Diagram of the Physical problem

We take into account the laminar convection flow of a viscous, incompressible, electrically conducting fluid between two parallel plate channel that are spaced apart by $2h$ and inclined horizontally by an angle γ . The plates are kept at two different temperatures that exponentially decay with time. Let x -axis be the central line of the channel along the motion of the fluid and y -axis be perpendicular to it. The fluid velocity (u) and dust particle velocity (v) are equal and opposite in direction. A uniform magnetic field B_0 is applied normally to the parallel plates.

ASSUMPTIONS

The following assumptions are taken to write down the governing equations:

- i. Because of the infinite length of the plates, the fluid velocity (u) and dust particle velocity (v) are functions of y and t only.
- ii. During fluid motion, the number density of dust particles remains constant and is negligibly small.
- iii. The dust particles are neither subject to chemical reactions nor heat radiation.
- iv. The effects of the Hall, Polarization, Buoyancy are insignificant.
- v. Magnetic Reynolds number is so small that the effect of induced magnetic field is negligible.
- vi. Dust particles are identical, solid, elastic sphere, symmetric in size, also they are equally distributed within the fluid motion and electrically non-conducting.
- vii. Initially(t=0) there is no flow and the parallel plates are at same temperature, and thereafter, (t>0) the plates are at two different temperatures i.e. t>0, T=T₀ at y=-h and t>0, T=T₁ at y=+h.
- viii. Throughout the channel, the fluid's density and viscosity are varying along the y-axis as follows:

$$\rho = \rho_0 e^{-n(\frac{y}{h+1})}, \text{ and } \mu = \mu_0 e^{-n(\frac{y}{h+1})},$$

where n is fluid's stratification factor and ρ₀, μ₀ are coefficient of density and viscosity on the line of the channel at y=-h respectively so that the velocity and magnetic field distribution are V= [u(y,t), 0, 0] and B= [0, B₀, 0] respectively.

MATHEMATICAL ANALYSIS

The governing equations under the above assumptions are given as:

Momentum equations

$$\frac{\partial u}{\partial t} = -\frac{1}{\rho} \frac{\partial p}{\partial x} - \frac{nv_1}{h} \frac{\partial u}{\partial y} + v_1 \frac{\partial^2 u}{\partial y^2} + v_2 \frac{\partial}{\partial t} \left(\frac{\partial^2 u}{\partial y^2} \right) - \frac{v_1}{k_1} u + g \sin \gamma + \frac{k_0 N}{\rho} (v - u) - \frac{\sigma}{\rho} (B_0^2 u). \tag{1}$$

$$m \frac{\partial v}{\partial t} - k_0 (u - v) = 0. \tag{2}$$

Equation of fluid static

$$\frac{\partial p}{\partial y} + \rho g \cos \gamma = 0. \tag{3}$$

Energy equation

$$\frac{\partial T}{\partial t} = \frac{k}{\rho c_p} \frac{\partial^2 T}{\partial y^2} + \frac{v_1}{c_p} \left(\frac{\partial u}{\partial y} \right)^2 + \frac{v_2}{c_p} \frac{\partial}{\partial t} \left(\frac{\partial u}{\partial y} \right)^2 + \frac{\sigma B_0^2}{\rho c_p} u^2. \tag{4}$$

Mass equation

$$\frac{\partial C}{\partial t} = D \frac{\partial^2 C}{\partial y^2}, \tag{5}$$

where v₁ is the kinematics coefficient of fluid viscosity, v₂ is the kinematics coefficient of viscoelasticity, k₁ is the porosity of the medium, g is gravitational acceleration, k₀ is the proportionality constant, N is the number density of the dust particles, σ and κ are the electrical and thermal conductivity of the fluid, m is the mass of the dust particle, T and C are dimensional temperature and concentration respectively, C_p is specific heat at constant pressure, D is the mass diffusion coefficient and p is the fluid pressure defined as:

$$p = \rho g (x \sin \gamma - y \cos \gamma) + \rho x a(t) + A, \tag{6}$$

where a(t) is a function of t alone and A is constant value.

using (6), equation (1) can be written as

$$\frac{\partial u}{\partial t} = -a(t) - \frac{nv_1}{h} \frac{\partial u}{\partial y} + v_1 \frac{\partial^2 u}{\partial y^2} + v_2 \frac{\partial}{\partial t} \left(\frac{\partial^2 u}{\partial y^2} \right) - \frac{v_1}{k_1} u + \frac{k_0 N}{\rho} (v - u) - \frac{\sigma}{\rho} (B_0^2 u). \tag{7}$$

The boundary conditions of the problem are

$$\left. \begin{aligned} u = 0, \quad v = 0, \quad T = T_0 e^{-2nt}, \quad C = C_0 e^{-2nt} \quad \text{at} \quad y = -h \\ u = u_0 e^{-nt}, \quad v = v_0 e^{-nt}, \quad T = T_1 e^{-2nt}, \quad C = C_1 e^{-2nt} \quad \text{at} \quad y = +h \end{aligned} \right\} \tag{8}$$

where T₀ and C₀ are the fluid's temperature and concentration at y=-h respectively and T₁ and C₁ are the temperature and concentration of fluid at y=+h respectively.

Now we consider the following non-dimensional parameters

$$\left. \begin{aligned} u^* = \frac{u}{u_0}, \quad v^* = \frac{v}{v_0}, \quad x^* = \frac{x}{h}, \quad y^* = \frac{y}{h}, \quad t^* = \frac{tu_0}{h} \\ a^* = \frac{ah}{u_0^2}, \quad T^* = \frac{T}{T_0}, \quad C^* = \frac{C}{C_0}, \quad K^* = \frac{h}{\sqrt{k_1}}, \quad \lambda = \frac{u_0}{v_0} \end{aligned} \right\} \tag{9}$$

Substituting (9) in the equations (7), (2), (4) and (5) and then removing the asterisks, we get

$$\frac{\partial u}{\partial t} = -a(t) - \frac{n}{R} \frac{\partial u}{\partial y} + \frac{1}{R} \frac{\partial^2 u}{\partial y^2} - \eta \left(\frac{\partial}{\partial t} \frac{\partial^2 u}{\partial y^2} \right) - \frac{K^2}{R} u + \frac{C}{R_t} \left(\frac{v}{\lambda} - u \right) - \frac{M^2}{R} u, \tag{10}$$

$$R_t \frac{\partial v}{\partial t} - (\lambda u - v) = 0, \tag{11}$$

$$\frac{\partial^2 T}{\partial y^2} = RP_r \frac{\partial T}{\partial t} - EP_r \left(\frac{\partial u}{\partial y} \right)^2 + \eta ERP_r \frac{\partial}{\partial t} \left(\frac{\partial u}{\partial y} \right)^2 - Ju^2, \tag{12}$$

$$\frac{\partial^2 C}{\partial y^2} = RS_c \frac{\partial C}{\partial t} \tag{13}$$

where,

$R = \frac{u_0 h}{\nu_1}$ is Reynolds number, $\eta = -\frac{\nu_2}{h^2}$ is viscoelastic parameter,

$C = \frac{mN}{\rho}$ is dust particle concentration, $P_r = \frac{\mu C_p}{k}$ is Prandtl number,

$M = \sqrt{\frac{B_0^2 h^2 \sigma}{\rho \nu_1}}$ is Hartmann number, $E = \frac{u_0^2}{C_p T_0}$ is Eckert number,

$R_t = \frac{m u_0}{k_0 h}$ is relaxation time parameter of dust particles,

$S_c = \frac{\nu_1}{D}$ is Schmidt number, $J = \frac{\sigma B_0^2 u_0^2 h^2}{\kappa T_0}$ is Joule heating parameter.

The non-dimensional boundary conditions are

$$\left. \begin{aligned} u = 0, \quad v = 0, \quad T = e^{-2nt}, \quad C = e^{-2nt} \quad \text{at } y = -h \\ u = e^{-nt}, \quad v = e^{-nt}, \quad T = \chi e^{-2nt}, \quad C = \psi e^{-2nt} \quad \text{at } y = +h \end{aligned} \right\} \tag{14}$$

where $\chi = \frac{T_1}{T_0}$ and $\psi = \frac{C_1}{C_0}$ are constant temperature and concentration respectively.

SOLUTIONS

To solve the equations (10) -(13) under the boundary conditions (14), we assume

$$u = f(y)e^{-nt}, \quad v = g(y)e^{-nt}, \quad T = \theta(y)e^{-2nt}, \quad C = \phi(y)e^{-2nt}, \quad a = a_0 e^{-nt}. \tag{15}$$

Substituting (15) in equations (10) -(13), we get

$$f''(y) - A_1 f'(y) + A_2 f(y) - A_3 = 0 \tag{16}$$

$$g(y) = A_4 f(y) \tag{17}$$

$$\theta''(y) + A_5 \theta(y) + A_6 (f'(y))^2 + A_7 (f(y))^2 = 0 \tag{18}$$

$$\phi''(y) + A_8 \phi = 0 \tag{19}$$

where,

$$\begin{aligned} A_1 = \frac{n}{1 + n\eta R}, \quad A_2 = \frac{R}{1 + n\eta R} \left[n - \left(\frac{K^2 + M^2}{R} \right) - C \frac{n}{1 - nR_t} \right], \quad A_3 = \frac{Ra_0}{1 + n\eta R}, \\ A_4 = \frac{\lambda}{1 - nR_t}, \quad A_5 = 2nRP_r, \quad A_6 = EP_r(1 + 2n\eta R), \quad A_7 = J = EM^2 P_r, \quad A_8 = 2nRS_c \end{aligned}$$

Now, the corresponding boundary conditions are

$$\left. \begin{aligned} f(-1) = 0, \quad g(-1) = 0, \quad \theta(-1) = 1, \quad \phi(-1) = 1 \\ f(+1) = 1, \quad g(+1) = \frac{\lambda}{A_4}, \quad \theta(+1) = \chi, \quad \phi(+1) = \psi \end{aligned} \right\} \tag{20}$$

The solutions of the equations (16) -(19) with respect to the boundary conditions (20) are

$$f(y) = \left[C_1 e^{m_1 y} + C_2 e^{m_2 y} + \frac{A_3}{A_2} \right]. \tag{21}$$

$$g(y) = A_4 \left[C_1 e^{m_1 y} + C_2 e^{m_2 y} + \frac{A_3}{A_2} \right], \tag{22}$$

$$\begin{aligned} \theta(y) = C_3 \cos \sqrt{A_5} y + C_4 \sin \sqrt{A_5} y - [(S_1 + S_4) e^{2m_1 y} + (S_2 + S_5) e^{2m_2 y} \\ + (S_3 + S_6) e^{(m_1 + m_2) y} + S_7 e^{m_1 y} + S_8 e^{m_2 y} + S_9] \end{aligned} \tag{23}$$

$$\phi(y) = C_5 \cos \sqrt{A_8} y + C_6 \sin \sqrt{A_8} y \tag{24}$$

where,

$$\begin{aligned}
 m_1 &= A_1 + \sqrt{\frac{(A_1^2 - 4A_2)}{2}}, & m_2 &= A_1 - \sqrt{\frac{(A_1^2 - 4A_2)}{2}}, & S_1 &= \frac{A_6 C_1^2 m_1^2}{4m_1^2 + A_5}, & S_2 &= \frac{A_6 C_1^2 m_2^2}{4m_2^2 + A_5}, \\
 C_1 &= \left[\frac{A_3}{A_2} \left(\frac{\sinh m_2}{\sinh(m_1 - m_2)} \right) + \frac{e^{-m_2}}{2 \sinh(m_1 - m_2)} \right], & C_2 &= - \left[\frac{A_3}{A_2} \left(\frac{\sinh m_1}{\sinh(m_1 - m_2)} \right) + \frac{e^{-m_1}}{2 \sinh(m_1 - m_2)} \right], \\
 S_3 &= \frac{2A_6 C_1 C_2 m_1 m_2}{(m_1 + m_2)^2 + A_5}, & S_4 &= \frac{A_7 C_1^2}{4m_1^2 + A_5}, & S_5 &= \frac{A_7 C_2^2}{4m_2^2 + A_5}, & S_6 &= \frac{2A_7 C_1 C_2}{(m_1 + m_2)^2 + A_5}, \\
 S_7 &= \frac{2A_3 A_7 C_1}{A_2(m_1^2 + A_5)}, & S_8 &= \frac{2A_3 A_7 C_2}{A_2(m_2^2 + A_5)}, & S_9 &= A_7 \left(\frac{A_3}{A_2} \right)^2, & C_5 &= \frac{1 + \psi}{2 \cos \sqrt{A_8}}, & C_6 &= \frac{\psi - 1}{2 \sin \sqrt{A_8}}, \\
 C_3 &= \left(\frac{1}{\cos \sqrt{A_5}} \right) \left[\frac{(1 + \chi)}{2} + (S_1 + S_4) \cosh 2m_1 + (S_2 + S_5) \cosh 2m_2 + (S_3 + S_6) \cosh(m_1 + m_2) \right. \\
 &+ S_7 \cosh m_1 + S_8 \cosh m_2 + S_9 \left. \right], & C_4 &= \left(\frac{1}{\sin \sqrt{A_5}} \right) \left[\frac{(\chi - 1)}{2} + (S_1 + S_4) \sinh 2m_1 + (S_2 + S_5) \sinh 2m_2 \right. \\
 &+ (S_3 + S_6) \sinh(m_1 + m_2) + S_7 \sinh m_1 + S_8 \sinh m_2 \left. \right]
 \end{aligned}$$

Putting the solutions of f(y), g(y), θ(y) and φ(y) from equations (21) -(24) in equation (15), we get the final solutions

$$u(y, t) = \left[C_1 e^{m_1 y} + C_2 e^{m_2 y} + \frac{A_3}{A_2} \right] e^{-nt} \tag{25}$$

$$v(y, t) = A_4 \left[C_1 e^{m_1 y} + C_2 e^{m_2 y} + \frac{A_3}{A_2} \right] e^{-nt} \tag{26}$$

$$T(y, t) = \left\{ C_3 \cos \sqrt{A_5} y + C_4 \sin \sqrt{A_5} y - [(S_1 + S_4) e^{2m_1 y} + (S_2 + S_5) e^{2m_2 y} + (S_3 + S_6) e^{(m_1+m_2)y} + S_7 e^{m_1 y} + S_8 e^{m_2 y} + S_9] \right\} e^{-2nt} \tag{27}$$

$$C(y, t) = [C_5 \cos \sqrt{A_8} y + C_6 \sin \sqrt{A_8} y] e^{-2nt} \tag{28}$$

Skin-Friction

The viscous drag (Skin friction) for fluid (τ_f) and for dust particles (τ_p) acting at the plates are defined as:

$$\tau_f = \left[\left(\frac{1}{R} - \eta \frac{\partial}{\partial t} \right) \left(\frac{\partial u}{\partial y} \right) \right]_{y=\pm 1} = \left[\left(\frac{1}{R} + n\eta \right) (C_1 m_1 e^{\pm m_1} + C_2 m_2 e^{\pm m_2}) \right] e^{-nt}, \tag{29}$$

$$\tau_p = \left[\left(\frac{1}{R} - \eta \frac{\partial}{\partial t} \right) \left(\frac{\partial v}{\partial y} \right) \right]_{y=\pm 1} = A_4 \left[\left(\frac{1}{R} + n\eta \right) (C_1 m_1 e^{\pm m_1} + C_2 m_2 e^{\pm m_2}) \right] e^{-nt}. \tag{30}$$

Fluid and Particle Flux

The flux of flow for fluid (Q_f) and for particle (Q_p) throughout the channel is defined as:

$$Q_f = \int_{-1}^1 u dy = 2 \left[\frac{C_1}{m_1} \sinh m_1 + \frac{C_2}{m_2} \sinh m_2 + \frac{A_3}{A_2} \right] e^{-nt}$$

$$Q_p = \int_{-1}^1 v dy = 2A_4 \left[\frac{C_1}{m_1} \sinh m_1 + \frac{C_2}{m_2} \sinh m_2 + \frac{A_3}{A_2} \right] e^{-nt}$$

Nusselt Number

The rate of heat transfer in terms of Nusselt number (N_u) at the plates is defined as:

$$\begin{aligned}
 N_u = \left[\frac{\partial T}{\partial y} \right]_{y=\pm 1} &= \left\{ \sqrt{A_5} (-C_3 \sin \sqrt{A_5} + C_4 \cos \sqrt{A_5}) - [2m_1 (S_1 + S_4) e^{\pm 2m_1} \right. \\
 &+ 2m_2 (S_2 + S_5) e^{\pm 2m_2} + (m_1 + m_2) (S_3 + S_6) e^{\pm (m_1+m_2)} + m_1 S_7 e^{\pm m_1} + m_2 S_8 e^{\pm m_2} \left. \right\} e^{-2nt}
 \end{aligned} \tag{31}$$

Sherwood Number

The rate of mass transfer in terms of Sherwood number (Sh) at the plates is given as:

$$Sh = \left[\frac{\partial C}{\partial y} \right]_{y=\pm 1} = \left[\sqrt{A_8} (-C_5 \sin \sqrt{A_8} + C_6 \cos \sqrt{A_8}) \right] e^{-2nt} \tag{32}$$

RESULT AND DISCUSSION

The aim of the study is to investigate the effect of stratification factor (n), Joule heating (J) and other physical parameters such as, Hartmann number (M), porosity of the medium (K), viscoelastic parameter (η), Prandtl number (Pr),

Eckert number (Ec), Schmidt number (Sc) on fluid and particle velocity, fluid temperature, fluid concentration, Skin friction for fluid and particle, rate of heat transfer in terms of Nusselt number, rate of mass transfer in terms of Sherwood number. The numerical results for Skin friction, Nusselt number, Sherwood number have been carried out at the upper wall ($y=+1$) of the channel. This helped us comprehend the problem's physical importance better. The governing equations are solved by using regular perturbation method, and the graphs are plotted in MATLAB which has been described in Figures (2) -(22).

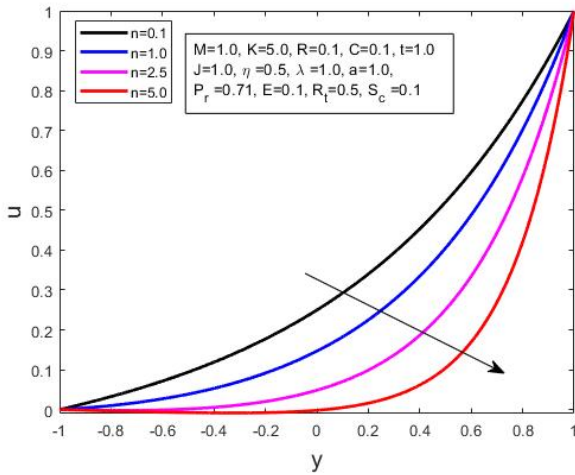


Figure 2. Effect of n on Fluid Velocity Profile

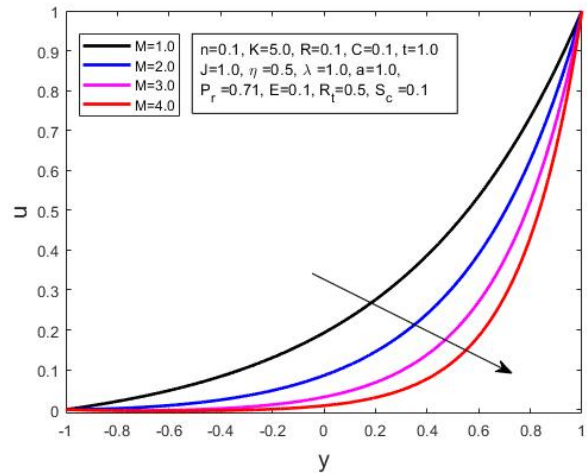


Figure 3. Effect of M on Fluid Velocity Profile

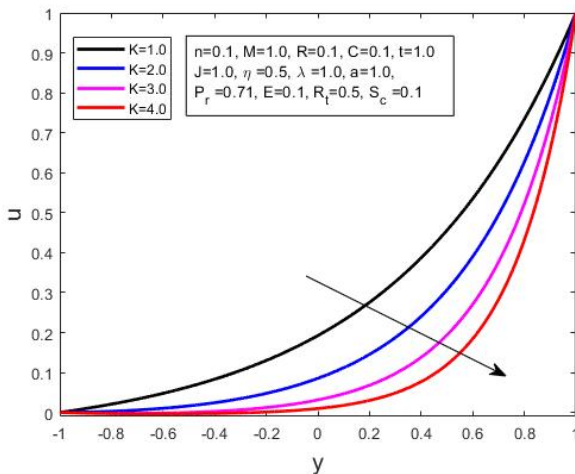


Figure 4. Effect of K on Fluid Velocity Profile

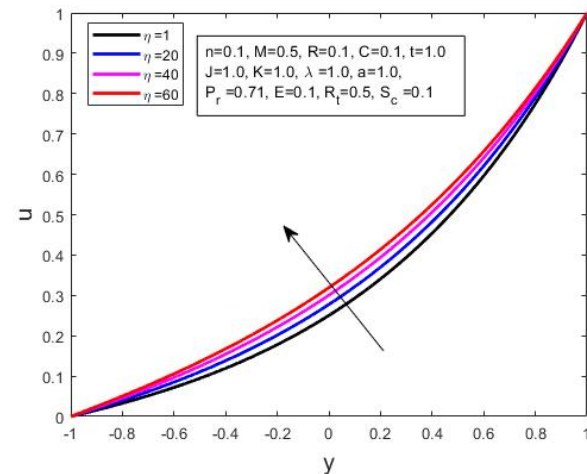


Figure 5. Effect of η on Fluid Velocity Profile

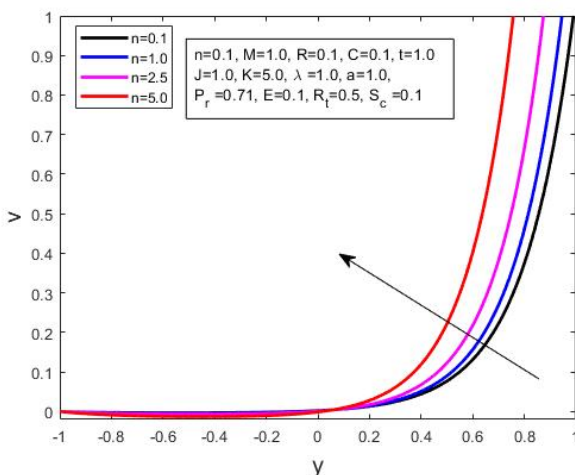


Figure 6. Effect of n on Particle Velocity Profile

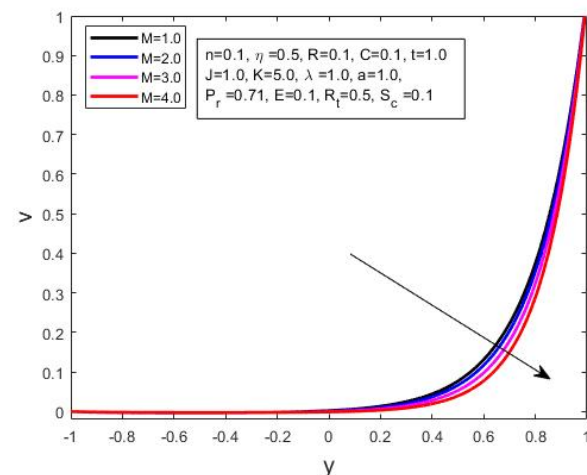


Figure 7. Effect of M on Particle Velocity Profile

Figures 2-5 show the impact of Stratification factor (n), Hartmann number (M), Porosity parameter (K) and Viscoelastic parameter (η) on fluid velocity. Figure 2 shows that the fluid velocity profile reduces with the increase in values of stratification factor. This arises due to the fact that increase in stratification factor increases the difference of density of momentum boundary layer, which illustrates a decrease in the fluid velocity profile. From Figure 3, it is clear that the fluid velocity reduces with the increase in values of Hartmann number. This is because the magnetic field creates a Lorentz force, which always produces resistance to the fluid flow and slows down the fluid velocity.

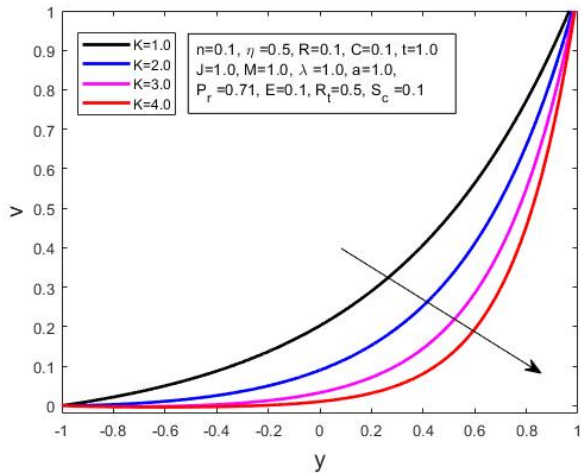


Figure 8. Effect of K on Particle Velocity Profile

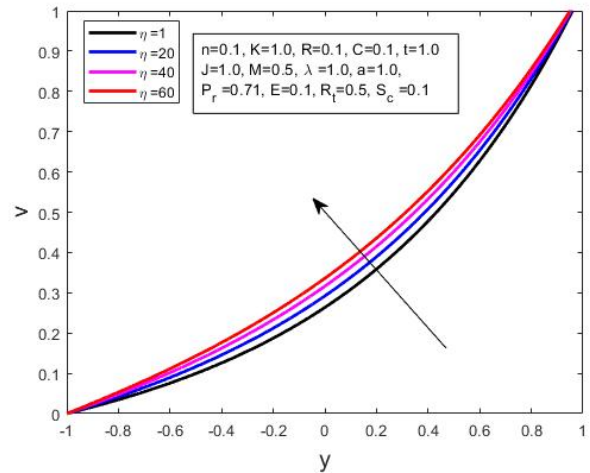


Figure 9. Effect of η on Particle Velocity Profile

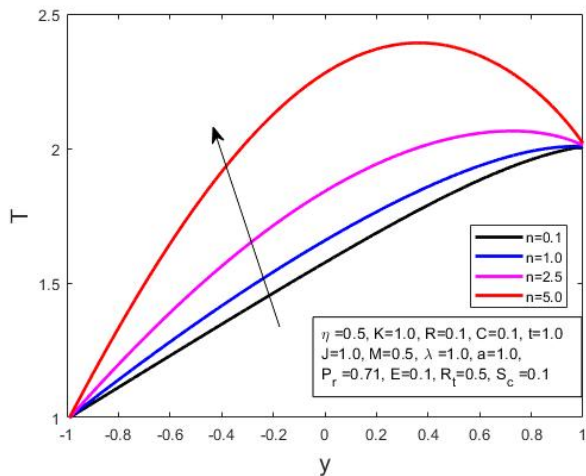


Figure 10. Effect of n on Fluid Temperature Profile

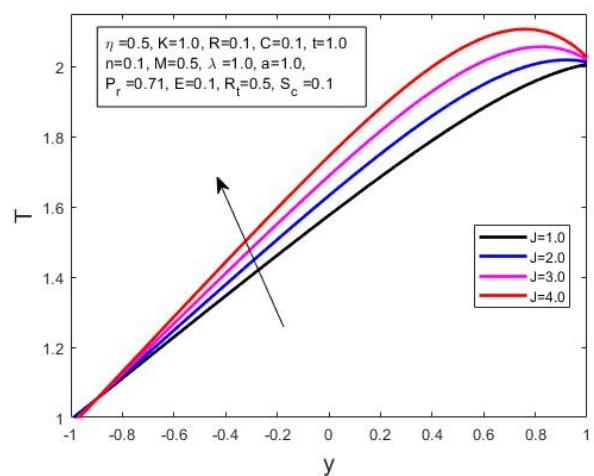


Figure 11. Effect of J on Fluid Temperature Profile

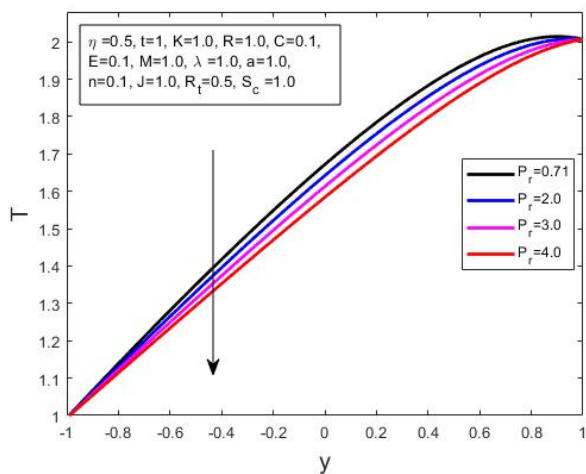


Figure 12. Effect of Pr on Fluid Temperature Profile

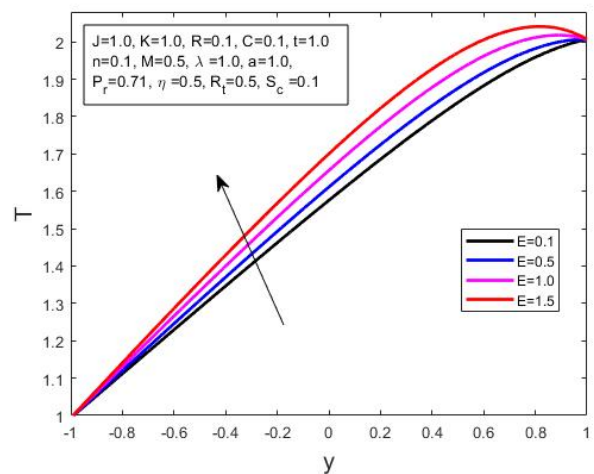


Figure 13. Effect of E on Fluid Temperature Profile

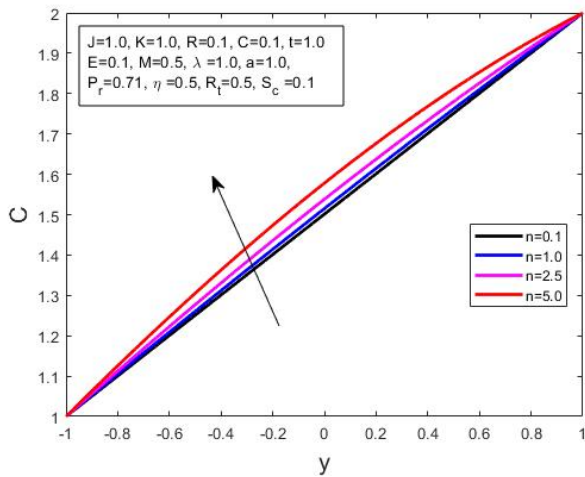


Figure 14. Effect of n on Fluid Concentration Profile

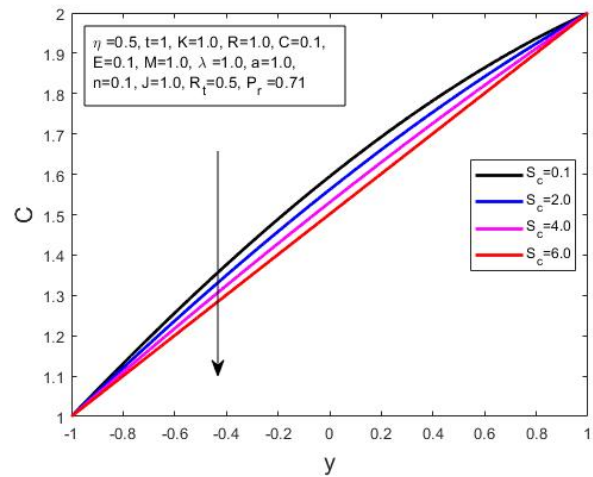


Figure 15. Effect of Sc on Fluid Concentration Profile

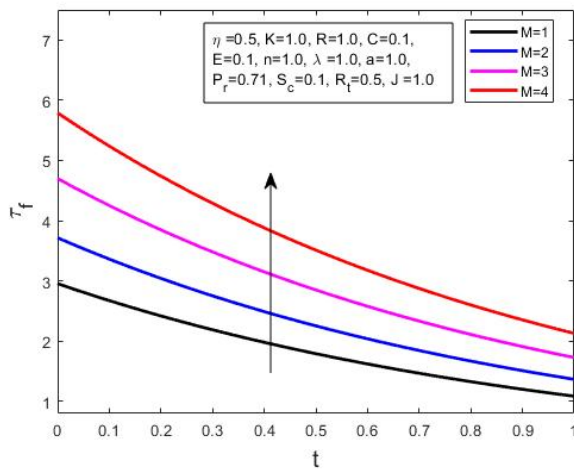


Figure 16. Effect of M on Fluid Skin friction

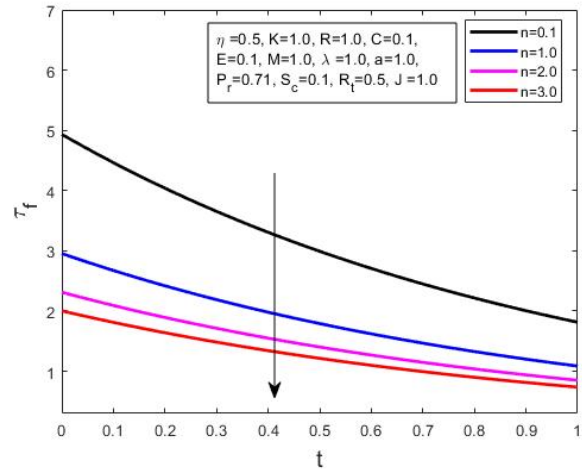


Figure 17. Effect of n on Fluid Skin friction

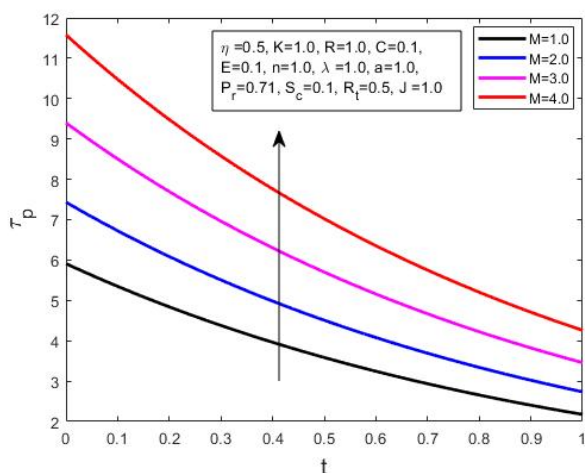


Figure 18. Effect of M on Particle Skin friction

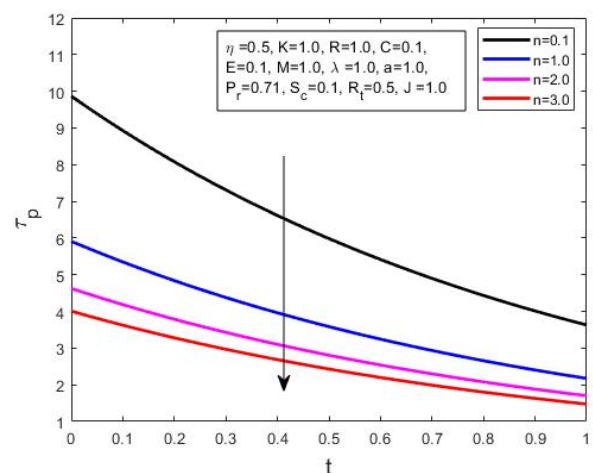


Figure 19. Effect of n on Particle Skin friction

Figure 4 depict that the fluid velocity profile decreases with the rise in values of porosity parameter. This occurs because the fluid flow is more restricted in the presence of porous medium, which slows the flow and lowers its velocity. Figure 5 elucidates that the fluid velocity profile increases with escalating values of viscoelastic parameter (η). Physically, η is negative to kinematic viscosity. Due to this low viscosity, enhancing values of η produce high fluid velocity.

Figures 6-9 represent the variation of particle velocity profile for different values of Stratification factor, Hartmann number, Porosity parameter and Viscoelastic parameter respectively. Figure 6 displays that the stratification factor

increases the particle velocity profile, which shows an opposite behaviour for fluid velocity as mentioned above. However, figure 7, 8, 9 show almost similar behaviour as those for fluid velocity.

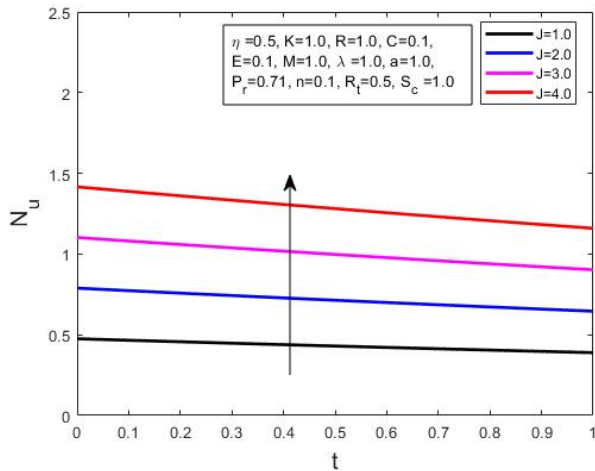


Figure 20. Effect of J on Nusselt number

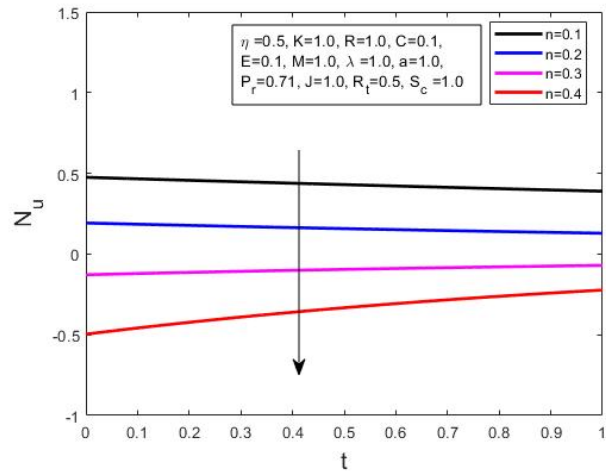


Figure 21. Effect of n on Nusselt number

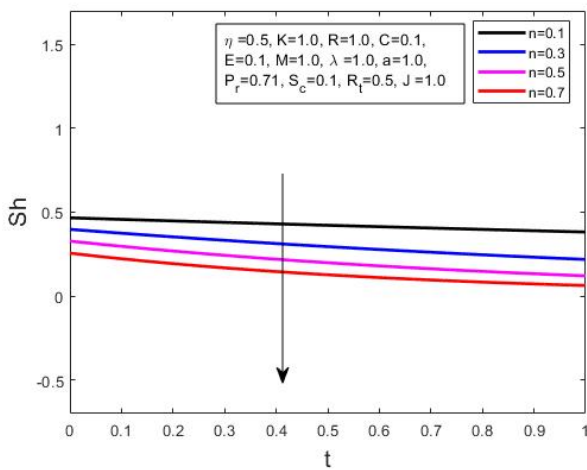


Figure 22. Effect of n on Sherwood number

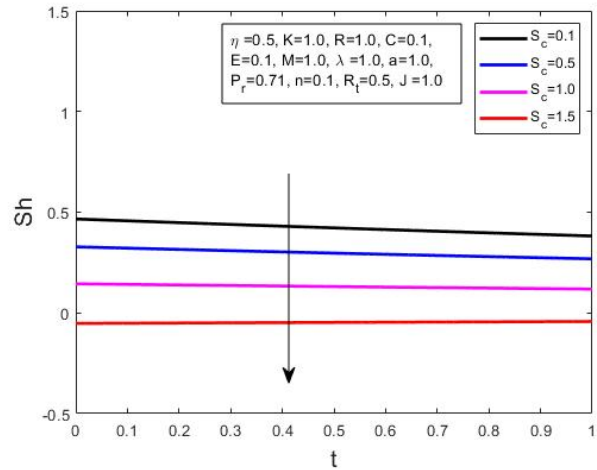


Figure 23. Effect of Sc on Sherwood number

Figures 10-13 illustrate the variation of fluid temperature for different values of Stratification factor, Joule heating parameter, Prandtl number and Eckert number respectively. Figure 10 and 11 admit that fluid temperature enhances due to the rise in stratification factor and Joule heating parameter respectively. Physically, with the increase in Joule heating, the heat generated is transferred to the surrounding of the channel, leading to an increase in temperature. Figure 12 shows an enhancement in Prandtl number causes a decrement in the temperature profile. It is due to the reason that the thermal conductivity declines with the enhancement in Prandtl number. On the other hand, figure 13 depicts that temperature increases with the escalating values of Eckert number. Physically, the thermal conductivity of the fluid rises as the dissipation is escalated which helps to enhance the thermal boundary layer thickness.

Figures 14 and 15 present the distribution of fluid concentration for different values of Stratification factor and Schmidt number respectively. Figure 14 reveals that the concentration exhibits an increasing trend with the escalating values of stratification factor. From figure 15, it is observed that the concentration profile de-escalates with the increase in Schmidt number. Physically, Schmidt number is the ratio of momentum diffusivity to mass diffusivity. So, with increasing Schmidt number, there is a strong reduction in concentration profile.

Figures 16 and 17 show how skin friction for fluid changes at the upper plate ($y=+1$) when a Hartmann number and Stratification factor change. It is observed that the skin friction exceeds with an increment as the Hartmann number increases. Further, skin friction falls as the stratification factor increases. Figure 18 and 19 registers the behaviour of skin friction for particle at the upper plate ($y=+1$) when Hartmann number and Stratification factor rises. A similar behaviour has been seen in figure 18 and 19 as those for figure 16 and 17 respectively.

Figures 20 and 21 show the variation of rate of heat transfer (N_u) at the upper plate ($y=+1$) with the rise in values of Joule heating parameter and Stratification factor respectively. It is observed that the Nusselt number increases with increasing Joule heating parameter and it decreases when stratification factor rises. The behaviour of Sherwood number at the upper plate ($y=+1$) has shown in figures 22 and 23. It is concluded that Sherwood number reduces for both increasing values of Stratification factor and Schmidt number.

CONCLUSIONS

The following conclusions can be made from the above results:

- i. The velocity of fluid decreases with stratification factor and reverse in nature with particle velocity, fluid temperature and fluid concentration.
- ii. Fluid and particle velocity enhance with raising value of viscoelastic parameter while opposite behaviour with Hartmann number and Porosity parameter.
- iii. Fluid temperature increases with the rise in Joule heating parameter and Eckert number. However, the temperature tends to fall when the Prandtl number is raised.
- iv. Increasing the Schmidt number decreases fluid concentration.
- v. Fluid and particle viscous drag enhance with the rise of Hartmann number and opposite behaviour with stratification factor.
- vi. The rate of heat transfer, in terms of Nusselt number, increases with the rise in Joule heating parameter but an opposite effect is observed with stratification factor.
- vii. The rate of mass transfer, in terms of Sherwood number, reduces for higher values of stratification factor and Schmidt number.

ORCID

©Saleem Javed Al Khayer, <https://orcid.org/0009-0003-6581-059X>

©Shyamanta Chakraborty, <https://orcid.org/0000-0001-5839-4856>

REFERENCES

- [1] G. Chakraborty, and P.R. Sengupta, "MHD flow of two immiscible visco-elastic Rivlin-Ericksen fluids through a non-conducting rectangular channel in presence of transient pressure gradient," *Czechoslovak journal of physics*, **42**(5), 525-531 (1992). <https://doi.org/10.1007/BF01605222>
- [2] P.S. Datti, K.V. Prasad, M.S. Ab, and A. Joshi, "MHD visco-elastic fluid flow over a non-isothermal stretching sheet," *International Journal of Engineering Science*, **42**(8-9), 935-946 (2004). <https://doi.org/10.1016/j.ijengsci.2003.09.008>
- [3] M. Khan, C. Fetecau, and T. Hayat, "MHD transient flows in a channel of rectangular cross-section with porous medium," *Physics letters A*, **369**(1-2), 44-54 (2007). <https://doi.org/10.1016/j.physleta.2007.04.076>
- [4] S. Islam, and C. Zhou, "Certain inverse solutions of a second-grade magnetohydrodynamic aligned fluid flow in a porous medium," *Journal of Porous Media*, **10**(4), (2007). <https://doi.org/10.1615/JPorMedia.v10.i4.60>
- [5] B.R. Kumar, and R. Sivaraj, "Heat and mass transfer in MHD viscoelastic fluid flow over a vertical cone and flat plate with variable viscosity," *International Journal of Heat and Mass Transfer*, **56**(1-2), 370-379 (2013). <https://doi.org/10.1016/j.ijheatmasstransfer.2012.09.001>
- [6] T. Akbar, Rab Nawaz, M. Kamran, and A. Rasheed, "Magnetohydrodynamic (MHD) flow analysis of second grade fluids in a porous medium with prescribed vorticity," *AIP Advances*, **5**(11), 117133 (2015). <https://doi.org/10.1063/1.4936184>
- [7] N. Sandeep, and C. Sulochana, "Dual solutions for unsteady mixed convection flow of MHD micropolar fluid over a stretching/shrinking sheet with non-uniform heat source/sink," *Engineering Science and Technology, an International Journal*, **18**(4), 738-745 (2015). <https://doi.org/10.1016/j.jestch.2015.05.006>
- [8] V.K. Verma, and S.K. Singh, "Magnetohydrodynamic flow in a circular channel filled with a porous medium," *Journal of Porous Media*, **18**(9), 9 (2015). <https://doi.org/10.1615/JPorMedia.v18.i9.80>
- [9] Y.D. Reddy, R. Dodda, and L.A. Babu, "Effect of thermal radiation on MHD boundary layer flow of nanofluid and heat transfer over a non-linearly stretching sheet with transpiration," *Journal of Nanofluids*, **5**(6), 889-897 (2016). <https://doi.org/10.1166/jon.2016.1284>
- [10] D.W. Kiema, Study of steady and unsteady viscous incompressible MHD fluid flow, PhD diss. University of Eldoret, 2017. <http://41.89.164.27:8080/xmlui/handle/123456789/1453>
- [11] B. Ramadevi, V. Sugunamma, K. Anantha Kumar, and J.V. Ramana Reddy, "MHD flow of Carreau fluid over a variable thickness melting surface subject to Cattaneo-Christov heat flux," *Multidiscipline Modelling in Materials and Structures*, **15**(1), 2-25 (2018). <https://doi.org/10.1515/jnet-2018-0069>
- [12] S. Ul Haq, W. Zahir, Z.A. Khan, I. Khan, F. Ali, and S. Ahmed, "Unsteady MHD Flow of Maxwell Fluid through a Channel with Porous Medium," *Journal of Porous Media*, **24**(5), 77-98 (2021). <https://doi.org/10.1615/JPorMedia.2021036508>
- [13] R. Kodi, and R. Mohanaramana, "Hall, Soret, and rotational effects on unsteady MHD rotating flow of a second-grade fluid through a porous medium in the presence of chemical reaction and aligned magnetic field," *International Communications in Heat and Mass Transfer*, **137**, 106287 (2022). <https://doi.org/10.1016/j.icheatmasstransfer.2022.106287>
- [14] M. Veera Krishna, and K. Vajravelu, "Hall effects on the unsteady MHD flow of the Rivlin-Ericksen fluid past an infinite vertical porous plate," *Waves in Random and Complex Media*, 1-24 (2022). <https://doi.org/10.1080/17455030.2022.2084178>
- [15] G. Kalpana, and S. Saleem, "Heat Transfer of Magnetohydrodynamic Stratified Dusty Fluid Flow through an Inclined Irregular Porous Channel," *Nanomaterials*, **12**(19), 3309 (2022). <https://doi.org/10.3390/nano12193309>
- [16] R. Kodi, C. Ganteda, A. Dasore, M.L. Kumar, G. Laxmaiah, M.A. Hasan, S. Islam, and A. Razak, "Influence of MHD mixed convection flow for Maxwell nanofluid through a vertical cone with porous material in the existence of variable heat conductivity and diffusion," *Case Studies in Thermal Engineering*, **44**, 102875 (2023). <https://doi.org/10.1016/j.csite.2023.102875>
- [17] R. Kodi, M. Obulesa, and K.V. Raju, "Radiation absorption on MHD free conduction flow through porous medium over an unbounded vertical plate with heat source," *International Journal of Ambient Energy*, **44**(1), 1712-1720 (2023). <https://doi.org/10.1080/01430750.2023.2181869>
- [18] J.K. Zhang, B.W. Li, and Y.Y. Chen, "The joule heating effects on natural convection of participating magnetohydrodynamics under different levels of thermal radiation in a cavity," *Journal of Heat Transfer*, **137**(5), 052502 (2015). <https://doi.org/10.1115/1.4029681>

- [19] S.M. Mousavi, B. Ehteshami, and A.A.R. Darzi, "Two-and-three-dimensional analysis of Joule and viscous heating effects on MHD nanofluid forced convection in microchannels," *Thermal Science and Engineering Progress*, **25**, 100983 (2021). <https://doi.org/10.1016/j.tsep.2021.100983>
- [20] M.A. Jamalabadi, and J.H. Park, "Thermal radiation, joule heating, and viscous dissipation effects on MHD forced convection flow with uniform surface temperature," *Open Journal of Fluid Dynamics*, **4**(2), 125-132 (2014). <https://doi.org/10.4236/ojfd.2014.42011>
- [21] M.M. Bhatti, and M.M. Rashidi, "Study of heat and mass transfer with Joule heating on magnetohydrodynamic (MHD) peristaltic blood flow under the influence of Hall effect," *Propulsion and Power Research*, **6**(3), 177-185 (2017). <https://doi.org/10.1016/j.jprr.2017.07.006>
- [22] T. Hayat, S. Ali, M. Awais, and A. Alsaedi, "Joule Heating Effects in MHD Flow of Burgers' fluid," *Heat Transfer Research*, **47**(12), 1083-1092 (2016). <https://doi.org/10.1615/HeatTransRes.2016008093>
- [23] N.B. Khedher, Z. Ullah, M. Alturki, C.R. Mirza, and S.M. Eldin, "Effect of Joule heating and MHD on periodical analysis of current density and amplitude of heat transfer of electrically conducting fluid along thermally magnetized cylinder," *Ain Shams Engineering Journal*, **15**(2), 102374 (2024). <https://doi.org/10.1016/j.asej.2023.102374>
- [24] Y.S. Daniel, Z.A. Aziz, Z. Ismail, and F. Salah, "Thermal stratification effects on MHD radiative flow of nanofluid over nonlinear stretching sheet with variable thickness," *Journal of Computational Design and Engineering*, **5**(2), 232-242 (2018). <https://doi.org/10.1016/j.jcde.2017.09.001>
- [25] W.N. Mutuku, and O.D. Makinde, "Double stratification effects on heat and mass transfer in unsteady MHD nanofluid flow over a flat surface," *Asia Pacific Journal on Computational Engineering*, **4**(2), 1-16 (2017). <https://doi.org/10.1186/s40540-017-0021-2>
- [26] N.S. Khashi'ie, N.M. Arifin, M.M. Rashidi, E.H. Hafidzuddin, and N. Wahi, "Magnetohydrodynamics (MHD) stagnation point flow past a shrinking/stretching surface with double stratification effect in a porous medium," *Journal of Thermal Analysis and Calorimetry*, **139**, 3635-3648 (2020). <https://doi.org/10.1007/s10973-019-08713-8>
- [27] M. Waqas, Z. Asghar, and W.A. Khan, "Thermo-solutal Robin conditions significance in thermally radiative nanofluid under stratification and magnetohydrodynamics," *The European Physical Journal Special Topics*, **230**(5), 1307-1316 (2021). <https://doi.org/10.1140/epjs/s11734-021-00044-w>
- [28] I. Khan, A. Hussain, M.Y. Malik, and S. Mukhtar, "On magnetohydrodynamics Prandtl fluid flow in the presence of stratification and heat generation," *Physica A: Statistical Mechanics and its Applications*, **540**, 123008 (2020). <https://doi.org/10.1016/j.physa.2019.123008>

ВПЛИВ СТРАТИФІКАЦІЇ ТА ДЖОУЛЕВОГО НАГРІВУ НА МГД ПОТІК ПИЛОВОЇ В'ЯЗКОПРУЖНОЇ РІДИНИ КРІЗЬ ПОХИЛІ КАНАЛИ У ПОРИСТОМУ СЕРЕДОВИЩІ ЗА НАЯВНОСТІ МОЛЕКУЛЯРНОЇ ДИФУЗІЇ

Салім Джабед Аль-Хайер^а, Шьяманта Чакраборті^б



^аДепартамент математики, Університет Гаухаті, Гувахаті, Камруп, 781014, Ассам, Індія

^бUGC-HRDC, Університет Гаухаті, Гувахаті, Камруп, 781014, Ассам, Індія

Проведено аналіз ламінарного МГД-конвекційного потоку запиленої в'язкопружної рідини другого порядку в пористому середовищі через похилий паралельний пластинчастий канал за наявності молекулярної дифузії. Пластини витримують при двох різних температурах, які з часом знижуються. Дослідження проводиться з урахуванням того, що в'язкість і щільність рідини є змінними в тій мірі, в якій це викликає розшарування і джоулевий ефект нагрівання в процесі потоку. Метою дослідження є вивчення того, як стратифікація та джоулеве нагрівання впливають на потік у зв'язку з фізичними величинами, а саме фактором стратифікації, числом Гартмана, коефіцієнтом в'язкопружності, параметром нагріву Джоуля, числом Прандтля, числом Еккерта, числом Шмідта та пористістю середовища. і т. д. Безвимірні керівні рівняння розв'язуються аналітично за допомогою методу регулярних збурень, а графіки будуються за допомогою мови програмування MATLAB. Оцінюються математичні вирази для швидкості рідини та частинок, температури рідини, концентрації рідини, поверхневого тертя для рідини та частинок, потоку рідини та частинок, числа Нуссельта, числа Шервуда на пластинах та їх характер варіацій для різних числових значень фізичних параметри показано графічно, обговорено та зроблено висновки.

Ключові слова: Джоулевий ефект нагріву; ефект стратифікації; похилий канал; в'язкопружний параметр; масопровідність; пористе середовище

A NUMERICAL STUDY ON THE MHD TERNARY HYBRID NANOFLUID ($Cu - Al_2O_3 - TiO_2/H_2O$) IN THE PRESENCE OF THERMAL STRATIFICATION AND RADIATION ACROSS A VERTICALLY STRETCHING CYLINDER IN A POROUS MEDIUM

 Rupam Shankar Nath*,  Rudra Kanta Deka

Department of Mathematics, Gauhati University, Guwahati-781014, Assam

*Corresponding Author e-mail: rupamnath23@gmail.com

Received January 7, 2024; revised January 31, 2024; accepted February 13, 2024

The primary objective of this study is to investigate the influence of thermal stratification on the magnetohydrodynamics (MHD) flow of water-based nano, hybrid, and ternary hybrid nanofluids, as they pass a vertically stretching cylinder within a porous media. The nanoparticles Cu , Al_2O_3 , and TiO_2 are suspended in a base fluid H_2O , leading to the formation of a ternary hybrid nanofluid ($Cu + Al_2O_3 + TiO_2/H_2O$). The use of a relevant similarity variable has been utilized to simplify the boundary layer equations which control the flow and transform the coupled nonlinear partial differential equations into a collection of nonlinear ordinary differential equations. The numerical results are calculated with the 3-stage Lobatto IIIa approach, specifically implemented by Bvp4c in MATLAB. This study presents a graphical and numerical analysis of the effects of various non-dimensional parameters, such as the Prandtl number, radiation parameter, heat source/sink parameter, magnetic parameter, porosity parameter, curvature parameter, thermal stratification parameter, and thermal buoyancy parameter, on the velocity, temperature, skin-friction coefficient, and Nusselt number. The impacts of these parameters are visually depicted through graphs and quantitatively represented in tables. The ternary hybrid nanofluid has a higher heat transfer rate than the hybrid nanofluid, and the hybrid nanofluid has a higher heat transfer rate than ordinary nanofluids.

Keywords: *Thermal Stratification; Stretching Vertical Cylinder; Ternary Hybrid Nanofluid; Porous Medium; Thermal Radiation; MHD; bvp4c*

PACS: 44.05.+e, 44.25.+f, 44.27.+g, 44.40.+a, 47.11.-j, 44.30.+v

1. INTRODUCTION

Ternary hybrid nanofluids are a specific kind of fluid that is made up of three distinct kinds of nanoparticles that are scattered throughout a base fluid. This article presents a study on the ternary hybrid nanofluid composed of copper (Cu), aluminum oxide (Al_2O_3), and titanium dioxide (TiO_2) nanoparticles, which are evenly distributed inside a water-based fluid. This ternary hybrid nanofluid has unique qualities that make it suitable for a variety of applications. The presence of copper (Cu) nanoparticles into the nanofluid has been found to improve thermal conductivity, whilst the addition of aluminum oxide (Al_2O_3) and titanium dioxide (TiO_2) nanoparticles has been observed to enhance heat transfer efficiency and stability. The utilization of this nanofluid is applicable in various applications such as heat exchangers, cooling systems, and electronic devices, with the purpose of enhancing heat dissipation and improving thermal management. Copper nanoparticles are known to possess antibacterial capabilities, whereas (TiO_2) nanoparticles have photocatalytic activity against bacteria and other bacteria. The application of the ternary hybrid nanofluid, comprising $Cu - Al_2O_3 - TiO_2$, presents a promising avenue for the development of antibacterial coatings on various surfaces, including medical equipment, textiles, and food packaging. These coatings effectively impede bacterial growth and contribute to the preservation of hygiene. Titanium dioxide (TiO_2) nanoparticles have photocatalytic properties, rendering them capable of facilitating the breakdown of organic contaminants and the disinfection of water. The use of the $Cu - Al_2O_3 - TiO_2$ ternary hybrid nanofluid has potential for application in water treatment procedures, facilitating the elimination of pollutants and enhancing the overall quality of water resources.

The term "nanofluid" refers to a type of artificial fluid that is characterized by the presence of very small particles in a base fluid suspended and typically have a size of less than 100 nanometers. The concept of nanofluid, first presented by [1], proposes that heat transfer fluids with floating metallic nanoparticles could provide a revolutionary new type of heat transfer fluids. [2] and [3] investigated the natural convective flow of nanofluids with radiation for moving vertical plate and vertical channel, respectively. In both research articles, the authors explored water-based nanofluids that include titanium dioxide, aluminum oxide, and copper. In the occurrence of heat production or absorption, [4] looks for a lie group solution to the problem of how the nanofluid moves past a horizontal plate reacting chemically. [5] uses the HAM to analyze the entropy of a nanofluid

consisting of water as the primary fluid and one of four distinct kinds of nanoparticles: TiO_2 , Al_2O_3 , Cu , and CuO flowing through a stretchable permeable surface. A numerical investigation on the flow of nanofluids in the boundary layer across a moving flat plate was performed by [6] to study the impacts of thermal radiation, viscous dissipation and thermal diffusion. In the context of velocity slip and temperature leap, [7] carried out an analytical investigation on the MHD nanofluid flow for a variety of water-based nanoparticles as they passed a continually stretching/shrinking permeable sheet. [8] applied the Lattice Boltzmann method for studying the MHD Cu-water nanofluid under the presence of Lorentz forces. Furthermore, [9] conducted a research on MHD Cu-water nanofluid flow across a cone and a wedge influenced by nonlinear thermal radiation. [10] and [11] researched the impacts of heat and mass transfer on nanofluid passing a moving or fixed vertical plate in the presence of a heat source and a chemical reaction, respectively. Additionally, MHD boundary layer nanofluid flow was studied by [12] as it passed over an exponentially accelerating vertical plate in presence of thermal radiation.

[13] and [14] examined the impacts of thermal and mass stratification over a vertical wavy truncated cone and a wavy surface, respectively. Furthermore, [15] have investigated how both stratification effects affect infinite vertical cylinders. [16] and [17] conducted a study to investigate the combined impact of thermal stratification and chemical reaction on the flow past an infinite vertical plate and an accelerated vertical plate, correspondingly. Similarly, [18] looks at how thermal stratification affects unsteady parabolic flow past an infinite vertical plate. [19] investigates the thermal stratification effects of a hybrid nanofluid consisting of $Cu - Al_2O_3/H_2O$ in a porous medium. Their study focuses on a vertically stretched cylinder and considers the influence of heat sink/source. They found that the thermal conductivity of hybrid nanofluids was significantly higher than that of nanofluids. Hence, the utilization of hybrid nanofluids exhibits a significant influence on enhancing thermal advancements.

[20] aims to investigate the heat transfer characteristics of the magnetohydrodynamic Casson hybrid nanofluid in the presence of a non-Fourier heat flux model and linear thermal radiation along a horizontal porous stretched cylinder. With melting/non-melting heat transfer in mind, [21] is interested in the laminar, stable electro magnetohydrodynamic flow and entropy formation of SWCNT-blood nanofluid. The study of magneto $Cu - Al_2O_3$ /water hybrid nanofluid flow in a non-Darcy porous square cavity was done by [22].

The study conducted by [23] focuses on investigating the phenomenon of natural convection within a sinusoidal wavy cavity that is filled with a hybrid nanofluid consisting of $TiO_2 - Cu$ particles suspended in water. The analysis takes into account the influence of internal heat generation, an angled magnetic field, and thermal radiation on the convection process. The investigation conducted by [24] focused on the nonlinear buoyancy-driven flow of hybrid nanofluid passing a spinning cylinder, taking into account the effects of quadratic thermal radiation.

[25] conducted a study on the impact of non-linear Darcy-Forchheimer flow in the context of electromagnetic hydrodynamics (EMHD) ternary hybrid nanofluid, namely composed of $Cu - CNT - Ti$ and water. They found that the ternary hybrid nanofluid had a greater impact on the temperature profile than either the nanofluid or the hybrid nanofluid alone. [26] conducted a study on the heat transport characteristics of ternary hybrid nanofluid flow in the presence of a magnetic dipole with nonlinear thermal radiation. [27] performed an investigation on the computational valuation of Darcy ternary-hybrid nanofluid flow through an extending cylinder with induction effects. In order to improve the heat transfer of a magnetized ternary hybrid nanofluid $Cu - Al_2O_3 - MWCNT$ /water, [28] investigated the influence of nanoparticle shape.

The primary objective of [29] research is to investigate the application of a water-based ternary hybrid nanofluid in the context of advanced cooling for radiators. This nanofluid comprises three distinct types of nanoparticles: spherical aluminum oxide (Al_2O_3) cylindrical carbon nanotubes (CNT), and platelet-shaped particles (Graphene). [30] analyze the behavior of a ternary hybrid nanofluid (THNF) with tangent hyperbolic (T-H) flow characteristics as it interacts with a rough-yawed cylinder. The motion of the cylinder is induced using impulsive means, and the study focuses on the mixed convection mechanism in conjunction with periodic magnetohydrodynamics. The impact of suction and heat source on MHD stagnation point flow of ternary hybrid nanofluid ($Cu - Fe_3O_4 - SiO_2$ /polymer) over convectively heated stretching/shrinking cylinder has been researched by [31]. [32] conducted research on the similarity solutions of the governing equations that describe the dynamics of a colloidal mixture consisting of water, spherical carbon nanotubes, cylindrical graphene, and platelet alumina nanoparticles. The study considered various levels of partial slip and examined the cases of forced convection, free convection, and mixed convection.

According to the literature review, as was mentioned in a previous research, no one has tried to show the MHD ternary nanofluid past a Vertically Stretching Cylinder in a porous medium. The main objective of the present study is to examine the heat transfer properties of a ternary hybrid nanofluid consisting of $Cu - Al_2O_3 - TiO_2$ particles dispersed in water. This investigation focuses on the heat transfer behavior around a Vertically Stretching Cylinder, taking into account the effects of thermal stratification, thermal radiation, and uniform heat sources and sinks. The governing equations of non-linear partial differential equations (PDEs) are transformed into ordinary differential equations (ODEs) by employing suitable self-similarity variables within the `bvp4c` solver of the MATLAB software. The `Bvp4c` technique utilized in this study to simulate the problem

is widely recognized, as demonstrated by its discussion and application in MATLAB by Shampine et al., [33] and Kierzenka et al., [34]. The graphical representation of the results is provided for several parameters such as δ, M, K, R, Q, Pr and λ .

2. MATHEMATICAL ANALYSIS

Consider a two-dimensional steady in-compressible ternary hybrid nanofluid consisting of $Cu - Al_2O_3 - TiO_2/H_2O$, which is immersed in a porous medium over a vertical stretchable cylinder of radius r_0 . The system is subjected to the influence of a heat source/sink, thermal stratification and thermal radiation. The flow of the ternary hybrid nanofluid is assumed to be in the axial x -direction, with the r coordinate representing the direction normal to the x -axis, as depicted in Figure 1. In this context, the variables "u" and "v" represent the velocity components of the ternary hybrid nanofluid along the r and x - axes, respectively. In this study, a magnetic field with a magnitude of B_0 is applied in a direction perpendicular to the propagation of the ternary hybrid nanofluid. The flow issue takes into account the thermal buoyancy effect while disregarding the Joule's impact. The velocity that causes linear stretching of the vertical cylinder is denoted as $u = a \frac{x}{l}$, where 'a' and 'l' represent the velocity and characteristic length of the cylinder, respectively. $T_w(x) = T_0 + A (\frac{x}{l})$ represents the assumed temperature of the wall, while $T_\infty(x) = T_0 + B (\frac{x}{l})$ represents the temperature of the ternary hybrid nanofluid at the ambient condition, where A, B , and T_0 are non-negative constants and the starting temperature, correspondingly. The governing equations for continuity, momentum, and energy in the context of a ternary hybrid nanofluid, as presented by [19], can be expressed as follows.

$$\frac{\partial(ru)}{\partial x} + \frac{\partial(rv)}{\partial r} = 0 \tag{1}$$

$$u \frac{\partial u}{\partial x} + v \frac{\partial u}{\partial r} = \frac{\mu_{mnf}}{\rho_{mnf}} \frac{1}{r} \frac{\partial}{\partial r} \left(r \frac{\partial u}{\partial r} \right) + \frac{(\rho\beta_T)_{mnf}}{\rho_{mnf}} g(T - T_\infty) - \frac{\sigma_{mnf}}{\rho_{mnf}} B_0^2 u - \frac{\mu_{mnf}}{\rho_{mnf}} \frac{u}{k'} \tag{2}$$

$$u \frac{\partial T}{\partial x} + v \frac{\partial T}{\partial r} = \frac{k_{mnf}}{(\rho c_p)_{mnf}} \frac{1}{r} \frac{\partial}{\partial r} \left(r \frac{\partial T}{\partial r} \right) - \frac{1}{(\rho c_p)_{mnf}} \frac{1}{r} \frac{\partial}{\partial r} \left(r \frac{\partial q'_r}{\partial r} \right) + \frac{Q_0}{(\rho c_p)_{mnf}} (T - T_\infty) \tag{3}$$

The following are the boundary conditions:

$$\begin{aligned} u = a \frac{x}{l}, \quad v = 0, \quad T = T_w(x) & \quad \text{when } r = r_0 \\ u = 0, \quad T \rightarrow T_\infty(x) & \quad \text{when } r \rightarrow \infty \end{aligned}$$

The radiative heat flux q'_r in Eqn. (2) is approximated by using the Rosseland approximation [35], as the nanofluid is assumed to be an optically thick fluid. In light of the research conducted by [7], the equation (3) can be rewritten as

$$u \frac{\partial T}{\partial x} + v \frac{\partial T}{\partial r} = \frac{k_f}{(\rho c_p)_{mnf}} \left(\frac{k_{mnf}}{k_f} + \frac{16\sigma^* T_\infty^3}{3k_f k} \right) \frac{1}{r} \frac{\partial}{\partial r} \left(r \frac{\partial T}{\partial r} \right) + \frac{Q_0}{(\rho c_p)_{mnf}} (T - T_\infty)$$

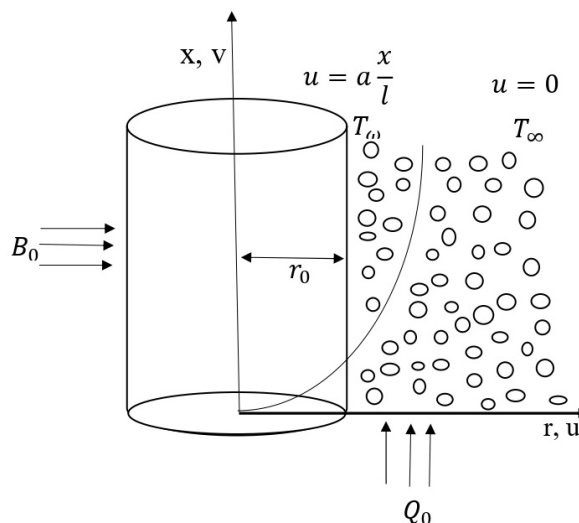


Figure 1. Physical Model and Coordinate system

The similarity transformation (Ref. [19]) used in Equations (1)-(3) are as follows

$$\eta = \frac{r^2 - r_0^2}{2r_0} \sqrt{\frac{a}{\nu_f l}}, \quad \psi = \sqrt{\frac{a\nu_f}{l}} x r_0 f(\eta), \quad \theta = \frac{T - T_\infty(x)}{T_w(x) - T_0}$$

and we provide non-dimensional quantities in the following:

$$M = \frac{l\sigma_f B_0^2}{a\rho_f}, \quad K = \frac{l\nu_f}{ak}, \quad \gamma = \sqrt{\frac{l\nu_f}{ar_0^2}}, \quad \lambda = \frac{Gr}{Re_x^2}, \quad \delta = \frac{B}{A}, \quad Q = \frac{Q_0 l}{a(\rho c_p)_f}$$

$$R = \frac{16\sigma^* T_\infty^3}{3k_f k}, \quad Pr = \frac{\nu_f(\mu c_p)_f}{k_f}$$

where, M is the magnetic parameter, K is the porosity parameter, γ is the curvature parameter, λ is the thermal buoyancy parameter, δ is the thermal stratification parameter, Q is the heat source/sink parameter, R is the radiation parameter, Pr is the Prandtl number.

The stream function ψ is introduced to satisfy continuity equation (1) in the manner that $u = \frac{1}{r} \frac{\partial \psi}{\partial r}$ and $v = -\frac{1}{r} \frac{\partial \psi}{\partial x}$. Hence, the non-dimensional forms of the transformed equations are given by

$$f'^2 - ff'' = a_1 [2\gamma f'' + (1 + 2\gamma\eta)f'''] + a_2 \lambda \theta - (a_3 M + a_1 K) f' \tag{4}$$

$$f'(\theta + \delta) - f\theta' = a_4 [2\gamma\theta' + (1 + 2\gamma\eta)\theta''] + a_5 \theta \tag{5}$$

where,

$$x_1 = \frac{\mu_{mnf}}{\mu_f}, \quad x_2 = \frac{\rho_f}{\rho_{mnf}}, \quad x_3 = \frac{(\rho\beta_T)_{mnf}}{(\rho\beta_T)_f}, \quad x_4 = \frac{(\rho C_p)_f}{(\rho C_p)_{mnf}}, \quad x_5 = \frac{\sigma_{mnf}}{\sigma_f}, \quad x_6 = \frac{k_{mnf}}{k_f}$$

$$a_1 = x_1 x_2, \quad a_2 = x_2 x_3, \quad a_3 = x_2 x_5, \quad a_4 = \frac{x_4 x_6 + R}{Pr}, \quad a_5 = Q x_4$$

Here, the symbols $\mu_{mnf}, \rho_{mnf}, (\beta_T)_{mnf}, (\rho C_p)_{mnf}, \sigma_{mnf}, k_{mnf}$ represent the ternary hybrid nanofluid's coefficient of viscosity, electrical conductivity, thermal expansion, heat capacity, density and thermal conductivity, respectively. Also, $\mu_f, \rho_f, (\beta_T)_f, (\rho C_p)_f, \sigma_f, k_f$ denote the base fluid's coefficient of viscosity, electrical conductivity, thermal expansion, heat capacity, density and thermal conductivity correspondingly.

The transformed boundary conditions are as follows :

$$\begin{array}{llll} f(\eta) = 0 & f'(\eta) = 1 & \theta(\eta) = 1 - \delta & \text{at } \eta = 0 \\ & f'(\eta) \rightarrow 0 & \theta(\eta) \rightarrow 0 & \text{as } \eta \rightarrow \infty \end{array} \tag{6}$$

The thermo-physical properties of ternary hybrid nanofluid are as follows:

$$\begin{aligned} \mu_{mnf} &= \frac{\mu_f}{(1 - \phi_1)^{2.5}(1 - \phi_2)^{2.5}(1 - \phi_3)^{2.5}} \\ \rho_{mnf} &= (1 - \phi_3) [(1 - \phi_2) \{ (1 - \phi_1)\rho_f + \phi_1\rho_{s1} \} + \phi_2\rho_{s2}] + \phi_3\rho_{s3} \\ (\rho c_p)_{mnf} &= (1 - \phi_3) [(1 - \phi_2) \{ (1 - \phi_1)(\rho c_p)_f + \phi_1(\rho c_p)_{s1} \} + \phi_2(\rho c_p)_{s2}] + \phi_3(\rho c_p)_{s3} \\ (\rho\beta_T)_{mnf} &= (1 - \phi_3) [(1 - \phi_2) \{ (1 - \phi_1)(\rho\beta_T)_f + \phi_1(\rho\beta_T)_{s1} \} + \phi_2(\rho\beta_T)_{s2}] + \phi_3(\rho\beta_T)_{s3} \\ k_{nf} &= \left[\frac{(k_{s1} + 2k_f) - 2\phi_1(k_f - k_{s1})}{(k_{s1} + 2k_f) + \phi_1(k_f - k_{s1})} \right] k_f, \quad k_{hnf} = \left[\frac{(k_{s2} + 2k_{nf}) - 2\phi_2(k_{nf} - k_{s2})}{(k_{s2} + 2k_{nf}) + \phi_2(k_{nf} - k_{s2})} \right] k_{nf} \\ k_{mnf} &= \left[\frac{(k_{s3} + 2k_{hnf}) - 2\phi_3(k_{hnf} - k_{s3})}{(k_{s3} + 2k_{hnf}) + \phi_3(k_{hnf} - k_{s3})} \right] k_{hnf}, \quad \sigma_{nf} = \left[\frac{(\sigma_{s1} + 2\sigma_f) - 2\phi_1(\sigma_f - \sigma_{s1})}{(\sigma_{s1} + 2\sigma_f) + \phi_1(\sigma_f - \sigma_{s1})} \right] \sigma_f \\ \sigma_{hnf} &= \left[\frac{(\sigma_{s2} + 2\sigma_{nf}) - 2\phi_2(\sigma_{nf} - \sigma_{s2})}{(\sigma_{s2} + 2\sigma_{nf}) + \phi_2(\sigma_{nf} - \sigma_{s2})} \right] \sigma_{nf}, \quad \sigma_{mnf} = \left[\frac{(\sigma_{s3} + 2\sigma_{hnf}) - 2\phi_3(\sigma_{hnf} - \sigma_{s3})}{(\sigma_{s3} + 2\sigma_{hnf}) + \phi_3(\sigma_{hnf} - \sigma_{s3})} \right] \sigma_{hnf} \end{aligned}$$

where ϕ_1, ϕ_2 and ϕ_3 are volume fraction of Cu (Copper), Al_2O_3 (aluminium oxide) and TiO_2 (titanium oxide) nanoparticles respectively. The suffixes mnf, hnf, nf, f, s1, s2, s3 denote ternary hybrid nanofluid, hybrid nanofluid, nanofluid, base fluid, solid nanoparticles of copper (Cu), aluminum oxide (Al_2O_3), and titanium dioxide (TiO_2) correspondingly.

The skin friction coefficient and local Nusselt number are defined by

$$C_f Re_x^{1/2} = \frac{1}{(1 - \phi_1)^{2.5}(1 - \phi_2)^{2.5}(1 - \phi_3)^{2.5}} f''(0) \quad \text{and} \quad Nu_x Re_x^{-1/2} = -\frac{k_{mnf}}{k_f} \theta'(0)$$

where, Re_x is the local Reynolds Number.

Table 1. Thermo-physical Properties of water and nanoparticles [2]

Physical Properties	H_2O (base fluid)	Cu (s1)	Al_2O_3 (s2)	TiO_2 (s3)
ρ (kg/m^3)	997.1	8933	3970	4250
C_p (J/kgK)	4179	385	765	686.2
k (W/mK)	0.613	401	40	8.9538
$\beta_t \times 10^5$ (K^{-1})	21	1.67	0.85	0.9
σ (s/m)	5.5×10^{-6}	59.6×10^6	35×10^6	2.6×10^6

3. METHOD OF SOLUTION

The `bvp4c` solver, built into the computational platform MATLAB, is used to numerically solve the system of higher-order nonlinear ODEs given by Equations (4)-(5) and the boundary conditions (6). This technique has been extensively utilized by professionals and researchers in order to solve fluid flow problems. The `bvp4c` solver, created by Jacek Kierzenka and Lawrence F. Shampine of Southern Methodist University in Texas, was introduced by Hale [36]. The `bvp4c` solver is a finite modification algorithm that uses the Lobatto IIIA implicit Runge-Kutta method to produce numerical solutions with fourth-order accuracy. This method gives the necessary accuracy when a guess is made for the initial mesh points and step-size changes. In the study conducted by Waini et al. [37], it was found that the `bvp4c` solver yielded satisfactory results in comparison to both the shooting technique and Keller box method. Here, we need to reduce the higher order derivatives with respect to η . This can be done by introducing the following new variables:

$$f = y(1), \quad f' = y(2), \quad f'' = y(3), \quad \theta = y(4), \quad \theta' = y(5)$$

$$\frac{d}{d\eta} \begin{bmatrix} y(1) \\ y(2) \\ y(3) \\ y(4) \\ y(5) \end{bmatrix} = \begin{bmatrix} y(2) \\ y(3) \\ \frac{y(2)^2 - y(1)y(3) - a_2\lambda y(4) + (a_3M + a_1K)y(2) - 2a_1\gamma y(3)}{(1+2\gamma\eta)a_1} \\ y(5) \\ \frac{y(2)(y(4)+\delta) - y(1)y(5) - 2a_4\gamma y(5) - a_5y(4)}{(1+2\gamma\eta)a_4} \end{bmatrix}$$

and boundary condition are expressed as

$$ya(1), \quad ya(2) - 1, \quad ya(4) - 1 + \delta, \quad yb(2), \quad yb(4)$$

where ya is the condition at $\eta = 0$ and yb is the condition at $\eta = \infty$

4. RESULT AND DISCUSSIONS

The numerical calculations were performed in `bvp4c` solver of MATLAB, and the outcomes are displayed in Figures (2)-(13) and Tables 3,5. Table 2 presents the absolute Skin friction Coefficient and local Nusselt Number values obtained from the current investigation, which are compared to the findings reported by Ashish et al. [19]. This comparison specifically excludes nanoparticle volume fractions of TiO_2 with $R = 0$. This study reveals that the `bvp4c` algorithm is capable of generating numerical results that are accurate and in agreement with the results obtained from alternative methods.

The following values are used in the study: $\delta = 0.2, \gamma = 0.1, M = 1.5, K = 2, R = 1, Q = 0.2, \lambda = 1.2, Pr = 6.2, \phi_1 = 0.05, \phi_2 = 0.15$ and $\phi_3 = 0.2$. The Fig. 2 displays the impact of thermal stratification(δ) parameters on the velocity $f'(\eta)$. The velocity decreases as thermal stratification(δ) increase. If the thermal stratification(δ) parameter rises, the efficient convective potential between the hot wall and the surrounding fluid drops. The buoyancy force is reduced as a result of this this, which reduces the flow velocity. As shown

Table 2. Comparison of Skin friction Coefficient and local Nusselt Number when $\phi_3 = R = 0$

Pr	M	δ	Ashish et al. $-C_f Re_x^{1/2}$	Present Study $-C_f Re_x^{1/2}$	Ashish et al. $Nu_x Re_x^{-1/2}$	Present Study $Nu_x Re_x^{-1/2}$
0.7 6.2	1.2	0.1	2.7886	2.7850	0.7266	0.7283
			2.9398	2.9297	2.7885	2.7889
	1.2	0.3	2.7076	2.6969	2.8622	2.8633
			3.0135	3.0090	2.6012	2.6044

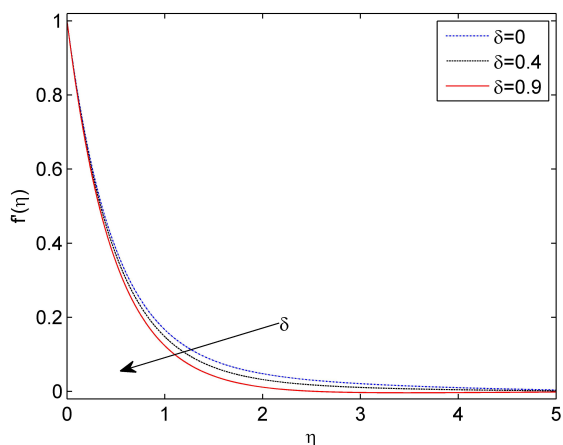


Figure 2. Effects of δ on Velocity Profile

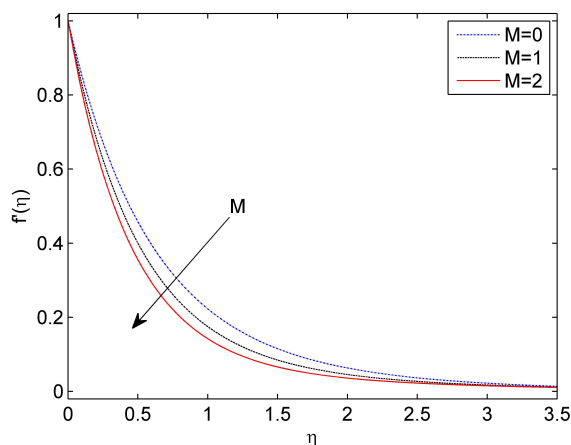


Figure 3. Effects of M on Velocity Profile

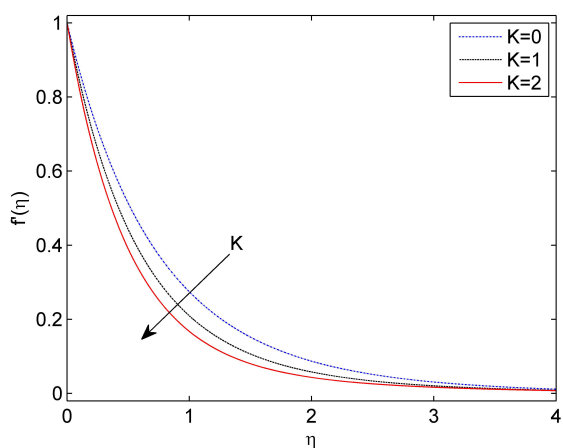


Figure 4. Effects of K on Velocity Profile

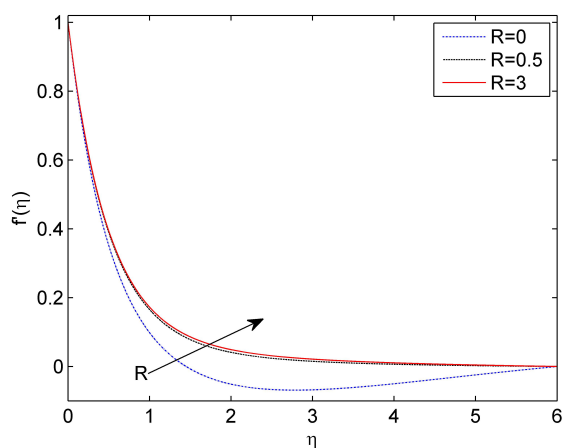


Figure 5. Effects of R on Velocity Profile

in Fig. 3, the fluid velocity $f'(\eta)$ decreases as the value of M is increased. As magnetic parameter(M) grows higher, the thickness of the momentum boundary layer shrinks. This pattern emerges because the Lorentz force produced by the horizontal magnetic field slows down the velocity of the ternary hybrid nanofluid. The impact of the porosity parameter(K) on velocity $f'(\eta)$ of the nanofluid is shown in Fig. 4. The velocity decreases as the porosity parameter value increases. The relationship between K and the diameter of the porous medium is inverse, implying that as K grows, the diameter of the porous medium decreases progressively. This reduction in diameter hinders the fluid's ability to flow through the porous medium. As a result of this obstruction, which was induced by porosity parameter(K), the velocity of the fluid dropped.

As shown in Fig. 5, as the value of R goes up, the velocity $f'(\eta)$ of the fluid goes up. With a higher value of R , the thermal conduction contribution becomes more important while the thermal radiative contribution increases. Since the radiative flux increases with increasing R , the velocity of the boundary layer of fluids increases. The effects of λ on the velocity of the fluid, is represented by Fig. 6. It is observed that the velocity will increase as the values of λ is increased. When λ is raised, the thermal buoyancy forces is made stronger. This indicates that the buoyancy forces tend to increase the velocity of the fluid.

The Fig. 7 displays that the temperature of the fluid goes down as the thermal stratification(δ) goes up. The temperature gradient between the heated wall and the surrounding fluid will decrease when the thermal stratification(δ) is present. Hence, the thermal boundary layer thickens and the temperature falls. The temperature of the fluid increases with increasing values of R in Fig. 8. This is because of the fact that higher R values indicate a higher thermal radiative flux, which ultimately results in higher temperatures. This can be seen as a manifestation of the fact that temperatures have increased.

The impact of a heat source parameter(Q) on temperature profile is seen in Fig. 9. Since the values of heat source parameter (Q) raises, the fluid temperature also increase. This characteristic matches how the fluid behaves physically in general. Fig. 10 illustrates the influence of Pr on the temperature profile of the fluid. As

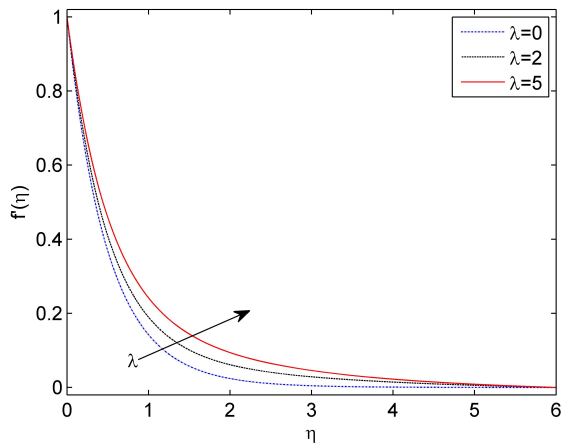


Figure 6. Effects of λ on Velocity Profile

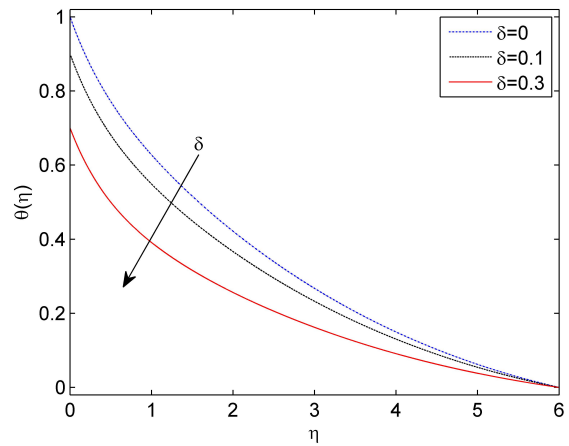


Figure 7. Effects of δ on Temperature Profile

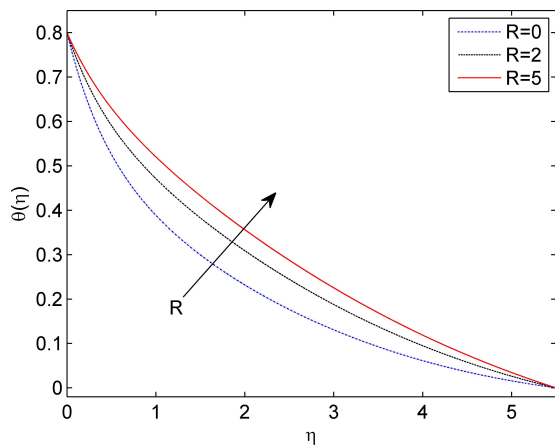


Figure 8. Effects of R on Temperature Profile

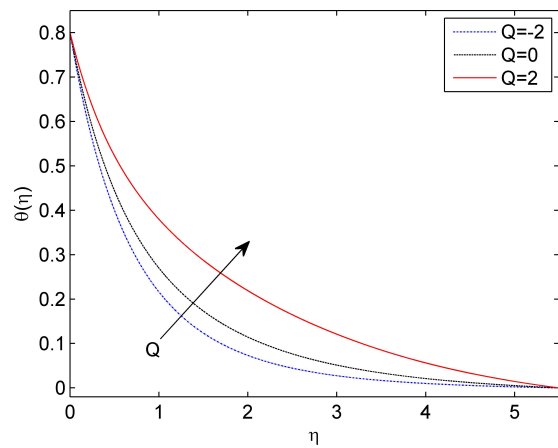


Figure 9. Effects of Q on Temperature Profile

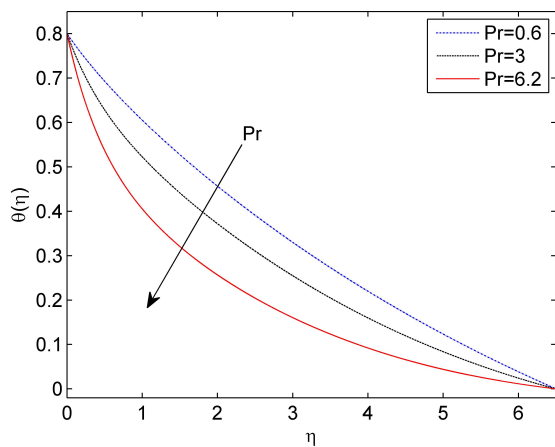


Figure 10. Effects of Pr on Temperature Profile

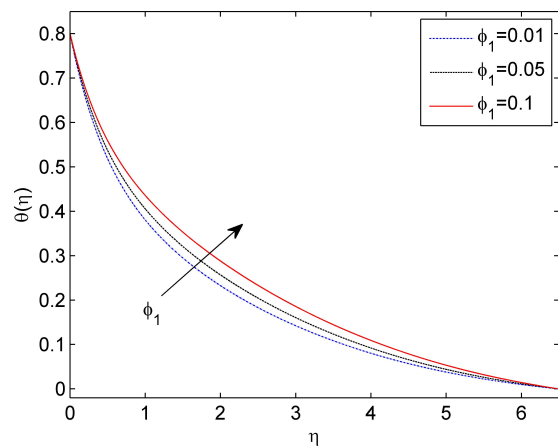


Figure 11. Effects of ϕ_1 on Temperature Profile

the Pr goes up, the temperature of the fluid goes down. It's clear that a fluid with a high Prandtl number has a low thermal conductivity. This means that heat doesn't move as easily through the fluid, so the transfer rate goes down and the thermal boundary layer gets thinner. Hence, the temperature of the fluid drops.

As the solid volume fraction of Cu nanoparticles increases, while the volume fractions of Al_2O_3 and TiO_2 remain constant, the temperature profile increases, as seen in Fig. 11. Furthermore, it can be observed from

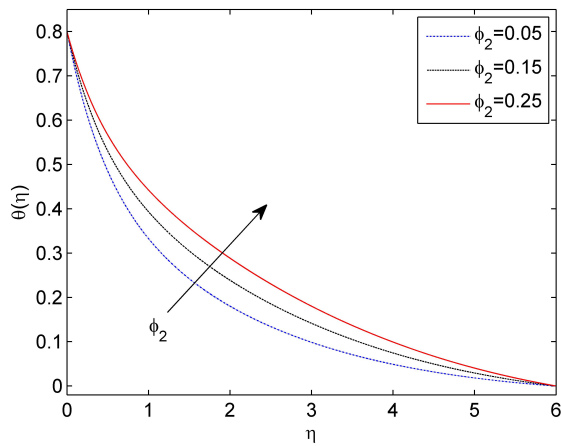


Figure 12. Effects of ϕ_2 on Temperature Profile

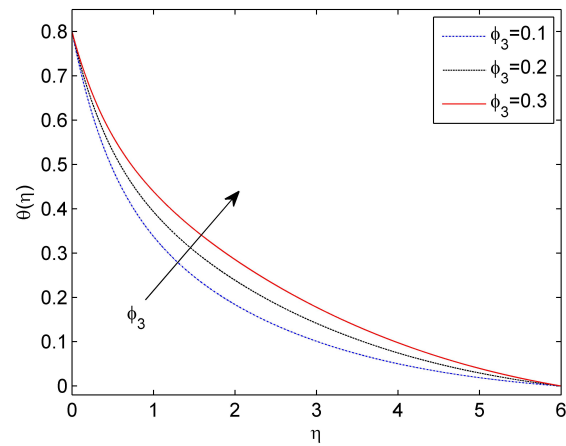


Figure 13. Effects of ϕ_3 on Temperature Profile

Fig. 12 that the temperature is increased with the increasing volume fraction of Al_2O_3 , while the volume fraction of Cu and TiO_2 remains constant. Similarly, ϕ_3 also increases the temperature profile as seen in Fig. 13.

Tables 3 present the effects on skin friction and local Nusselt number for different flow parameters. As the value of thermal stratification (δ) increases, there is a decrease in both skin friction and the local Nusselt number. An decrease in the magnitude of skin friction and Nusselt number is observed when the values of magnetic parameter(M) and porosity parameter(K) increase. The skin friction and Nusselt number exhibit an increase as the value of λ increases. For Pr , there is a decrease in skin friction while there is a rise in the Nusselt number. A decrease in the rate of heat transfer is observed as the radiation parameter (R) increases, while the opposite tendency is observed for the skin friction with an increase in R . Similarly, it can be noticed that an increase in the heat source (Q) leads to a decrease in the rate of heat transfer, although an increase in Q results in an opposite trend for the skin friction. The skin friction decreases as the curvature parameter (γ) grows, but the Nusselt number increases with an increase in the value of γ .

Table 3. Skin friction Coefficient and Local Nusselt number for different values of $\delta, M, K, \lambda, Pr, R, Q, \gamma$

δ	M	K	λ	Pr	R	Q	γ	Skin-friction Coefficient	Local Nusselt Number
0								-6.0075	2.0495
0.1	1.5	2	1.2	6.2	1	0.2	0.1	-6.0465	2.0140
0.3								-6.1272	1.9747
0.2	0	2	1.2	6.2	1	0.2	0.1	-4.8297	2.4280
	0.5							-5.2804	2.2742
	1.2							-5.8562	2.0760
0.2	1.5	0	1.2	6.2	1	0.2	0.1	-4.4138	2.5682
		1						-5.3132	2.2630
		2						-6.0870	1.9962
0.2	1.5	2	0	6.2	1	0.2	0.1	-6.3426	1.7157
			1.5					-6.0270	2.0411
			3					-5.7398	2.2105
0.2	1.5	2	1.2	0.6	1	0.2	0.1	-6.0352	0.6625
				3				-6.0567	1.2203
				6.2				-6.0870	1.9962
0.2	1.5	2	1.2	6.2	0	0.2	0.1	-6.1139	2.6133
					0.5			-6.0960	2.2254
					2			-6.0750	1.6861
0.2	1.5	2	1.2	6.2	1	-0.2	0.1	-6.1368	3.0531
						0		-6.1209	2.6547
						0.2		-6.0870	1.9962
0.2	1.5	2	1.2	6.2	1	0.2	0	-5.9506	1.9767
							0.1	-6.0870	1.9962
							0.2	-6.2286	2.1174

The absolute skin friction ($-C_f Re_x^{1/2}$) and local nusselt number ($Nu_x Re_x^{-1/2}$) of nanofluid, hybrid nanofluid, and ternary hybrid nanofluid are compared in tables 4 and 5. The absolute value of skin friction of the ($Cu - Al_2O_3 - TiO_3/H_2O$) ternary hybrid nanofluid shows a significant improvement of up to 174% in comparison to the (Cu/H_2O) nanofluid. Additionally, it has been found that the difference between ternary hybrid nanofluid and common nanofluid reduces with thermal stratification(δ) for $-C_f Re_x^{1/2}$. The Nusselt Number of the ternary hybrid nanofluid displays a significant enhancement of up to 32% when compared to the conventional nanofluid. In addition, it has been discovered that thermal stratification(δ) increases the difference between ternary hybrid nanofluid and regular nanofluid for $Nu_x Re_x^{-1/2}$.

Table 4. Comparison of $-C_f Re_x^{1/2}$

δ	Cu Nanofluid	$Cu - Al_2O_3$ Hybrid Nanofluid	$Cu - Al_2O_3 - TiO_3$ Ternary Hybrid Nanofluid	Change in %
0	2.1858	3.4001	6.0075	174.8
0.1	2.2290	3.4416	6.0465	171.2
0.2	2.2747	3.4800	6.0870	167.6
0.3	2.3186	3.5245	6.1272	164.3



Table 5. Comparison of Local Nusselt Number

δ	Cu Nanofluid	$Cu - Al_2O_3$ Hybrid Nanofluid	$Cu - Al_2O_3 - TiO_3$ Ternary Hybrid Nanofluid	Change in %
0	1.6333	1.9355	2.0495	25.8
0.1	1.5823	1.8842	2.0140	27.3
0.2	1.5419	1.8095	1.9962	29.5
0.3	1.4926	1.7798	1.9747	32.3

5. CONCLUSION

The impact of thermal stratification on the flow of a ternary hybrid nanofluid ($Cu - Al_2O_3 - TiO_3/H_2O$) with magnetohydrodynamics (MHD) properties along a vertical stretchable cylinder has been studied. This investigation takes into consideration the presence of a thermal bouncy effect, thermal radiation, and heat source/sink inside a porous medium. In addition, the analysis takes into account the flow characteristics and their impact on the velocity and temperature profiles, skin friction, and local Nusselt number. The velocity profile reveals a declining tendency when the parameters δ, M and K are increased, whereas it exhibits an ascending trend with higher values of R and λ . The temperature exhibits a decrease as the magnitudes of δ and Pr increase, while it exhibits an increase with the increase of R and Q . The skin friction exhibits an increase with respect to the parameters λ, R , and Q , but it experiences a decrease in relation to the factors δ, M, K, Pr and γ . An upward trend in the local Nusselt number is noted as the values of λ, Pr , and γ grow, whereas it exhibits a downward trend with increasing values of δ, M, K, R and Q . The ternary hybrid nanofluid exhibits a higher magnitude of absolute skin friction ($-C_f Re_x^{1/2}$) in comparison to the hybrid nanofluid. Similarly, the absolute skin friction of hybrid nanofluids exhibits a higher value when compared to that of conventional nanofluids. The ternary hybrid nanofluid demonstrates a superior heat transfer rate in contrast to the hybrid nanofluid, whereas the hybrid nanofluid displays a higher heat transfer rate in comparison to conventional nanofluids.

ORCID

 **Rupam Shankar Nath**, <https://orcid.org/0009-0002-2352-0538>;  **Rudra Kanta Deka**, <https://orcid.org/0009-0007-1573-4890>

REFERENCES

- [1] S.U.S. Choi, and J.A. Eastman, *Enhancing thermal conductivity of fluids with nanoparticles*, Technical report, (Argonne National Lab. Argonne, IL, United States, 1995).
- [2] S. Das, and R.N. Jana, "Natural convective magneto-nanofluid flow and radiative heat transfer past a moving vertical plate," *Alexandria Engineering Journal*, **54**(1), 55-64 (2015). <https://doi.org/10.1016/j.aej.2015.01.001>
- [3] S. Das, R.N. Jana, and O.D. Makinde, "Transient natural convection in a vertical channel filled with nanofluids in the presence of thermal radiation," *Alexandria Engineering Journal*, **55**(1), 253-262 (2016). <https://doi.org/10.1016/j.aej.2015.10.013>

- [4] M.M. Rashidi, E. Momoniat, M. Ferdows, and A. Basiriparsa, "Lie group solution for free convective flow of a nanofluid past a chemically reacting horizontal plate in a porous media," *Mathematical Problems in Engineering*, **2014**, 239082 2014. <https://doi.org/10.1155/2014/239082>
- [5] M.H. Abolbashari, N. Freidoonimehr, F. Nazari, and M.M. Rashidi, "Entropy analysis for an unsteady mhd flow past a stretching permeable surface in nano-fluid," *Powder Technology*, **267**, 256–267 2014. <https://doi.org/10.1016/j.powtec.2014.07.028>
- [6] T.G. Motsumi, and O.D. Makinde, "Effects of thermal radiation and viscous dissipation on boundary layer flow of nanofluids over a permeable moving flat plate," *Physica Scripta*, **86**(4), 045003 (2012). <https://doi.org/10.1088/0031-8949/86/04/045003>
- [7] M. Turkyilmazoglu, "Exact analytical solutions for heat and mass transfer of mhd slip flow in nanofluids," *Chemical Engineering Science*, **84**, 182–187 (2012). <https://doi.org/10.1016/j.ces.2012.08.029>
- [8] M. Sheikholeslami, M.G. Bandpy, R. Ellahi, and A. Zeeshan, "Simulation of mhd cuo–water nanofluid flow and convective heat transfer considering lorentz forces," *Journal of Magnetism and Magnetic Materials*, **369**, 69–80 (2014). <https://doi.org/10.1016/j.jmmm.2014.06.017>
- [9] N. Sandeep, and M.G. Reddy, "Heat transfer of nonlinear radiative magnetohydrodynamic cu-water nanofluid flow over two different geometries," *Journal of Molecular Liquids*, **225**, 87–94 (2017). <https://doi.org/10.1016/j.molliq.2016.11.026>
- [10] P.C. Reddy, M.C. Raju, and G.S.S. Raju, "Free convective heat and mass transfer flow of heat-generating nanofluid past a vertical moving porous plate in a conducting field," *Special Topics and Reviews in Porous Media: An International Journal*, **7**(2), 161–180 (2016). <https://doi.org/10.1615/SpecialTopicsRevPorousMedia.2016016973>
- [11] B. Mahanthesh, B.J. Gireesha, and R.S.R. Gorla, "Heat and mass transfer effects on the mixed convective flow of chemically reacting nanofluid past a moving/stationary vertical plate," *Alexandria engineering journal*, **55**(1), 569–581 (2016). <https://doi.org/10.1016/j.aej.2016.01.022>
- [12] S.P. Jeevandhar, V. Kedla, N. Gullapalli, and S.K. Thavada, "Natural convective effects on mhd boundary layer nanofluid flow over an exponentially accelerating vertical plate," *Biointerface Research in Applied Chemistry*, **11**(6), 13790–13805 (2021). <https://doi.org/10.33263/BRIAC116.1379013805>
- [13] C.-Y. Cheng, "Double-diffusive natural convection along a vertical wavy truncated cone in non-newtonian fluid saturated porous media with thermal and mass stratification," *International Communications in Heat and Mass Transfer*, **35**(8), 985–990 (2008). <https://doi.org/10.1016/j.icheatmasstransfer.2008.04.007>
- [14] C.-Y. Cheng, "Combined heat and mass transfer in natural convection flow from a vertical wavy surface in a power-law fluid saturated porous medium with thermal and mass stratification," *International Communications in Heat and Mass Transfer*, **36**(4), 351–356 (2009). <https://doi.org/10.1016/j.icheatmasstransfer.2009.01.003>
- [15] A. Paul, and R.K. Deka, et al., "Unsteady natural convection flow past an infinite cylinder with thermal and mass stratification," *Int. J. Eng. Math.* **2017**, 8410691 (2017). <https://doi.org/10.1155/2017/8410691>
- [16] R.S. Nath, and R.K. Deka, "The effect of thermal stratification on flow past an infinite vertical plate in presence of chemical reaction," *East European Journal of Physics*, **3**, 223–232 (2023). <https://doi.org/10.26565/2312-4334-2023-3-19>
- [17] N. Kalita, R.K. Deka, and R.S. Nath, "Unsteady flow past an accelerated vertical plate with variable temperature in presence of thermal stratification and chemical reaction," *East European Journal of Physics*, **3**, 441–450 (2023). <https://doi.org/10.26565/2312-4334-2023-3-49>
- [18] R.S. Nath, R.K. Deka, and H. Kumar, "The Effect of Thermal Stratification on Unsteady Parabolic Flow past an Infinite Vertical Plate with Chemical Reaction," *East European Journal of Physics*, **4**, 77–86 (2023) <https://doi.org/10.26565/2312-4334-2023-4-08>
- [19] A. Paul, J.M. Nath, and T.K. Das, "An investigation of the MHD Cu-Al₂O/H₂O hybrid-nanofluid in a porous medium across a vertically stretching cylinder incorporating thermal stratification impact," *Journal of Thermal Engineering*, **9**(3), 799–810 (2023). <https://doi.org/10.18186/thermal.1300847>
- [20] N. Shanmugapriyan, and S. Jakeer, "Biomedical aspects of entropy generation on MHD flow of TiO₂-Ag/blood hybrid nanofluid in a porous cylinder," *Computer Methods in Biomechanics and Biomedical Engineering*, **14**, 1–18 (2023). <https://doi.org/10.1080/10255842.2023.2245520>
- [21] S. Suneetha, L. Wahidunnisa, S.R.R. Reddy, and P.B.A. Reddy, "Entropy generation on the variable electric field and emhd swcnt-blood nanofluid with melting/non-melting heat transfer," *Proceedings of the Institution of Mechanical Engineers, Part E: Journal of Process Mechanical Engineering*, **237**(6), 2314–2322 (2022). <https://doi.org/10.1177/09544089221140223>
- [22] S. Jakeer, P.B.A. Reddy, A.M. Rashad, and H.A. Nabwey, "Impact of heated obstacle position on magneto-hybrid nanofluid flow in a lid-driven porous cavity with Cattaneo-Christov heat flux pattern," *Alexandria Engineering Journal*, **60**(1), 821–835 (2021). <https://doi.org/10.1016/j.aej.2020.10.011>
- [23] J. Shaik, B.A.R. Polu, M.M. Ahmed, and R.A. Mohamed, "Characteristics of moving hot block and non-fourier heat flux model on sinusoidal wavy cavity filled with hybrid nanofluid," *The European Physical Journal Plus*, **137**(1), 131 (2022). <https://doi.org/10.1140/epjp/s13360-022-02361-y>

- [24] P. Rana, and A. Kumar, "Nonlinear buoyancy driven flow of hybrid nanofluid past a spinning cylinder with quadratic thermal radiation," *International Communications in Heat and Mass Transfer*, **139**, 106439 (2022). <https://doi.org/10.1016/j.icheatmasstransfer.2022.106439>
- [25] S. Jakeer, S.R.R. Reddy, A.M. Rashad, M.L. Rupa, and C. Manjula, "Nonlinear analysis of Darcy-Forchheimer flow in EMHD ternary hybrid nanofluid (Cu-CNT-Ti/water) with radiation effect," *Forces in Mechanics*, **10**, 100177 (2023). <https://doi.org/10.1016/j.finmec.2023.100177>
- [26] S. Nasir, S. Sirisubtawee, P. Juntharee, A.S. Berrouk, S. Mukhtar, and T. Gul, "Heat transport study of ternary hybrid nanofluid flow under magnetic dipole together with nonlinear thermal radiation," *Applied Nanoscience*, **12**(9), 2777–2788 (2022). <https://doi.org/10.1007/s13204-022-02583-7>
- [27] K.A.M. Alharbi, A.El-Sayed Ahmed, M.O. Sidi, N.A. Ahammad, A. Mohamed, M.A. El-Shorbagy, et al., "Computational valuation of Darcy ternary-hybrid nanofluid flow across an extending cylinder with induction effects," *Micromachines*, **13**(4), 588 (2022). <https://doi.org/10.3390/mi13040588>
- [28] M. Shanmugapriya, R. Sundareswaran, P.S. Kumar, and G. Rangasamy, "Impact of nanoparticle shape in enhancing heat transfer of magnetized ternary hybrid nanofluid," *Sustainable Energy Technologies and Assessments*, **53**, 102700 (2022). <https://doi.org/10.1016/j.seta.2022.102700>
- [29] M. Arif, P. Kumam, W. Kumam, and Z. Mostafa, "Heat transfer analysis of radiator using different shaped nanoparticles water-based ternary hybrid nanofluid with applications: A fractional model," *Case Studies in Thermal Engineering*, **31**, 101837 (2022). <https://doi.org/10.1016/j.csite.2022.101837>
- [30] P.M. Patil, B. Goudar, and M.A. Sheremet, "Tangent hyperbolic ternary hybrid nanofluid flow over a rough-yawed cylinder due to impulsive motion," *Journal of Taibah University for Science*, **17**(1), 2199664 (2023). <https://doi.org/10.1080/16583655.2023.2199664>
- [31] Z. Mahmood, Z. Iqbal, M.A. Alyami, B. Alqahtani, M.F. Yassen, and U. Khan, "Influence of suction and heat source on mhd stagnation point flow of ternary hybrid nanofluid over convectively heated stretching/shrinking cylinder," *Advances in Mechanical Engineering*, **14**(9), (2022). <https://doi.org/10.1177/16878132221126278>
- [32] W. Cao, I. Animasaun, S.-J. Yook, V.A. Oladipupo, and X. Ji, "Simulation of the dynamics of colloidal mixture of water with various nanoparticles at different levels of partial slip: Ternary-hybrid nanofluid," *International Communications in Heat and Mass Transfer*, **135**, 106069 (2022). <https://doi.org/10.1016/j.icheatmasstransfer.2022.106069>
- [33] L.F. Shampine, J. Kierzenka, and M.W. Reichelt, *Solving boundary value problems for ordinary differential equations in Matlab with bvp4c. Tutorial notes*, (2000). https://classes.engineering.wustl.edu/che512/bvp_paper.pdf
- [34] J. Kierzenka, and L.F. Shampine, "A bvp solver based on residual control and the Matlab pse," *ACM Transactions on Mathematical Software*, **27**(3), 299–316 (2001). <https://doi.org/10.1145/502800.502801>
- [35] S Rosseland, *Astrophysik und atom-theoretische Grundlagen*, (Springer-Verlag, Berlin, 1931).
- [36] N.P. Hale, *A sixth-order extension to the matlab bvp4c software of j. kierzenka and l. shampine*, (Department of Mathematics, Imperial College London, 2006).
- [37] I. Waini, A. Ishak, and I. Pop, "Mixed convection flow over an exponentially stretching/shrinking vertical surface in a hybrid nanofluid," *Alexandria Engineering Journal*, **59**(3), 1881–1891 (2020). <https://doi.org/10.1016/j.aej.2020.05.030>

ЧИСЕЛЬНЕ ДОСЛІДЖЕННЯ ПОТРІЙНОЇ ГІБРИДНОЇ МГД НАНОРІДИНИ ($Cu - Al_2O_3 - TiO_2/H_2O$) ЗА НАЯВНОСТІ ТЕПЛОВОЇ СТРАТИФІКАЦІЇ ТА ВИПРОМІНЮВАННЯ ЧЕРЕЗ ВЕРТИКАЛЬНО РОЗТЯГНУТИЙ ЦИЛІНДР У ПОРИСТОМУ СЕРЕДОВИЩІ

Рупам Шанкар Нат, Рудра Канта Дека

Факультет математики, Університет Гаухаті, Гувахаті-781014, Ассам

Основною метою цього дослідження є дослідження впливу термічної стратифікації на магнітогідродинамічний (МГД) потік нано-, гібридних і потрійних гібридних нанофлюїдів на водній основі, коли вони проходять повз вертикально розтягнутий циліндр у пористому середовищі. Наночастинки Cu , Al_2O_3 і TiO_2 суспендовані в базовій рідині H_2O , що призводить до утворення потрійної гібридної нанорідини ($Cu + Al_2O_3 + TiO_2/H_2O$). Використання відповідної змінної подібності було використано для спрощення рівнянь граничного шару, які керують потоком і перетворюють пов'язані нелінійні диференціальні рівняння в частинних похідних у набір нелінійних звичайних диференціальних рівнянь. Числові результати обчислюються за допомогою 3-етапного підходу Lobatto Ша, спеціально реалізованого Bvp4c у MATLAB. У цьому дослідженні представлено графічний і числовий аналіз впливу різних безрозмірних параметрів, таких як число Прандтля, параметр випромінювання, параметр джерела тепла/стоку, магнітний параметр, параметр пористості, параметр кривизни, параметр термічної стратифікації та параметр теплової плавучості, від швидкості, температури, коефіцієнта поверхневого тертя та числа Нуссельта. Вплив цих параметрів візуально зображено на графіках і кількісно представлено в таблицях. Потрійна гібридна нанофлюїд має вищу швидкість теплопередачі, ніж гібридна нанофлюїд, а гібридна нанофлюїд має вищу швидкість теплопередачі, ніж звичайні нанофлюїди.

Ключові слова: термічна стратифікація; вертикальний циліндр, що розтягується; тернарний гібридний нанофлюїд; пористе середовище; теплове випромінювання; МГД; bvp4c

CASSON FLUID FLOW PAST A SHRINKING SURFACE WITH HEAT AND MASS TRANSFERS

 **Rajesh Kumar Das**^{a*},  **Debasish Dey**^{b†}

^aDepartment of Mathematics, Pandit Deendayal Upadhyaya Adarsha Mahavidyalaya Amjonga, Goalpara, India-783124

^bDepartment of Mathematics, Dibrugarh University, Dibrugarh, India-786004

*Corresponding Author e-mail: rajeshkumardas91@gmail.com, †Co-author e-mail: debasish41092@gmail.com

Received December 12, 2023; revised January 19, 2024; accepted January 24, 2024

In this study, we have numerically investigated the heat and mass transfers behaviour of Casson fluid flow past a porous shrinking sheet in existence of a magnetic field, thermal radiation, and suction or blowing at the surface. Applying suitable similarity transformations, the leading partial nonlinear differential equations of mass, flow, and heat transfer are converted into solvable ordinary differential equations, which can then be solved numerically with the help of the MATLAB bvp4c scheme. We have analyzed and shown graphically the implications of several non-dimensional controlling factors on the profiles of temperature, concentration, and velocity. Additionally, the Sherwood, Nusselt, and Skin friction for Casson fluids are examined and tabulated. The current study's findings for Casson fluid exhibit great consistency with previous research under specific circumstances.

Keywords: Casson fluid; heat and mass transfers; permeability; MHD; shrinking sheet

PACS: 44.05.+e

1. INTRODUCTION

There are numerous uses for the study of non-Newtonian fluids in industries and engineering, particularly in the process of separating fossil oil from petroleum goods. A Casson fluid is a non-Newtonian fluid with yield stress. Additionally, due to the chain structure of blood cells and the materials they carry, such as protein, fibrinogen, rouleaux, etc., human blood may also be considered a Casson fluid. Thus, the Casson fluid plays a significant role in both biological science and engineering. The problem of the flow by reason of stretching or shrinking sheets has attracted many researchers, and it is a topic of attention in the literature (Grubka and Bobby [1], Banks [2], Crane [3], Keller and Magyari [4], Lio and Pop [5], etc.). Boundary layer flows have many significant applications in industrial manufacturing processes. Though there aren't enough works on the flow past on shrinking sheets, Wang [6] was the foremost to study the unstable viscous flow caused by a shrinking sheet. Mikalavcic and Wang [7] have examined the viscous hydrodynamic flow caused by the shrinking surface for particular values of the suction parameter and came to the conclusion that, for both two-dimensional and axi-symmetric flows, the shrinking sheet solution might not be unique at particular suction rates. After that, Fang and Zhang [8] have clarified how an external magnetic field affects the flow of a shrinking sheet and discovered that a high magnetic field ensures a constant flow of the boundary layer. Following that, several scholars [9–21] examine the non-Newtonian fluid flow past a diminishing sheet from a variety of physical angles.

On the contrary, Hayat *et al.* [22–24] have examined non-Newtonian fluid flow over a shrinking surface. Since most fluids encountered in scientific processes exhibit non-Newtonian fluid characteristics [25–31], research on non-Newtonian flows is important from a technological standpoint. Notable studies on the non-Newtonian fluid flow over a shrinking surface were published by Rosali *et al.* [32], Yacob *et al.* [33, 34], and Ishak *et al.* [35, 36].

Dey *et al.* [37] explored the stability of MHD Casson fluid over a porous elongating sheet. Bhattacharyya *et al.* [38] studied the MHD Casson fluid over a porous stretching/shrinking surface in the existence of wall mass transmission. Das *et al.* [39] have studied numerically to examine the nanofluid flow in permeable media past a vertical stretching surface with heat and mass transfers.

Pramanik [40] studied the characteristics of Casson fluid heat transfer via thermal radiation and porous media. Sarkar *et al.* [41] enlightened the significance of this fluid model in various contexts and in relation to heat radiation is investigated through the use of an inclined cylindrical surface. Elucidation of the non-Newtonian Casson fluid dynamics across a rotating non-uniform surface under the influence of coriolis force was enlightened by Oke *et al.* [42]. Dey *et al.* [43] have investigated the energy transfer and entropy creation of hydro-magnetic stagnation point flow in micropolar fluids under uniform suction and injection.

Kinetic processes like heat and mass transmission can happen and be studied individually or together. While studying them separately is easier, in the case of diffusion and convection, both processes are modelled by comparable mathematical equations. In certain situations, such as evaporative cooling and ablation, mass transfer must be taken into account in addition to heat. Problems with combined mass and heat transfer are significant in many processes, and they have gained attention recently in the chemical industry, drying, evaporation on a water surface, and the process of connecting with thermal retrieval.

In this research paper, we have examined the heat and species concentration transmission of Casson fluid through a permeable medium past a shrinking sheet. This motion is mathematically controlled by a system of non-linear PDEs that,

with the suitable transformation, are converted into non-linear ODEs. The velocity, temperature, and concentration profiles are obtained by numerically solving this system under the proper boundary conditions. The effects of the problem's physical characteristics on these results are explored graphically and numerically using a series of figures and tables. A quick analysis can produce a model that helps explain the mechanics of physiological fluxes.

2. MATHEMATICAL FORMULATION

Consider a two-dimensional, incompressible, electrically conducting hydromagnetic Casson fluid flow over a permeable, shrinking sheet with heat and mass transfer. To scrutinize the suction and blowing processes, the wall permeability characteristics have been used. Figure 1 illustrates how the non-Newtonian fluid drenches the porous material $y > 0$ while the flow dynamics take place in the area $y < 0$. A magnetic field $B(x)$ has been implemented in the flow. Following Dey *et al.* [37], the rheological equation of an incompressible and isotropic Casson fluid is as follows:

$$\tau_{ij} = \begin{cases} 2\left(\mu_\beta + \frac{P_y}{\sqrt{2\pi}}\right)e_{ij}, & \pi > \pi_c \\ 2\left(\mu_\beta + \frac{P_y}{\sqrt{2\pi_c}}\right)e_{ij}, & \pi < \pi_c \end{cases}$$

where, $\pi = e_{ij}e_{ij}$ and e_{ij} is the (i, j) th component of deformation rate.

Considering the above assumptions, the leading equations for the projected fluidic model are given by:

$$\frac{\partial u}{\partial x} + \frac{\partial v}{\partial y} = 0 \tag{1}$$

$$u \frac{\partial u}{\partial x} + v \frac{\partial u}{\partial y} = \nu \left(1 + \frac{1}{\beta}\right) \frac{\partial^2 u}{\partial y^2} - \frac{\sigma B^2(x)}{\rho} u - \frac{\nu}{k} u \tag{2}$$

$$u \frac{\partial T}{\partial x} + v \frac{\partial T}{\partial y} = \alpha \frac{\partial^2 T}{\partial y^2} \tag{3}$$

$$u \frac{\partial C}{\partial x} + v \frac{\partial C}{\partial y} = D \frac{\partial^2 C}{\partial y^2} \tag{4}$$

The relevant boundary restrictions are

$$\begin{aligned} u = -ax, v = V_0, T = T_0, C = C_0 \text{ at } y = 0, \\ u \rightarrow 0, T = T_\infty, C = C_\infty \text{ as } y \rightarrow \infty \end{aligned} \tag{5}$$

where u, v denotes velocity components along x and y directions, ν stands for kinematic viscosity, β represents casson fluid parameter, σ is the electrical conductivity, ρ stands for fluid density, k is the porous medium permeability, T represents fluid temperature, α denotes thermal conductivity, C describes species concentration, D is the coefficient of mass diffusion, $V_0 > 0$ and $V_0 < 0$ are assumed as blowing and suction conditions, respectively.

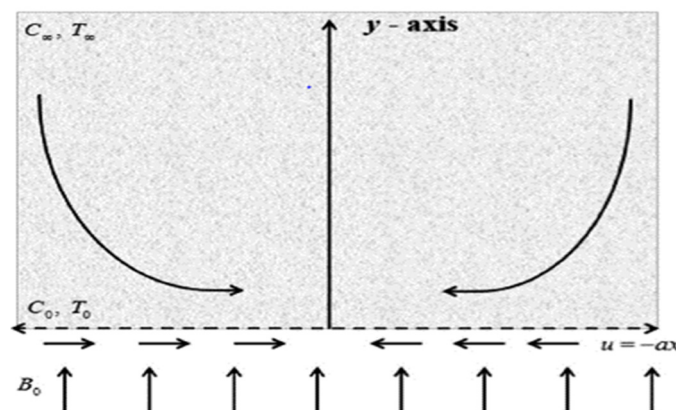


Figure 1. Flow Model

3. METHOD OF SOLUTION

Using the following similarity transformations:

$$\eta = \sqrt{\frac{a}{\nu}} y, \quad \psi = \sqrt{a\nu} x f(\eta), \quad \theta(\eta) = \frac{T - T_\infty}{T_0 - T_\infty}, \quad \phi(\eta) = \frac{C - C_\infty}{C_0 - C_\infty}$$

$$M = \frac{\sigma B^2}{a\rho}, \quad Pr = \frac{\nu}{\alpha}, \quad Sc = \frac{\nu}{D}, \quad K_1 = \frac{\nu}{ak} \tag{6}$$

Using equation (6) in equations (2)-(5), it transforms as follows:

$$\left(1 + \frac{1}{\beta}\right) f''' + ff'' - f'^2 - M^2 f' - K_1 f' = 0 \tag{7}$$

$$\theta'' + Prf\theta' = 0 \tag{8}$$

$$\phi'' + Scf\phi' = 0 \tag{9}$$

The relevant boundary restrictions are given by

$$\begin{aligned} f(0) = S, \quad f'(0) = -1, \quad \theta(0) = 1, \quad \phi(0) = 1, \\ f'(\infty) = 0, \quad \theta(\infty) = 0, \quad \phi(\infty) = 0 \end{aligned} \tag{10}$$

The physical parameters that are important for our studies are Sherwood number, Nusselt number, skin friction coefficient. They are expressed as

$$C_f \left(Re_x^{\frac{1}{2}} \right) = \left(1 + \frac{1}{\beta}\right) f''(0), \tag{11}$$

$$Nu_x \left(Re_x^{-\frac{1}{2}} \right) = -\theta'(0), \tag{12}$$

$$Sh_x \left(Re_x^{-\frac{1}{2}} \right) = -\phi'(0), \tag{13}$$

4. RESULT AND DISCUSSION

The resultant ordinary differential equations and related surface limitations are numerically computed via the bvp4c MATLAB software. The flow behaviour patterns for diverse values of the leading parameters are displayed in both tabular and graphical form. Figure 2 exhibits the velocity profile for various values of magnetic field parameter (M). It is found that with increment in M, the magnitude of the velocity profile increase. This is because, with increment of M will dominate the Lorentz force and lessen the impact of the fluid's viscosity at the surface, increasing the fluid's speed.

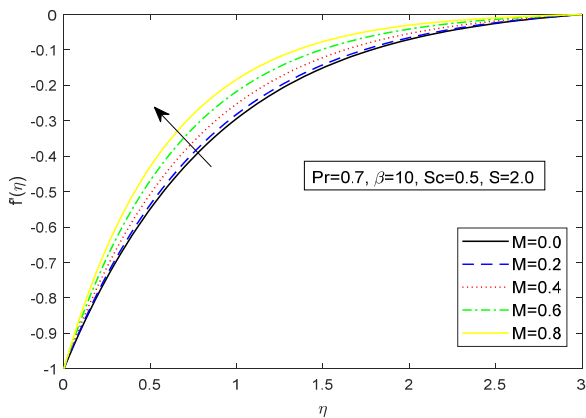


Figure 2. Velocity profile for M

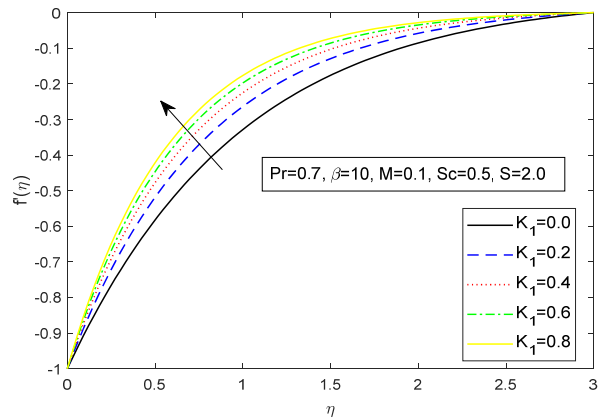


Figure 3. Velocity profile for K₁

Figure 3 portrays the velocity profile for diverse values of porosity parameter (K₁). Here we have seen that with enhancement of K₁, the velocity profile increases. As K₁ grows, the fluid has a larger area to move, which causes its velocity to rise. Figure 4 displays the thermal profile for various values of Prandtl number (Pr). From the figure it is clear that with rise in Pr, the thermal profile decreases. As Pr increases, the temperature drops. The thickness of the thermal boundary layer decreases with an increase in Prandtl number. The ratio of momentum diffusivity to heat diffusivity is known as the Prandtl number. Pr regulates the relative thickness of the thermal and momentum boundary layers in heat transfer issues. Figure 5 elucidates the variation of Schmidt number for species concentration profile. It is seen that the concentration falls, as Sc intensifies. The mass transfer rate rises with a higher Schmidt number, which causes the concentration profiles to fall. Figures 6 gives the impression that the fluid's velocity is accelerated by increasing Casson fluid parameter (β) values. Enhancement of β generally causes the fluid's motion to slow down since it increases the plastic dynamic viscosity. However, throughout the flow, an opposite behaviour is shown, and this is only possible

because geometry (shrinking sheet) is taken into consideration. Figure 7 and 8 presents the influence of Casson fluid parameter (β) on thermal, and species concentration profiles, respectively. It is evident from figure 7 that the fluid's temperature drops as it flows. Higher values of β may be physically attributed to improving the fluid's resistance and lessening the impacts of yield stress on the fluid, which causes the temperature pattern to slow down. Figure 9 represents the effect of suction parameter (S) on velocity profile. It is noted from the figure that velocity increases with enhancement of S, decreasing the thickness of the boundary layer.

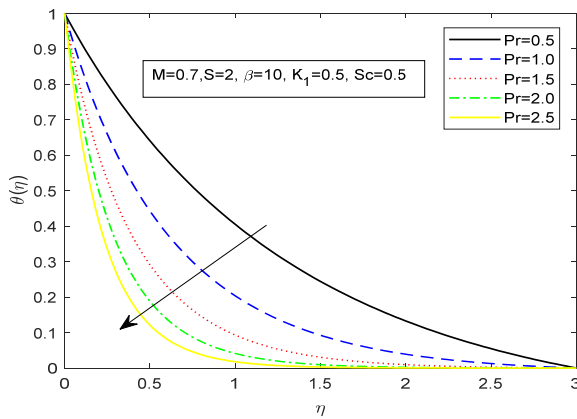


Figure 4. Temperature profile for Pr

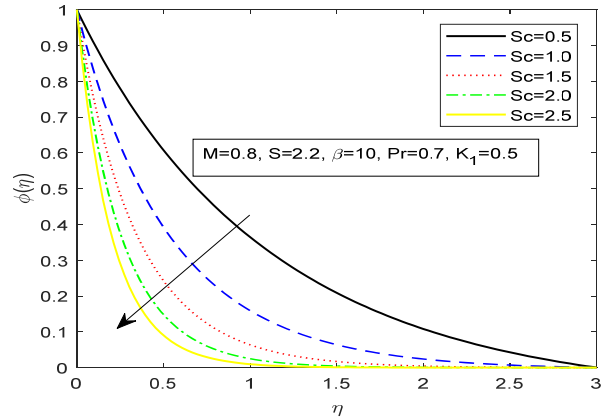


Figure 5. Concentration profile for Sc

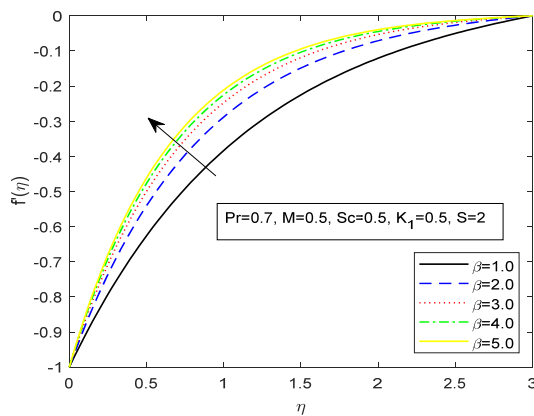


Figure 6. Velocity profile for β

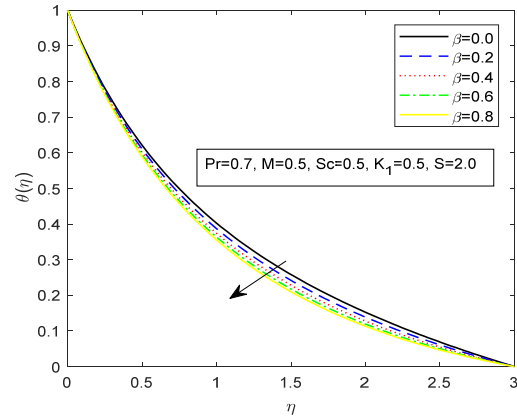


Figure 7. Temperature profile for β

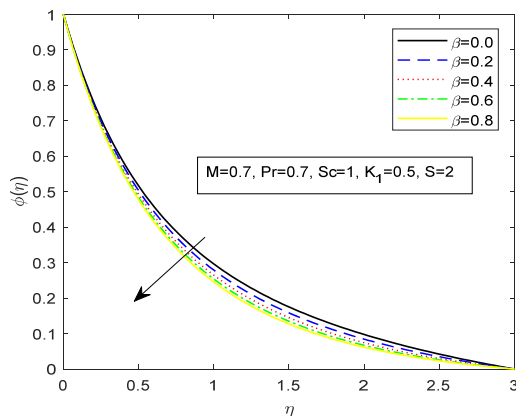


Figure 8. Concentration profile for β

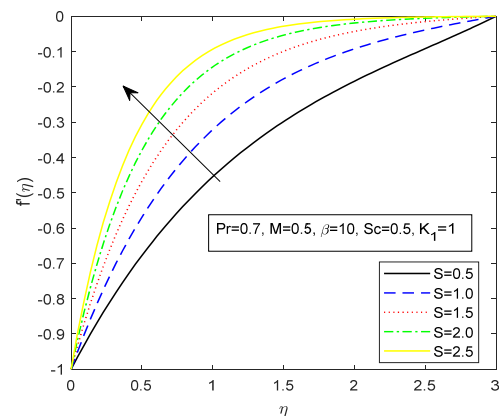


Figure 9. Velocity profile for S

4.1 VALIDATION OF RESULTS

To validate our numerical scheme, we compare our results with Bhattacharyya *et al.* [17], and they are found to be in good agreement with the result. (Table 1.)

In our experiment, Table 2 reflects the influence of the Magnetic parameter on the skin friction coefficient ($f''(0)$), Sherwood number ($-\phi'(0)$), and Nusselt number ($-\theta'(0)$). We have seen that Nusselt number, and Sherwood number exhibit a declining trend while skin friction increases as the Magnetic parameter increases. Table 3 elucidates the influence of porosity parameter (K_1) on the skin friction coefficient ($f''(0)$), Sherwood number ($-\phi'(0)$), and Nusselt number ($-\theta'(0)$). From the table it is evident that as K_1 enhances, the skin friction coefficient trends enhancement on the other

hand the Nusselt number, and Sherwood number exhibit a declining trend. Table 4 depicts the impact of the Casson fluid variable on Sherwood number ($-\phi'(0)$), Nusselt number ($-\theta'(0)$), and skin friction coefficient $f''(0)$ accordingly. We have identified that with an increase in the Casson fluid parameter, the skin friction coefficient experiences growth, but Nusselt number and Sherwood number experience a decline trend. Table 5 exhibits the influence of suction parameter (S) on the skin friction coefficient ($f''(0)$), Sherwood number ($-\phi'(0)$), and Nusselt number ($-\theta'(0)$). From the table, it is clear that as S increases, $f''(0)$ increases but Sherwood number and Nusselt number decrease.

Table 1. Numerical values of $f''(0)$, for $Pr=0$, $Sc=0$, $K_1=0$, $M=0$, $\beta=1$.

S	Bhattacharyya <i>et al.</i> [17]	Present Study
3.0	1.00000	1.0010
3.5	1.39039	1.3905
4.0	1.70711	1.7074
4.5	2.00000	2.0064
5.0	2.28078	2.2807

Table 2. Numeric data of Sherwood number, Nusselt number and Skin fraction for magnetic parameter (M)

Pr	Sc	S	K_1	β	M	Skin Friction	Nusselt number	Sherwood number
0.7	0.5	2.0	0.1	10	0.0	1.1803	-1.1622	-0.8682
					0.2	1.2272	-1.1667	-0.8715
					0.4	1.3473	-1.1778	-0.8794
					0.6	1.5070	-1.1914	-0.8892
					0.8	1.6846	-1.2049	-0.8990

Table 3. Numeric data of Sherwood number, Nusselt number and Skin fraction for porosity parameter (K_1)

Pr	Sc	S	M	β	K_1	Skin Friction	Nusselt number	Sherwood number
0.7	0.5	2.0	0.1	10	0.0	1.3380	-1.1770	-0.8789
					0.2	1.4999	-1.1908	-0.8888
					0.4	1.6317	-1.2010	-0.8962
					0.6	1.7452	-1.2092	-0.9021
					0.8	1.8461	-1.2160	-0.9070

Table 4. Numeric data of Sherwood number, Nusselt number and Skin fraction for Casson fluid parameter (β)

Pr	Sc	S	M	K_1	β	Skin Friction	Nusselt number	Sherwood number
0.7	0.5	2.0	0.5	0.1	0.0	0.3333	-1.0284	-0.7751
					0.2	0.3881	-1.0428	-0.7849
					0.4	0.4577	-1.0582	-0.7954
					0.6	0.5344	-1.0732	-0.8056
					0.8	0.6114	-1.0868	-0.8150

Table 5. Numeric data of Sherwood number, Nusselt number and Skin fraction for suction parameter (S)

Pr	Sc	β	M	K_1	S	Skin Friction	Nusselt number	Sherwood number
0.7	0.5	10	0.5	1	0.5	0.7730	-0.2918	-0.3046
					1.0	1.1238	-0.5451	-0.4759
					1.5	1.5187	-0.8662	-0.6819
					2.0	1.9376	-1.2218	-0.9112
					2.5	2.3694	-1.5896	-1.1548

5. CONCLUSION

We have numerically investigated the thermal and species concentration transmission of Casson fluid model over a shrinking surface. The governing equations are transformed into solvable ODEs, and bvp4c solver scheme is used to solve them. The key points of our study are listed below.

- As the magnetic parameter enhances, the motion of the Casson fluid increases.
- The porosity parameter enhances the velocity profile.
- With rises in Prandtl number, the temperature profile falls.
- The Casson fluid parameter is very important for controlling the fluid's temperature and concentration, which helps prevent damage to the system, as well as for helping the fluid develop its velocity.
- Schmit number retards the concentration profile.
- Suction phenomenon increases the velocity of the fluids.

ORCID

REFERENCES

- [1] I.J. Grubka, and K.M. Bpbba, "Heat transfer characteristics of a continuous stretching surface with variable temperature," ASME J. Heat Transfer, **107**, 248-250 (1985). <https://doi.org/10.1115/1.3247387>
- [2] W.H.H. Banks, "Similarity solutions of boundary layer equations for a stretching wall," J. Mech. Theor. Appl. **2**, 375-392 (1983).
- [3] L.J. Crane, "Flow past a stretching plate," J. Appl. Math. Phys. (ZAMP), **21**, 645-647 (1970). <https://doi.org/10.1007/BF01587695>
- [4] E. Magyari, and B. Keller, "Exact solution for self-similar boundary layer flows induced by permeable stretching walls," Eur. J. Mech. B/Fluids, **19**, 109-122 (2000). [https://doi.org/10.1016/S0997-7546\(00\)00104-7](https://doi.org/10.1016/S0997-7546(00)00104-7)
- [5] S. Liao, and I. Pop, "On explicit analytic solutions of boundary layer equations about a flows in a porous medium or for a stretching wall," Int. J. Heat and Mass Transfer, **47**, 75-85 (2004). [https://doi.org/10.1016/S0017-9310\(03\)00405-8](https://doi.org/10.1016/S0017-9310(03)00405-8)
- [6] C.Y. Wang, "Liquid film on an unsteady stretching sheet," Quart. Appl. Math. **48**, 601-610 (1990). <https://doi.org/10.1090/qam/1079908>
- [7] M. Miklavcic, and C.Y. Wang, "Viscous flow due to a shrinking sheet," Quart. Appl. Math. **64**, 283-290 (2006). <https://doi.org/10.1090/S0033-569X-06-01002-5>
- [8] T. Fang, and J. Zhang, "Closed-form exact solution of MHD viscous flow over a shrinking sheet," Commun. Nonlinear Sci. Num. Simulat. **14**, 2853-2857 (2009). <https://doi.org/10.1016/j.cnsns.2008.10.005>
- [9] C.S.K. Raju, G. Neeraja, P.A. Dinesh, K. Vidya, and B.R. Kumar, "MHD Casson fluid in a suspension of convective conditions and cross diffusion across a surface of paraboloid of revolution," Alexandria Eng. J. **57**(4), 3615-3622 (2018). <https://doi.org/10.1016/j.aej.2017.11.022>
- [10] M. Prameela, K. Gangadhar, and G.J. Reddy, "MHD free convective non-Newtonian Casson fluid flow over an oscillating vertical plate," Partial Differ. Equ. Appl. Math. **5**, 100366 (2022). <https://doi.org/10.1016/j.padiff.2022.100366>
- [11] M.V. Krishna, "Chemical reaction, heat absorption and Newtonian heating on MHD free convective Casson hybrid nanofluids past an infinite oscillating vertical porous plate," Int. Commun. Heat Mass Transf. **138**, 106327 (2022). <https://doi.org/10.1016/j.icheatmasstransfer.2022.106327>
- [12] M.S. Aghighi, A. Ammar, and H. Masoumi, "Double-diffusive natural convection of Casson fluids in an enclosure," Int. J. Mech. Sci. **236**, 107754 (2022). <https://doi.org/10.1016/j.ijmecsci.2022.107754>
- [13] F. Hussain, M. Nazeer, M. Altanji, A. Saleem, and M.M. Ghafar, "Thermal analysis of Casson rheological fluid with gold nanoparticles under the impact of gravitational and magnetic forces," Case Stud. Therm. Eng. **28**, 101433 (2021). <https://doi.org/10.1016/j.csite.2021.101433>
- [14] P.P. Humane, V.S. Patil, A.B. Patil, MD. Shamshuddin, and G.R. Rajput, "Dynamics of multiple slip boundaries effect on MHD Casson-Williamson double-diffusive nanofluid flow past an inclined magnetic stretching sheet," Proc. Inst. Mech. Eng. Part E: J. Process Mech. Eng. **236**(5), (2022). <https://doi.org/10.1177/09544089221078153>
- [15] M. Awais, T. Salahuddin, and S. Muhammad, "Evaluating the thermo-physical characteristics of non-Newtonian Casson fluid with enthalpy change," Thermal Science and Engineering Progress, **42**, 101948 (2023). <https://doi.org/10.1016/j.tsep.2023.101948>
- [16] E.N. Maraj, U. Faizan, and S. Shaiq, "Influence of joule heating and partial slip on casson nanofluid transport past a nonlinear stretching planar sheet," in: *International Conference on Applied and Engineering Mathematics, ICAEM*, (Taxila, Pakistan, 2019), pp.31-36. <https://doi.org/10.1109/ICAEM.2019.8853731>
- [17] K. Bhattacharyya, M.S. Uddin, and G.C. Layek, "Exact solution for thermal boundary layer in casson fluid flow over permeable shrinking sheet with variable wall temperature and thermal radiation," Alexandria Engineering Journal, **55**, 1703-1712 (2016). <https://doi.org/10.1016/j.aej.2016.03.010>
- [18] D. Dey, and B. Chutia, "Dusty nanofluid flow with bioconvection past a vertical stretching surface," **34**(6), 375-380 (2022). Journal of King Saud University- Engineering Sciences. <https://doi.org/10.1016/j.jksues.2020.11.001>
- [19] D. Dey, and R. Borah, "Stability analysis on dual solutions of second-grade fluid flow with heat and mass transfers over a stretching sheet," International Journal of Thermofluid Science and Technology, **8**(2), 080203 (2021). <https://doi.org/10.36963/IJTST.2021080203>
- [20] D. Dey, and B. Chutia, "Modelling of multi-phase fluid flow with volume fraction past a permeable stretching vertical cylinder and its numerical study," Latin American Applied Research, **51**(3), 165-171 (2021). <https://doi.org/10.52292/j.laar.2021.604>
- [21] Y. Khan, A. Hussain, and N. Faraz, "Unsteady linear viscoelastic fluid model over a stretching/shrinking sheet in the region of stagnation point flows," Sci. Iran. **19**, 1541-1549 (2012). <https://doi.org/10.1016/j.scient.2012.10.019>
- [22] T. Hayat, T. Javed, and M. Sajid, "Analytic solution for MHD rotating flow of a second grade fluid over a shrinking surface," Phys. Lett. A, **372**, 3264-3273 (2008). <https://doi.org/10.1016/j.physleta.2008.01.069>
- [23] T. Hayat, Z. Abbas, and N. Ali, "MHD flow and mass transfer of an upper-convected Maxwell fluid past a porous shrinking sheet with chemical reaction species," Phys. Lett. A, **372**, 4698-4704 (2008). <https://doi.org/10.1016/j.physleta.2008.05.006>
- [24] T. Hayat, S. Iram, T. Javed, and S. Asghar, "Shrinking flow of second grade fluid in a rotating frame: an analytic solution," Commun. Nonlinear Sci. Num. Simul. **15**, 2932-2941 (2010). <https://doi.org/10.1016/j.cnsns.2009.11.030>
- [25] G.R. Rajput, M.D. Shamshuddin, Sulyman, and O. Salawu, "Thermosolutal convective non-Newtonian radiative Casson fluid transport over a vertical plate propagated by Arrhenius kinetics with heat source/sink," Heat Transfer, **50**(3), 2829-2848 (2021). <https://doi.org/10.1002/htj.22008>
- [26] M.D. Shamshuddin, and W. Ibrahim, "Finite element numerical technique for magneto-micropolar nanofluid flow filled with chemically reactive Casson fluid between parallel plates subjected to rotatory system with electrical and Hall currents," Int. J. Model. Simul. **42**(6), 985-1004 (2022). <https://doi.org/10.1080/02286203.2021.2012634>
- [27] W. Alghamdi, T. Gul, M. Nullah, A. Rehman, S. Nasir, A. Saeed, and E. Bonyah, "Boundary layer stagnation point flow of the casson hybrid nanofluid over an unsteady stretching surface," AIP Advances, **11**, 015016 (2020). <https://doi.org/10.1063/5.0036232>
- [28] D. Dey, and R. Borah, "Dual solutions of boundary layer flow with heat and mass transfers over an exponentially shrinking cylinder: stability analysis," Latin American Applied Research, **50**(4), 247-253 (2020). <https://doi.org/10.52292/j.laar.2020.535>
- [29] Z. Shah, P. Kumam, and W. Deebani, "Radiative MHD casson nanofluid flow with activation energy and chemical reaction over past nonlinearly stretching surface through entropy generation," Scientific Reports, **10**(1), 4402 (2020). <https://doi.org/10.1038/s41598-020-61125-9>

- [30] S. Nadeem, R. Mehmood, and N.S. Akbar, "Nanoparticle analysis for non-orthogonal stagnation point flow of a third order fluid towards a stretching surface," *J. Comput. Theor. Nanosci.* **10**, 2737–2747 (2013). <https://doi.org/10.1166/jctn.2013.3274>
- [31] S. Nadeem, R.U. Haq, Z.H. Khan, "Numerical study of MHD boundary layer flow of a Maxwell fluid past a stretching sheet in the presence of nanoparticles," *J. Taiwan Inst. Chem. Eng.* **45**, 121–126 (2014). <https://doi.org/10.1016/j.jtice.2013.04.006>
- [32] H. Rosali, A. Ishak, and I. Pop, "Micropolar fluid flow towards a stretching/shrinking sheet in a porous medium with suction," *Int. Commun. Heat Mass Transf.* **39**, 826–829 (2012). <https://doi.org/10.1016/j.icheatmasstransfer.2012.04.008>
- [33] N.A. Yacob, and A. Ishak, "Micropolar fluid flow over a shrinking sheet," *Meccanica*, **47**, 293–299 (2012). <https://doi.org/10.1007/s11012-011-9439-8>
- [34] N.A. Yacob, A. Ishak, and I. Pop, "Melting heat transfer in boundary layer stagnation-point flow towards a stretching/shrinking sheet in a micropolar fluid," *Comput. Fluids*, **47**, 16–21 (2011). <https://doi.org/10.1016/j.compfluid.2011.01.040>
- [35] A. Ishak, Y.Y. Lok, and I. Pop, "Non-Newtonian power-law fluid flow past a shrinking sheet with suction," *Chem. Eng. Commun.* **199**, 142–150 (2012). <https://doi.org/10.1080/00986445.2011.578696>
- [36] A. Ishak, Y.Y. Lok, and I. Pop, "Stagnation-point flow over a shrinking sheet in a micropolar fluid," *Chem. Eng. Commun.* **197**, 1417–1427 (2010). <https://doi.org/10.1080/00986441003626169>
- [37] D. Dey, R. Borah, and A.S. Khound, "Stability analysis on dual solutions of MHD Casson fluid flow with thermal and chemical reaction over a permeable elongating sheet," *Heat Transfer*, **51**(4), 3401–3417 (2022). <https://doi.org/10.1002/htj.22456>
- [38] T. Sarkar, S. Reza-E-Rabbi, S.M. Arifuzzaman, R. Ahmed, M.S. Khan, and S.F. Ahmmed, "MHD radiative flow of Casson and Williamson nanofluids over an inclined cylindrical surface with chemical reaction effects," *Int. J. Heat Technol.* **37**, 1117–1126 (2019). <https://doi.org/10.18280/ijht.370421>
- [39] K. Bhattacharyya, T. Hayat, and A. Ahmed, "Analytic solution for magnetohydrodynamic boundary layer flow of Casson fluid over a stretching/shrinking sheet with wall mass transfer," *Chin. Phys. B*, **22**(2), 024702 (2013). <https://doi.org/10.1088/1674-1056/22/2/024702>
- [40] D. Dey, R.K. Das, R. Borah, "A Simulation of Nanofluid Flow with Variable Viscosity and Thermal Conductivity Over a Vertical Stretching Surface," in: *Emerging Technologies in Data Mining and Information Security. Lecture Notes in Networks and Systems*, vol. 491, edited by P. Dutta, S. Chakrabarti, A. Bhattacharya, S. Dutta, V. Piuri, (Springer, Singapore, 2023). https://doi.org/10.1007/978-981-19-4193-1_18
- [41] S. Pramanik, "Casson Fluid Flow and Heat Transfer past an Exponentially Porous Stretching Sheet in Presence of Thermal Radiation," *Ain Shams Engineering Journal*, **5**(1), 205–212 (2014). <https://doi.org/10.1016/j.asej.2013.05.003>
- [42] A.S. Oke, W.N. Mutuku, M. Kimathi, and I.L. Animasaun, "Insight into the dynamics of non-newtonian casson fluid over a rotating non-uniform surface subject to coriolis force," *Nonlinear Engineering*, **9**(1), 398–411 (2020). <https://doi.org/10.1515/nleng-2020-0025>
- [43] D. Dey, and M. Hazarika, "Entropy generation of hydro-magnetic stagnation point flow of micropolar fluid with energy transfer under the effect of uniform suction / injection," *Latin American Applied Research*, **50**(3), 209–214 (2020). <https://doi.org/10.52292/j.laar.2020.206>

ПОТІК РІДИНИ КАССОНА ПОВЗ ПОВЕРХНІ, ЩО СТИСКУЄТЬСЯ, З ТЕПЛО-ТА МАСОПЕРЕНОСОМ

Раджеш Кумар Дас^а, Дебасіш Дей^б

^аДепартамент математики, Пандіт Діндаял Упадхья Адарша Махавідьялайя Амджонга, Гоалтара, Індія

^бДепартамент математики, Університет Дібругарх, Дібругарх, Індія

У цьому дослідженні чисельно досліджено поведінку тепло- та масопередачі потоку рідини Кассона повз пористий лист що стискається за наявності магнітного поля, теплового випромінювання та всмоктування або видування на поверхні. Застосовуючи відповідні перетворення подібності, основні часткові нелінійні диференціальні рівняння маси, потоку та теплопередачі перетворюються на звичайні диференціальні рівняння, які потім можна розв'язувати чисельно за допомогою схеми MATLAB bvp4c. Ми проаналізували та графічно показали вплив кількох безрозмірних керуючих факторів на профілі температури, концентрації та швидкості. Крім того, досліджено та зведено в таблиці тертя Шервуда, Нуссельта та Скіна для рідин Кассона. Результати поточного дослідження щодо рідини Кассона демонструють значну узгодженість із попередніми дослідженнями за конкретних обставин.

Ключові слова: *рідина Кассона; тепломасообмін; проникність; МГД; лист що стискається*

A COMPARATIVE STUDY ON MHD FORCED CONVECTIVE FLOW OF DIFFERENT NANOFUIDS WITH WATER (H₂O) AS BASE FLUID IN A VERTICAL RECTANGULAR DUCT

 Bishnu Ram Das*,  P.N. Deka[#]

Department of Mathematics, Dibrugarh University, Dibrugarh-786004, Assam, India

**Corresponding Author e-mail: e-mail: bishnuram.das84@gmail.com; pndeka@dibru.ac.in*

Received December 21, 2023; revised January 24, 2024; accepted January 28, 2024

In this paper, a comparative study on MHD forced convective flow for heat transfer efficiency of different nanofluids with water (H₂O) as base fluid has been carried out. Here, in this study flow through vertical rectangular has been considered in presence of strong magnetic field. In this laminar flow we consider duct walls as electrically non-conducting where the transverse magnetic field acting normally on the duct walls. Joule heat and the viscous dissipation effects are included in the energy equation and furthermore the walls of the duct are kept at constant temperature. An explicit finite difference method has been adopted with fine grid in the control volume for solving the governing equations of this MHD nanofluid flow. Computational processes are carried out using MATLAB code. In this present work we have plotted the flow fields velocity, induced magnetic field, and temperature for various values of MHD flow parameters graphically by varying thermal Grashof number (G_r), Hartmann number (Ha), Reynold number (Re), Eckert number (Ec), Prandtl number (Pr), magnetic Reynold number (Re_m), and nanoparticle volume fraction (ϕ) respectively.

Keywords: *MHD forced convective flow; Nanofluids; Steady; Explicit finite difference method (EFDM); Vertical rectangular duct*

PACS: 95.30.Qd, 94.30.cq, 94.30.Kq

1. INTRODUCTION

Inclusion of nanoparticles in the base fluid is an innovative way to enhance heat transfer. There are large variety of nanoparticles used in water based nanofluids and each of them exhibit performance in heat transfer process and possess different nanofluid flow characteristics. Nanofluids have better suspension stability, Newtonian behavior, healthier thermal conductivity, and huge chaotic movements of nanoparticles are believed to be liable for the increased of heat transfer characteristic. In natural convection, the base fluid has a low thermal conductivity, which limits the heat transfer performance. Use of nanofluid is an innovative technique in which the colloidal suspension of nanometer sized particles in a base fluid (nanofluid) was first introduced by Choi [1] at the Argonne National Laboratory, U.S.A.

Latter, Lee *et al.* [2] analyze the thermal conductivity of nonidentical metal oxides and in this way, they have got the shape and size provide considerably to the more acceptable thermal conductivity of the nanofluid. Forced convection is the most important aspect investigation for applications in a rectangular duct. The applications are thermal power plants, solar collectors, chemical catalytic reactors and cooling systems. Thermal conductivity of TiO₂/water nano-fluid up to 7.5% nanoparticle concentration experimentally found by Xuan *et al.* [3]. Heat transfer efficiency with nano-fluid was examined by many researchers [4, 5].

In another study Ellahi *et al.* [6] considered water base nanofluid with Al₂O₃ as nanoparticles to study aggregation effect on such nanofluid having permeable wedge in the presence of mixed convection. An analytical solution of natural convection flow problem nanofluid over a linearly stretching sheet under magnetic field was attempted by Hamad [7]. Kodi *et al.* [8] investigated influence of MHD mixed convection flow for Maxwell nanofluid through a vertical cone with porous material in the existence of variable heat conductivity and diffusion. Ragulkumar *et al.* [9] studied dissipative MHD free convective nanofluid flow past a vertical cone under radiative chemical reaction with mass flux.

Mixed convection of Casson nanofluid over a stretching sheet with convectively heated chemical reaction and heat source/sink observed by Hayat *et al.* [10]. The focus of this study is to learn about the effects of solid volume fraction on heat transfer quantity and on differential pressure. It was about in the such that increasing concentration of nanoparticle has no significant effect on heat transfer but pressure drop enhancement has affected on heat transfer process. Ferdows *et al.* [11] considered nanofluid inclusion with diverse types of nanoparticles for the incompressible, laminar, steady and convective viscous flow. They observed that heat transfer was constantly increased with increase value of nanoparticle volume fraction parameter. Numerical investigation of solar radiation on the effects on heat-mass transfer phenomena of nanofluids recently studied by [12, 13] Rao and Deka. In another study, very recently Das *et al.* [14] investigated in a vertical square duct numerical analysis on magnetohydrodynamics (MHD) mixed convection flow of Al₂O₃/water nanofluids. Many authors who had investigated heat transfer nanofluids boundary layer problem given in ref. [15, 16]. Paul *et al.* [17] studied Darcy-Forchheimer MHD radiative flow through a porous space incorporating viscous dissipation, heat source, and chemical reaction effect across an exponentially stretched surface. Arruna *et al.* [18] have been investigated effect of chemical reaction and radiation absorption on MHD Casson fluid over an exponentially stretching sheet with slip conditions: ethanol as solvent. On a non-Newtonian nanofluid flow and heat mass transfer in a two-dimensional steady laminar boundary layer caused by a horizontally stretching sheet investigated by

Alrihieli *et al.* [19]. The study includes heat generation/absorption near a stagnation point and on the radially stretching plate. In a vertical stretching surface Jawad [20] studied on magnetohydrodynamics (MHD) stagnation point flow of micropolar fluids with buoyancy and thermal radiation. Shoeibi *et al.* [21] have been observed about the utilize of hybrid nanofluids in solar system. In a vertical duct containing metallic/carbon nanofluids Beg *et al.* [22] have been studied with Dufour and Soret double cross repetition counting of thermo-solutal convection. Bhatti *et al.* [23] have been studied swimming of Gyrotactic microorganism in MHD Williamson nanofluid flow between rotating circular plates embedded in porous medium. Hussain *et al.* [24] have been investigated MHD instability of Hartmann flow of nanoparticles Fe_2O_3 in water. [25] Umavathi and Beg investigated double diffusive convection in a dissipative electrically conducting nanofluid under orthogonal electrical and magnetic fields. [26] Bhatti and Abdelsalam observed Bio-inspired peristaltic propulsion of hybrid nanofluid flow with Tantalum (Ta) and Gold (Au) nanoparticles under magnetic effects.

The aim of this present work is to numerically investigate the laminar steady forced convective flow of different nanofluids with water (H_2O) as base fluid in presence of strong magnetic field in a vertical rectangular duct. We have presented result of our investigation for different type of nanofluid flow and we have drawn conclusion heat transfer efficiency of different water based nanofluid.

Table (i). Numerical values of water (H_2O) and nanoparticles titanium oxide (TiO_2), aluminium oxide (Al_2O_3), ferric oxide (Fe_2O_3), and silicon oxide (SiO_2)

	Density (ρ)	Specific heat capacity (C_p)	Thermal conductivity (k)	Electrical conductivity (σ)
H_2O	997.1	4179	0.613	5.5×10^{-6}
TiO_2	4250	686.2	8.9528	2.58×10^{-7}
Al_2O_3	3970	765	40	35×10^6
Fe_2O_3	5180	765	9.7	25×10^3
SiO_2	2200	703	1.2	2.58×10^{-7}

2. MATHEMATICAL FORMULATION

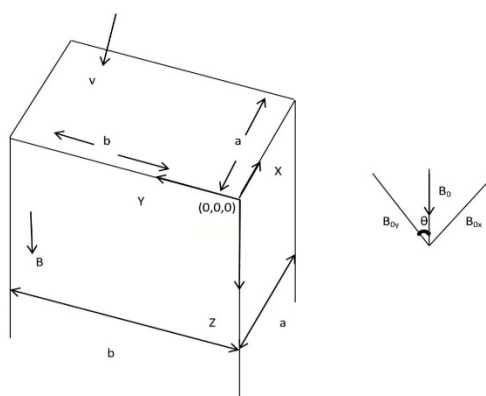


Figure 1. Physical configuration

In this paper, we have considered a laminar steady flow of incompressible fluid through a duct which is vertically positioned, where cross section of the duct has length a and breadth b . Both the parallel walls of the duct are kept at $x = 0$ and $x = a$, and the other parallel walls are kept at $y = 0$ and at $y = b$. Here we consider that the duct has cross section on the xy - plane where the fluid velocity, induced magnetic field and temperature are in the z -direction. In this case applied uniform magnetic field B_0 of the fluid acts in a direction lying in the xy - plane but making an angle θ with the y -axis. The flow is handled in presence of a constant pressure gradient $\frac{\partial p}{\partial z}$ and the MHD force. In this work, the physical parameters except pressure are independent of variable z , the fluid properties in the buoyancy term are considered as constant. Moreover, Joule heating and the effects of viscous dissipation are considered in the energy equation. Our fluid is viscous and incompressible and flow is laminar and steady. We have also assumed that there is no net flow of current in the z -direction. The velocity, induced magnetic field, and the temperature \vec{V} , \vec{B} , and T as:

$$\vec{V} = \{0, 0, V_z(x, y)\}, \vec{B} = \{B_{ox}, B_{oy}, B_z(x, y)\}, T = T(x, y) \text{ in where } B_{ox} = B_0 \sin \theta, B_{oy} = B_0 \cos \theta$$

3. GOVERNING EQUATIONS

Equation of continuity is

$$\nabla \cdot \vec{V} = 0. \quad (1)$$

The MHD momentum equation is

$$\rho_{nf} \left[\frac{\partial \vec{V}}{\partial t} + (\vec{V} \cdot \nabla) \vec{V} \right] = -\nabla p + \mu_{nf} \nabla^2 \vec{V} + (\vec{J} \times \vec{B}) + \vec{X}, \quad (2)$$

in where $\vec{X} = g(\rho\beta)_{nf}(T - T_o)$
 Maxwell's equation is

$$\nabla \cdot \vec{B} = 0. \tag{3}$$

Ampere's law

$$\nabla \times \vec{B} = (\mu_e)_{nf} \vec{J}. \tag{4}$$

Definition of Ohm's law:

$$\vec{J} = \sigma_{nf}(\vec{E} + \vec{V} \times \vec{B}). \tag{5}$$

Equation of magnetic induction is

$$\frac{\partial \vec{B}}{\partial t} = \nabla \times (\vec{V} \times \vec{B}) + \lambda_{nf} \nabla^2 \vec{B}. \tag{6}$$

Now using equation (1) & equation (3) in equation (6) we get

$$\frac{\partial \vec{B}}{\partial t} + (\vec{V} \cdot \nabla) \vec{B} = (\vec{B} \cdot \nabla) \vec{V} + \lambda_{nf} \nabla^2 \vec{B}. \tag{7}$$

The Energy equation is

$$(\rho C_p)_{nf} \left[\frac{\partial T}{\partial t} + (\vec{V} \cdot \nabla) T \right] = k_{nf} \nabla^2 T + \mu_{nf} \phi + \frac{J^2}{\sigma_{nf}}. \tag{8}$$

Again, we get

$$\nu_{nf} = \frac{\mu_{nf}}{\rho_{nf}}. \tag{9}$$

and

$$\lambda_{nf} = \frac{1}{\sigma_{nf}(\mu_e)_{nf}} \tag{10}$$

We know that the dynamic viscosity of nanofluid, effective density of nanofluid, magnetic permeability of nanofluid, electrical conductivity of nanofluid, heat capacity of nanofluid, thermal expansion coefficient of nanofluid, and thermal conductivity of nanofluid as:

$$\mu_{nf} = \mu_f(1 - \phi)^{-2.5}, \tag{11}$$

$$\rho_{nf} = \left[1 - \phi + \phi \frac{\rho_s}{\rho_f} \right] \rho_f, \tag{12}$$

$$(\mu_e)_{nf} = \left[1 - \phi + \phi \frac{(\mu_e)_s}{(\mu_e)_f} \right] (\mu_e)_f, \tag{13}$$

$$\sigma_{nf} = \left[1 + \frac{3(\sigma-1)\phi}{(\sigma+2)-(\sigma-1)\phi} \right] \sigma_f, \tag{14}$$

$$(\rho C_p)_{nf} = \left[1 - \phi + \phi \frac{(\rho C_p)_s}{(\rho C_p)_f} \right]. \tag{15}$$

$$(\rho\beta)_{nf} = \left[1 - \phi + \phi \frac{(\rho\beta)_s}{(\rho\beta)_f} \right] (\rho\beta)_f \tag{16}$$

$$k_{nf} = \left[\frac{k_s + 2k_f - 2\phi(k_f - k_s)}{k_s + 2k_f + \phi(k_f - k_s)} \right] k_f. \tag{17}$$

For the problem the corresponding the initial & boundary conditions are given by

$$\begin{aligned} V_z = 0, B_z = 0, T = T_o, \text{ when } x = 0 \\ V_z = 0, B_z = 0, T = T_o, \text{ when } x = a, \text{ for } 0 \leq y \leq b \\ V_z = 0, B_z = 0, T = T_o, \text{ when } y = 0 \\ V_z = 0, B_z = 0, T = T_o, \text{ when } y = b, \text{ for } 0 \leq x \leq b. \end{aligned} \tag{18}$$

The following dimensionless variables:

$$\bar{V} = \frac{V}{V_o}, \bar{B} = \frac{B}{B_o}, \bar{T} = \frac{T - T_o}{\Delta T}, \bar{x} = \frac{x}{a}, \bar{y} = \frac{y}{Aa}, \tag{19}$$

where:

$$A = \frac{b}{a}, B_o = -a^2(\mu_e)_{nf} \sqrt{\frac{\sigma_{nf}}{\rho_{nf}\nu_{nf}}} \frac{\partial p}{\partial z}, V_o = -\frac{a^2}{\rho_{nf}\nu_{nf}} \frac{\partial p}{\partial z}, T - T_o = \frac{V_o^2}{(C_p)_f},$$

Now using above dimensionless parameters and after simplification we get,

$$\frac{\partial^2 V}{\partial x^2} + \frac{1}{A^2} \frac{\partial^2 V}{\partial y^2} + \frac{B_0^2 a^2 \left[1 + \frac{3(\sigma-1)\phi}{(\sigma+2)-(\sigma-1)\phi} \right] \frac{\sigma_f}{\mu_f} (1-\phi)^{2.5}}{V_0 a \left[1 - \phi + \phi \frac{(\mu_e)_s}{(\mu_e)_f} \right] (\mu_e)_f \left[1 + \frac{3(\sigma-1)\phi}{(\sigma+2)-(\sigma-1)\phi} \right] \sigma_f} \sin\theta \frac{\partial B}{\partial x} + \frac{1}{A} \frac{B_0^2 a^2 \left[1 + \frac{3(\sigma-1)\phi}{(\sigma+2)-(\sigma-1)\phi} \right] \frac{\sigma_f}{\mu_f} (1-\phi)^{2.5}}{V_0 a \left[1 - \phi + \phi \frac{(\mu_e)_s}{(\mu_e)_f} \right] (\mu_e)_f \left[1 + \frac{3(\sigma-1)\phi}{(\sigma+2)-(\sigma-1)\phi} \right] \sigma_f} \cos\theta \frac{\partial B}{\partial y} + \frac{g\beta_f a^3 (T-T_0)}{\nu_f^2} \cdot \frac{\nu_f}{V_0 a} T + 1 = 0. \quad (20)$$

$$\frac{\partial^2 B}{\partial x^2} + \frac{1}{A^2} \frac{\partial^2 B}{\partial y^2} + V_0 a \left[1 - \phi + \phi \frac{(\mu_e)_s}{(\mu_e)_f} \right] (\mu_e)_f \left[1 + \frac{3(\sigma-1)\phi}{(\sigma+2)-(\sigma-1)\phi} \right] \sigma_f \sin\theta \frac{\partial V}{\partial x} + \frac{1}{A} V_0 a \left[1 - \phi + \phi \frac{(\mu_e)_s}{(\mu_e)_f} \right] (\mu_e)_f \left[1 + \frac{3(\sigma-1)\phi}{(\sigma+2)-(\sigma-1)\phi} \right] \sigma_f \cos\theta \frac{\partial V}{\partial y} = 0. \quad (21)$$

$$\frac{\partial^2 T}{\partial x^2} + \frac{1}{A^2} \frac{\partial^2 T}{\partial y^2} + \frac{\mu_f C_p}{(1-\phi)^{2.5} k_f \left[\frac{k_s + 2k_f - 2\phi(k_f - k_s)}{k_s + 2k_f + \phi(k_f - k_s)} \right]} \cdot \frac{V_0^2}{C_p \Delta T} \left[\left(\frac{\partial V}{\partial x} \right)^2 + \frac{1}{A^2} \left(\frac{\partial V}{\partial y} \right)^2 \right] + \frac{B_0^2 a^2 \left[1 + \frac{3(\sigma-1)\phi}{(\sigma+2)-(\sigma-1)\phi} \right] \frac{\sigma_f}{\mu_f}}{V_0^2 a^2 \left[1 - \phi + \phi \frac{(\mu_e)_s}{(\mu_e)_f} \right]^2 \left[1 + \frac{3(\sigma-1)\phi}{(\sigma+2)-(\sigma-1)\phi} \right]^2 \sigma_f^2 (\mu_e)_f^2 \left[\frac{k_s + 2k_f - 2\phi(k_f - k_s)}{k_s + 2k_f + \phi(k_f - k_s)} \right]} \cdot \frac{\mu_f C_p}{k_f} \cdot \frac{V_0^2}{C_p \Delta T} \left[\left(\frac{\partial B}{\partial x} \right)^2 + \frac{1}{A^2} \left(\frac{\partial B}{\partial y} \right)^2 \right] = 0. \quad (22)$$

Let

$$E_1 = \frac{1}{(1-\phi)^{2.5}}, E_2 = \left[1 - \phi + \phi \frac{\rho_s}{\rho_f} \right], E_3 = \left[1 - \phi + \phi \frac{(\mu_e)_s}{(\mu_e)_f} \right], E_4 = \left[1 + \frac{3(\sigma-1)\phi}{(\sigma+2)-(\sigma-1)\phi} \right], E_5 = \left[1 - \phi + \phi \frac{(\rho C_p)_s}{(\rho C_p)_f} \right], E_6 = \left[1 - \phi + \phi \frac{(\rho\beta)_s}{(\rho\beta)_f} \right], E_7 = \left[\frac{k_s + 2k_f - 2\phi(k_f - k_s)}{k_s + 2k_f + \phi(k_f - k_s)} \right]$$

Therefore, the equations (20), (21), (22) in terms $E_1, E_2, E_3, E_4, E_5, E_6, E_7$ are

$$\frac{\partial^2 V}{\partial x^2} + \frac{1}{A^2} \frac{\partial^2 V}{\partial y^2} + \frac{Ha^2}{R_m} \sin\theta \frac{E_4}{E_1 E_3 E_4} \frac{\partial B}{\partial x} + \frac{1}{A} \frac{Ha^2}{R_m} \cos\theta \frac{E_4}{E_1 E_3 E_4} \frac{\partial B}{\partial y} + \frac{G_r}{R_e} T + 1 = 0. \quad (23)$$

$$\frac{\partial^2 B}{\partial x^2} + \frac{1}{A^2} \frac{\partial^2 B}{\partial y^2} + R_m \sin\theta E_3 E_4 \frac{\partial V}{\partial x} + \frac{1}{A} R_m \cos\theta E_3 E_4 \frac{\partial V}{\partial y} = 0. \quad (24)$$

$$\frac{\partial^2 T}{\partial x^2} + \frac{1}{A^2} \frac{\partial^2 T}{\partial y^2} + \frac{E_1}{E_7} P_r Ec \left[\left(\frac{\partial V}{\partial x} \right)^2 + \frac{1}{A^2} \left(\frac{\partial V}{\partial y} \right)^2 \right] + \frac{Ha^2 P_r Ec}{R_m^2} \frac{E_4}{E_3^2 E_4^2 E_7} \left[\left(\frac{\partial B}{\partial x} \right)^2 + \frac{1}{A^2} \left(\frac{\partial B}{\partial y} \right)^2 \right] = 0. \quad (25)$$

Where:

$Ha = B_0 a \sqrt{\frac{\sigma_f}{\mu_f}}$, is the Hartmann number,

$G_r = \frac{g\rho_f\beta_f(T-T_0)a^3}{\mu_f^2}$, is the thermal Grashof number,

$P_r = \frac{\mu_f(Cp)_f}{k_f}$, is the Prandtl number,

$Ec = \frac{V_0^2}{(Cp)_f \Delta T}$, is the Eckert number,

$R_e = \frac{V_0 a}{\mu_f}$, is the Reynolds number,

and

$R_m = V_0 a (\mu_e)_f \sigma_f$, is the magnetic Reynolds number

The corresponding boundary conditions (21) gives

$$\begin{aligned} V = 0, B = 0, T = 0, \text{ when } x = 0 \\ V = 0, B = 0, T = 0, \text{ when } x = 1, \text{ for } 0 \leq y \leq A \\ V = 0, B = 0, T = 0, \text{ when } y = 0 \\ V = 0, B = 0, T = 0, \text{ when } y = A, \text{ for } 0 \leq x \leq 1. \end{aligned} \quad (26)$$

4. NUMERICAL TECHNIQUE AND GRID INDEPENDENCE STUDY

With the boundary conditions given in equation (26), the dimensionless governing equations (23), equation (24) and equation (25) were discretized using explicit finite difference method. We know that the finite difference second order $\frac{\partial^2 V}{\partial x^2}$ and the first order $\frac{\partial V}{\partial x}$, were discretized as $\frac{\partial^2 V}{\partial x^2} = \frac{V_{i+1,j} - 2V_{i,j} + V_{i-1,j}}{\Delta x^2} + O(\Delta x^2)$ and $\frac{\partial V}{\partial x} = \frac{V_{i+1,j} - V_{i-1,j}}{2\Delta x} + O(\Delta x^2)$, respectively. Therefore, after simplification the equations (23), (24), and (25) we get

$$V_{i,j} = A_9(V_{i+1,j} + V_{i-1,j}) + A_{10}(V_{i,j+1} + V_{i,j-1}) + A_{11}(B_{i+1,j} - B_{i-1,j}) + A_{12}(B_{i,j+1} - B_{i,j-1}) + A_{13}(T_{i,j}) + A_{14}, \tag{27}$$

$$B_{i,j} = A_9(B_{i+1,j} + B_{i-1,j}) + A_{10}(B_{i,j+1} + B_{i,j-1}) + A_{15}(V_{i+1,j} - V_{i-1,j}) + A_{16}(V_{i,j+1} - V_{i,j-1}), \tag{28}$$

$$T_{i,j} = A_9(T_{i+1,j} + T_{i-1,j}) + A_{10}(T_{i,j+1} + T_{i,j-1}) + A_{17}(V_{i+1,j} - V_{i-1,j})^2 + A_{18}(V_{i,j+1} - V_{i,j-1})^2 + A_{19}(B_{i+1,j} - B_{i-1,j})^2 + A_{20}(B_{i,j+1} - B_{i,j-1})^2, \tag{29}$$

Where $A_1 = \frac{1}{A^2}$, $A_2 = \frac{(Ha)^2}{(R_m)} \sin\theta \frac{E_4}{E_1 E_3 E_4} \theta$, $A_3 = \frac{1}{A} \frac{(Ha)^2}{(R_m)} \cos\theta \frac{E_4}{E_1 E_3 E_4}$, $A_4 = \frac{(G_r)}{(R_e)}$, $A_5 = \frac{k^2}{2(A_1 h^2 + k^2)}$, $A_6 = \frac{A_1 h^2}{2(A_1 h^2 + k^2)}$, $A_7 = \frac{A_2 h k^2}{2(A_1 h^2 + k^2)}$, $A_8 = \frac{A_3 h^2 k}{2(A_1 h^2 + k^2)}$, $A_9 = \frac{A_4 h^2 k^2}{A_1 h^2 + k^2}$, $A_{10} = \frac{h^2 k^2}{A_1 h^2 + k^2}$, $A_{11} = R_m \sin\theta E_3 E_4$,

$A_{12} = \frac{1}{A} R_m \cos\theta E_3 E_4$, $A_{13} = \frac{A_{11} h k^2}{2(A_1 h^2 + k^2)}$, $A_{14} = \frac{A_{12} h^2 k}{2(A_1 h^2 + k^2)}$, $A_{15} = \frac{E_1}{E_6} P_r E_c$, $A_{16} = \frac{(Ha)^2 (E_c) (P_r)}{(R_m)^2} \frac{E_4}{E_3^2 E_4^2 E_6}$, $A_{17} = \frac{A_{15} k^2}{4(A_1 h^2 + k^2)}$, $A_{18} = \frac{A_1 A_{15} h^2}{4(A_1 h^2 + k^2)}$, $A_{19} = \frac{A_{16} k^2}{4(A_1 h^2 + k^2)}$, $A_{20} = \frac{A_1 A_{16} h^2}{4(A_1 h^2 + k^2)}$,

are constants and in where $\Delta x = h = 0.001$ and $\Delta y = k = 0.001$.

Discretized boundary conditions are given by

$$\begin{aligned} V_{i,1} = 0, B_{i,1} = 0, T_{i,1} = 0, \text{ when } j = 1 \\ V_{i,m+1} = 0, B_{i,m+1} = 0, T_{i,m+1} = 0, \text{ when } j = n + 1, \\ \text{for } 1 \leq i \leq m + 1 \\ V_{1,j} = 0, B_{1,j} = 0, T_{1,j} = 0, \text{ when } i = 1 \\ V_{m+1,j} = 0, B_{m+1,j} = 0, T_{m+1,j} = 0, \text{ when } i = m + 1 \\ \text{for } 1 \leq j \leq n + 1, \end{aligned} \tag{30}$$

5. RESULTS AND DISCUSSION

The outcome of parameters like, thermal Grashof number (G_r), Hartmann number (Ha), Reynold number (R_e), Prandtl number (P_r), Eckert number (Ec), magnetic Reynold number (R_m), and the nanoparticle volume fraction (ϕ) on the velocity, induced magnetic field, and temperature distributions are exhibits in graphical presentation. We have taken $Ha = 2$, $A = 2.5$, $P_r = 6.93$, $R_m = 1$, $Ec = 0.001$, $h = k = 0.001$, $m = n = 200$, $\phi = 0.02$, $k_f = 0.613$, $k_s = 429$, $\theta = \pi/2$.

The graphs are plotted by utilizing numerical out come through an explicit finite difference method in MATLAB operating system. The velocity distribution of titanium oxide/water nanofluid for various values of Hartmann number (Ha) is depicted in **Figure 2**. We have observed from **Figure 2** that the fluid velocity distribution decreases due to increase in value of Hartmann number (Ha). We know that in the middle of the rectangular duct, the fluid has maximum value of velocity, so in this step the electromagnetic force resists the fluid's motion and this electromagnetic force slow down convection a flatten velocity distribution. Similar nature of induced magnetic field is observed and seen in **Figure 3**. Further, in **Figure 4**. It is observed that temperature (T) is increased with increased value of Hartmann number (Ha) in boundary layer region. The magnetic field introduced to the electrically conducting nanofluid and acting normal to boundary is responsibility for resistive pressure force in the duct which is part of Lorentz force. In the cooling sector magnetic field's effect on nanofluid has many industrial accomplishments too. The velocity distribution of titanium oxide/water nanofluid for various values of thermal Grashof number (G_r) is depicted in Fig. 5. We have seen in **Figure 5** that the velocity distribution enhanced owing to enhancement of parametric values of the thermal Grashof number (G_r). An enlarge in the value of thermal Grashof number has the tendency to induce much flow in the boundary layer due to the effect of thermal buoyancy. Similar nature we have observed in induced magnetic field in **Figure 6**. But it is observed in **Figure 7**, that the temperature profile decreases owing to increase in parametric value of thermal Grashof number (G_r). This means that buoyancy force decreases the temperature field. The velocity distribution of titanium oxide/water nanofluid for different values of Reynold number (R_e) is depicted in **Figure 8**.

It is observed from **Figure 8**, that the velocity profile enhanced owing to enhancement of parametric values of Reynold number (Re). Due to enhancement in values of (Re), in the thermal boundary layer, frictional heating increases.

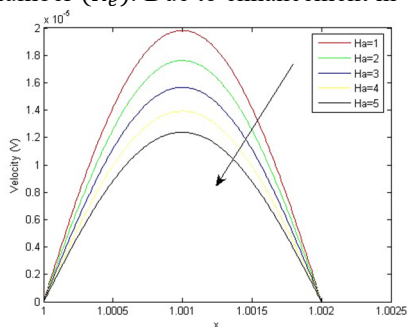


Figure 2. Variation in (V) with Ha

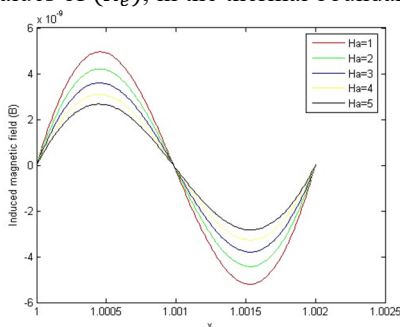


Figure 3. Variation in (B) with Ha

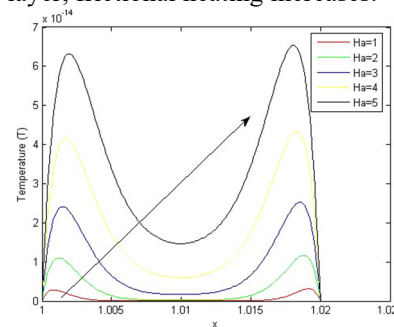


Figure 4. Variation in (T) with Ha

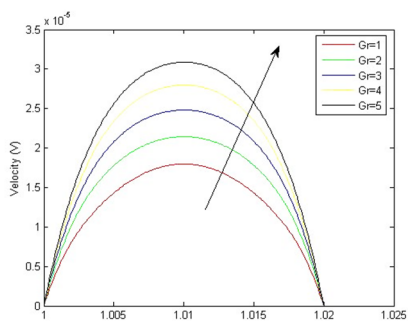


Figure 5. Variation in (V) with Gr

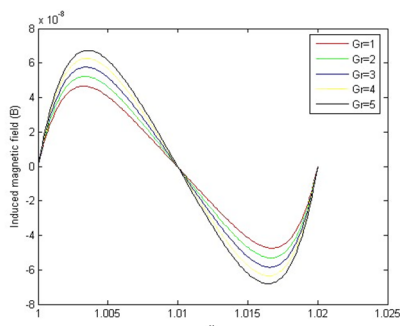


Figure 6. Variation in (B) with Gr

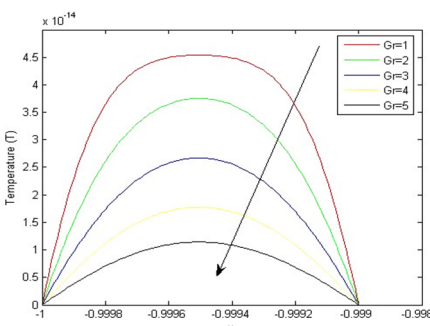


Figure 7. Variation in (T) with Gr

This in results reflect in enhancement of kinetic energy of the fluid particles in the middle layers as a consequence we have the flow rate accelerates and, in this way, increases the velocity. Similar effect we have observed in induced magnetic field in **Figure 9**. The temperature distribution of titanium oxide/water nanofluid for different values of Reynold number (Re) is depicted in **Figure 10**. But we have seen in **Figure 10**, that the temperature profile decreases due to increase in value of Reynold number (Re). The increase in values of Reynold number (Re) enhanced the strength of the discharge velocity on the plate which minimizes the growth of thermal boundary layer. This diminishes the temperature near to the plate surface. The velocity distribution of titanium oxide/water nanofluid for distinct values of Prandtl number (Pr) is represented in graph given in **Figure 11**. We have seen in **Figure 11**, that the velocity profile is enhanced owing to enhancement in the value of Prandtl number (Pr). Due to impact of additional nanoparticles periodic motion of nanoparticle is observed an increase of Prandtl number (Pr). So, the kinetic energy is transform into heat energy, and so the velocity increases.

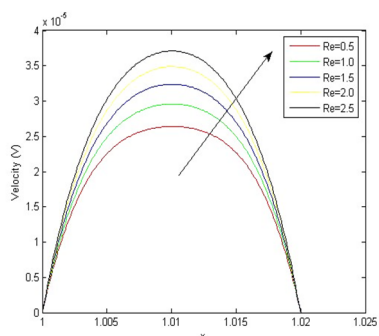


Figure 8. Variation in (V) with Re

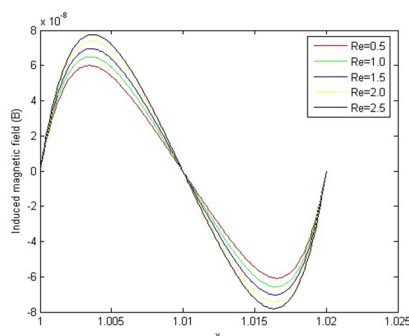


Figure 9. Variation in (B) with Re

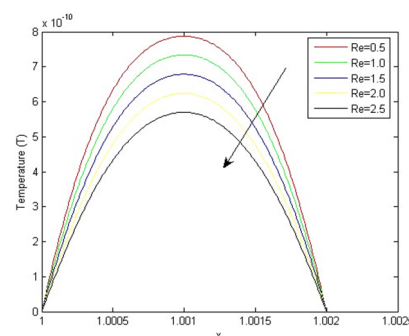


Figure 10. Variation in (T) with Re

Similar effect we have observed in induced magnetic field in **Figure 12**. The temperature distribution of titanium oxide/water nanofluid for those distinct values of Prandtl number (Pr) is depicted in **Figure 13**. But it is observed from **Figure 13**, that the fluid temperature distribution decreases due to increase in value of Prandtl number (Pr). With the large value of (Pr), the momentum diffuses additional rapidly than the heat, indicating that fluids with a large Prandtl number have low thermal conductivity and an exquisite thermal boundary layer. The velocity distribution of titanium oxide/water nanofluid for different values of Eckert number (Ec) is observed in **Figure 14**. We have seen in **Figure 14**, that the fluid velocity distribution decreases due to increase in value of Eckert number (Ec). Again, owing to increase in values of Eckert number (Ec), the plate decants velocity increases. This in turn again decreases the flow rate within the boundary layer and thus diminishes the velocity. Similar pattern is observed in

Figure 15. The temperature distribution of titanium oxide/water nanofluid for different values of Eckert number (Ec) is depicted in **Figure 16**. We have seen in **Figure 16**, that the fluid temperature profile enhanced owing to enhancement in parametric values of Eckert number (Ec). Owing to enhanced in values of (Ec), the fluid occurrence frictional heating in the middle layers, furthermore, there is the thickening of thermal boundary layer and consequently increases the temperature within the boundary layer significantly.

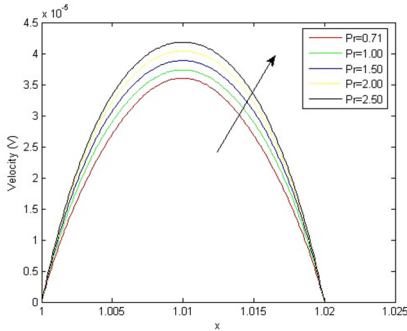


Figure 11. Variation in (V) with Pr

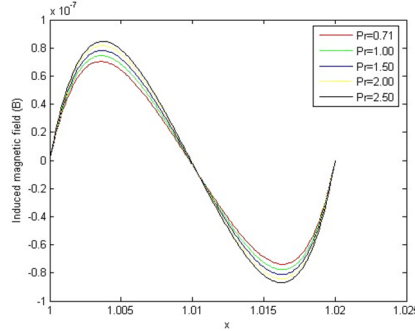


Figure 12. Variation in (B) with Pr

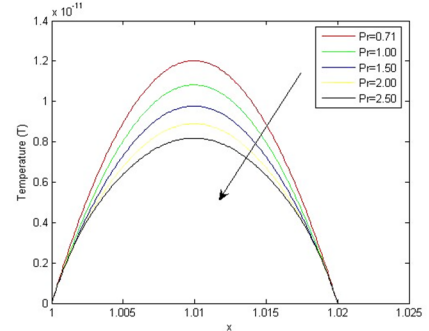


Figure 13. Variation in (T) with Pr

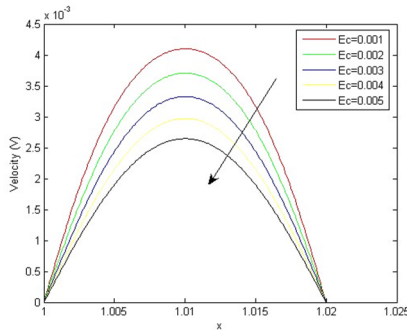


Figure 14. Variation in (V) with Ec

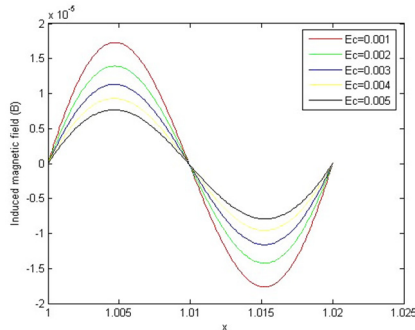


Figure 15. Variation in (B) with Ec

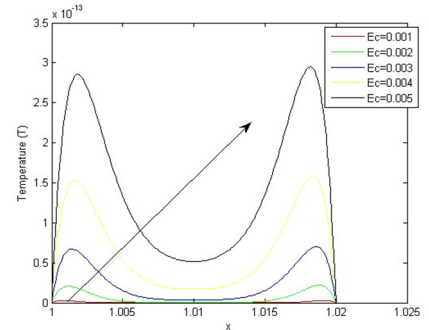


Figure 16. Variation in (T) with Ec

The velocity distribution of titanium oxide/water nanofluid for distinct values of magnetic Reynolds number (R_m) is illustrate in **Figure 17**. We have seen in **Figure 17**, that the fluid velocity distribution increases due to increase in parametric value of magnetic Reynolds number (R_m). The magnetic Reynolds number is the magnetic correspondent of the Reynold number, a fundamental dimensionless classification that take place in magnetohydrodynamics (MHD). It gives an estimate of the respective effects of convective of a magnetic field by the movement of a conducting medium, frequently a fluid, to magnetic diffusion. Similar nature we have observed in **Figure 18**. The temperature distribution of titanium oxide/water nanofluid for different values of magnetic Reynolds number (R_m) is depicted in **Figure 19**. But we have seen in **Figure 19**, that the temperature profile decreases owing to enhancement in parametric values of magnetic Reynolds number (R_m). The enhanced in values of (R_m) enhanced the strength of the decant velocity on the plate and this decant velocity minimizes the growth of thermal boundary layer. Thus, as a consequence diminishes the temperature near to the plate surface.

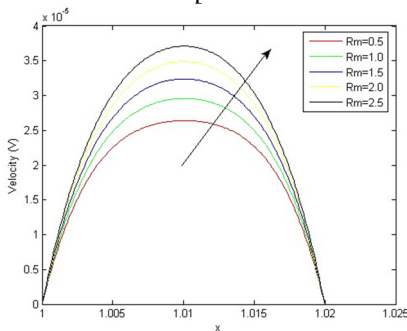


Figure 17. Variation in (V) with Rm

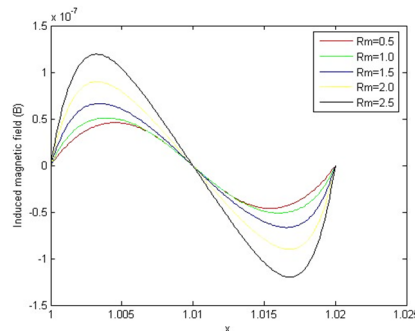


Figure 18. Variation in (B) with Rm

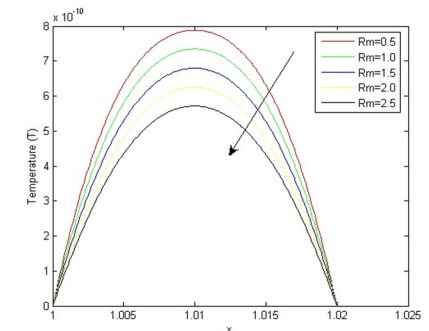


Figure 19. Variation in (T) with Rm

The velocity distribution of titanium oxide/water nanofluid for different values of nanoparticle volume fraction (ϕ) is illustrate graphically in **Figure 20**. We have seen in **Figure 20**, that the fluid velocity distribution decreases due to increase in value of nanoparticle volume fraction (ϕ). Similar pattern is in **Figure 21**, where induced magnetic field variation is shown against volume fraction. The temperature distribution of titanium oxide/water nanofluid for different values of nanoparticle volume fraction (ϕ) is depicted in **Figure 22**. But it is observed from **Figure 22**, that the temperature profile enhanced owing to enhancement in parametric value of nanoparticle volume fraction (ϕ).

We have plotted (Figure 23) values of rate of rise leading velocity for different nanofluids against value of corresponding Reynold number (Re) in the duct under same configuration. We have plotted the graphs for the following nanofluid: titanium oxide (TiO_2), aluminium oxide (Al_2O_3), ferric oxide (Fe_2O_3) and silicon oxide (SiO_2). These plottings provides us a comparative mass transfer advantages of different nano fluids at a certain temperature. From the plottings of (Figure 23), we have seen that with increasing Reynold number (Re) difference of flow rate for different nano fluids is reducing. For low value of Reynold number (Re), ferric oxide (Fe_2O_3) gives high flow rate and silicon oxide (SiO_2) gives low flow rate. For high Reynold number Re all the nanofluid consider shows no significance different in volumetric flow rate.

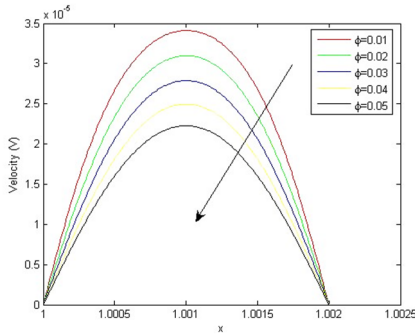


Figure 20. Variation in (V) with ϕ

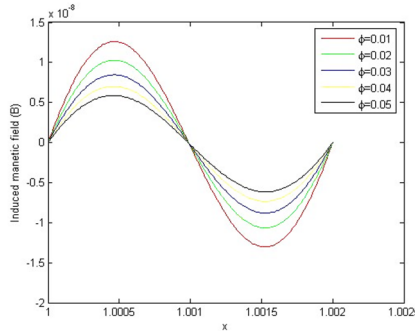


Figure 21. Variation in (B) with ϕ

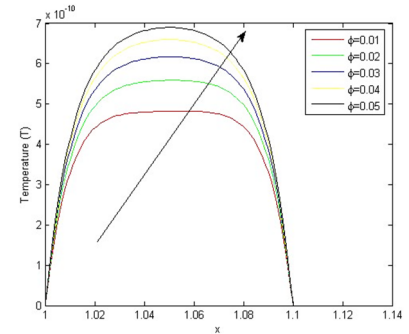


Figure 22. Variation (T) with ϕ

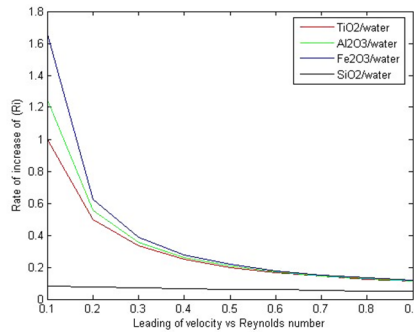


Figure 23. Rate of increase of Reynolds number for (TiO_2), (Al_2O_3), (Fe_2O_3) and (SiO_2) nanoparticles

We have plotted in Figure 24 mesh (x, y, V) for ($Ha = 0$), in Figure 25 contour (x, y, V) for ($Ha = 10$), in Figure 26 mesh (x, y, B) for ($Ha = 0$), in Figure 27 contour (x, y, B) for ($Ha = 10$), in Figure 28 mesh (x, y, T) for ($Ha = 0$), in Figure 29 contour (x, y, T) for ($Ha = 10$) i.e. in the absence of magnetic field for velocity and nanoparticle volume fraction ($\phi = 0.02$). i.e when ($Ha = 0$), the velocity of the $TiO_2 - water$ nanofluid decreases with increase in nanoparticles volume fraction ϕ . In this case 100×100 grid has been used at $x(1) = -1$ and $y(1) = -1$. And another study, in Figure 30 mesh (x, y, V) for ($Ha = 10$), in Figure 31 contour (x, y, V) for ($Ha = 10$), in Figure 32 mesh (x, y, B) for ($Ha = 10$), in Figure 33 contour (x, y, B) for ($Ha = 10$), in Figure 34 mesh (x, y, T) for ($Ha = 10$), in Figure 35 contour (x, y, T) for ($Ha = 10$) i.e. in the presence of large magnetic field and nanoparticle volume fraction ($\phi = 0.02$) for titanium oxide nanoparticle. i.e when ($Ha = 10$) the reverse effect of the nanoparticle volume fraction ϕ . Similarly, we can show for other nanoparticles.

3D graph for $TiO_2 - water$ nanofluid

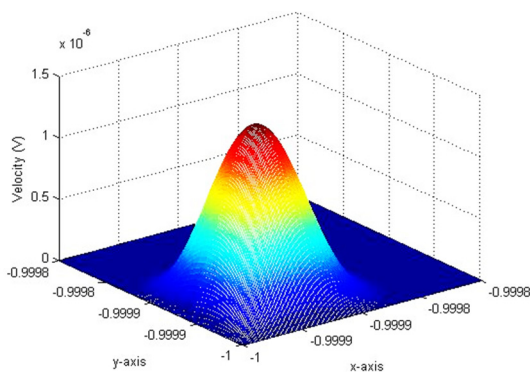


Figure 24. Velocity mesh in (x, y, V) with $Ha = 0, \phi = 0.02$,

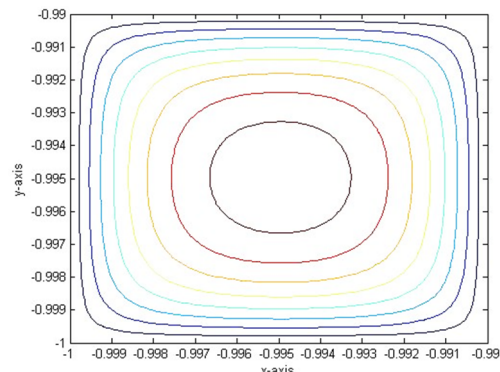


Figure 25. Velocity contour in (x, y, V) $Ha = 10, \phi = 0.02$

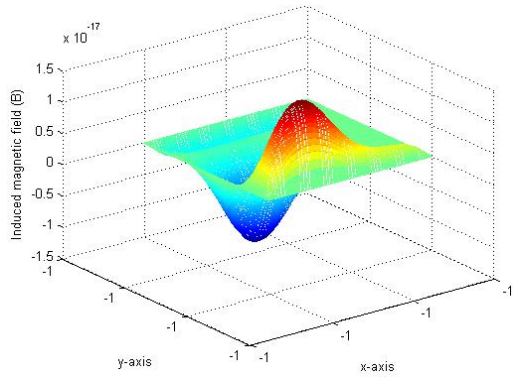


Figure 26. Velocity mesh in (x, y, B) with $Ha = 0, \phi = 0.02$

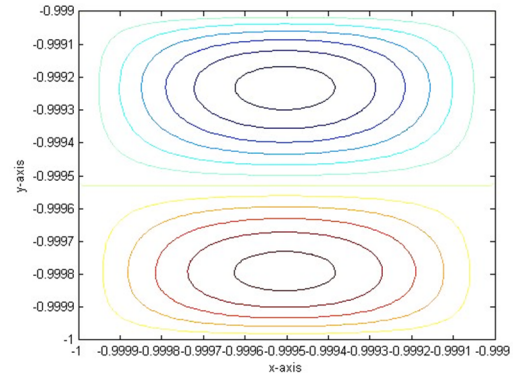


Figure 27. Velocity contour in (x, y, B) $Ha = 10, \phi = 0.02$

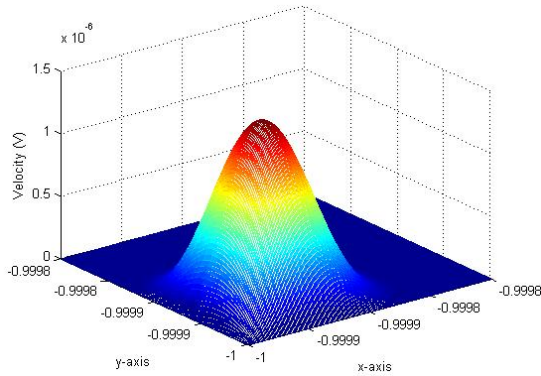


Figure 28. Velocity mesh in (x, y, T) with $Ha = 0, \phi = 0.02$

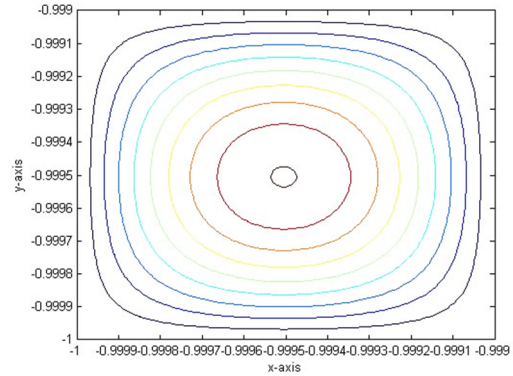


Figure 29. Velocity contour in (x, y, T) $Ha = 10, \phi = 0.02$

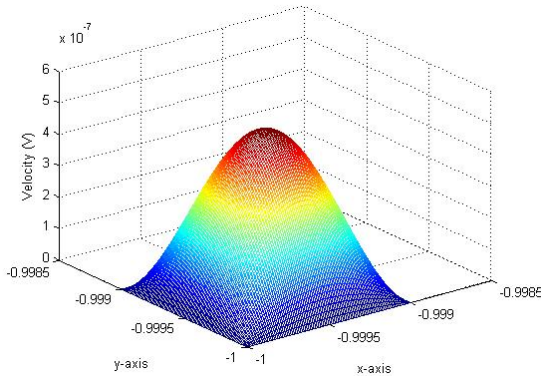


Figure 30. Velocity mesh in (x, y, V) with $Ha = 10, \phi = 0.02$

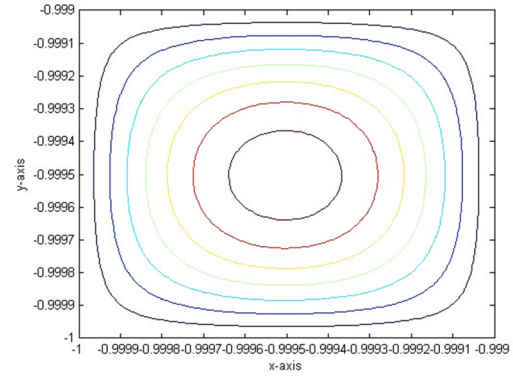


Figure 31. Velocity contour in (x, y, V) $Ha = 10, \phi = 0.02$

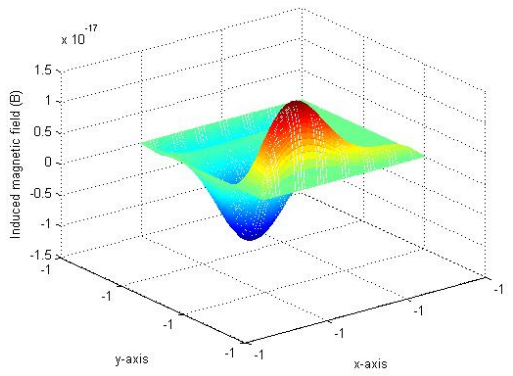


Figure 32. Velocity mesh in (x, y, B) with $Ha = 10, \phi = 0.02$

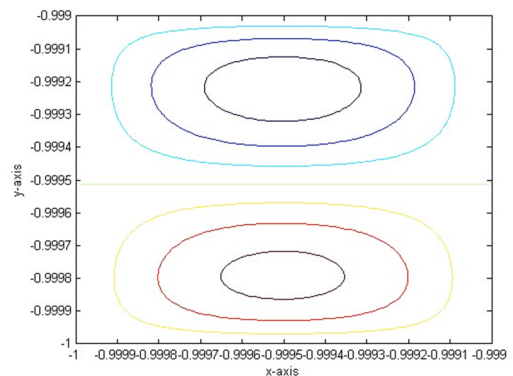


Figure 33. Velocity contour in (x, y, B) $Ha = 10, \phi = 0.02$

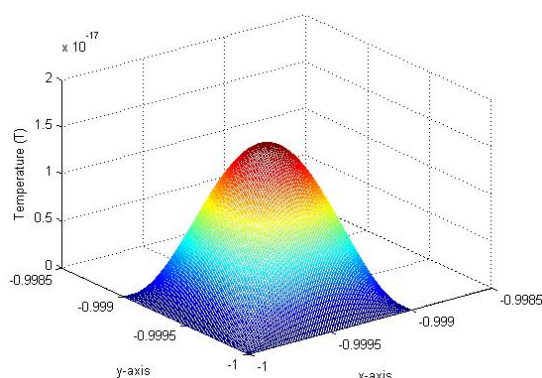


Figure 34. Velocity mesh in (x, y, T) with $Ha = 10, \phi = 0.02$

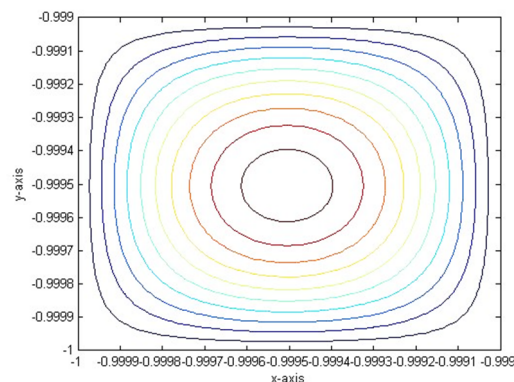


Figure 35. Velocity contour in (x, y, T) with $Ha = 10, \phi = 0.02$

6. CONCLUSIONS

In this paper, a comparative study on MHD forced convective flow for heat transfer efficiency of different nanofluids with water (H_2O) as base fluid has been carried out. Here, in this study flow through vertical rectangular has been considered in presence of strong magnetic field. An explicit finite difference method has been adopted with fine grid in the control volume for solving the governing equation of this MHD nanofluid flow. Computational process is carried out using MATLAB code. In this paper we have plotted the flow fields velocity, induced magnetic field and temperature for various values of MHD flow parameters graphically. The remarkable results of the examination are as follows:

1. From the plottings of (Fig. 23), we have seen that with increasing Reynold number (Re) difference of flow rate for different nano fluids is reducing. For low value of Reynold number (Re) ferric oxide (Fe_2O_3) gives high flow rate and silicon oxide (SiO_2) gives low flow rate. For high Reynold number (Re) all the nanofluid consider shows no significance different in volumetric flow rate.
2. The fluid velocity decreases due to increase in Hartmann number (Ha), Eckert number (Ec) and nanoparticle volume fraction (ϕ).
3. The fluid velocity increases due to increase in Reynold number (Re), thermal Grashof number (G_r), Prandtl number (P_r) and magnetic Reynolds number (R_m).
4. The induced magnetic field decreases due to increase in Hartmann number (Ha), nanoparticle volume fraction (ϕ), and Eckert number (Ec).
5. The induced magnetic field increases due to increase in Reynold number (Re), thermal Grashof number (G_r), Prandtl number (P_r) and magnetic Reynolds number (R_m).
6. The fluid temperature of decreases due to increase in Reynold number (Re), thermal Grashof number (G_r), Prandtl number (P_r) and magnetic Reynolds number (R_m).
7. An increase in values of Hartmann number (Ha), Eckert number (Ec), and nanoparticle volume fraction (ϕ) increases the fluid temperature.

Nomenclature

\vec{V} velocity vector	p fluid pressure, [Pa]	σ electrical conductivity, [$S m^{-1}$]
\vec{J} current density	θ oblique angle	ρC_p effective heat capacity of the nanoparticle, [$J m^{-3} K^{-1}$]
B_0 magnetic field	T temperature of the fluid, [K]	ϕ volume fraction, [-]
C_p specific heat at constant pressure, [$J kg^{-1} K^{-1}$]	ρ_{nf} nanofluid density	λ magnetic diffusivity
\vec{E} electric field	σ_{nf} nanofluid electrical conductivity	μ dynamic viscosity
Ha Hartmann number	μ_{nf} nanofluid dynamic viscosity	Subscripts
G_r thermal Grashof number	k_{nf} nanofluid thermal conductivity	nf nanofluids
Re Reynold number	$(\mu_e)_{nf}$ nanofluid magnetic permeability	f base fluid
P_r Prandtl number	ν_{nf} nanofluid kinematic viscosity	s solid particles of nanofluid
Ec Eckert number		
R_m magnetic Reynolds number		
k thermal conductivity of nanofluid, [$W m^{-1} K^{-1}$]		

Greek Letters

ρ density, [$kg m^{-3}$]
 ν kinematic viscosity, [$m^2 s^{-1}$]

ORCID

REFERENCES

- [1] S.U.S. Choi, "Enhanced thermal conductivity of nanofluids with nano particles, development and applications of Newtonian flows," *FED*, **231**/MD, 99-105 (1995).
- [2] S. Lee, S.U.S. Choi, S. Li, and J.A. Eastman, "Measuring Thermal Conductivity of Fluids Containing Oxide Nanoparticles," *Journal of Heat Transfer*, **121**(2), 280-289 (1999). <https://doi.org/10.1115/1.2825978>
- [3] Y. Xuan, and Q. Li, "Heat transfer enhancement of nano-fluids," *Int. J. Heat Fluid Flow*, **21**, 58-64 (2000). [https://doi.org/10.1016/S0142-727X\(99\)00067-3](https://doi.org/10.1016/S0142-727X(99)00067-3)
- [4] S.K. Das, S.U.S. Choi, Yu. and W. Pradet, *Nanofluids: Science and Technology*, (Wiley, New Jersey, 2007).
- [5] S. Kakac, and A. Parmuanjaroenkij, "Review of Convective Heat Transfer Enhancement with Nanofluids," *International Journal of Heat Mass Transfer*, **52**, 3187-3196. <http://dx.doi.org/10.1016/j.ijheatmasstransfer.2009.02.006>, (2009)
- [6] R. Ellahi, M. Hassan, and A. Zeeshan, "Aggregation Effects on Water Base Al₂O₃- Nanofluid over Permeable Wedge in Mixed Convection", *Asia-Pacific Journal of Chemical Engineering*, **11**, 179-186 (2015). <https://dx.doi.org/10.1002/apj.1954>
- [7] M.A.A. Hamad, "Analytical Solution of Natural Convection Flow of a Nanofluid over a Linearly Stretching Sheet in the Presence of Magnetic Field," *International Communications in Heat and Mass Transfer*, **38**, 487-492 (2011). <http://dx.doi.org/10.1016/j.icheatmasstransfer.2010.12.042>
- [8] R. Kodi, C. Ganteda, A. Dasore, M.L. Kumar, G. Laxmaiah, M.A. Hasan, S. Islam, and A. Razak, "Influence of MHD mixed convection flow for Maxwell nanofluid through a vertical cone with porous material in the existence of variable heat conductivity and diffusion," *Case Stud. Therm. Eng.* **44**, 102875 (2023). <https://doi.org/10.1016/j.csite.2023.102875>
- [9] E. Ragulkumar, G. Palani, P. Sambath, and A.J. Chamkha, "Dissipative MHD free convective nanofluid flow past a vertical cone under radiative chemical reaction with mass flux," *Sci. Rep.* **13** (1), 2878 (2023). <https://doi.org/10.1038/s41598-023-28702-0>
- [10] T. Hayat, M.B. Ashraf, S.A. Shehzad, and A. Alsaedi, "Mixed Convection Flow of Casson Nanofluid over a Stretching Sheet with Convectively Heated Chemical Reaction and Heat Source/Sink," *J. Appl Fluid Mechanics*, **8**, 803-813 (2015). <http://doi.org/10.18869/acadpub.jafm.73.238.22995>
- [11] M. Ferdows, M.D. Shamshuddin, S.O. Salawu, and K. Zaimi, *SN Appl. Sci.* **3**, 264 (2021). <https://doi.org/10.1007/s42452-021-04224-0>
- [12] S. Rao, and P.A. Deka, "Numerical investigation on Transport Phenomena in a Nanofluid Under the Transverse Magnetic Field Over a Stretching Plate Associated with Solar Radiation," in: *Nonlinear Dynamics and Applications*, edited by S. Banerjee, and A. Saha, (Springer Proceedings in Complexity, Springer, Cham, 2022), pp. 473-492. https://doi.org/10.1007/978-3-030-99792-2_39
- [13] S. Rao, and P.A. Deka, "Numerical solution using EFDm for unsteady MHD radiative Casson nanofluid flow over a porous stretching sheet with stability analysis," *Heat Transfer*, **51**(8), 8020-8042 (2022). <https://doi.org/10.1002/htj.22679>
- [14] B.R. Das, P.N. Deka, and S. Rao, "Numerical analysis on MHD mixed convection flow of aluminium-oxide/water nanofluids in a vertical square duct," *East European Journal of Physics*, **2**, 51-62 (2023). <https://doi.org/10.26565/2312-4334-2023-2-02>
- [15] V. Rajesh, A.J. Chamkha, and M.P. Mallesh, "Transient MHD Free Convection Flow and Heat Transfer of Nanofluid past an Impulsively Started Semi-Infinite Vertical Plate," *Journal of Applied Fluid Mechanics* **9**, 2457-2467 (2015). <https://doi.org/10.18869/acadpub.jafm.68.236.23443>
- [16] M. Jawad, M.K. Hameed, K.S. Nisar, A.H. Majeed, "Darcy-Forchheimer flow of Maxwell nanofluid flow over a porous stretching sheet with Arrhenius activation energy and nield boundary conditions," *Case Studies in Thermal Engineering*, **44**, 102830 (2023). <https://doi.org/10.1016/j.csite.2023.102830>
- [17] A. Paul, and T.K. Nath, "Darcy -Forchheimer MHD radiative flow through a porous space incorporating viscous dissipation, heat source, and chemical reaction effect across an exponentially stretched surface," *Heat Transfer*, **52** (1), 807-825 (2023). <https://doi.org/10.1002/htj.22717>
- [18] C.A. Nandhini, S. Jothimani, and A.J. Chamkha, "Effect of chemical reaction and radiation absorption on MHD Casson fluid over an exponentially stretching sheet with slip conditions: ethanol as solvent," *The European Physical Journal Plus*, **138**(1), 1-17 (2023). <https://doi.org/10.1140/epjp/s13360-023-03660-8>
- [19] H. Alriheli, M. Alrehili, and A.M. Megahed, "Radiative MHD Nanofluid Flow Due to a Linearly Stretching Sheet with Convective Heating and Viscous Dissipation," *Mathematics*, **10**(24), 4743 (2022). <https://doi.org/10.3390/math10244743>
- [20] M. Jawad, "A Computational Study on MHD Stagnation Point Flow of Micropolar Fluids with Buoyancy and Thermal Radiation due to a Vertical Stretching Surface," *Journal of Nanofluids*, **12**(3), 759-766 (2023). <https://doi.org/10.1166/jon.2023.1958>
- [21] S. Shoeibi, H. Kargarsharifabad, N. Rahbar, G. Ahmadi, M.R. and Safaei, "Performance evaluation of a solar still using hybrid nanofluid glass cooling- CFD simulation and environmental analysis," *Sustainable Energy Technologies and Assessments*, **49**, 101728 (2022). <https://doi.org/10.1016/j.seta.2021.101728>
- [22] O.A. Beg, and J.C. Umavathi, "Computation of thermo-solutal convection with Soret-Dufour cross diffusion in a vertical duct containing carbon/metallic nanofluids," in: *Proceedings of the Institution of Mechanical Engineers, Part C: Journal of Mechanical Engineering Science*, **236**(13), (2022). <http://dx.doi.org/10.1177/09544062211072693>
- [23] M.M. Bhatti, M.B. Arain, A. Zeeshan, R. Ellahi, and M.H. Doranehgard, "Swimming of Gyrotactic microorganism in MHD Williamson nanofluid flow between rotating circular plates embedded in porous medium: Application of thermal energy storage," *J. of Energy Storage*, **45**, 103511 (2021). <https://doi.org/10.1016/j.est.2021.103511>
- [24] Z. Hussain, A.U. Rehman, R. Zeeshan, F. Sultan, T.A. Hamid, M. Ali, and M. Shahzad, "MHD instability of Hartmann flow of nanoparticles Fe₂O₃ in water," *Appl. Nanosci.* **10**, 5149-5165 (2020). <https://doi.org/10.1007/s13204-020-01308-y>
- [25] J.C. Umavathi, and O.A. Beg, "Double diffusive convection in a dissipative electrically conducting nanofluid under orthogonal electrical and magnetic fields: a numerical study," *Nanoscience and Technology: An International Journal*, **12**(2), 59-90 (2021). <https://doi.org/10.1615/NanoSciTechnolIntJ.2021036786>
- [26] M.M. Bhatti, and S.I. Abdelsalam, "Bio-inspired peristaltic propulsion of hybrid nanofluid flow with Tantalum (Ta) and Gold (Au) nanoparticles under magnetic effects," *Waves in Random and Complex Media*, 1745-5030 (2021). <https://doi.org/10.1080/17455030.2021.1998728>

ПОРІВНЯЛЬНЕ ДОСЛІДЖЕННЯ МГД ПРИМУШЕНОГО КОНВЕКТИВНОГО ПОТОКУ РІЗНИХ НАНОРІДИН З ВОДОЮ (H₂O) ЯК ОСНОВНОЮ РІДИНОЮ У ВЕРТИКАЛЬНОМУ ПРЯМОКУТНОМУ КАНАЛІ**Бішну Рам Дас, П.Н. Дека***Факультет математики, Університет Дібругарх, Дібругарх-786004, Ассам, Індія*

У цій статті було проведено порівняльне дослідження МГД вимушеної конвективної течії для ефективності теплопередачі різних нанофлюїдів з водою (H₂O) як базовою рідиною. У цьому дослідженні потік через вертикальний прямокутний канал розглядався в присутності сильного магнітного поля. У цьому ламінарному потоці ми розглядаємо стінки каналу як електрично непровідні, де поперечне магнітне поле діє нормально на стінки каналу. Джоулева теплота та ефекти розсіювання в'язкої рідини враховуються в енергетичному рівнянні, і, крім того, стінки каналу зберігаються при постійній температурі. Було прийнято явний кінцево-різницевий метод із дрібною сіткою в контрольному об'ємі для розв'язання керівних рівнянь цього МГД-потіку нанорідини. Обчислювальні процеси здійснюються за допомогою коду MATLAB. У цій роботі ми графічно побудували графіки швидкості полів потоку, індукованого магнітного поля та температури для різних значень МГД параметрів потоку шляхом зміни теплового числа Грасгофа (G_r), числа Гартмана (H_a), числа Рейнольдса (Re), числа Екерта (Ec), числа Прандтля (Pr), магнітне число Рейнольдса (R_m) і об'ємну частку наночастинок (ϕ) відповідно.

Ключові слова: *вимушена конвективна МГД течія; нанофлюїди; стійкий; явний метод кінцевих різниць (EFDM); вертикальний прямокутний канал*

EFFECT OF INDUCED MAGNETIC FIELD ON MHD FLOW BETWEEN TWO PARALLEL POROUS PLATES AT CONSTANT TEMPERATURE GRADIENT IN PRESENCE OF INCLINED MAGNETIC FIELD

 Kankana Rabha^{a*},  Saleem Javed Al Khayer^{a†},  Shyamanta Chakraborty^{b§}

^aDepartment of Mathematics, Gauhati University, Guwahati, Assam, India

^bUGC-HRDC, Gauhati University, Guwahati, Assam, India

*Corresponding Author e-mail: rabhakankana@gmail.com

Received December 23, 2023; revised January 20, 2024; accepted January 30, 2024

The paper studies effect of induced magnetic field on laminar convection flow of a viscous electrically conducting incompressible fluid between two parallel porous plates at constant temperature gradient in presence of a uniform inclined magnetic field. An angle (θ) is formed with the vertical line by applying a magnetic field in that direction and field is strong enough to induce another field along the line of flow. Using the proper similarity transformations, the flow equations are converted into ordinary differential equations, which are then numerically solved by using MATLAB's `bvp4c` solver. Plotting of the graphs allows one to examine the effects of several critical parameters such as Hartmann number, Darcy number, Magnetic Reynolds number, Prandtl number, and Field inclination on velocity field, induced magnetic field, temperature field at the plates. The acquired results demonstrate that the flow system is effectively influenced by the field inclination, the magnetic parameter, and the plate porosity. The rise in field inclination leads to an increase in magnetic drag force.

Keywords: *Induced magnetic field; Free convection; Porous plate; MHD; Temperature gradient*

PACS: 47.85.-g

INTRODUCTION

Since last two decades, many researchers have studied on the Magnetohydrodynamics viscous incompressible flow in the presence of an external magnetic field (magnetohydrodynamic flow) and receiving great attention because of its large number of applications such as in the field of industry, technology, energy generation, geophysics and geo-thermal activities, astrophysics, nuclear science, combustion modelling, plasma studies, oil exploration and many others. For example, nowadays MHD generators are widely used for power generation, MHD pumps are used in chemical energy technology for pumping electrically conducting fluids at atomic energy centre, pinching hot plasma, purification of crude oil, in the case of manufacturing of glass, use of MHD flow meter in measuring the speed of a ship etc. Such kind of flow are normally designed under the supposition of unchanged temperature and constant heat flow rate intensity in presence of externally applied magnetic field. However, the flow is always influenced by the imposed magnetic field by means of its induced magnetic field. The field induces electromotive magnetic force that in turn effects the velocity field and ultimately controls the flow. Further, direction of applied magnetic field is always important, because in comparison to a magnetic field that applied along the flow, a transversed magnetic field acts differently, it generates more drag force and thereby dissipates much energy. The magnetic drag force acts upon the suspended particles and rearrange them according to their concentration depending upon the strengths of the field. This also strongly changes the pattern of heat transfer and energy density within the flow system. Thus, the behaviour of flow system highly depends upon the strength of the applied magnetic field and its inclination with respect to the direction of flow. This is why the consideration of effect of induced magnetic field and its inclination are highly important both in terms of theoretical and experimental point of view. In MHD flow, energy balance is considered by the internal energy due to conduction and convection of heat with the stream, generation and dissipation of heat due to viscous friction and porosity friction, and energy dissipation due to effect of induced magnetic field. Although the effect of heat radiation is always there, but its contribution is much smaller and negligible within the moderate range of temperature.

There has been a significant undivided attention in research activities in MHD free convection flow within vertical parallel plates. As far our knowledge goes, the most relevant problem of magnetohydrodynamic flow in the presence of applied transverse magnetic field between two parallel plates was first discussed by Hartmann [1]. Later on, by Schercliff [2], Soundalgekar [3], Raptis and Singh [4]. Between two vertical plates, laminar convection flow through a porous media was examined by Soundalgekar and Bhatt [5]. In their discussion of laminar convection flow between two vertical porous plates in the presence of uniform magnetic field under varying medium permeabilities, Das and Sanyal [6] addressed conducting incompressible fluid flow behaviour. A vertical channel with constant temperature and constant heat flux on the walls was studied by Paul et al. [7] for transient free convective flow. Chakraborty and Borkakati [8] had studied unstable free convection MHD flow.

Pop et al. [9] have discussed the laminar boundary layer flow due to a continuously moving flat plate. Unsteady magnetohydrodynamic free convective flow and heat transfer along a vertical porous plate with variable suction and internal heat generation was studied by Sharma and Singh [10]. Palani and Srikanth [11] also studied the hydrodynamic

flow past a semi-infinite vertical with mass transfer. A numerical analysis of the hydromagnetic free convective flow in the presence of induced magnetic field has been studied by Singh et al., [12]. Jha and Sani [13] have investigated the symmetric heating caused by induced magnetohydrodynamic natural convection flow of an electrically conducting and viscous incompressible fluid in a vertical channel. Kumer and Singh [14] have discussed the unsteady magnetohydrodynamic free convective flow past a semi-infinite vertical wall by taking into account the induced magnetic field. Sarveshanand and A.K. Singh [15] studied the MHD free convection between vertical parallel porous plates in the presence of induced magnetic field. Hamza [16] studied the free convection slip flow of an exothermic fluid in a convectively heated vertical channel. Recently, Goswami et al. [17] have studied unsteady MHD free convection flow between two heated vertical parallel plates in the presence of a uniform magnetic field. Induced magnetic field effect on MHD free convection flow in nonconducting and conducting vertical microchannel walls has been investigated by Goud [18]. In a vertical annular micro-channel with a radial magnetic field, B.K. Jha and Babatunde Aina investigate the effect of an induced magnetic field on magnetohydrodynamic (MHD) natural convection flow. A discussion of Jumanne Mng'ang'a [20] is found in Effect of chemical reaction and joule heating on MHD generalized couette flow between two parallel vertical porous plates with induced magnetic field and Newtonian heating/cooling.

In this paper, we have studied the laminar convection flow of a viscous electrically conducting incompressible fluid between two parallel plates in presence of a uniform inclined magnetic field at constant temperature gradient. Magnetic field is applied in the direction making an angle θ to the vertical line and field is strong enough to induce another field along the line of flow. In almost all the previous such kind of studies, the inclination of the applied magnetic field and heat dissipation due to porosity of the medium are ignored, so we have considered those along with the effect of induced magnetic field. The aim of this paper is to make computational study and analysis of velocity field, induced magnetic field, temperature field at the plates for different values of non-dimensional physical quantities such as Hartmann Number, Darcy number, Magnetic Reynolds number, Prandtl number and the field inclination $\lambda(\cos \theta)$. The problem has its significant in numerous applications, including the extrusion of polymers in the production of nylon and rayon, the pulp and textile industries, in power technology, in petroleum industry on purification of crude oil, solid fuel rocket nozzles used in guided missile system, flow of polymer solutions in industry, construction of wet-bulb thermometer, and in many other engineering and industrial fields. When such a conducting fluid flows in presence of a magnetic field, the flow is influenced not only by the applied magnetic field but also the induced magnetic field. There are interactions among the conducting fluid particles with the magnetic flux that in turn modifies the flow pattern, flow properties, and the heat transfer. It is also possible to control effectively the flow by adjusting the magnitude and direction of the applied magnetic field applied. Understanding the dynamics of such kind of flow, may be a help in controlling technology involving MHD flow and devices, such as MHD power generator, thermonuclear power devices including industrial, geophysical, astronomical, and in variety of geophysical and geothermal settings.

MATHEMATICAL ANALYSIS

In the horizontal direction, we have studied a laminar convection flow of an electrically conducting viscous incompressible fluid between two porous parallel plates (Fig. 1); the X-axis is taken horizontally along the fluid motion, and the Y-axis is perpendicular to it. Allowing a uniform magnetic field B_0 to be applied in a direction that forms an angle with the vertical line, this will cause B to induce another magnetic field along the fluid's motion.

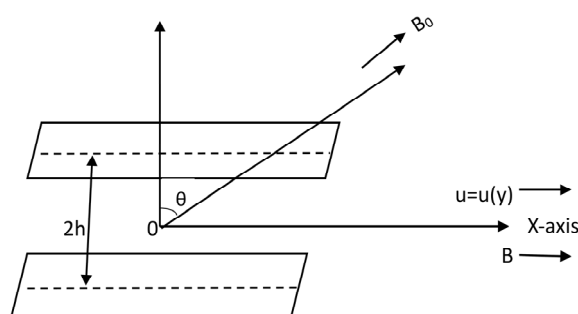


Figure 1. Physical Model of the Problem.

The distance between the plates is '2h'. The plates are maintained at constant temperature gradient (Γ/h). We considered the plate temperature T_w as $T_w = T_0 + (\Gamma/h)x$, where, T_0 is the temperature at the origin. The fluid temperature is assumed to be vary along vertical direction while temperature gradient is supposed to be constant along horizontal direction. Let u be the fluid velocity along X-axis, therefore the fluid velocity, magnetic field and induced magnetic field are $\{u(y), v_0, 0\}$, $\{B_0(\sqrt{1-\lambda^2}), B_0(\lambda), 0\}$ and $\{B(y), 0, 0\}$ respectively.

The investigation is carried out on the following basic assumptions,

- Hall effects and polarization effects are neglected.
- The fluid moves with the uniform velocity so that all the physical variables are assumed to be time independent.

The governing equations representing flow are as follows:

$$\frac{\partial u}{\partial x} = 0, \tag{1}$$

$$\vartheta \left(\frac{\partial^2 u}{\partial y^2} \right) - v_0 \left(\frac{\partial u}{\partial y} \right) + \left(\frac{B_0 \lambda}{\rho \mu_e} \right) \left(\frac{\partial B}{\partial y} \right) - k_0 - \frac{\vartheta}{k_1} u = 0, \tag{2}$$

$$\vartheta_m \left(\frac{\partial^2 B}{\partial y^2} \right) - v_0 \left(\frac{\partial B}{\partial y} \right) + B_0 \lambda \left(\frac{\partial u}{\partial y} \right) = 0, \tag{3}$$

$$\rho C_p \left(u \frac{\partial T}{\partial x} + v_0 \frac{\partial T}{\partial y} \right) = k \frac{\partial^2 T}{\partial y^2} + \rho \vartheta \left(\frac{\partial u}{\partial y} \right)^2 + \left[\frac{1}{\sigma \mu_e^2} \left(\frac{\partial B}{\partial y} \right)^2 \right] + \frac{\mu}{k_1} u^2 = 0. \tag{4}$$

Where k_0 is constant.

The boundary conditions associated with physics of the problem are

$$u=0, \quad B=0, \quad T=T_w \quad \text{at } y = \pm h. \tag{5}$$

Equations (2)-(4) can be converted to a system of non-linear ordinary differential equations via the similarity variables,

$$x^* = \frac{x}{h}, y^* = \frac{y}{h}, u^* = \frac{uh}{\alpha}, \phi = \left(\frac{T_w - T}{\Gamma} \right), B^* = \left(\frac{B}{B_0} \right). \tag{6}$$

After removing asterisks, the transformed equations are

$$\frac{\partial^2 u}{\partial y^2} - Re \frac{\partial u}{\partial y} + \frac{M^2 \lambda}{R_m} \frac{\partial B}{\partial y} - k_0 - \frac{1}{Da} u = 0, \tag{7}$$

$$\frac{\partial^2 B}{\partial y^2} - Re \frac{\partial B}{\partial y} + \lambda R_m \frac{\partial u}{\partial y} = 0, \tag{8}$$

$$\frac{\partial^2 \phi}{\partial y^2} - Pr \left[Re \frac{\partial \phi}{\partial y} + E \left\{ \left(\frac{\partial u}{\partial y} \right)^2 + \frac{M^2}{R_m^2} \left(\frac{\partial B}{\partial y} \right)^2 + \frac{1}{Da} u^2 \right\} \right] - Ku = 0. \tag{9}$$

It is notable that the continuity equation (1) is identically satisfied i.e. the proposed velocity is suitable with the continuity equation.

The boundary conditions (5) in terms of the similarity variables (6) becomes

$$u=0, \quad B=0, \quad \phi=0 \quad \text{at } y = \pm 1. \tag{10}$$

SOLUTIONS OF THE EQUATIONS

In this paper, solutions of the nonlinear coupled equations (7)-(9) subject to the boundary conditions (10) are solved by using ‘‘MATLAB built-in bvp4c solver technique’’ for different values of physical parameters. Therefore, we have transformed the ordinary differential equations into a set of first order differential equations as given below:

Let,

$$u = y(1), \quad u' = y(2), \quad B = y(3), \quad B' = y(4), \quad \phi = y(5), \quad \phi' = y(6). \tag{11}$$

The transformed first order differential equations are

$$y'(2) = Re * y(2) - \frac{M^2 \lambda}{R_m} * y(4) + k_0 + \frac{1}{Da} * y(1), \tag{12}$$

$$y'(4) = Re * y(4) - \lambda * R_m * y(2), \tag{13}$$

$$y'(6) = Pr \left[Re * y(6) + E \{ y(2)^2 + \frac{M^2}{R_m^2} * y(4)^2 + \frac{1}{Da} y(1)^2 + K * y(1) \} \right]. \tag{14}$$

The transformed boundary conditions are:

$$y_0(1) = 0, \quad y_0(3) = 0, \quad y_0(5) = 0, \quad y_1(1) = 0, \quad y_1(3) = 0, \quad y_1(5) = 0. \tag{15}$$

RESULTS AND DISCUSSIONS

In order to get the physical insight of the problem, the non-dimensional physical quantities representing velocity field (u), induced magnetic field (B) and temperature field (ϕ) are computed for different values of the other parameters such as Hartmann Number (M), Magnetic Reynolds Number (R_m), Darcy Number (Da), Prandtl Number (Pr), and inclination of the field λ ($=\cos \theta$). The effect of these different parameters is shown and analysed graphically in the Figures (2-13).

Velocity Profiles

Figures 2–5 present the variation of the u with λ , Da, M and R_m respectively. The nature of variation within the channel from lower to upper plate are in almost parabolic shape. Figure 2 elucidates the effect inclination of the applied field λ on u; at a point within the channel, with the rise λ (from 0.1 to 1.0) i.e. as the field inclined more and more towards

vertical, u increases gradually. This is because of decrease of magnetic drag force acting on the flow as the field shifted towards vertical from horizontal. Figure 3 show that the variation of u for different values of Da where with the increase of Da , fluid velocity (u) decreases within the channel. Figure 4 shows velocity distribution with respect to M ; with the increase of M maintaining R_m fixed ($\cong 1.0$), u increases. Figure 5 shows the effect of R_m on fluid velocity u ; with increase of with R_m , fluid velocity decreases significantly. This is due to the force, called Lorentz force, which causes reduction in the fluid velocity.

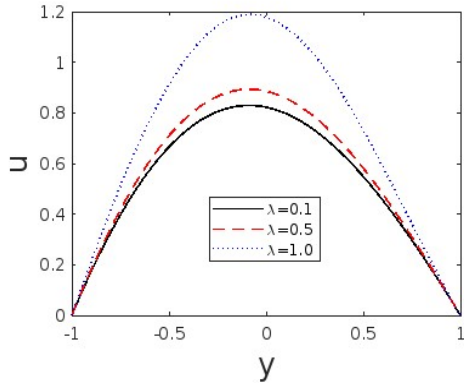


Figure 2. Variation of u with λ for $Re=1.5$; $M=3.5$; $R_m=1.0$; $Da=1.0$

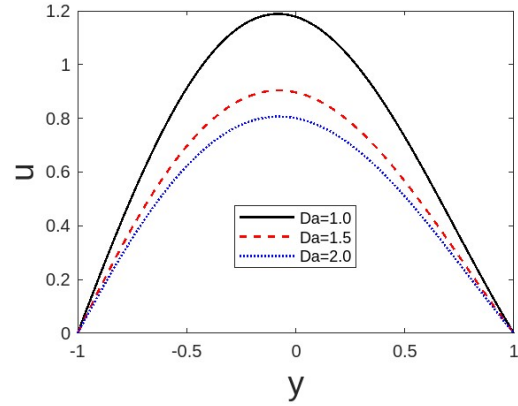


Figure 3. Variation of u with Da for $Re=1.5$; $M=3.5$; $R_m=1$; $\lambda=1$

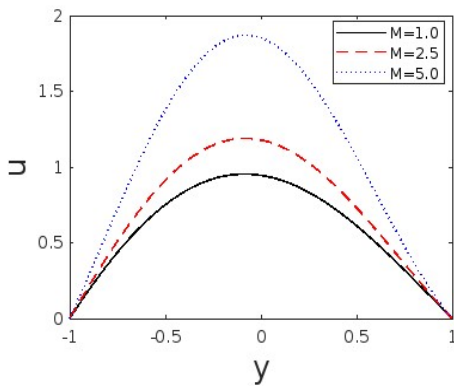


Figure 4. Variation of u with M for; $Re=1.5$; $R_m=1.0$; $Da=1.0$

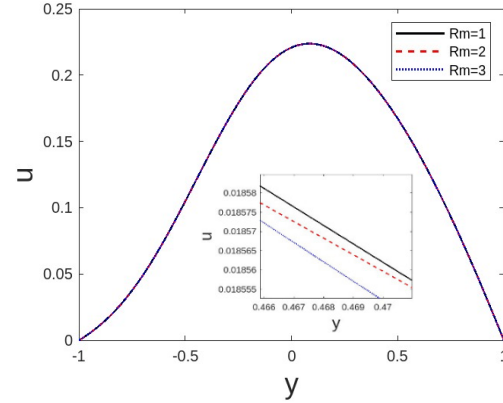


Figure 5. Variation of u with R_m for $Re=1.5$; $M=3.5$; $Da=1.0$; $\lambda=1.0$

Induced Magnetic field profiles

Figure 7 presents distribution of induced magnetic field (B) within the channel for different values of λ ; Within the channel, from lower to upper plate, the variation of B seems to be sinusoidal where the magnitude of B increases as it inclined more and more towards vertical i.e. field inclination has an effect on generation of induced magnetic field. Figure 8 presents distribution of B within the channel for different values of R_m ; with the increase of R_m the magnitude of B also increases within the channel.

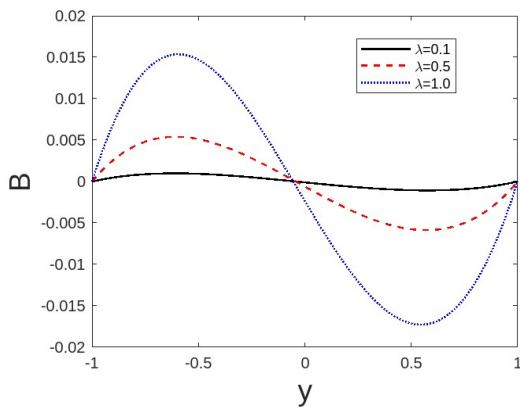


Figure 7. Variation of B with λ for $Re=1.5$; $M=3.5$; $R_m=1.0$

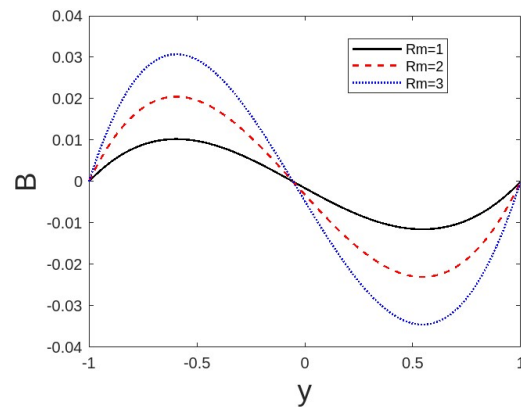


Figure 8. Variation of B with R_m for $Re=1.5$; $\lambda=1.0$; $M=3.5$

Temperature profiles

Figure 9-13 each of them illustrates the variation of temperature profile (ϕ) with Da , M , R_m , K and Pr respectively, which are also seen to be almost parabolic shape within the channel from lower to upper plate. Figure 9 elucidates the temperature profile (ϕ) within the channel for various values of Da , ϕ increases with the rise of Da . There is an increase in the temperature profile across the wall as the Darcy number increases. This is because of the increased permeability of the material; the convective mode becomes stronger as the Darcy number rises. The rate of variation of fluid temperature (ϕ) is more in upper half than the lower one within the channel. Figure 10 depicts the temperature profile with M , it is seen that, an increases of Hartman M leads to a decrease in the temperature profile. Figure 11 shows the variation of temperature with R_m . It is observed that with rises of R_m , fluid temperature (ϕ) increases. Figure 12 shows the variation of temperature profiles (ϕ) within the channel for various values of K ; (ϕ) increases with the rise of K . The rate of variation of fluid temperature (ϕ) is more in upper half than the lower one within the channel. Figure 13 shows that the impact of Pr on temperature profile (ϕ); fluid temperature decreases with the increase of Pr .

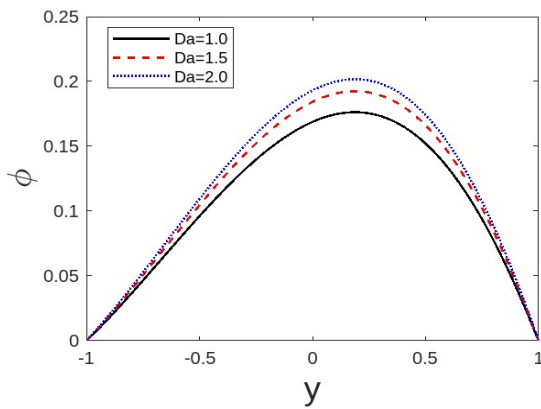


Figure 9. Variation of ϕ with Da for $M=1.5$; $K=1.5$; $Pr=0.71$; $R_m=1.0$

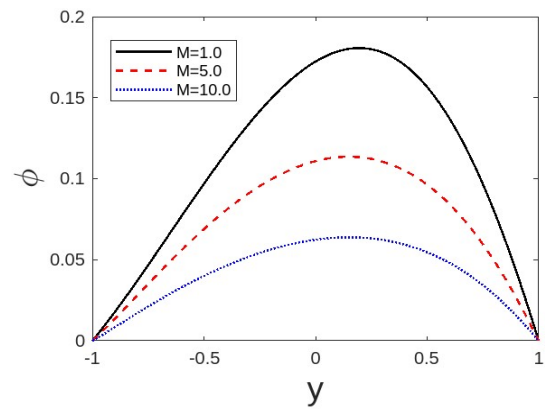


Figure 10. Variation of ϕ with M for $Pr=0.71$; $Da=1.0$; $R_m=1$; $K=1.5$

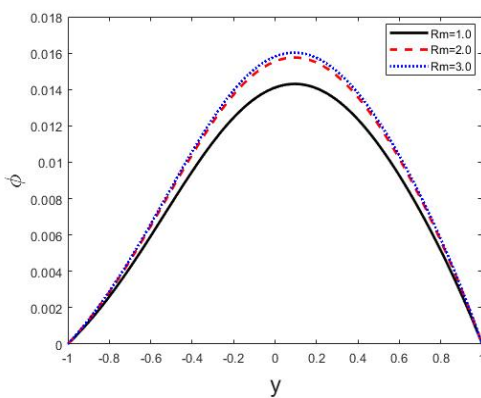


Figure 11. Variation of ϕ with R_m for $Pr=0.71$; $Da=1$; $M=3.5$; $K=1.5$

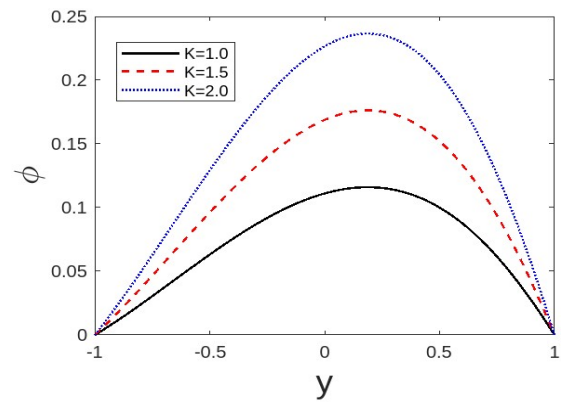


Figure 12. Variation of ϕ with K for $Pr=0.71$; $Da=1.0$; $R_m=1.0$; $M=1.5$

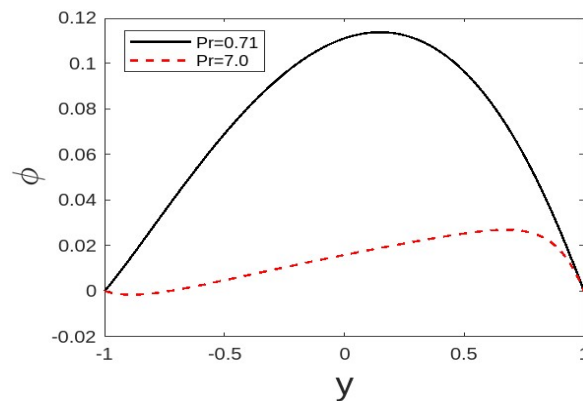


Figure 13. Variation of ϕ with Pr for $Da=1.0$; $R_m=1.0$; $K=1.5$; $M=1.5$

CONCLUSIONS

We have studied the effect of magnetic field inclination under the action of induced magnetic field on laminar convection flow of a viscous electrically conducting incompressible fluid between two parallel porous plates at constant temperature gradient. From above results and discussion, it can be concluded that fluid velocity increases with rise of field inclination of the applied magnetic field from horizontal to vertical. Induced magnetic field and permeability of the medium have influence on fluid velocity, fluid temperature as well. Fluid velocity decreases with the increase of the Darcy number and magnetic Reynolds number. In the present physical setup of the problem, within the channel the induced field varies sinusoidally from lower to upper plate; magnitude of which increases with the rise of field inclination from horizontal to vertical. Medium permeability and induced magnetic field affects the fluid temperature significantly. Fluid temperature increases with the increase of the medium Permeability, Magnetic Reynolds number and the temperature gradient but decreases with the rise of Hartmann number and Prandtl number. Such kind of hydrodynamic behaviour often occurs in a fluid motion where a conducting fluid flows in presence of magnetic field that induces another field where working velocity, temperature and other flow parameters may be manageable by adjusting the magnitude and direction of the applied magnetic field. The results have relevance in the applications advent of technology that involves MHD flow system and devices such as MHD power generator, thermonuclear power devices, in petroleum industry, on purification of crude oil, solid fuel rocket nozzles used in guided missile system, flow of polymer solutions in industry (in case of extrusion of polymers in the production of nylon and rayon), construction of wet-bulb thermometer, and in many such fluid flow relating to engineering and industrial fields.

Nomenclature

$$\vartheta = \frac{\mu}{\rho}, \text{ Kinematic viscosity;}$$

$$Re = \left(\frac{v_0 h}{\vartheta}\right), \text{ Reynolds number;}$$

$$Pr = \left(\frac{\vartheta}{\alpha}\right), \text{ Prandtl number,}$$

$$E = \frac{\alpha^2}{\Gamma c_p h^2}, \text{ Eckert number;}$$

$$Da = \frac{k_1}{h^2}, \text{ Darcy number;}$$

$$\frac{\partial \phi}{\partial x} = K, \text{ Temperature gradient.}$$

$$M = B_0 h \sqrt{\frac{\sigma}{\rho \vartheta}}, \text{ Magnetic parameter}$$

$$R_m = (\alpha \mu_e \sigma), \text{ Magnetic Reynolds number;}$$

$$\vartheta_m = \frac{1}{(\sigma \mu_e)}, \text{ Magnetic diffusivity.}$$

ORCID

✉ Kankana Rabha, <https://orcid.org/0009-0002-5749-5561>; ✉ Shyamanta Chakraborty, <https://orcid.org/0000-0001-5839-4856>
 ✉ Saleem Javed Al Khayer, <https://orcid.org/0009-0003-6581-059X>

REFERENCES

- [1] J. Hartmann, "Theory of the laminar flow of an electrically conductive liquid in a homogeneous magnetic field," *Fys. Med.* **15**, 1-28 (1937).
- [2] J.A. Schercliff, *A textbook of magnetohydrodynamics*, (Pergamon press, London, 1965).
- [3] V.M. Soundalgekar, "Free convective effects on Stokes problem for an infinite vertical plate, *Proceeding of the Mathematical Society*," BHU, **12**, 47 (1977).
- [4] A. Raptis, and A.K. Singh, "MHD free convection flow past an accelerated vertical plate," *International Communications in Heat and mass transfer*, **10**(4), 313-321 (1983). [https://doi.org/10.1016/0735-1933\(83\)90016-7](https://doi.org/10.1016/0735-1933(83)90016-7)
- [5] V.M. Soundalgekar, and Bhatt, "Oscillatory MHD channel flow and heat transfer," *Indian J. Pure Applied Math.* **15**, 819-828 (1984).
- [6] K. Das, and D.C. Sanyal, "Hydromagnetic convecting slip flow through a horizontal channel," *Indian Journal of Theoretical Physics*, **42**(1), 63-72 (1994).
- [7] T. Paul, B. Jha, and A. Singh, "Transient free convective flow in a vertical channel with constant temperature and constant heat flux on walls," *Heat and Mass Transfer*, **32**(1-2), 61-63 (1996). <https://doi.org/10.1007/s002310050092>
- [8] S. Chakraborty, and A.K. Borkakati, "Unsteady free convection MHD flow between two heated vertical parallel plates in induced magnetic field," *Indian Journal of Theoretical Physics*, **47**(1), 43-60 (1999).
- [9] D. Lensis, D. Ingham, Pop I and C. Storr, "Free convection boundary layer flow above a nearly horizontal surface in a porous medium with Newtonian heating," *Heat and Mass Transfer*, **40**(9), 665-672 (2004). <http://dx.doi.org/10.1007%2Fs00231-003-0435-y>
- [10] P.R. Sharma, and G. Singh, "Unsteady MHD free convective flow and heat transfer along a vertical porous plate with variable suction and heat generation," *Int. J. Appl. Math. Mech.* **4**(5), 1-8 (2008).
- [11] G. Palani, and U. Srikanth, "MHD flow past a semi infinite vertical plate with mass transfer," *Nonlinear Analysis: Modeling and Control*, **14**(3), 345-356 (2009). <https://doi.org/10.15388/NA.2009.14.3.14500>
- [12] R.K. Singh, A.K. Singh, N.C. Sacheti, and P. Chandran, "On hydromagnetic free convection in the presence of induced magnetic field," *Heat and Mass Transfer*, **46**, 523-529 (2010). <https://doi.org/10.1007/s00231-010-0594-6>
- [13] B.K. Jha, and I. Sani, "Computational treatment of MHD of transient natural convection flow in a vertical channel due to symmetric heating in presence of induced magnetic field," *Journal of the Physical Society of Japan*, **82**, 084401 (2013). <https://doi.org/10.1515/ijame-2017-0036>
- [14] A. Kumer, and A.K. Singh, "Unsteady magnetohydrodynamic free convective flow past a semi-infinite vertical wall by taking into account the induced magnetic field," *Applied Mathematics and Computation*, **222**, 462-471 (2015). <https://doi.org/10.1016/j.amc.2013.07.044>
- [15] Sarveshanand, and A.K. Singh, "MHD free convection between vertical parallel porous plates in the presence of induced magnetic field," *Springer plus*, **4**, 333 (2015). <https://doi.org/10.1186/s40064-015-1097-1>

- [16] M.M. Hamza, "Free convection slip flow of an exothermic fluid in a convectively heated vertical channel," *Ain Shams Engineering Journal*, **9**(4), 1313-1323 (2016). <https://doi.org/10.1016/j.asej.2016.08.011>
- [17] A. Goswami, M. Goswami and K.G. Singha, "Unsteady MHD free convection flow between two heated vertical parallel plates in the presence of a uniform magnetic field," *International Journal of Scientific Research in Mathematical and Statistical Sciences*, **7**, 86-94 (2020). https://www.isroset.org/pdf_paper_view.php?paper_id=1837&12-IJSRMSS-03181.pdf
- [18] B.K. Goud, P.P. Kumer, and B.S. Malga, "Induced magnetic field effect on MHD free convection flow in nonconducting and conducting vertical microchannel," *Heat Transfer*, **51**, 2201-2218 (2021). <https://doi.org/10.1002/htj.22396>
- [19] B.K. Jha, and B. Aina, "Impact of induced magnetic field on magnetohydrodynamic (MHD) natural convection flow in a vertical annular micro-channel in the presence of radial magnetic field," *Propulsion and power research*, **7**(2), 171-181 (2018). <https://doi.org/10.1016/j.jprr.2018.04.004>
- [20] J. Mng'ang'a, "Effect of chemical reaction and joule heating on MHD generalized couette flow between two parallel vertical porous plates with induced magnetic field and Newtonian heating/cooling," **2023**, 9134811 (2023). <https://doi.org/10.1155/2023/9134811>

ВПЛИВ ІНДУКОВАНОГО МАГНІТНОГО ПОЛЯ НА МГД ПОТІК МІЖ ДВОМА ПАРАЛЕЛЬНИМИ ПОРИСТИМИ ПЛАСТИНАМИ ПРИ НАЯВНОСТІ ПОСТІЙНОГО ГРАДІЄНТА ТЕМПЕРАТУРИ НАХИЛЕНОГО МАГНІТНОГО ПОЛЯ

Канкана Рабха^a, Салім Джабед Аль-Хаср^a, Шьяманга Чакраборті^b

^a*Кафедра математики, Університет Гаухаті, Гувахаті, Ассам, Індія*

^b*UGC-HRDC, Університет Гаухаті, Гувахаті, Ассам, Індія*

Досліджено вплив індукованого магнітного поля на ламінарну конвекцію в'язкої електропровідної нестисливої рідини між двома паралельними пористими пластинами при постійному градієнті температури за наявності однорідного похилого магнітного поля. Кут (θ) утворюється з вертикальною лінією шляхом застосування магнітного поля в цьому напрямку, і поле є достатньо сильним, щоб індукувати інше поле вздовж лінії потоку. За допомогою належних перетворень подібності рівняння потоку перетворюються на звичайні диференціальні рівняння, які потім чисельно розв'язуються за допомогою розв'язувача `bvp4c` MATLAB. Побудова графіків дозволяє досліджувати вплив кількох критичних параметрів, таких як число Гартмана, число Дарсі, магнітне число Рейнольдса, число Прандтля та нахил поля на поле швидкості, індуковане магнітне поле, температурне поле на пластинах. Отримані результати демонструють, що на систему течії ефективно впливають нахил поля, індуковане магнітне поле та пористість пластини. Підвищення нахилу поля призводить до збільшення сили магнітного опору.

Ключові слова: *індуковане магнітне поле; вільна конвекція; плита пористого типу; МГД; температурний градієнт*

HEAT AND MASS TRANSFER ON FLOW PAST AN ACCELERATED PLATE THROUGH POROUS MEDIUM WITH VARIABLE TEMPERATURE AND MASS DIFFUSION IN PRESENCE OF HEAT SOURCE/SINK

 Rakesh Rabha*,  Rudra Kanta Deka

Department of Mathematics, Gauhati University, Guwahati-781014, Assam

*Corresponding Author e-mail: rakeshrabha0568@gmail.com

Received January 2, 2024; revised February 2, 2024; accepted February 6, 2024

A study to look at how heat and mass transfer affect unsteady MHD flow across an accelerated plate with changing temperature and mass diffusion in the appearance of a heat source (or sink) through porous medium is presented. Initially the temperature and concentration of the fluid and plate are considered to be same at $t' \leq 0$. At $t' > 0$, an impulsive uniform acceleration A is applied to the plate in a vertical upward direction. The non-dimensionalised governing equations defining the flow problem are solved using Laplace transform approach. Effect of various physical quantities involved in the velocity, concentration, temperature, the rate of heat transfer and also the rate of mass transfer are investigated through graphs and tables and discussed.

Keywords: Heat transfer; Mass transfer; Accelerated plate; Porous medium; Laplace Transform

PACS: 44.30.+v, 44.05.+e, 66.10.cd, 47.11.-j

1. INTRODUCTION

In nature, the action of mass and heat transfer inside a fluid occurs because of the concentration differences and temperature differences. The outcome of heat and mass transfer on MHD fluid has drawn the attraction of numerous researchers due to its diverse applications. Many researchers have carried out numerous studies in this field under various flow situation. Heat and mass transmission play crucial role in many different fields including pump, compressor, steam-electric power generation, automobiles, power plant, gas turbine, energy utilization, food processing, etc. MHD effect on an impulsively begun perpendicular unbounded plate with uncertain temperature in the appearance of a transverse magnetic field were investigated by Soundalgekar et al [12]. Soundalgekar et al. [11] also examined how the mass transfer can effect on the flow of an incompressible, electrically conducting fluid past an impulsively begun unbounded isothermal vertical plate for a transversely applied magnetic field. Kumar et al. [8] studied the impact of an impulsive motion on the growth of two-dimensional boundary layer having applied magnetic field. Variations in mixed convection on an isothermal perpendicular plate due to radiation have been taken into account by Hossain and Takhar [5]. The stationary vertical plate was taken into account in all of the investigations above. The effects of MHD and radiation along a moving, isothermal perpendicular plate with variable mass diffusion have been explored by Muthucumaraswamy et al. [9]. The impacts of heat radiation and free convection flow through a moving perpendicular plate were investigated by Raptis and Perdikis [10]. Das et al. [4] have explored the impact of radiation on flow past an abruptly began unbounded isothermal perpendicular plate.

The thermal diffusion effect on MHD free convection and mass transfer flows have been examined by Alam and Sattar [3]. Jha and Singh [6] conducted research on the content of thermal-diffusion effects (mass diffusion caused by temperature differential). The thermal-diffusion effect on impulsively started perpendicular porous plates, changeable MHD free convection, and also mass transfer flow was examined by Alam et al. [1]. Alam et al [2] investigated coupled free convection and mass transfer flow and thermal diffusion in porous medium through a perpendicular plate. The impacts of heat radiation and diffusion on MHD flow via a perpendicular plate with varying temperature and mass diffusion were investigated by Rajesh and Varma [13]. The effects of radiation and thermal diffusion on changeable MHD flow through porous media having inconsistent mass diffusion and changing temperature were studied by Kumar and Varma [14]. Khan et al. [15] examine the combined impacts of heat and mass transport on the free convection, unstable magnetohydrodynamic flow of viscous fluid immersed in a porous media. They found that with the increasing values of Prandtl number, the fluid concentration rises. The impacts of radiation and thermal diffusion on changeable MHD flow via a vertically accelerated porous plate with changeable temperature and changeable mass diffusion while being affected by an applied transverse magnetic field, when a heat source or sink is present are investigated by Ramana Reddy et al. [16]. Thermal Stratification's impact on the flow through an infinite vertical plate was studied by Nath et al. [18]. Kalita et al. [19] examined the effect of thermal stratification on the flow passing

an accelerated plate with changeable temperature. Kumar et al. [20] studied how mass stratification effects the unsteady flow while passing an accelerated plate with variable temperature.. Motivated from the study of the above discussions the current objective is to understand the effect of heat and mass transfer in the presence of a heat source or sink through a porous media on changeable MHD flow past an accelerating plate with varying temperature and mass diffusion. Laplace transform approach is used to derived the solution. The Sherwood and Nusselt numbers are derived. The found answer is represented in respects of complementary error functions and exponential functions.

2. MATHEMATICAL FORMULATION

We consider the unstable laminar free convection flow of an incompressible viscous fluid past a plate that is propelled impulsively and has variable mass diffusion and temperature. Also the fluid is electrically conducting fluid. Here, the plate is taken vertically upward along the x'-axis, and the y'-axis is considered perpendicular with respect to plate. It is considered that the fluid and plate are initially at the same concentration C'_∞ and temperature T'_∞ at $t' \leq 0$. At $t' > 0$, an impulsive uniform acceleration A is applied to the plate in a vertical upward direction. Both the temperature level and concentration level are raised from T'_∞ and C'_∞ to T'_w and C'_w respectively . The viscous dissipation is regarded as insignificant. Also the induced magnetic field is considered insignificant. With the standard Boussinesq's approximation under this supposition, the governing equations are:

$$\frac{\partial u'}{\partial t'} = g\beta(T' - T'_\infty) - \frac{\sigma\beta_0^2 u'}{\rho} + g\beta^*(C' - C'_\infty) + \nu \frac{\partial^2 u'}{\partial y'^2} - \nu \frac{u'}{K'} \tag{1}$$

$$\rho C_p \frac{\partial T'}{\partial t'} = \kappa \frac{\partial^2 T'}{\partial y'^2} - \frac{\partial q_r}{\partial y'} + Q'(T'_\infty - T') \tag{2}$$

$$\frac{\partial C'}{\partial t'} = D \frac{\partial^2 C'}{\partial y'^2} + D_1 \left(\frac{\partial^2 T'}{\partial y'^2} \right) \tag{3}$$

with the following initial and boundary conditions

$$\begin{aligned} t' \leq 0 : u' = 0, T' = T'_\infty, C' = C'_\infty, \quad \text{for all } y' \\ t' > 0 : u' = At', T' = T'_\infty + (T'_w - T'_\infty)Bt', C' = C'_\infty + (C'_w - C'_\infty)Bt' \quad \text{at } y' = 0 \\ u' = 0, T' \rightarrow T'_\infty, C' \rightarrow C'_\infty \quad \text{as } y' \rightarrow \infty \end{aligned} \tag{4}$$

where $B = \frac{u_0^2}{\nu}$ and A \rightarrow uniform acceleration of the plate.

Using the Roseland approximation, the radioactive heat flux term of an optically very thin fluid is made simpler.

$$q_r = - \frac{4\sigma^*}{3k'} \frac{\partial T'^4}{\partial y'} \tag{5}$$

It is assumed that T'^4 may be represented as a linear function of temperature and that the temperature differences inside the flow are suitably modest. This is achieved by disregarding the higher order terms and expanding T'^4 in a Taylor series up to T'_∞ , thus we get

$$T'^4 \cong 4T'^3_\infty T' - 3T'^4_\infty \tag{6}$$

With the help equations (5) and (6), from equation (2) we have

$$\frac{\rho C_p}{\kappa} \frac{\partial T'}{\partial t'} = \frac{\partial^2 T'}{\partial y'^2} \left(1 + \frac{16\sigma^* T'^3_\infty}{3\kappa k'} \right) + \frac{Q'}{\kappa} (T'_\infty - T') \tag{7}$$

On defining the following dimensionless variables:

$$\begin{aligned} u = \frac{u'}{(A\nu)^{\frac{1}{3}}}, \quad t = t' \left(\frac{A^2}{\nu} \right)^{\frac{1}{3}}, \quad y = y' \left(\frac{A}{\nu^2} \right)^{\frac{1}{3}}, \quad C = \frac{C' - C'_\infty}{C'_w - C'_\infty}, \quad \theta = \frac{T' - T'_\infty}{T'_w - T'_\infty}, \\ Pr = \mu \frac{C_p}{\kappa}, \quad Gr = \frac{g\beta(T'_w - T'_\infty)}{A}, \quad M^2 = \frac{\sigma\beta_0^2 \nu^{\frac{1}{3}}}{\rho A^{\frac{2}{3}}}, \quad Gm = \frac{g\beta^*(C'_w - C'_\infty)}{A}, \end{aligned}$$

$$Sc = \frac{\nu}{D}, \quad K = \frac{K' A^{\frac{2}{3}}}{\nu^{\frac{4}{3}}}, \quad R = \frac{16\sigma^* T_{\infty}'^3}{3\kappa k'}, \quad S_0 = \frac{D_1(T_w' - T_{\infty}')}{\nu(C_w' - C_{\infty}')}, \quad H = \frac{Q'}{\kappa} \left(\frac{\nu^2}{A} \right)^{\frac{2}{3}} \quad (8)$$

we get the following dimensionless governing equation:

$$\frac{\partial u}{\partial t} = \frac{\partial^2 u}{\partial y^2} + Gr\theta + GmC - Zu \quad (9)$$

$$\frac{\partial \theta}{\partial t} = \frac{(1+R)}{Pr} \frac{\partial^2 \theta}{\partial y^2} - \frac{H\theta}{Pr} \quad (10)$$

$$\frac{\partial C}{\partial t} = \frac{1}{Sc} \frac{\partial^2 C}{\partial y^2} + S_0 \frac{\partial^2 \theta}{\partial y^2} \quad (11)$$

and the relevant corresponding initial and boundary conditions are:

$$\begin{aligned} t \leq 0: \quad u &= 0, \quad \theta = 0, \quad C = 0 \quad \text{for all } y \\ t > 0; \quad u &= t, \quad \theta = t, \quad C = t \quad \text{at } y = 0 \\ u &\rightarrow 0, \quad \theta \rightarrow 0, \quad C \rightarrow 0 \quad \text{as } y \rightarrow \infty \end{aligned} \quad (12)$$

Here the non-dimensional velocity, concentration, temperature and time are denoted by u , C , θ and t respectively. $C_p \rightarrow$ specific heat at constant pressure, β' and $\beta \rightarrow$ concentration and thermal expansion coefficients respectively, D is chemical mass diffusivity, $D_1 \rightarrow$ coefficient of thermal diffusivity, $\rho \rightarrow$ fluid density, $\beta_0 \rightarrow$ magnetic induction, $\mu \rightarrow$ coefficient of viscosity, ν is the kinematic viscosity, $R \rightarrow$ Radiation parameter, $Gr \rightarrow$ Thermal Grashof number, $Gm \rightarrow$ Mass Grashof number, $M \rightarrow$ magnetic field parameter, $Pr \rightarrow$ Prandtl number, $Sc \rightarrow$ Schmidt number, $S_0 \rightarrow$ Soret number, $K \rightarrow$ permeability parameter, $H \rightarrow$ Heat source parameter.

3. ANALYTICAL SOLUTION

Solutions of the non-dimensional governing equations (9), (10) and (11) with regard to the boundary condition (12) are solved using Laplace transform approach. We attained solutions as :

$$\begin{aligned} \theta(y, t) &= \left(\frac{t}{2} + \frac{yX}{4\sqrt{Y}} \right) \exp(y\sqrt{Y}) \operatorname{erfc} \left(\frac{y\sqrt{X}}{2\sqrt{t}} + \sqrt{\frac{Yt}{X}} \right) + \left(\frac{t}{2} - \frac{yX}{4\sqrt{Y}} \right) \exp(-y\sqrt{Y}) \\ &\quad \operatorname{erfc} \left(\frac{y\sqrt{X}}{2\sqrt{t}} - \sqrt{\frac{Yt}{X}} \right) \end{aligned} \quad (13)$$

$$\begin{aligned} C(y, t) &= (1+e) \left[\left(t + \frac{y^2 Sc}{2} \right) \operatorname{erfc} \left(\frac{y\sqrt{Sc}}{2\sqrt{t}} \right) - y \sqrt{\frac{tSc}{\pi}} \exp \left(-\frac{y^2 Sc}{4t} \right) \right] + \left(d - \frac{e}{j} \right) \operatorname{erfc} \left(\frac{y\sqrt{Sc}}{2\sqrt{t}} \right) \\ &\quad - \frac{1}{2} \left(d - \frac{e}{j} \right) \exp(-jt) \left[\exp(y\sqrt{-jSc}) \operatorname{erfc} \left(\frac{y\sqrt{Sc}}{2\sqrt{t}} + \sqrt{-jt} \right) + \exp(-y\sqrt{-jSc}) \right. \\ &\quad \left. \operatorname{erfc} \left(\frac{y\sqrt{Sc}}{2\sqrt{t}} - \sqrt{-jt} \right) \right] - \frac{1}{2} \left(d - \frac{e}{j} \right) \left[\exp(y\sqrt{Y}) \operatorname{erfc} \left(\frac{y\sqrt{X}}{2\sqrt{t}} + \sqrt{\frac{Yt}{X}} \right) + \exp(-y\sqrt{Y}) \right. \\ &\quad \left. \operatorname{erfc} \left(\frac{y\sqrt{X}}{2\sqrt{t}} - \sqrt{\frac{Yt}{X}} \right) \right] - e \left[\left(\frac{t}{2} + \frac{yX}{4\sqrt{Y}} \right) \exp(y\sqrt{Y}) \operatorname{erfc} \left(\frac{y\sqrt{X}}{2\sqrt{t}} + \sqrt{\frac{Yt}{X}} \right) \right. \\ &\quad \left. + \left(\frac{t}{2} - \frac{yX}{4\sqrt{Y}} \right) \exp(-y\sqrt{Y}) \operatorname{erfc} \left(\frac{y\sqrt{X}}{2\sqrt{t}} - \sqrt{\frac{Yt}{X}} \right) \right] + \frac{1}{2} \left(d - \frac{e}{j} \right) \exp(-jt) \left[\exp(y\sqrt{(Y-jX)}) \right. \\ &\quad \left. \operatorname{erfc} \left(\frac{y\sqrt{X}}{2\sqrt{t}} + \sqrt{\left(\frac{Y}{X} - j \right) t} \right) + \exp(-y\sqrt{(Y-jX)}) \operatorname{erfc} \left(\frac{y\sqrt{X}}{2\sqrt{t}} - \sqrt{\left(\frac{Y}{X} - j \right) t} \right) \right] \end{aligned} \quad (14)$$

$$\begin{aligned} u(y, t) &= \left(\frac{t}{2} + \frac{y}{4\sqrt{Z}} \right) \exp(y\sqrt{Z}) \operatorname{erfc} \left(\frac{y}{2\sqrt{t}} + \sqrt{Zt} \right) + \left(\frac{t}{2} - \frac{y}{4\sqrt{Z}} \right) \exp(-y\sqrt{Z}) \\ &\quad \operatorname{erfc} \left(\frac{y}{2\sqrt{t}} - \sqrt{Zt} \right) + A_1 \left[\left(\frac{t}{2} + \frac{yX}{4\sqrt{Y}} \right) \exp(y\sqrt{Y}) \operatorname{erfc} \left(\frac{y\sqrt{X}}{2\sqrt{t}} + \sqrt{\frac{Yt}{X}} \right) \right. \\ &\quad \left. + \left(\frac{t}{2} - \frac{yX}{4\sqrt{Y}} \right) \exp(-y\sqrt{Y}) \operatorname{erfc} \left(\frac{y\sqrt{X}}{2\sqrt{t}} - \sqrt{\frac{Yt}{X}} \right) \right] + A_2 \left[\left(t + \frac{y^2 Sc}{2} \right) \operatorname{erfc} \left(\frac{y\sqrt{Sc}}{2\sqrt{t}} \right) \right. \end{aligned}$$

$$\begin{aligned}
 & -y\sqrt{\frac{tSc}{\pi}}\exp\left(-\frac{y^2Sc}{4t}\right) - (A_1 + A_2)\left[\left(\frac{t}{2} + \frac{y}{4\sqrt{Z}}\right)\exp(y\sqrt{Z})\operatorname{erfc}\left(\frac{y}{2\sqrt{t}} + \sqrt{Zt}\right)\right. \\
 & \left. + \left(\frac{t}{2} - \frac{y}{4\sqrt{Z}}\right)\exp(-y\sqrt{Z})\operatorname{erfc}\left(\frac{y}{2\sqrt{t}} - \sqrt{Zt}\right)\right] + \frac{A_3}{2}\exp(-jt)\left[\exp(-y\sqrt{(Y-jX)})\right. \\
 & \left.\operatorname{erfc}\left(\frac{y\sqrt{X}}{2\sqrt{t}} - \sqrt{\left(\frac{Y}{X} - j\right)t}\right) + \exp(y\sqrt{(Y-jX)})\operatorname{erfc}\left(\frac{y\sqrt{X}}{2\sqrt{t}} + \sqrt{\left(\frac{Y}{X} - j\right)t}\right)\right] \\
 & - \frac{A_4}{2}\exp(-jt)\left[\exp(y\sqrt{-jSc})\operatorname{erfc}\left(\frac{y\sqrt{Sc}}{2\sqrt{t}} + \sqrt{-jt}\right) + \exp(-y\sqrt{-jSc})\operatorname{erfc}\left(\frac{y\sqrt{Sc}}{2\sqrt{t}} - \sqrt{-jt}\right)\right] \\
 & + \frac{A_5}{2}\exp(-lt)\left[\exp(y\sqrt{Z-l})\operatorname{erfc}\left(\frac{y}{2\sqrt{t}} + \sqrt{(Z-l)t}\right) + \exp(-y\sqrt{Z-l})\right. \\
 & \left.\operatorname{erfc}\left(\frac{y}{2\sqrt{t}} - \sqrt{(Z-l)t}\right)\right] - \frac{A_5}{2}\exp(-lt)\left[\exp(y\sqrt{Y-lX})\operatorname{erfc}\left(\frac{y\sqrt{X}}{2\sqrt{t}} + \sqrt{\left(\frac{Y}{X} - l\right)t}\right)\right. \\
 & \left. + \exp(-y\sqrt{Y-lX})\operatorname{erfc}\left(\frac{y\sqrt{X}}{2\sqrt{t}} - \sqrt{\left(\frac{Y}{X} - l\right)t}\right)\right] + \frac{A_6}{2}\exp(ft)\left[\exp(y\sqrt{Z+f})\right. \\
 & \left.\operatorname{erfc}\left(\frac{y}{2\sqrt{t}} + \sqrt{(Z+f)t}\right) + \exp(-y\sqrt{Z+f})\operatorname{erfc}\left(\frac{y}{2\sqrt{t}} - \sqrt{(Z+f)t}\right)\right] \\
 & - \frac{A_6}{2}\exp(ft)\left[\exp(y\sqrt{fSc})\operatorname{erfc}\left(\frac{y\sqrt{Sc}}{2\sqrt{t}} + \sqrt{ft}\right) + \exp(-y\sqrt{fSc})\operatorname{erfc}\left(\frac{y\sqrt{Sc}}{2\sqrt{t}} - \sqrt{ft}\right)\right] \\
 & + \frac{A_7}{2}\left[\exp(y\sqrt{Y})\operatorname{erfc}\left(\frac{y\sqrt{X}}{2\sqrt{t}} + \sqrt{\frac{Yt}{X}}\right) + \exp(-y\sqrt{Y})\operatorname{erfc}\left(\frac{y\sqrt{X}}{2\sqrt{t}} - \sqrt{\frac{Yt}{X}}\right)\right] + A_8\operatorname{erfc}\left(\frac{y\sqrt{Sc}}{2\sqrt{t}}\right) \\
 & - \frac{(A_7 + A_8)}{2}\left[\exp(y\sqrt{Z})\operatorname{erfc}\left(\frac{y}{2\sqrt{t}} + \sqrt{Zt}\right) + \exp(-y\sqrt{Z})\operatorname{erfc}\left(\frac{y}{2\sqrt{t}} - \sqrt{Zt}\right)\right] \tag{15}
 \end{aligned}$$

where

$$Z = M^2 + \frac{1}{K}, \quad X = \frac{Pr}{1+R}, \quad Y = \frac{H}{1+R}, \quad b = \frac{S_0Sc}{1+R}$$

$$j = \frac{Y}{X - Sc}, \quad d = \frac{bPr}{Y}, \quad e = \frac{b}{1+R}, \quad f = \frac{Z}{Sc - 1}$$

$$A_1 = \frac{eGm - Gr}{Y - Z}, \quad A_2 = \frac{(1 + e)Gm}{Z}$$

$$A_3 = \frac{bGm(Y - jPr(1 + R))}{jY(1 + R)(Y - Z + j - jX)}$$

$$A_4 = \frac{bGm(Y - jPr(1 + R))}{jY(1 + R)(Y - Z + j - jX)}$$

$$A_5 = \frac{(X - 1)[YGr(Y - Z + j - jX) + bjGm(Pr(Z - Y) - \frac{Y(1-X)}{1+R})]}{Y(Y - Z)^2(Y - Z + j - jX)}$$

$$A_6 = \frac{(Sc - 1)Gm[Y(1 + R)(Z - j + jSc) + bjY(Sc - 1) + bjZPr(1 + R)]}{YZ^2(1 + R)(Z - j + jSc)}$$

$$A_7 = \frac{jY(X - 1)[Gr(1 + R) - bGm] + bGm[jPr(1 + R) - Y]}{jY(1 + R)(Y - Z)^2}$$

$$A_8 = \frac{Gm[(1+R)j(Y(Sc-1) + bPrZ) + bY(j(Sc-1) - Z)]}{jYZ^2(1+R)}$$

NUSSELT NUMBER

From temperature profile (13), the change rate of heat transfer is obtained as

$$\begin{aligned} Nu &= - \left[\frac{\partial \theta}{\partial y} \right]_{y=0} \\ Nu &= t\sqrt{Y} \operatorname{erf}\left(\sqrt{\frac{Yt}{X}}\right) + \sqrt{\frac{tX}{\pi}} \exp\left(-\frac{Yt}{X}\right) + \frac{X}{2\sqrt{Y}} \operatorname{erf}\left(\sqrt{\frac{Yt}{X}}\right) \end{aligned} \quad (16)$$

SHERWOOD NUMBER

From concentration profile (14), the change rate of mass transfer is obtained as

$$\begin{aligned} Sh &= - \left[\frac{\partial C}{\partial y} \right]_{y=0} \\ Sh &= 2(1+e)\sqrt{\frac{tSc}{\pi}} + \left(d - \frac{e}{j}\right)\sqrt{\frac{Sc}{\pi t}} - \left(d - \frac{e}{j}\right)\exp(-jt) \left[\sqrt{-jSc} \operatorname{erf}\left(\sqrt{-jt}\right) \right. \\ &\quad \left. + \sqrt{\frac{Sc}{\pi t}} \exp(jt) \right] - \left(d - \frac{e}{j}\right) \left[\sqrt{Y} \operatorname{erf}\left(\sqrt{\frac{Yt}{X}}\right) + \sqrt{\frac{X}{\pi t}} \exp\left(-\frac{Yt}{X}\right) \right] \\ &\quad - e \left[\frac{X}{2\sqrt{Y}} \operatorname{erf}\left(\sqrt{\frac{Yt}{X}}\right) + t\sqrt{Y} \operatorname{erf}\left(\sqrt{\frac{Yt}{X}}\right) + \sqrt{\frac{Xt}{\pi}} \exp\left(-\frac{Yt}{X}\right) \right] \\ &\quad + \left(d - \frac{e}{j}\right)\exp(-jt) \left[\sqrt{Y - jX} \operatorname{erf}\left(\sqrt{\left(\frac{Y}{X} - j\right)t}\right) + \sqrt{\frac{X}{\pi t}} \exp\left(-\left(\frac{Y}{X} - j\right)t\right) \right] \end{aligned} \quad (17)$$

4. RESULTS AND DISCUSSION

To examine the physical behaviour related to the problems, figures and tables are presented for velocity (u), temperature (θ), concentration (C), Nusselt number (Nu), and Sherwood number (Sh), illustrating the results of numerous parameters involved in the problems. Figure (1) demonstrate how a magnetic field parameter affects fluid velocity. We have seen that when the magnetic parameter M increases, the velocity drops. It is due to the result of application of transverse magnetic fields, a drag-like resistive force is created that tends to impede the flow of the fluid, reducing its velocity. Figure (2) and (3) are used to illustrate graphically how temperature and mass Grashof numbers (Gr and Gm) affect the velocity field. The fluid velocity increases as the thermal Grashof number or mass Grashof number increases when all other parameters remain constant. Figure (4) shows how the velocity field is affected by the thermal-diffusion parameter (S_0). As the Soret number rises, the velocity rises as well. To investigate the impact of permeability parameter K , Figure (5) is sketched. It is discovered that the velocity grows as K is raised. From Figure (6), it can be found that when the radiation parameter (R) increases, the velocity rises up to a specific y value (distance from the plate), after which it falls off in the event that the plate cools. Figure (7) reveals how the velocity decreases as the heat source parameter (H) is increased. The radiation parameter (R) and heat source parameter (H) have a significant impact on the flow field's temperature. Figure (8) illustrates how these characteristics affect the flow field's temperature. The temperature of the boundary layer rises as radiation parameter increases and temperature falls with the increase of heat source parameter.

Figure (9) reveals that as the Soret number S_0 is increased, the concentration profiles rise. It can be seen from Figure (10) that as the Schmidt number rises, the concentration field decreases. From figure (11) it is revealed that the greater the values of radiation parameter the concentration decreases. From Figure (12), we can see that the greater the values of the Prandtl number Pr , the fluid concentration rises.

It is cleared from Table (1) that Nusselt number rises with rising Prandtl number Pr values, but falls with rising radiation parameter values. It is evident from Table (2) that Sherwood number rises as Sc rises, while the pattern is the opposite for high values of Pr and S_0 .

5. CONCLUSION

We looked at how heat and mass transfer affected an accelerating plate with changing temperature and mass diffusion when there was a heat source or sink present through a porous medium. Based on the results

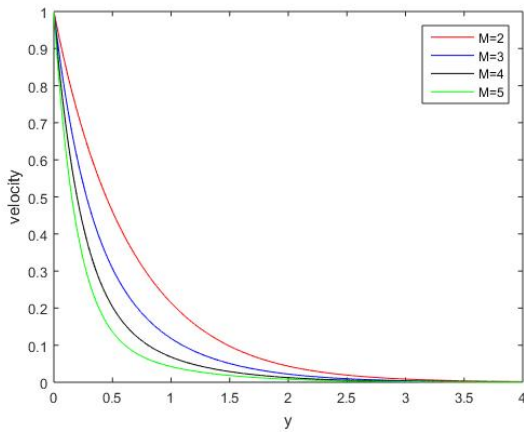


Figure 1. Effect of various M on Velocity profile with $S_0 = 5$, $Sc = 2.01$, $Gm = 1$, $Pr = 0.71$, $Gr = 1$, $K = 0.5$, $R = 2$, $H = 8$, $t = 1$ and $Sc = 2.01$.

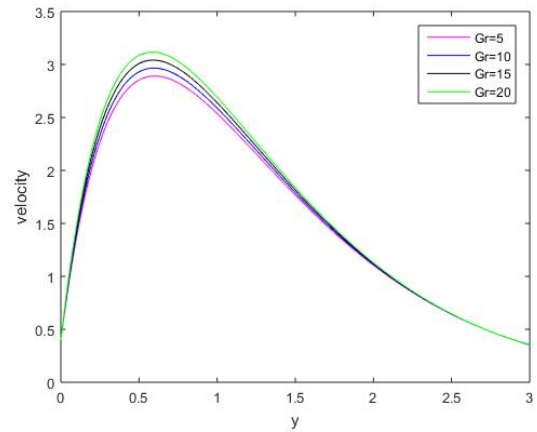


Figure 2. Effect of various Gr on velocity profile with $Sc = 2.01$, $S_0 = 5$, $Pr = 0.71$, $K = 0.5$, $Gm = 5$, $H = 2$, $t = 0.4$, $Sc = 2.01$, $R = 2$ and $M = 2$.

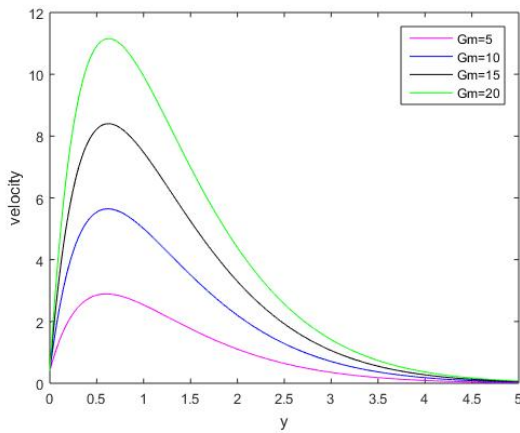


Figure 3. Effect of various Gm on velocity profile with $S_0 = 5$, $Pr = 0.71$, $H = 2$, $K = 0.5$, $t = 0.4$, $Sc = 2.01$, $M = 2$, $R = 2$ and $Gr = 5$.

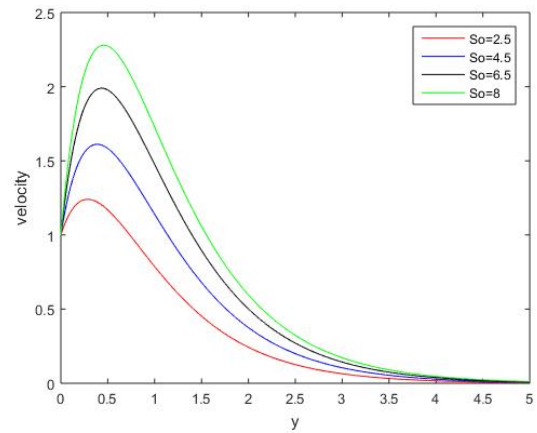


Figure 4. Effect of various S_0 on velocity profile with $Pr = 0.71$, $Gm = 5$, $Gr = 5$, $K = 0.5$, $Sc = 2.01$, $H = 5$, $t = 1$, $R = 2$ and $M = 2$.

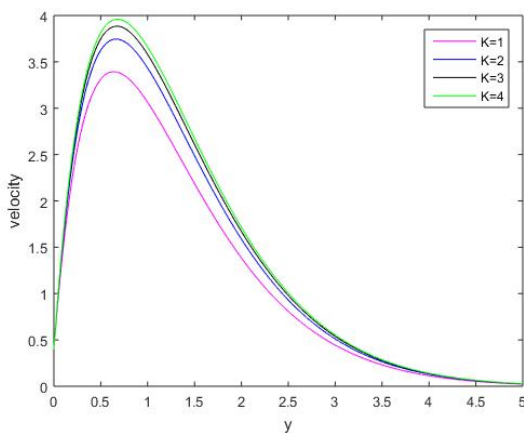


Figure 5. Effect of various K on velocity profile with $S_0=5$, $Sc = 2.01$, $Gm = 5$, $H = 2$, $Pr = 0.71$, $t = 0.4$, $M = 2$, $R = 2$ and $Gr = 5$.

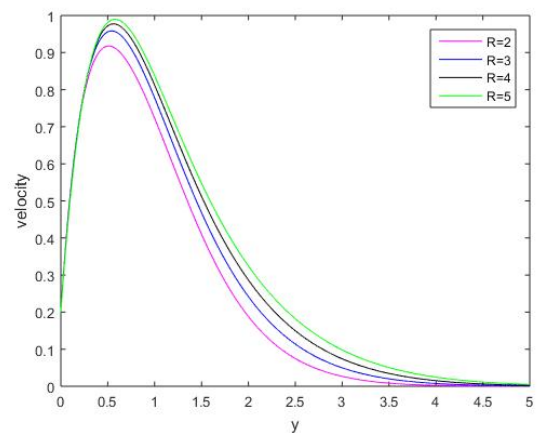


Figure 6. Effect of various R on velocity profile with $S_0 = 5$, $Pr = 0.71$, $Gm = 5$, $Gr = 5$, $K = 0.5$, $Sc = 2.01$, $H = 5$, $t = 0.2$ and $M = 2$.

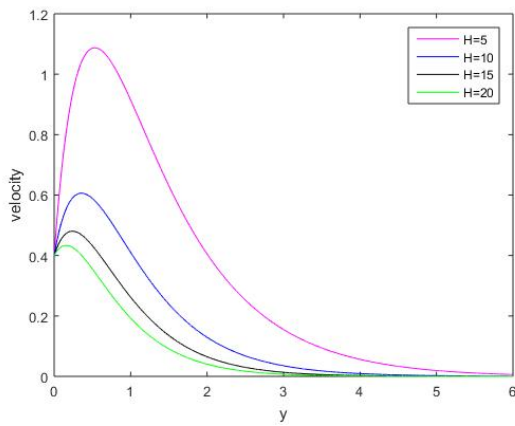


Figure 7. Effect of various H on velocity profile with $S_0=5$, $Sc = 2.01$, $Gm = 5$, $K = 0.5$, $Pr = 0.71$, $t = 0.4$, $M = 2$, $R = 5$ and $Gr = 5$.

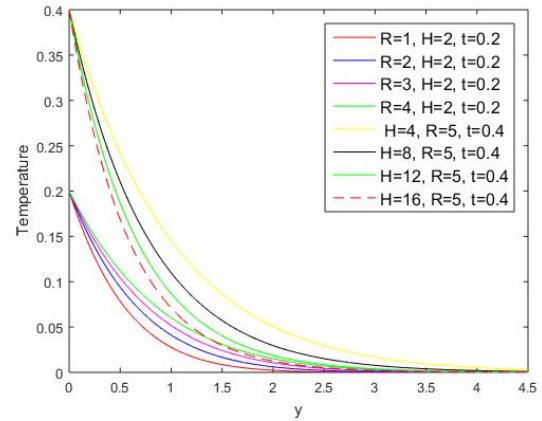


Figure 8. Effects of R and H on temperature

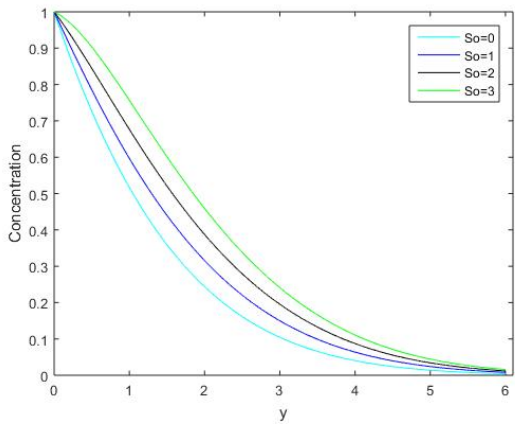


Figure 9. Effect of S_0 on concentration with $Pr = 0.71$, $t = 1$, $R = 0.4$, $H = 1$ and $Sc = 0.3$.

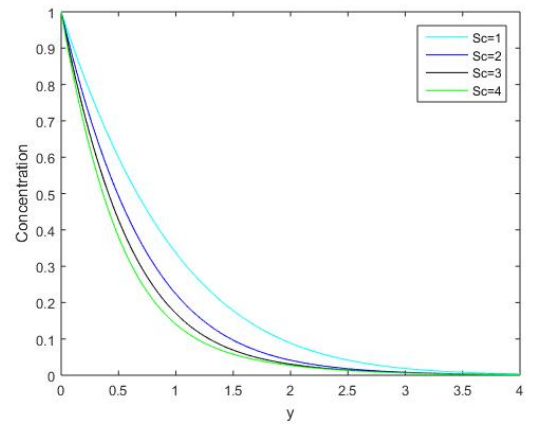


Figure 10. Effect of Sc on concentration with $S_0 = 0.4$, $Pr = 0.71$, $R = 0.4$, $H = 1$ and $t = 1$.

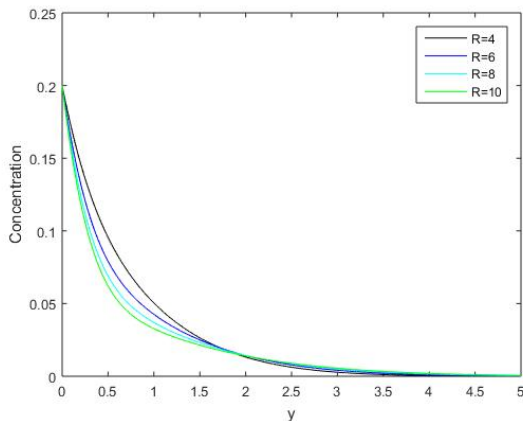


Figure 11. Effect of R on concentration with $S_0 = 5$, $H = 1$, $t = 0.2$, $Pr = 0.71$ and $Sc = 2.01$.

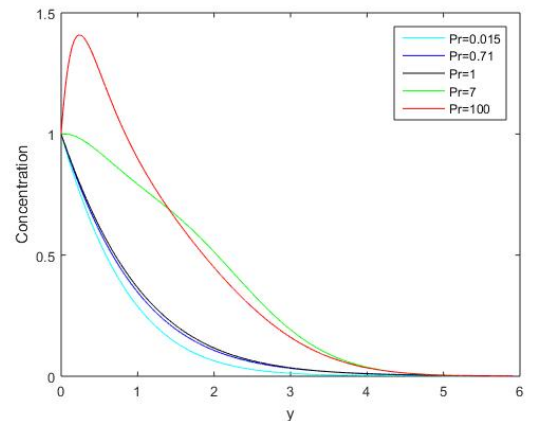


Figure 12. Concentration profiles for various Pr with $S_0 = 0.9$, $R = 2$, $H = 1$, $t = 1$ and $Sc = 1$.

of our current investigation and graphical analysis, as the values of K and Gr grows, the velocity rises but it decreases as M increases. The temperature inside the boundary layer increases with rising value of radiation parameter. The concentration grows with rising value of S_0 and Pr , whereas it falls when Sc is increased.


Table 1. The impact of different parameters on Nusselt number with $H = 1, t = 1$.

Pr	R	Nu
0.71	0.2	1.2277
1	0.2	1.4018
0.71	0.4	1.0545

Table 2. The impact of different parameters on Sherwood number with $R = 0.1, H = 2$ and $t = 1$.

Pr	Sc	So	Sh
0.71	0.6	1	0.3371
1	0.6	1	0.2745
0.71	1	1	0.594
0.71	1	2	0.0596

ORCID

 **Rakesh Rabha**, <https://orcid.org/0009-0002-6842-6596>;  **Rudra Kanta Deka**, <https://orcid.org/0009-0007-1573-4890>

REFERENCES

- [1] M.S. Alam, M.M. Rahman, and M.A. Maleque, "Local similarity solutions for unsteady MHD free convection and mass transfer flow past an impulsively started vertical porous plate with Dufour and Soret effects," *Science & Technology Asia*, **10**(3) 1-8 (2005). <https://ph02.tci-thaijo.org/index.php/SciTechAsia/article/view/41571/34358>
- [2] M.S. Alam, M.M. Rahman, and M.A. Samad, "Numerical study of the combined free-forced convection and mass transfer flow past a vertical porous plate in a porous medium with heat generation and thermal diffusion," *Nonlinear Analysis: Modelling and Control*, **11**(4), 331-343 (2006). <https://doi.org/10.15388/NA.2006.11.4.14737>
- [3] M.M. Alam, and M.A. Sattar, "Transient MHD heat and mass transfer flow with thermal diffusion in a rotating system," *Journal of Energy, Heat and Mass Transfer*, **21**(1), 9-21 (1999).
- [4] U.N. Das, R.K. Deka, and V.M. Soundalgekar, "Radiation effects on flow past an impulsively started vertical infinite plate," *J. theo. Mech*, **1**, 111-115 (1996).
- [5] M.A. Hossain, and H.S. Takhar, "Radiation effect on mixed convection along a vertical plate with uniform surface temperature," *Heat and Mass transfer*, **31**(4), 243-248 (1996). <https://doi.org/10.1007/BF02328616>
- [6] J.H.A.B. Kumar, and A.K. Singh, "Soret effects on free-convection and mass transfer flow in the stokes problem for a infinite vertical plate," *Astrophysics and Space Science*, **173**, 251-255 (1990). <https://doi.org/10.1007/BF00643934>
- [7] N.G. Kafoussias, "MHD thermal-diffusion effects on free-convective and mass-transfer flow over an infinite vertical moving plate," *Astrophysics and space science*, **192**, 11-19 (1992). <http://dx.doi.org/10.1007/BF00653255>
- [8] M. Kumari, and G. Nath, "Development of two-dimensional boundary layer with an applied magnetic field due to an impulsive motion," *Indian Journal of pure and applied mathematics*, **30**(7), 695-708 (1999).
- [9] R. Muthucumaraswamy, and B. Janakiraman, "MHD and radiation effects on moving isothermal vertical plate with variable mass diffusion," *Theoretical and Applied Mechanics*, **33**(1), 17-29 (2006). <https://doi.org/10.2298/TAM0601017M>
- [10] A. Raptis, and C. Perdikis, "Radiation and free convection flow past a moving plate," *Applied Mechanics and Engineering*, **4**(4), 817-821 (1999).
- [11] V.M. Soundalgekar, S.K. Gupta, and N.S. Birajdar, "Effects of mass transfer and free convection currents on MHD Stokes' problem for a vertical plate," *Nuclear Engineering and Design*, **53**(3), 339-346 (1979). [https://doi.org/10.1016/0029-5493\(79\)90060-8](https://doi.org/10.1016/0029-5493(79)90060-8)
- [12] V.M. Soundalgekar, M.R. Patil, and M.D. Jahagirdar, "MHD Stokes problem for a vertical infinite plate with variable temperature," *Nuclear Engineering and design*, **64**(1), 39-42 (1981). [https://doi.org/10.1016/0029-5493\(81\)90030-3](https://doi.org/10.1016/0029-5493(81)90030-3)
- [13] V. Rajesh, and S.V.K. Varma, "Thermal diffusion and radiation effects on MHD flow past an infinite vertical plate with variable temperature and mass diffusion," *JP Journal of Heat and Mass Transfer*, **3**(1), 41-57 (2009).
- [14] A.V. Kumar, Y.R. Goud, S.V.K. Varma, and K. Raghunath, "Thermal diffusion and radiation effects on unsteady MHD flow through porous medium with variable temperature and mass diffusion in the presence of heat source/sink," *Acta Technica Corviniensis-Bulletin of Engineering*, **6**(2), 79 (2013). <https://acta.fih.upt.ro/pdf/2013-2/ACTA-2013-2-12.pdf>

- [15] F. Ali, I. Khan, S. Shafie, and N. Musthapa, "Heat and mass transfer with free convection MHD flow past a vertical plate embedded in a porous medium," *Mathematical Problems in Engineering*, **2013**, 346281 (2013). <https://doi.org/10.1155/2013/346281>
- [16] M. Venkateswarlu, G.R. Reddy, and D.V. Lakshmi, "Thermal diffusion and radiation effects on unsteady MHD free convection heat and mass transfer flow past a linearly accelerated vertical porous plate with variable temperature and mass diffusion," *J. Korean Soc. Ind. Appl. Math.*, **18**(3), 257-268 (2014). <https://doi.org/10.12941/jksiam.2014.18.257>
- [17] E.M. Sparrow, and R.D. Cess, *Radiation Heat Transfer, Hemisphere*, (Washington, Augmented edition, 1978)
- [18] R.S. Nath, and R.K. Deka, (2023). The Effects of Thermal Stratification on Flow Past an Infinite Vertical Plate in Presence of Chemical Reaction. *East European Journal of Physics*, (3), 223-232. <https://doi.org/10.26565/2312-4334-2023-3-19>
- [19] N. Kalita, R.K. Deka, and R.S. Nath, "Unsteady Flow Past an Accelerated Vertical Plate with Variable Temperature in Presence of Thermal Stratification and Chemical Reaction." *East European Journal of Physics*, (3), 441-450. <https://doi.org/10.26565/2312-4334-2023-3-49>
- [20] H. Kumar, and R.K. Deka. "Thermal and Mass Stratification Effects on Unsteady Flow Past an Accelerated Infinite Vertical Plate With Variable Temperature and Exponential Mass Diffusion in Porous Medium". *East European Journal of Physics*, 4, 87-97 (2023), <https://doi:10.26565/2312-4334-2023-4-09>

**ТЕПЛО- ТА МАСОПЕРЕНОС ПРИ РУХУ ПОТОКУ ПОВЗ ПРИСКОРЕНУ ПЛАСТИНУ
ЧЕРЕЗ ПОРИСТЕ СЕРЕДОВИЩЕ ЗІ ЗМІННОЮ ТЕМПЕРАТУРОЮ ТА
МАСОДИФУЗИЄЮ ЗА НАЯВНОСТІ ДЖЕРЕЛА/ПОГЛИНАЧА ТЕПЛА
Ракеш Рабха, Рудра Канга Дека**

Факультет математики, Університет Гаухаті, Гувахаті-781014, Ассам

Представлено дослідження впливу як тепло- та масообміну на нестационарний МГД-потік через прискорену пластину зі змінною температури та дифузії маси у вигляді джерела (або поглиначка) тепла через пористе середовище. Спочатку температура та концентрація рідини та пластини вважаються однаковими при $t' \leq 0$. При $t' > 0$ до пластини прикладається імпульсне рівномірне прискорення A у вертикальному напрямку вгору. Безрозмірні керівні рівняння, що визначають проблему потоку, вирішуються за допомогою перетворення Лапласа. Вплив різних фізичних величин, пов'язаних із швидкістю, концентрацією, температурою, швидкістю теплопередачі, а також швидкістю масообміну, досліджується за допомогою графіків і таблиць і обговорюється.

Ключові слова: *теплопередача; масообмін; прискорена пластинка; пористе середовище; перетворення Лапласа*

La_{0.8}Bi_{0.2}FeO₃ PEROVSKITE-TYPE: HIGH-PERFORMANCE OF PHOTOCATALYTIC DEGRADATION OF ORTHO-TOLUIDINE BLUE UNDER VISIBLE LIGHT IRRADIATION

Ouarda Ben Ali^a, Mohammed Sadok Mahboub^{a*}, Soria Zeroual^a, Samir Bayou^b,
Azzeddine Beggas^a, Mebrouk Ghougali^a, Adel Benarfa^c, Souhaila Meneceur^d

^a LEVRES Laboratory, University of El Oued, 39000 El Oued, Algeria

^b Chemistry department, Faculty of Exact Sciences, University of El Oued, 39000 El Oued, Algeria

^c Centre de Recherche Scientifique et Technique en Analyses Physico-Chimiques (CRAPC)-PTAPC,
P.O. Box 0354, Laghouat 03000, Algeria

^d Laboratory of Biotechnology biomaterial and condensed matter, Faculty of Technology, University of El Oued,
El-Oued 39000, Algeria

*Corresponding author e-mail: mahboub-mohammedsadok@univ-eloued.dz

Received January 5, 2024; revised February 5, 2024; accepted February 17, 2024

In this study, La_{1-x}Bi_xFeO₃ (x=0.0, 0.2, 0.4, and 0.6) perovskite nanoparticles were synthesized by a modified Pechini method. Rigorous analysis through XRD and SEM/EDX confirmed the absence of secondary phases in both pure and Bi-substituted LaFeO₃ samples, indicating the formation of a single-phase perovskite. SEM images revealed the quasi-spherical shape of the particles. The photocatalytic activity of La_{1-x}Bi_xFeO₃ (x=0.0, 0.2, 0.4, and 0.6) was evaluated by the degradation of ortho-Toluidine Blue under visible light irradiation, indicating that La_{0.8}Bi_{0.2}FeO₃ exhibited excellent photocatalytic activity. The overall removal rate of o-Toluidine Blue reached 90.09% after visible light irradiation lasting for 60 min. We attribute this heightened photocatalytic activity to the grain size and optical properties of prepared sample. Consequently, the La_{0.8}Bi_{0.2}FeO₃ can be considered as a very promising photocatalyst in future industrial application to treat effectively wastewater of dyes.

Keywords: La_{1-x}Bi_xFeO₃; Ortho-Toluidine Blue dye; Modified Pechini method; Visible-light photocatalysis; Wastewater treatment

PACS: 81.20.Ka, 81.16.Hc, 89.60.-k

INTRODUCTION

The rapid expansion of urbanization and industrialization, coupled with soaring global population growth, has significantly exacerbated the issue of water pollution [1]. Approximately 1.2 billion people worldwide, particularly in developing nations, grapple with the alarming consequences of water contamination, which extend far beyond environmental degradation [2]. Water pollutants pose a grave threat to human health, contributing to respiratory disorders, dermatitis, asthma, mutagenicity, and even cancer and other diseases [2-7]. This dire scenario underscores the need for innovative and effective wastewater treatment technologies. Dye wastewater is one of the most difficult degradable industrial wastewater, due to its variety, complicated organic composition and poor biochemical degradability, even including toxic ingredients which can weaken the microbial mineralization of organic pollutants and lead to the destruction of water ecological system [8]. Effective wastewater treatment plays a pivotal role in safeguarding public health and the environment. This vital process involves the removal of contaminants and pollutants from wastewater, rendering it suitable for safe discharge into the ecosystem or potential reuse. However, the complexity and scale of this challenge have prompted the exploration of innovative, sustainable solutions [9].

In recent years, photocatalytic technologies have emerged as promising strategies for advanced wastewater treatment [10-12]. These methods harnesses the power of photocatalysts, typically semiconducting materials, to accelerate the degradation of both organic and inorganic pollutants when exposed to light irradiation. Semiconductor photocatalysis, in particular, has attracted considerable attention due to its cost-effectiveness, non-toxicity, high chemical and thermal stability, and eco-friendly nature [13,14]. Traditional semiconductor photocatalysts, like TiO₂ [15, 16], ZnO [15, 17], and SnO₂ [18], have been extensively employed in photocatalysis due to their affordability, stability, and low environmental impact. However, their limited ability to utilize solar energy, primarily in the UV range, has driven the exploration of narrow band gap semiconductors, which can absorb a broader spectrum of solar radiation, especially in the visible light region [19].

Perovskite materials, have emerged as a compelling class of narrow band gap semiconductors for photocatalytic applications [20]. Their unique structural characteristics and synthesis processes significantly influence their photocatalytic efficiency, making them versatile for diverse applications, including gas sensing [21], water splitting [22], and the photocatalytic degradation of organic pollutants [23, 24]. Among the narrow band gap semiconductors, LaFeO₃ stands out as a promising photocatalyst, with several studies emphasizing its synthesis and efficacy in the photodegradation of organic dyes under visible light irradiation [25-28]. LaFeO₃, with a narrow band gap of only 2.0 eV, exhibits exceptional potential for utilizing visible light from the solar spectrum, rendering it highly suitable for

photocatalysis under sunlight [29]. Its outstanding photocatalytic properties have propelled LaFeO₃ into the spotlight, attracting attention for its applications in water treatment.

The catalytic performance of LaFeO₃ perovskite in wastewater dye removal processes has been investigated. Thirumalairajan et al. [30] studied the catalytic activity of the LaFeO₃ microsphere to degrade Rhodamine B (RhB), whereas Deng et al. [31] studied its adsorption behaviour for RhB. On another hand, Mocwana et al. [32] studied the activity of the lanthanum ferrite using the photocatalytic degradation of ortho-toluidine blue (o-TB) under visible light. To further enhance the photocatalytic performance of LaFeO₃, modification strategies, such as doping with various elements, have been widely explored [33]. In this context, Cu-doped LaFeO₃ catalysts have demonstrated remarkable efficiency in the decolorization of both cationic and anionic dyes under visible light irradiation [34]. Also, experiments of radical trapping in Sr-doped porous LaFeO₃ samples reveal that •OH species are dominant intermediate oxidants involved in the oxidation of 2,4-DCP and RhB over the optimized sample [35].

The visible light-driven degradation of o-Toluidine Blue (o-TB) will be the focus of this investigation, shedding light on the potential of Bi-substituted LaFeO₃ perovskite photocatalysis in addressing these pressing challenges. Photocatalysis can be used to degrade or break down certain organic compounds, including dyes like o-TB, that may be present in water and contribute to water pollution. The effect of photocatalysis on o-TB as a water dye may result in the degradation of the dye molecules, reducing its concentration in the water. This process can be effective in treating water contaminated with certain organic dyes, which are common pollutants in industrial wastewater. In this study, the structural, morphological, optical evaluation and photocatalytic performance of a series of La_{1-x}Bi_xFeO₃ (x=0.0, 0.2, 0.4, and 0.6) would be emphatically discussed.

EXPERIMENTAL

Material Preparation

The technique of modified Pechini method was employed for the synthesis of Bismuth-doped Lanthanum ferrite La_{1-x}Bi_xFeO₃. Specifically, precise amounts of Lanthanum nitrate (La(NO₃)₃·6H₂O, Sigma-Aldrich, ≥99.0%), Bismuth nitrate (Bi(NO₃)₃·5H₂O, Sigma-Aldrich, ≥98.0%), and Ferric nitrate (Fe(NO₃)₃·9H₂O, Sigma-Aldrich, ≥98.0%) were utilized as initial reagents to produce La_{1-x}Bi_xFeO₃ (x = 0, 0.2, 0.4, and 0.6). The raw materials were dissolved in 100 ml of double-distilled water to create a transparent solution, which was then evaporated at 60 °C while being continuously stirred using a magnetic stirrer. Additionally, nitric acid was incrementally introduced during the stirring process to regulate the pH. The solution was then supplemented with citric acid (Sigma-Aldrich, ≥98.0%), Ethylene Diamine Tetra Acetic acid (EDTA, Sigma-Aldrich, ≥98.0%), and ethylene glycol (Sigma-Aldrich, ≥98.0%), as well as other chemicals to create a brown precursor solution. The solution is then heated to 120 °C (10 °C/min) until it solidifies into a dry gel. The gel then turns into a puff as the temperature rises to 350 °C. The resulting puff was dried for 10 hours at 110 °C to produce a dark brown powder, and the soft powders were then calcined for 12 hours at 600 °C with a 5 °C/min rate. The light brown powder was then heated for 24 hours at 800 °C in the air using a tubular furnace (R 50/500/13 Nabertherm model). To obtain the phase, this operation is repeated twice (Fig. 1).

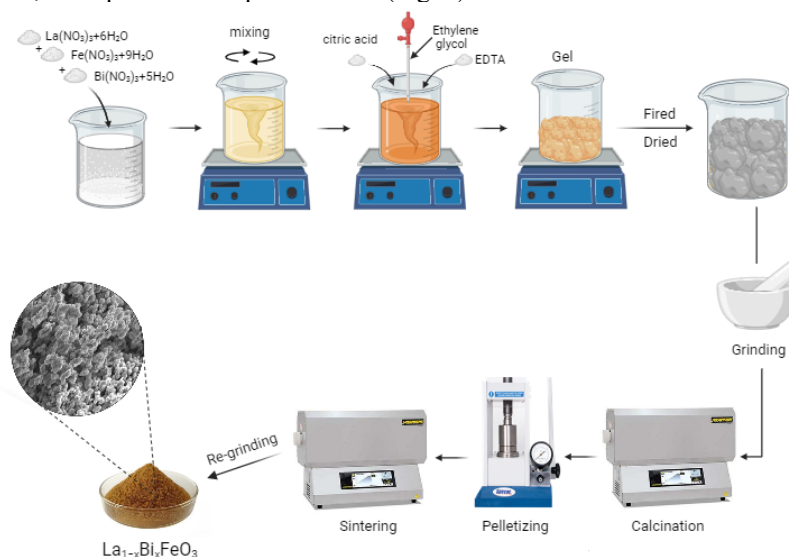


Figure 1. Schematic representation of the elementary steps of La_{1-x}Bi_xFeO₃ (x = 0.0, 0.2, 0.4, 0.6) perovskite preparation using the modified Pechini method

Material Characterization

Phase identification and unit cell parameter determination were checked using powder X-ray diffraction (XRD) at room temperature. Powder X-ray diffraction (PXRD) patterns were recorded on a Proto AXRD Benchtop diffractometer in Bragg-Brentano θ -2 θ -geometry with CuK α radiation ($\lambda=1.5418$ Å) operating at 30 kV and 20 mA. Regarding the

examination of the synthesized samples, their morphology was investigated utilizing a Thermo Scientific Quattro ESEM scanning electron microscope. Simultaneously, the compositions were analyzed using energy dispersive X-ray (EDX) spectroscopy, employing a Zeiss SmartEDX detector integrated into the Zeiss Evo15 Scanning Electron Microscope (SEM). This setup is designed for observing dry and conducting samples. In addition, Fourier transform infrared (FTIR) spectra were recorded in the range of 2000-450 cm^{-1} using an IR Spirit - Shimadzu Fourier transform infrared (FTIR) spectrometer. The as-synthesized powders were also analyzed using a Shimadzu UV-visible spectrometer, specifically the Shimadzu UV-1900.

Photocatalytic Activity

In this study, we investigate the photocatalytic degradation of o-TB in the presence of $\text{La}_{1-x}\text{Bi}_x\text{FeO}_3$ ($x = 0.0, 0.2, 0.4, 0.6$). The experimental work begins by adding 5 mg of the catalyst to a 5 ml o-TB solution. The prepared solution is made using distilled water at a concentration of $4 \times 10^{-5} \text{ mol/L}$. Following this, the solution is exposed to sunlight for varying durations (10, 20, 30, and 60 min) at room temperature and a neutral pH. On the other hand, the catalyst is separated through centrifugation, and a spectrophotometer (Shimadzu 1900 model) is used to detect absorbance values at 629 nm. Furthermore, the calculation method for degradation efficiency is presented in the following equation:

$$\text{degradation}(\%) = \frac{(C_0 - C_t)}{C_0} \times 100. \quad (1)$$

Where C_0 is the concentration of o-TB solution at the reaction's beginning and C_t its concentration of pollutants at time t .

RESULTS AND DISCUSSION

Structural, Morphological and Elemental Analysis

In Fig. 2, the X-Ray Powder Diffraction patterns of the pure and Bi^{3+} -substituted LaFeO_3 samples are displayed.

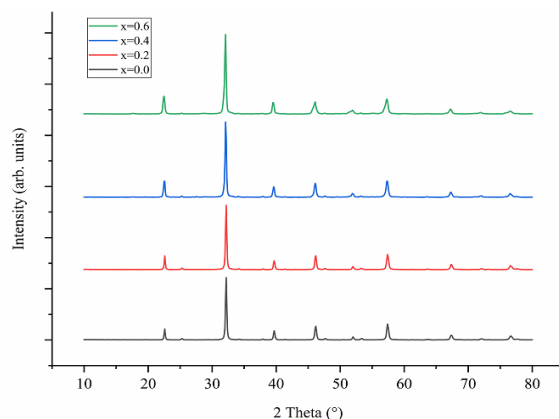


Figure 2. X-Ray powder diffraction pattern of $\text{La}_{1-x}\text{Bi}_x\text{FeO}_3$ (a) $x=0.0$, (b) $x=0.2$ (c) $x=0.4$ and (d) $x=0.6$

The Rietveld refinement method [36] has been used for structural analysis, and using the ReX is a powder diffraction software [37]. On the orthorhombic Pbnm ($N^\circ 62$) space group, it is possible to refine all of the peaks of $\text{La}_{1-x}\text{Bi}_x\text{FeO}_3$ ($x = 0.0, 0.2, 0.4, \text{ and } 0.6$) samples. The calculated lattice parameters, unit cell volume, refinement factors are summarized in Table 1, and the final Rietveld refinement plot is presented in Fig. 3.

Table 1. Crystallographic parameters of $\text{La}_{1-x}\text{Bi}_x\text{FeO}_3$ samples as obtained from Rietveld refinement

Samples	$x=0.0$	$x=0.2$	$x=0.4$	$x=0.6$
Lattice parameters (\AA):				
a	5.5561	5.5513	5.5577	5.5522
b	5.5679	5.5695	5.5788	5.5905
c	7.8428	7.8542	7.8438	7.8395
Unit cell volume (\AA^3):				
V	242.62	242.84	243.20	243.33
Fit goodness:				
R_p (%)	11.42	7.49	12.84	14.28
R_{wp} (%)	17.39	12.81	17.96	20.40

The absence of a second phase in the doped samples shows that the Bi^{3+} ions have completely dissolved into the host lattice by taking the place of the La^{3+} . The $\text{La}_{1-x}\text{Bi}_x\text{FeO}_3$ ($0 \leq x \leq 0.6$) unit cell volume is constant in the range of the error standard deviation (e.s.d.) with the addition of Bi. This result is due to the very close radius of Bi^{3+} ion ($r(\text{Bi}^{3+}) = 1.17 \text{ \AA}$) compared to the La^{3+} ion ($r(\text{La}^{3+}) = 1.16 \text{ \AA}$) [38], which is evident from the XRD peak's slight shift towards a higher 2θ value in Fig. 3.

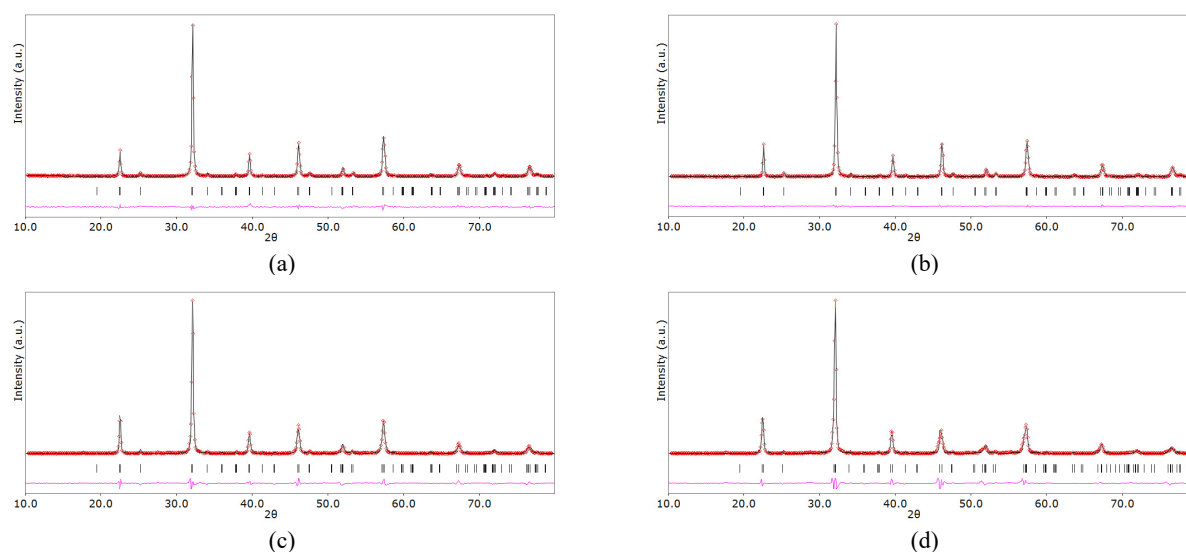


Figure 3. Rietveld refinement of experimental XRD pattern of La_{1-x}Bi_xFeO₃ samples (a) x=0.0, (b) x=0.2, (c) x=0.4 and (d) x=0.6 refined at room temperature

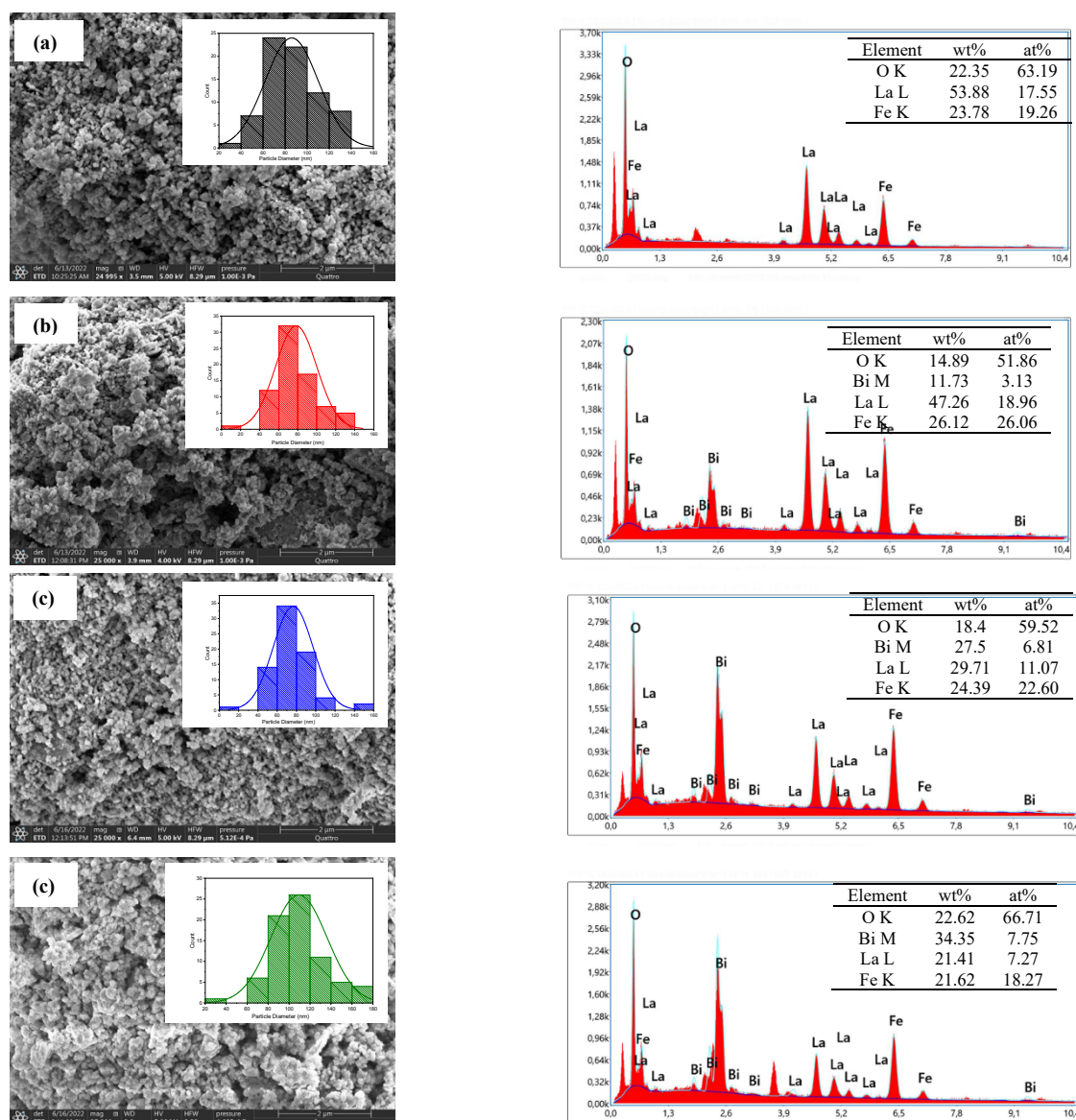


Figure 4. SEM morphology and EDX spectra of La_{1-x}Bi_xFeO₃ samples (a) x=0.0, (b) x=0.2, (c) x=0.4 and (d) x=0.6

Using spot measurements on powder samples, energy dispersive x-ray (EDX) spectroscopy was used to determine the quantitative composition of pure and Bi³⁺-substituted LaFeO₃ nanoparticles. Within the limit of experimental error, the EDX analysis shows consistency with the predicted stoichiometry. The EDX spectrum confirms the desired samples (Fig. 4). Also, scanning electron microscopy (SEM) was utilized to examine the surface morphology of the prepared samples. As illustrated in Figure 4, the morphology of the studied samples shows a spherical shape of grains, similar to that of sand grains.

Both the dispersion and morphology of grains remained largely unchanged despite doping samples with Bi³⁺ ions. However, as the concentration of Bi substitution increased, agglomerated spherical particles began to form and grew in size.

FTIR Analysis

Figure 5 displays the FTIR spectra of pure and Bi-substituted LaFeO₃ in the range of [2000–450] cm⁻¹. It is important to note that the respective spectral ratios are almost similar from one to another, differing primarily in peak intensity. This difference can be attributed to variations in molar concentration composition. The strong absorption band at approximately 536 cm⁻¹ can be attributed to the (Fe-O) bending vibration characteristics of the octahedral FeO₆ groups in La_{1-x}Bi_xFeO₃. Additionally, the bands between 700 and 400 cm⁻¹ are mainly attributed to the formation of metal oxides [39].

On the other hand, the bending vibration of the La-O bonds may be responsible for the bands 717 cm⁻¹ [23]. Additionally, we observe that there are two closely bands, the first of which is at 1385 cm⁻¹ and the second at 1485 cm⁻¹. They are attributed to NO₃⁻ and N-H respectively, and both come from reacted precursor raw materials; they are neighbors and weak [40].

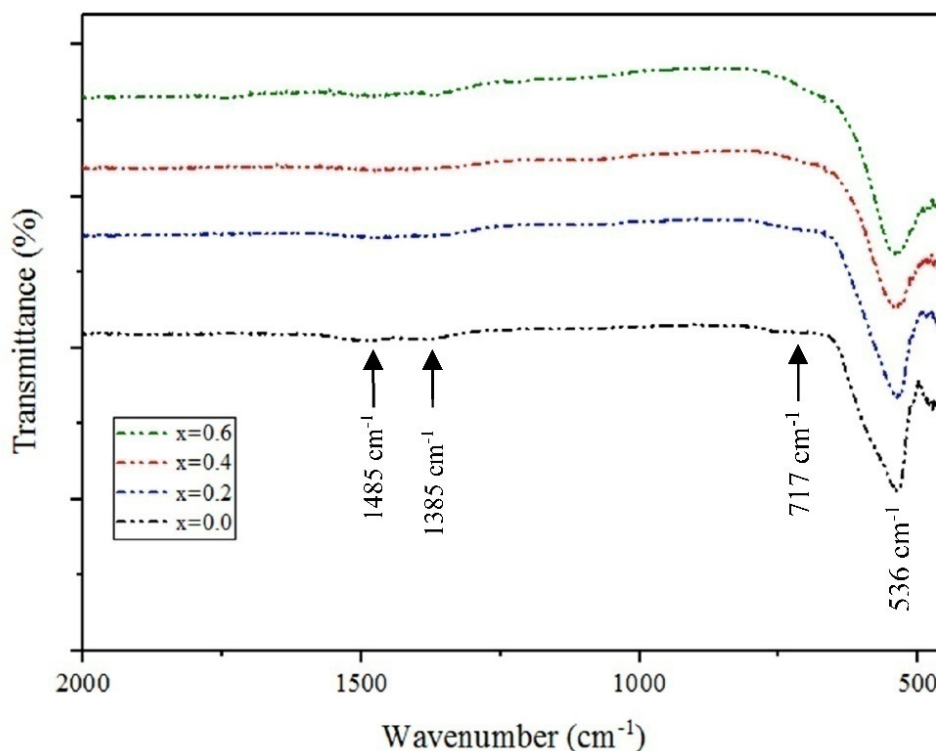


Figure 5. FTIR spectra of La_{1-x}Bi_xFeO₃ (x=0.0, 0.2, 0.4 and 0.6) nanoparticles

The La/Fe-O bending vibration modes do not change in frequency with increasing Bi content up to x=0.6, confirming that there has been no lattice deformation and, consequently, no changes in the length of the La/Fe-O bond, as supported by the XRD analysis.

Optical Study

In order to describe the optical properties of the La_{1-x}Bi_xFeO₃ (x=0.0, 0.2, 0.4 and 0.6) nanoparticles, UV-Visible spectroscopy is used. From Tauc's plot, the bandgaps of the prepared samples were taken. Tauc's equation [41] mentioned below in eqt. 2 can be used to calculate the relationship between absorption coefficient (α) and incident photon energy ($h\nu$).

$$(\alpha h\nu)^2 = A(h\nu - E_g) \quad (2)$$

where α is the optical absorption coefficient, $h\nu$ is the photon energy, E_g is the direct band gap, and A is constant.

E_g for direct transitions is obtained by extrapolating the linear parts of the curves toward absorption equal to zero (Fig. 6). Pure LaFeO₃ is thought to have a direct band gap of 2.2 eV. However, E_g values decrease to 1.86, 1.76, and 1.54 eV, respectively, for Bi substitutions of 20, 40, and 60%.

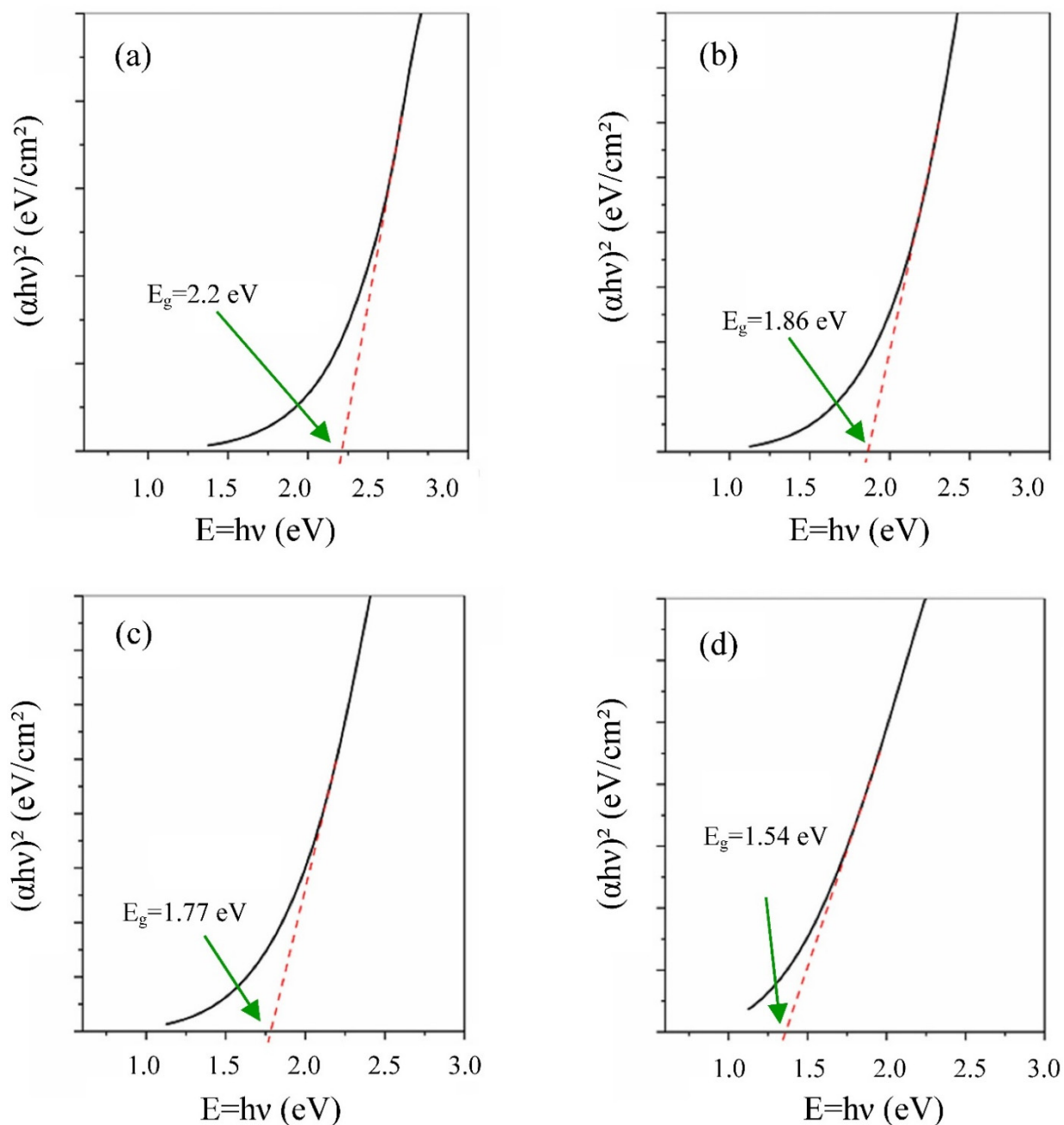


Figure 6. Tauc plots for optical absorption curves of La_{1-x}Bi_xFeO₃ samples (a) $x=0.0$, (b) $x=0.2$, (c) $x=0.4$, and (d) $x=0.6$.

Furthermore, the value of E_g can be decreased through Fe–O octahedral restructuring of molecular orbitals and nanoparticles length scale [42–44]. This reduction could also be attributed to the direct energy transfer occurring between the excited states of the semiconductor and the 3d levels of Bi³⁺ ions [45].

Evaluation of the Photocatalytic Efficiency

The photocatalytic degradation of O-toluidine blue (o-TB) was examined using La_{1-x}Bi_xFeO₃ ($x = 0.0, 0.2, 0.4, 0.6$) under the influence of solar irradiation. The results show that most of the o-TB dye is removed within 60 minutes (Fig. 7).

Table 2 shows that the photocatalytic activity of La_{1-x}Bi_xFeO₃ ($x = 0.0, 0.2, 0.4$ and 0.6) samples decreases with an increase in their average grain size. This can be attributed to the fact that smaller particle size with a larger surface area per unit volume provide more active sites for photocatalytic reactions, leading to a higher photocatalytic degradation rate, especially in the case of spherical nanoparticles with smaller particle sizes [46–48]. This principle applies to the spherical shape of the grain morphology in the studied samples.

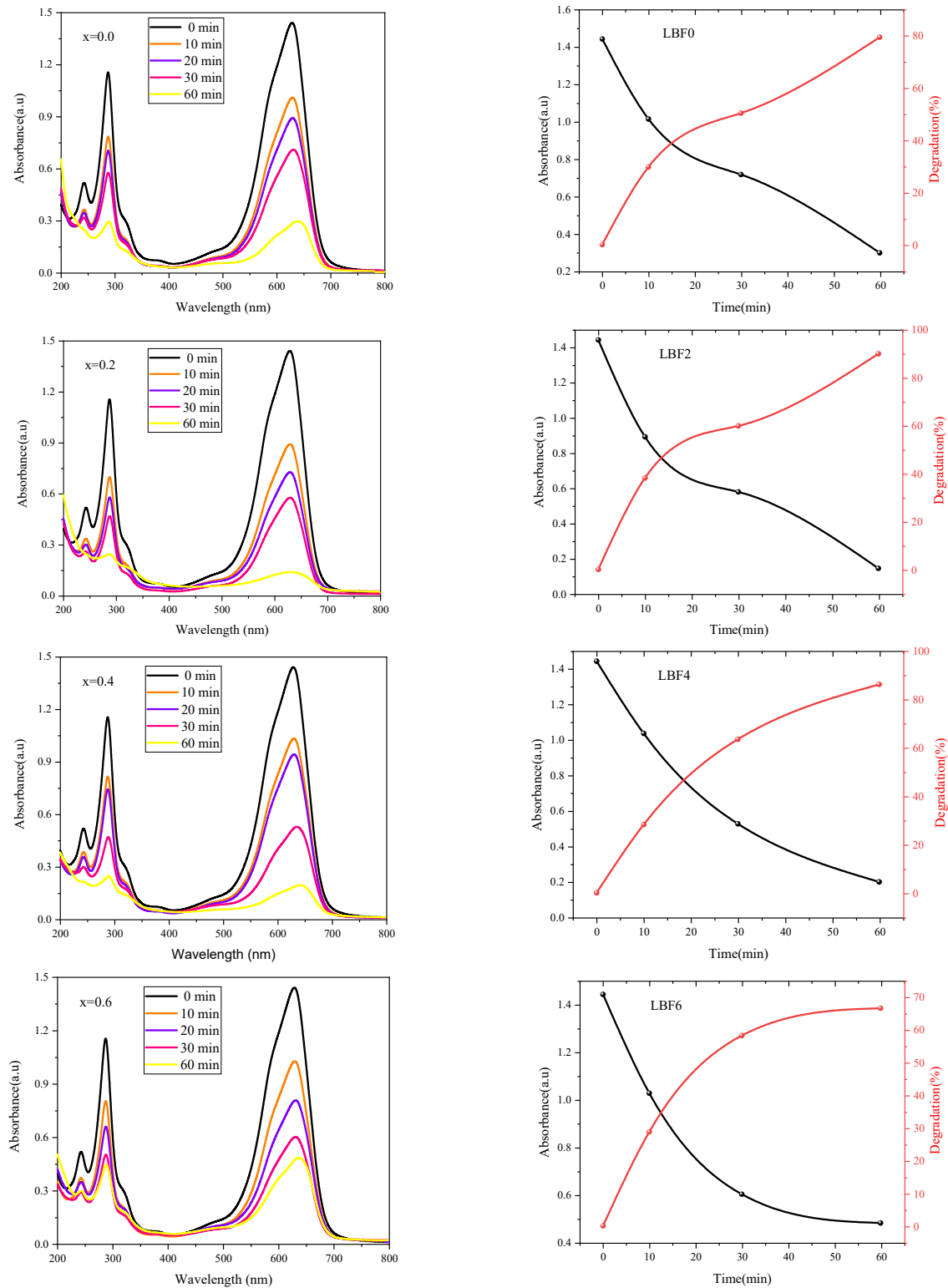


Figure 7. UV-Vis time-dependent absorption spectrum during the photocatalytic reaction of o-TB for $\text{La}_{1-x}\text{Bi}_x\text{FeO}_3$ ($x = 0.0, 0.2, 0.4$ and 0.6) samples

Table 2. Photocatalytic activity vs. Average particle size for $\text{La}_{1-x}\text{Bi}_x\text{FeO}_3$ ($x = 0.0, 0.2, 0.4$ and 0.6) samples.

Catalyst	Photocatalytic activity (%)	Average particle size (nm)
LaFeO_3	79.50	85
$\text{La}_{0.8}\text{Bi}_{0.2}\text{FeO}_3$	90.09	76
$\text{La}_{0.6}\text{Bi}_{0.4}\text{FeO}_3$	86.28	78
$\text{La}_{0.4}\text{Bi}_{0.6}\text{FeO}_3$	66.68	108

The highest photocatalytic activity (90.09%) was observed for La_{0.8}Bi_{0.2}FeO₃, which has the smallest average grain size (76 nm). Additionally, the photocatalytic activity of La_{0.6}Bi_{0.4}FeO₃ (78 nm) was slightly lower (86.28%), but still higher than that of LaFeO₃ (79.50%) and La_{0.4}Bi_{0.6}FeO₃, which exhibited a rate of 66.68% (Fig. 7). Therefore, these results support the notion that the average grain size and the shape of grains are an important factor in determining the photocatalytic activity of La_{1-x}Bi_xFeO₃.

In contrast, data obtained by Mocwana et al. [32] indicate that the optimal degradation rates for o-TB, using LaFeO₃ nanosheets, resulted in a catalytic degradation of 37% over 30 minutes. Notably, this rate remains lower than all the values obtained in our experiments for the same duration.

Furthermore, it was observed that an increase in the amount of Bi up to 20% within 60 minutes of the reaction time significantly enhances removal efficiency. This improvement can be attributed to the increased formation of hydroxyl radicals.

Conversely, a further increase in the Bi ratio decreases the removal efficiency of the o-TB dye. This can be attributed to (i) the increase in the average grain sizes, and (ii) the blocking of UV light penetration with an increasing amount of Bi [49, 50].

This can be interpreted as when the catalyst load is small, the catalyst absorbs fewer photons for the photocatalytic reaction, resulting in lower photocatalytic activity. As the catalyst loading increases, the number of photon absorption centers and activity centers on the catalyst surface increases, thereby increasing the catalyst's activity. However, with further increases in catalyst loading, the number of photons tends to become saturated. This heightened catalyst loading may lead to light blockage, consequently affecting the photocatalytic efficiency [51]. Thus, the narrow band gap value of La_{0.8}Bi_{0.2}FeO₃ (1.86 eV) nanoparticle suggests its potential as a promising candidate for the excellent purification of wastewater containing o-TB dye.

CONCLUSIONS

In conclusion, the perovskite-type La_{1-x}Bi_xFeO₃ photocatalysts was successfully synthesized using the modified Pechini route, and their performance for photodegradation of o-TB dye wastewater was studied. XRD and EDX combination studies proved that all samples have an orthorhombic structure with a single-crystalline orthorhombic structure, and the average grain size samples increased by increasing of Bi-substitution to be 85 nm, 76 nm, 78 nm, and 108 nm for x=0.0, 0.2, 0.4, and 0.6 respectively. Morphological and optical properties of the perovskite-type La_{1-x}Bi_xFeO₃ samples exhibited a well-crystalline form and excellent band gap energy respectively. A photocatalytic reaction was conducted to test the degradation ability of the synthesized samples towards o-TB dye. The reaction was monitored over a period of 60 min while using the UV-Vis to observe the degradation activity. The most photocatalytically active sample for decomposition of o-TB under visible light was La_{0.8}Bi_{0.2}FeO₃. This nanoparticle acts as an excellent photocatalyst for the degradation of o-TB dye with 90.09% efficiency in 60 min under natural sunlight irradiation. This sample have the smallest average grain size and a band gap energy in the range of semiconductor materials. These results give hope for future application of this material in photocatalytic degradation of various organic pollutants present in polluted water under natural sunlight. Hence, this nanoparticle may be well exploited for the remediation of the polluted water under natural sunlight on a large scale.

Acknowledgements

The authors gratefully acknowledge the financial support of Directorate General for Scientific Research and Technological Development –DGRSDT– (PRFU Project N°. B00L02UN390120180003), Ministry of Higher Education and Scientific Research – ALGERIA.

ORCID

- Mohammed Sadok Mahboub, <https://orcid.org/0000-0001-5495-5249>; • Soria Zeroual, <https://orcid.org/0000-0002-5922-9980>
- Samir Bayou, <https://orcid.org/0000-0001-8553-3428>; • Mebrouk Ghougali, <https://orcid.org/0000-0003-0496-4555>
- Adel Benarfa, <https://orcid.org/0000-0002-0377-0161>; • Souhaila Meneceur, <https://orcid.org/0000-0002-6890-3762>

REFERENCES

- [1] M. Strokhal, Z. Bai, W. Franssen, et al., "Urbanization: an increasing source of multiple pollutants to rivers in the 21st century," *NPJ Urban Sustain*, **1**, 24 (2021). <https://doi.org/10.1038/s42949-021-00026-w>
- [2] Z.N. Garba, W. Zhou, M. Zhang, and Z. Yuan, "A review on the preparation, characterization and potential application of perovskites as adsorbents for wastewater treatment," *Chemosphere*, **244**, 125474 (2020). <https://doi.org/10.1016/j.chemosphere.2019.125474>
- [3] L. Lin, H. Yang, and X. Xu, "Effects of Water Pollution on Human Health and Disease Heterogeneity: A Review," *Front. Environ. Sci.* **10**, 880246 (2022). <https://doi.org/10.3389/fenvs.2022.880246>
- [4] A. Zhitkovich, "Chromium in Drinking Water: Sources, Metabolism, and Cancer Risks," *Chem. Res. Toxicol.*, **24**(10), 1617–1629 (2011). <https://doi.org/10.1021/tx200251t>
- [5] S.K. Gupta, R.C. Gupta, A.B. Gupta, A.K. Seth, J.K. Bassin, and A. Gupta, "Recurrent acute respiratory tract infections in areas with high nitrate concentrations in drinking water," *Environmental health perspectives*, **108**(4), 363–366 (2000). <https://doi.org/10.1289/ehp.00108363>
- [6] C.L. Gray, D.T. Lobdell, K.M. Rappazzo, Y. Jian, J.S. Jagai, L.C. Messer, A.P. Patel, et al., "Associations between environmental quality and adult asthma prevalence in medical claims data," *Environ Res.*, **166**, 529–536 (2018). <https://doi.org/10.1016/j.envres.2018.06.020>

- [7] S.T. Matsumoto, M.S. Mantovani, M.I.A. Malagutti, A.L. Dias, I.C. Fonseca, and M.A. Marin-Morales, "Genotoxicity and mutagenicity of water contaminated with tannery effluents, as evaluated by the micronucleus test and comet assay using the fish *Oreochromis niloticus* and chromosome aberrations in onion root-tips," *Genetics and Molecular Biology*, **29**(1), 148–158 (2006). <https://doi.org/10.1590/S1415-47572006000100028>
- [8] J.H. Wang, J. Qiao, J.L. Tu, and X.-H. Huang, "Research Progress on Photocatalytic Degradation of Dye by Perovskite-type Metal Oxides (In Chinese)," *Rare Metals and Cemented Carbides*, **41**(1), 50–54 (2013).
- [9] J.A. Silva, "Wastewater Treatment and Reuse for Sustainable Water Resources Management: A Systematic Literature Review," *Sustainability*, **15**(14), 10940 (2023). <https://doi.org/10.3390/su151410940>
- [10] S.K. Loeb, P.J.J. Alvarez, J.A. Brame, E.L. Cates, W. Choi, J. Crittenden, D.D. Dionysiou, et al., "The Technology Horizon for Photocatalytic Water Treatment: Sunrise or Sunset?" *Environ. Sci. Technol.*, **53**(6), 2937–2947 (2019). <https://doi.org/10.1021/acs.est.8b05041>
- [11] M.N. Chong, B. Jin, C.W.K. Chow, and C. Saint, "Recent developments in photocatalytic water treatment technology: A review," *Water Research*, **44**(10), 2997–3027 (2010). <https://doi.org/10.1016/j.watres.2010.02.039>
- [12] J. Blanco-Galvez, P. Fernández-Ibáñez, and S. Malato-Rodríguez, "Solar photocatalytic detoxification and disinfection of water: recent overview," *J. Sol. Energy Eng.*, **129**(1), 4–15 (2007). <https://doi.org/10.1115/1.2390948>
- [13] S.D. Khairnar, and V.S. Shrivastava, "Facile Synthesis of Nickel Oxide Nanoparticles for the Degradation of Methylene Blue and Rhodamine B dye: A Comparative Study," *J. Taibah. Univ. Sci.*, **13**, 1108–1118 (2019). <https://doi.org/10.1080/16583655.2019.1686248>
- [14] V.A. Adole, T.B. Pawar, P.B. Koli, and B.S. Jagdale, "Exploration of Catalytic Performance of Nano-La₂O₃ as an Efficient Catalyst for Dihydropyrimidinone/Thione Synthesis and gas Sensing," *J. Nanostructure Chem.*, **9**, 61–76 (2019). <https://doi.org/10.1007/s40097-019-0298-5>
- [15] A. Fujishima, and K. Honda, "Electrochemical photolysis of water at a semiconductor electrode," *Nature*, **238**(5358), 37–38 (1972). <https://doi.org/10.1038/238037a0>
- [16] S. Singh, H. Mahalingam, and P.K. Singh, "Polymer-supported Titanium Dioxide Photocatalysts for Environmental Remediation: A Review," *Appl. Catal. A: Gen.*, **462–463**, 178–195 (2013). <https://doi.org/10.1016/j.apcata.2013.04.039>
- [17] R.S. Shinde, S.D. Khairnar, M.R. Patil, V.A. Adole, P.B. Koli, V.V. Deshmane, D.K. Halwar, et al., "Synthesis and Characterization of ZnO/CuO Nanocomposites as an Effective Photocatalyst and gas Sensor for Environmental Remediation," *J. Inorg. Organomet. Polym.*, **32**, 1045–1066, (2022). <https://doi.org/10.1007/s10904-021-02178-9>
- [18] M. Periyasamy, and A. Kar, "Modulating the Properties of SnO₂ Nanocrystals: Morphological Effects on Structural, Photoluminescence, Photocatalytic, Electrochemical and gas Sensing Properties," *J. Mater. Chem. C*, **8**, 4604–4635 (2020). <https://doi.org/10.1039/C9TC06469A>
- [19] C. Xu, P.R. Anusuyadevi, C. Aymonier, R. Luque, and S. Marre, "Nanostructured Materials for Photocatalysis," *Chem. Soc. Rev.*, **48**, 3868–3902 (2019). <https://doi.org/10.1039/C9CS00102F>
- [20] S. Dhariwal, and M. Mittal, "Wastewater treatment with perovskite-based photocatalysts: Environmental sustainability from a green perspective," *Materials Today: Proceedings*, (2023). <https://doi.org/10.1016/j.matpr.2023.03.048>
- [21] N.N. Toan, S. Saukko, and V. Lantto, "Gas sensing with semiconducting perovskite oxide LaFeO₃," *Physica B: Condensed Matter*, **327**(2–4), 279–282 (2003). [https://doi.org/10.1016/S0921-4526\(02\)01764-7](https://doi.org/10.1016/S0921-4526(02)01764-7)
- [22] N.S. Tijare, V.M. Joshi, S.P. Padole, A.P. Manguklar, S.S. Rayalu, and K.N. Labhsetwar, "Photocatalytic hydrogen generation through water splitting on nano-crystalline LaFeO₃ perovskite," *Int. J. Hydrog. Energy*, **37**, 10451–10456 (2012). <https://doi.org/10.1016/j.ijhydene.2012.01.120>
- [23] M. Ismael, and M. Wark, "Perovskite-type LaFeO₃: Photoelectrochemical Properties and Photocatalytic Degradation of Organic Pollutants Under Visible Light Irradiation," *Catalysts*, **9**(4), 342 (2019). <https://doi.org/10.3390/catal9040342>
- [24] L. Li, L. Pan, D. Zhang, and J. Rong, "Ultrasonic-assisted synthesis of LaFeO₃/CeO₂ heterojunction for enhancing the photocatalytic degradation of organic pollutants," *Materials Science in Semiconductor Processing*, **152**, 107058 (2022). <https://doi.org/10.1016/j.mssp.2022.107058>
- [25] X.J. Wang, H.Y. Shen, H.Y. Tian, and Q.H. Yang, "Photocatalytic Degradation of Water-Soluble Azo Dyes by LaFeO₃ and YFeO₃," *Adv. Mater. Res.*, **465**, 37–43 (2012). <https://doi.org/10.4028/www.scientific.net/AMR.465.37>
- [26] L. Hou, G. Sun, K. Liu, Y. Li, and F. Gao, "Preparation, characterization and investigation of catalytic activity of Li-doped LaFeO₃ nanoparticles," *J. Sol-Gel Sci. Technol.*, **40**, 9–14 (2006). <https://doi.org/10.1007/s10971-006-8368-9>
- [27] P. Tang, M. Fu, H. Chen, and F. Cao, "Synthesis of Nanocrystalline LaFeO₃ by Precipitation and its Visible-Light Photocatalytic Activity," *Mater. Sci. Forum*, **694**, 150–154 (2011). <https://doi.org/10.4028/www.scientific.net/MSF.694.150>
- [28] S. Thirumalairajan, K. Girija, R.V. Masteralo, and N. Ponpandian, "Photocatalytic degradation of organic dyes under visible light irradiation by floral-like LaFeO₃ nanostructures comprised of nanosheet petals," *New J. Chem.*, **38**, 5480–5490 (2014). <https://doi.org/10.1039/C4NJ01029A>
- [29] H. Wu, R. Hu, T. Zhou, C. Li, W. Meng, and J. Yang, "A Novel Efficient Boron-Doped LaFeO₃ Photocatalyst with Large Specific Surface Area for Phenol Degradation Under Simulated Sunlight," *CrystEngComm*, **17**, 3859–3865 (2015). <https://doi.org/10.1039/C5CE00288E>
- [30] S. Thirumalairajan, K. Girija, I. Ganesh, D. Mangalaraj, C. Viswanathan, A. Balamurugan, and N. Ponpandian, "Controlled synthesis of perovskite LaFeO₃ microsphere composed of nanoparticles via self-assembly process and their associated photocatalytic activity," *Chem. Eng. J.*, **209**, 420–428 (2012). <https://doi.org/10.1016/j.cej.2012.08.012>
- [31] H. Deng, Z. Mao, H. Xu, L. Zhang, Y. Zhong, and X. Sui, "Synthesis of fibrous LaFeO₃ perovskite oxide for adsorption of Rhodamine B," *Ecotoxicol. Environ. Saf.*, **168**, 35–44 (2019). <https://doi.org/10.1016/j.ecoenv.2018.09.056>
- [32] M.L. Mocwana, P.P. Mokoena, P.S. Mbule, I.N. Beas, G.L. Kabongo, S.N. Ogugua, and T.E. Tshabalala, "Photocatalytic Degradation of Methylene Blue and Ortho-Toluidine Blue: Activity of Lanthanum Composites La_xMO_y (M: Fe, Co, Ni)," *Catalysts*, **12**(11), 1313 (2022). <https://doi.org/10.3390/catal12111313>
- [33] M. Dhiman, and S. Singhal, "Effect of Doping of Different Rare Earth (Europium, Gadolinium, Dysprosium and Neodymium) Metal Ions on Structural, Optical and Photocatalytic Properties of LaFeO₃ Perovskites," *J. Rare. Earth*, **37**, 1279–1287 (2019). <https://doi.org/10.1016/j.jre.2018.12.015>

- [34] T.T.N. Phan, A.N. Nikoloski, P.A. Bahri, and D. Li, "Heterogeneous Photo-Fenton Degradation of Organics Using Highly Efficient Cu-Doped LaFeO₃ Under Visible Light," *J. Indus. Eng. Chem*, **61**, 53–64 (2018). <https://doi.org/10.1016/j.jiec.2017.11.046>
- [35] X.-T. Yin, H. Huang, J.-L. Xie, D. Dastan, J. Li, Y. Liu, X.-M. Tan, X.-C. Gao, W. A. Shah, and X.-G. Ma, "High-performance visible-light active Sr-doped porous LaFeO₃ semiconductor prepared via sol-gel method," *Green Chemistry Letters and Reviews*, **15**(3), 546–556 (2022). <https://doi.org/10.1080/17518253.2022.2112093>
- [36] G. Will, "Powder Diffraction: The Rietveld Method and the Two Stage Method to Determine and Refine Crystal Structures from Powder Diffraction Data," Berlin Heidelberg: Springer-Verlag, 2006.
- [37] M. Bortolotti, L. Lutterotti, and I. Lonardelli, "ReX: a computer program for structural analysis using powder diffraction data," *J. Appl. Cryst.*, **42**, 538–539 (2009). <https://doi.org/10.1107/S0021889809008309>
- [38] R.D. Shannon, "Revised effective ionic radii and systematic studies of interatomic distances in halides and chalcogenides," *Acta Crystallogr. A*, **32**, 751–767 (1976). <https://doi.org/10.1107/s0567739476001551>
- [39] M. Čebela, B. Janković, R. Hercigonja, M.J. Lukić, Z. Dohčević-Mitrović, D. Milivojević, and B. Matović, "Comprehensive characterization of BiFeO₃ powder synthesized by the hydrothermal procedure," *Processing and Application of Ceramics*, **10**(4), 201–208 (2016). <https://doi.org/10.2298/PAC1604201C>
- [40] P. Desai, and A. Athawale, "Microwave Combustion Synthesis of Silver Doped Lanthanum Ferrite Magnetic Nanoparticles," *Defence Science Journal*, **63**(3), 285–291 (2013). <https://doi.org/10.14429/dsj.63.2387>
- [41] J.I. Pankove, "Optical Processes in Semiconductors," New Jersey: Prentice-Hall, Englewood Cliffs, 1971.
- [42] M. Sivakumar, A. Gedanken, W. Zhong, Y.H. Jiang, Y.W. Du, I. Brukental, D. Bhattacharya, Y. Yeshurun, and I. Nowik, "Sonochemical synthesis of nanocrystalline LaFeO₃," *J. Mater. Chem.*, **14**, 764–769 (2004). <https://doi.org/10.1039/B311011J>
- [43] M. Popa, J. Frantti, and M. Kakihana, "Lanthanum ferrite LaFeO_{3+d} nanopowders obtained by the polymerizable complex method," *Solid State Ionics*, **154**, 437–445 (2002). [https://doi.org/10.1016/S0167-2738\(02\)00480-0](https://doi.org/10.1016/S0167-2738(02)00480-0)
- [44] M.A. Matin, M.N. Hossain, M.M. Rhaman, F.A. Mozahid, M.A. Ali, M.A. Hakim, and M.F. Islam, "Dielectric and optical properties of Ni-doped LaFeO₃ nanoparticles," *SN Appl. Sci.*, **1**, 14792 (2019). <https://doi.org/10.1007/s42452-019-1453-9>
- [45] F. J. Brieler, M. Fröba, L. Chen, P. J. Klar, W. Heimbrod, H.A.K. von Nidda, and A. Loidl, "Ordered Arrays of II/VI Diluted Magnetic Semiconductor Quantum Wires: Formation within Mesoporous MCM-41 Silica," *Chem. Eur. J.*, **8**(1), 185–194 (2002). [https://doi.org/10.1002/1521-3765\(20020104\)8:1<185::AID-CHEM185>3.0.CO;2-L](https://doi.org/10.1002/1521-3765(20020104)8:1<185::AID-CHEM185>3.0.CO;2-L)
- [46] C. Retamoso, N. Escalona, M. González, L. Barrientos, P. Allende-González, S. Stancovich, R. Serpell, J. L. G. Fierro, and M. Lopez, "Effect of particle size on the photocatalytic activity of modified rutile sand (TiO₂) for the discoloration of methylene blue in water," *Journal of Photochemistry and Photobiology A: Chemistry*, **378**, 136–141 (2019). <https://doi.org/10.1016/j.jphotochem.2019.04.021>
- [47] Z. Cui, L. Zhang, Y. Xue, Y. Feng, M. Wang, J. Chen, B. Ji, C. Wang, and Y. Xue, "Effects of shape and particle size on the photocatalytic kinetics and mechanism of nano-CeO₂," *Int. J. Miner. Metall. Mater.*, **29**(12), 2221–2231 (2022). <https://doi.org/10.1007/s12613-021-2332-0>
- [48] S. Chaturvedi, P.N. Dave, and N.K. Shah, "Applications of nano-catalyst in new era," *Journal of Saudi Chemical Society*, **16**(3), 307–325 (2012). <https://doi.org/10.1016/j.jscs.2011.01.015>
- [49] M. Saquib, M. Abu Tariq, M. M. Haque, and M. Muneer, "Photocatalytic degradation of disperse blue 1 using UV/TiO₂/H₂O₂ process," *Journal of Environmental Management*, **88**(2), 300–306 (2008). <https://doi.org/10.1016/j.jenvman.2007.03.012>
- [50] H. A. M. Salim, and S. A. M. Salih, "Photodegradation Study of Toluidine Blue Dye in Aqueous Solution using Magnesium Oxide as a Photocatalyst," *Int. Journal of Chemistry*, **7**(2), 143–149 (2015). <https://doi.org/10.5539/ijc.v7n2p143>
- [51] D. Zhang, S. Lv, and Z. Luo, "A study on the photocatalytic degradation performance of a [KNbO₃]_{0.9}-[BaNi_{0.5}Nb_{0.5}O_{3-d}]_{0.1} perovskite," *RSC Adv.*, **10**, 1275–1280 (2020). <https://doi.org/10.1039/c9ra07310h>

La_{0.8}Bi_{0.2}FeO₃ ПЕРОВСКІТНОГО ТИПУ: ВИСОКА ЕФЕКТИВНІСТЬ ФОТОКАТАЛІТИЧНОЇ ДЕГРАДАЦІЇ ОРТОТОЛУЇДИНОВОГО СИНЬОГО ПІД ОПРОМІНЕННЯМ ВИДИМИМ СВІТЛОМ

Уарда Бен Алі^а, Мохаммед Садок Махбуб^а, Сорія Зеруал^а, Самір Баю^б, Аззеддін Беггас^а,
Мабрук Гугалім, Адель Бенарфа^с, Сухайла Менесер^д

^аЛабораторія LEVRES, Університет Ель-Уед, 39000 Ель-Уед, Алжир

^бХімічний факультет, факультет точних наук, Університет Ель-Уед, 39000 Ель-Уед, Алжир

^сЦентр наукових і технічних досліджень фізико-хімічного аналізу (CRAPC)-PTAPC, P.O. Box 0354, Лагуат 03000, Алжир

^дЛабораторія біотехнології біоматеріалу та конденсованих речовин, Технологічний факультет, Університет Ель-Уеда, Ель-Уед 39000, Алжир

У цьому дослідженні наночастинки перовскіту La_{1-x}Bi_xFeO₃ (x=0,0, 0,2, 0,4 і 0,6) були синтезовані модифікованим методом Пекіні. Ретельний аналіз за допомогою XRD та SEM/EDX підтвердив відсутність вторинних фаз як у чистих, так і в Bi-заміщених зразках LaFeO₃, що вказує на утворення однофазного перовскіту. SEM-зображення виявили квазісферичну форму частинок. Фотокаталітичну активність La_{1-x}Bi_xFeO₃ (x=0,0, 0,2, 0,4 і 0,6) оцінювали за деградацією орто-толуїдинового синього під опроміненням видимим світлом, що вказує на те, що La_{0.8}Bi_{0.2}FeO₃ демонструє чудову фотокаталітичну активність. Загальна швидкість видалення о-Toluidine Blue досягла 90,09% після опромінення видимим світлом протягом 60 хв. Ми пояснюємо цю підвищену фотокаталітичну активність розміром зерна та оптичними властивостями підготовленого зразка. Отже, La_{0.8}Bi_{0.2}FeO₃ можна розглядати як дуже перспективний фотокаталізатор у майбутньому промисловому застосуванні для ефективного очищення стічних вод від барвників.

Ключові слова: La_{1-x}Bi_xFeO₃; барвник орто-толуїдиновий синій; модифікований метод Пекіні; фотокаталіз видимим світлом; очищення стічних вод

INFLUENCE OF EXCHANGE AND CORRELATION INTERACTIONS ON THE SPIN POLARIZED ELECTRONIC STRUCTURE AND MAGNETIC PROPERTIES OF $\text{Ga}_{0.75}\text{Mn}_{0.25}\text{P}$ IN THE B3 ZINC BLENDE STRUCTURE

 **Noureddine Bouteldja**^{a*},  **Mohamed Belabbas**^b, **Rachid Taleb**^c

^a *Laboratoire de Physique Théorique et de Physique des Matériaux (LTPM), Faculty of Exact Sciences and Informatics, Hassiba Benbouali University of Chlef, Algeria*

^b *Department of Physics, Faculty of Exact Sciences and Informatics, Hassiba Benbouali University of Chlef, Algeria*

^c *Laboratoire Génie Electrique et Energies Renouvelables (LGEER), Faculty of Technology, Hassiba Benbouali University of Chlef, Algeria*

*Corresponding Author e-mail: n.bouteldja@univ-chlef.dz

Received November 8, 2023; revised December 11, 2023; accepted December 20, 2023

This study focuses on investigating the influence of exchange and correlation interactions on the spin polarized electronic structure and magnetic properties of $\text{Ga}_{0.75}\text{Mn}_{0.25}\text{P}$ in the B3 Zinc Blende phase. First-principle calculations were performed by systematically varying the Hartree-Fock (HF) exchange (α) value from 0 to 25% using the onsite exact-exchange functional for the treatment of the correlated electrons. The electronic and magnetic properties unveil that $\text{Ga}_{0.75}\text{Mn}_{0.25}\text{P}$ manifests a half-metallic ferromagnetic behaviour at deferent values of HF exchange. Moreover, as the fraction (α) parameter increases, the band gap increases, leading to modifications in the spin polarized band structures. Additionally, our investigations indicate that exchange and correlation interactions cause an increase in the lattice parameter and volume of the compound. Furthermore, these interactions result in a decrease in the magnetic moments of P and Ga atoms, while the Mn moments increase. These findings provide valuable insights into the behavior of $\text{Ga}_{0.75}\text{Mn}_{0.25}\text{P}$ and offer potential applications in the design of spintronic devices.

Keywords: *HF Exchange; Correlated electrons; GaMnP; Magnetic material; Half-metallic; Spintronic*

PACS: 31.15.eg, 75.50.-y, 81.05.Ea, 85.75.-d

INTRODUCTION

Diluted Magnetic Semiconductors (DMS) and spintronics (spin-based electronics) are two fascinating fields of research in semiconductor physics that intersect through the study of materials like III-V (GaX , InX , AlX ,..... $\text{X} = \text{As}$, P , N ,....) or II-VI (CdX , ZnX , MgX ,..... $\text{X} = \text{S}$, Se , Te ,....) doped with magnetic ions having a 3d layer or a 4f layer of transition metals or rare earths (lanthanides). These materials have gained considerable interest for their potential in spintronics applications.

Spintronics seeks to exploit the charge and spin of electrons for the development of new functionalities and devices. Diluted Magnetic Semiconductors, specifically, Mn-doped III-V compounds, offer unique features that allow for precise modulation of carrier spin dynamics, a crucial aspect for the advancement of spintronic devices [1]. One prominent application of these materials is in the field of Magnetic Random Access Memory (MRAM), where they enable efficient spin injection and manipulation [2]. Mn-doped III-V compounds have also found applications in magneto resistive sensors, such as Tunnelling Magneto-Resistance (TMR) and Giant Magneto-Resistance (GMR) sensors to detect and amplify magnetic fields [3,4]. They also hold promise for advanced mass storage devices like hard disks, as they allow for precise spin orientations manipulation and detection [5].

Researchers are actively investigating GaMnP's potential for spin injection, spin manipulation and spin detection, which are fundamental components of spintronic systems. This exploration is focused on establishing the connection between DMS materials and spintronics. S.J. Pearton et al., [6] synthesized ferromagnetic GaMnN and GaMnP compounds at high temperatures to prevent amorphization and enhance their magnetic properties. Iftibhar Ahmed et al., [7] used the FP-LAPW method to investigate the spin polarization of GaMnP and GaMnAs at $x = 0.125$. Y. Yuang et al., [8] examined the structural transport and magnetic properties of GaMnP with varying Mn concentrations using pulsed laser annealing (PLA) and ion implantation. A. Laref et al., [9] conducted calculations on hexagonal $\text{GaN}_{1-x}\text{P}_x$, revealing direct energy gaps and strong polarization dependence in their optical properties, making them promising for solar-cell applications. Z. Young-Zhi et al., [10] found room temperature ferromagnetism in GaAs and GaP compounds doped with V, Cr and Mn atoms at a concentration 25%. J. Mašek et al., [11] focused an investigation the electronic structure of Mn doped Ga(P,As) and (Ga,Al)As materials in the ferromagnetic state. W. Sukkabet., [12] studied magnetism in GaP with transition metal doping using spin density functional calculations. Co and Fe dopants transformed GaP into metal while V retained semiconducting with a reduced band gap. K. Kirandish et al., [13] explored the effect of the pressure on the properties of $\text{Ga}_{0.75}\text{Cr}_{0.25}\text{P}$ utilizing the SIESTA code (Spanish Initiative for Electronic Simulations with Thousands of Atoms). P. Mahadevan et al., [14] delved into the inherent mechanism of ferromagnetism in GaAs, GaP, GaN and GaSb diluted magnetic alloys with Mn substitution focusing on the analysis of the electronic structure trends. N Benbouchi et al., [15] applied spin-dependent density functional theory to study Co doping in GaP,

revealing that Co-doped GaP for spin-based electronic applications due to their complete half-metallic properties and integer total magnetic moments.

Exchange and correlation interactions exert a substantial effect on the distinct properties and behaviors of semiconductors. The exchange interaction reflects the tendency of electrons to align their spins. Meanwhile, the correlation interaction refers to the influence of electrons on each other, impacting the electronic structure and transport characteristics.

This paper investigates the impact of these interactions on the spin polarization of $\text{Ga}_{0.75}\text{Mn}_{0.25}\text{P}$ electronic structure and magnetic properties in the B3 Zinc Blende phase. The study utilizes the Density Functional Theory (DFT) with onsite exact-exchange functional, incorporation variations in the HF exchange parameter (α) ranging from 0 to 25%.

METHOD OF CALCULATIONS

The calculations were conducted utilizing the WIEN2k computer package, employing the FP-LAPW method (Full Potential Linearized Augmented Plane Wave) [16,17]. For spin polarized calculations, the PBE+E parameterization was used, which combines for the PBE (Perdew, Burke and Ernzerhof [18]) method with an onsite exact-exchange treatment for correlated electrons. This approximation effectively considered the exchange and correlation effect. The onsite exact-exchange energy expression as defined by Novák et al [19] can be represented as:

$$E_{XC}^{DFT+E} = E_{XC}^{DFT+E}[\rho] + (\alpha E_{XC}^{HF}[\varphi] - E_{XC}^{DFT}[\rho]). \quad (1)$$

Where (ρ) represents the electron density, (φ) denotes the wave function and (α) signifies the fraction of HF exchange, which can take on either a short-range or long-range value [20]. The long-range value of HF exchange up to 50% is required to obtain acceptable thermo chemistry for the Local Spin Density Approximation (LSDA) [21]. In the Generalized Gradient Approximation (GGA) of PBE, typically uses a short-range value of $\alpha=0.25$ it has been theoretically deduced and this choice has proven notable success [22,23].

The wave functions and potential are expanded using Muffin-tin approach with a cutoff $I_{\max} = 9$. For the Interstitial Region (IR), a cutoff $R_{\min} = 8$ is employed. The chosen cut-off energy is 10^{-3} Ryd which separates core states from valence states. For first-consistent results, 1000 k-points are used in the first Brillouin zone.

The crystal structure of $\text{Ga}_{0.75}\text{Mn}_{0.25}\text{P}$ was generated using eight atoms super cell with dimensions $1 \times 1 \times 1$. Specifically, the Mn atom replaced the Ga atom located at the position (0,0,0). The atomic spheres radii for Ga, Mn and P were set to 1.95, 1.99 and 1.55 respectively. The total energy was optimized by adjusting the volume of the super cell utilizing the Package of Two-Dimensional Optimize [24].

RESULTS AND DISCUSSION

Structural properties

To determine the ground state of the $\text{Ga}_{0.75}\text{Mn}_{0.25}\text{P}$ compound, The Murnaghan's equation of state [25] is employed for the purpose of fitting to calculate the total energy in term of its volume. This calculation is performed for ferromagnetic state using PBE+E approximation.

The resulting values for various structural parameters of $\text{Ga}_{0.75}\text{Mn}_{0.25}\text{P}$ such like the Lattice Parameter (LP), the Volume (V), the Bulk modulus (B), derivative of bulk modulus (B') and the Total Energy (E_{Tot}) show observable convergence with other data [26-28] presented in Table 1.

Table 1. Structural properties of $\text{Ga}_{0.75}\text{Mn}_{0.25}\text{P}$ at different values of HF exchange parameter (α)

α	LP (Ang)	V (Ang ³)	B (GPa)	B'	E_{Tot} (Ryd)
0	5.493 5.49 ^[26]	165.719	79.03 88.61 ^[26]	4.894 4.68 ^[27]	-16718,973 -16718.97441 ^[28]
0.05	5.571	172.882	76.86	4.487	-16718,97859
0.10	5.629	178.364	53.64	5.257	-16718,98954
0.15	5.690	184.301	67.58	5.201	-16719,00784
0.20	5.787	193.854	70.18	4.733	-16719,05385
0.25	5.854	200.687	82.46	5.051	-16719,0992

Figure 1 demonstrates that as exchange and correlation interactions increase, both the LP and Volume of $\text{Ga}_{0.75}\text{Mn}_{0.25}\text{P}$ increase. This indicates significant influence of these interactions on the unit cell size. Specifically, exchange and correlation interactions directly affect the equilibrium positions of atoms and their bonding behavior within the unit cell, ultimately leading to an expansion of the unit cell size.

Figure 2 shows that increasing exchange and correlation interactions lead to a significant decrease in total energy of $\text{Ga}_{0.75}\text{Mn}_{0.25}\text{P}$. These interactions strongly influence the electronic properties by modifying the distribution and behavior of electrons, resulting in a pronounced reduction in total energy.

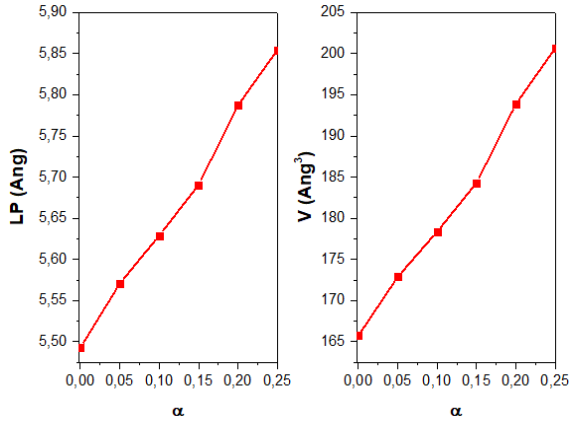


Figure 1. Influence of exchange and correlation interactions on lattice parameter (LP) and volume (V) of Ga_{0.75}Mn_{0.25}P

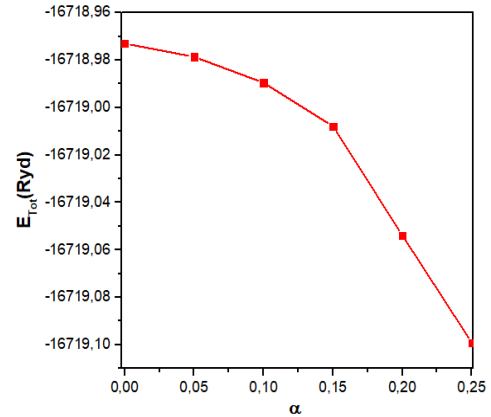


Figure 2. Influence of exchange and correlation interactions on total energy (E_{Tot}) of Ga_{0.75}Mn_{0.25}P

Electronic properties

The spin polarized band structures of Ga_{0.75}Mn_{0.25}P have been computed within the first Brillouin zone. Figure 3 depicts that the electrons in the spin up (↑) state outnumber those in the spin down (↓) state. There is a band gap present around the Fermi level (E_f) for spin down state, while a few valence bands in the spin up state intersect the Fermi level and transition into the conduction band. Consequently, based on the occurred interactions range of 0 to 25%, Ga_{0.75}Mn_{0.25}P compound is predicted to exhibit metallic behavior for spin up state and semiconductor behavior for the spin down state. Further investigation indicates that this compound is a half metallic ferromagnetic material.

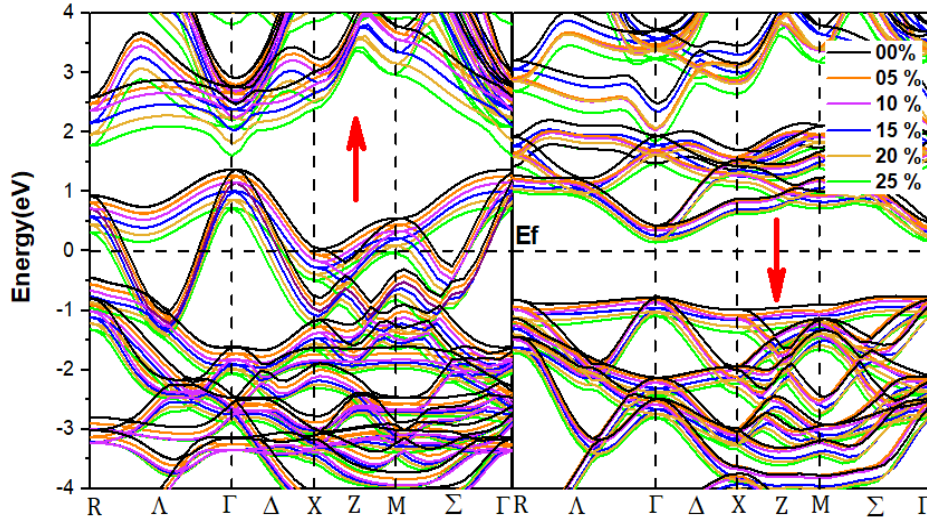


Figure 3. Influence of exchange and correlation interactions on spin polarized band structures of Ga_{0.75}Mn_{0.25}P

In the Figure 4, the calculated band structures highlight a noticeable increase in the forbidden energy gap (E_g) for spin down state. This increase is attributed to significant changes in the maximum of the conduction band and the minimum of the valence band, resulting from the increasing exchange and correlation interactions.

The calculated electronic properties are summarized in Table 2, it includes conduction band minimum of spin down state and spin up state ($E_{CBM}^{up}, E_{dn}^{CBM}$), valence band maximum of spin down state and spin up state ($E_{VBM}^{up}, E_{dn}^{VBM}$), the band edge spin splitting (ΔE_c) for the conduction band minimum and the band edge spin splitting (ΔE_v) for the valence band maximum are determined using specific formulas:

$$\Delta E_c = E_{CBM}^{up} - E_{dn}^{CBM}, \quad (2)$$

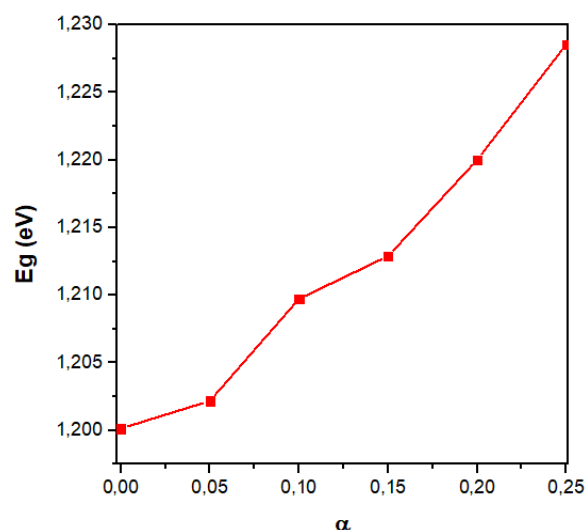
$$\Delta E_v = E_{VBM}^{up} - E_{dn}^{VBM}. \quad (3)$$

These formulas are commonly used to analyze band structure and determine various properties of electronic states at (Γ) symmetry point.

In the Figure 4, the calculated band structures highlight a noticeable increase in the forbidden energy gap (E_g) for spin down state. This increase is attributed to significant changes in the maximum of the conduction band and the minimum of the valence band, resulting from the increasing exchange and correlation interactions.

Table 2. Electronic properties of $\text{Ga}_{0.75}\text{Mn}_{0.25}\text{P}$ at different values of HF exchange parameter (α)

α	0	0.05	0.10	0.15	0.20	0.25
E_{gdn} (eV)	1.20013 1.20 ^[28]	1,20218	1,20973	1.21289	1,22001	1,22857
$E_{\text{VBM}}^{\text{up}}$ (eV)	0	0	0	0	0	0
$E_{\text{dn}}^{\text{VBM}}$ (eV)	-0,77277	-0,80629	-0.86033	-0,95136	-1,02482	-1.08531
$E_{\text{CBM}}^{\text{up}}$ (eV)	0	0	0	0	0	0
$E_{\text{dn}}^{\text{CBM}}$ (eV)	0,42736	0,39589	0.3494	0,26153	0,19519	0.14326
ΔE_{v} (eV)	0,77277	0,80629	0.86033	0,95136	1,02482	1.08531
ΔE_{c} (eV)	-0,42736	-0,39589	-0.3494	-0,26153	-0,19519	-0.14326

**Figure 4.** Influence of exchange and correlation interactions on band gap energy (E_{g}) of $\text{Ga}_{0.75}\text{Mn}_{0.25}\text{P}$

Magnetic properties

Upon substituting Ga atoms with Mn in GaP, the resulting GaMnP compound exhibits magnetic properties attributed to Mn-3d. The coupling between the 3d orbital of Mn and the 3p orbital of P atoms results in the emergence of small local magnetic moments in both Ga and P atoms. Notably, for $\text{Ga}_{0.75}\text{Mn}_{0.25}\text{P}$, the local magnetic moment of P exhibits a negative value, indicating an anti-parallel alignment with the Mn spin, whereas the positive value observed on Ga signifies a parallel alignment.

Figure 5 illustrates the variation of the both local and total magnetic moments of $\text{Ga}_{0.75}\text{Mn}_{0.25}\text{P}$ under the influence of exchange and correlation interactions. As the interactions increase, the total magnetic moment remains constant at 4.00 μ_{B} . Nonetheless, the magnetic moment of Mn atom increases, whereas the local magnetic moments at P and Ga atoms decrease. These findings are in agreement with other data [29] presented in Table 3.

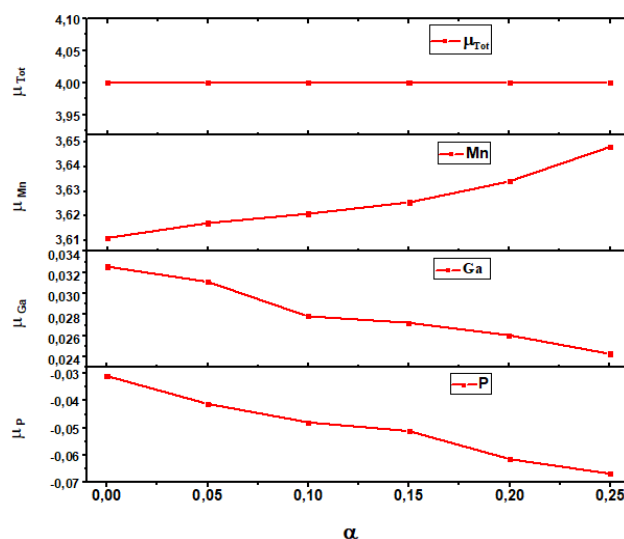
**Figure 5.** Influence of exchange and correlation interactions on magnetic moment μ_{Tot} , μ_{Mn} , μ_{Ga} and μ_{P} of $\text{Ga}_{0.75}\text{Mn}_{0.25}\text{P}$.

Table 3. Magnetic properties of Ga_{0.75}Mn_{0.25}P at different values of HF exchange parameter (α)

α	μ_{Mn} (μB)	μ_{Ga} (μB)	μ_P (μB)	μ_{Tot} (μB)
0	3,61121 3,382 ^[29]	0,03255 0,023 ^[29]	-0,03091 -0,039 ^[29]	4,00042 4,05 ^[29]
0.05	3,61718	0,03112	-0,04114	4,00068
0.10	3,62101	0,02784	-0,0479	4,00068
0.15	3,62559	0,02723	-0,05113	4,00068
0.20	3,63412	0,02603	-0,06142	4,00068
0.25	3,64813	0,02428	-0,06673	4,00068

CONCLUSIONS

The interactions studied affect the structural properties of Ga_{0.75}Mn_{0.25}P by increasing the lattice parameter and volume, and decreasing the total energy. The electronic structures show a downward shift of the valence and conduction bands, resulting in an increased band gap. The compounds exhibit half metallic ferromagnetism within the range of 0 to 25% of HF exchange. The magnetic properties indicate a noteworthy phenomenon in which the coupling between the 3d orbital of Mn and the 3p orbital of P atoms induces local magnetic moments in the Ga and P atoms. Moreover, as the interactions strength intensifies, the magnetic moment of Mn atom increases, while it decreases on Ga and P atoms. However, it is important to note that despite these changes, the total magnetic moment remains unchanged.

ORCID

©Noureddine Bouteldja, <https://orcid.org/0000-0002-9356-7238>; ©Mohamed Belabbas, <https://orcid.org/0000-0003-1325-8011>

REFERENCES

- [1] G. Zho, Z. Deng, and C. Jin, Journal of semiconductors, **40**(8), 081505 (2019). <https://doi.org/10.1088/1674-4926/40/8/081505>
- [2] I.A. Iusipova, Semiconductors, **52**, 1982 (2018). <https://doi.org/10.1134/S10637826181>
- [3] A. Doll, S. Lecurieux-Lafayette, J. Moulin, C. Chopin, G. Jasmin-Lebras, M. Pannetier-Lecoeur, A. Solignac, and C. Fermon, Proc. SPIE, Spintronics XII, **11090**, 110903M, 146 (2019). <https://doi.org/10.1117/12.2529246>
- [4] M. Oogane, K. Fujiwara, A. Kanno, T. Nakano, H. Wagatsuma, T. Arimoto, and S. Mizukami, Applied Physics Express, **14**(12), 123002 (2021). <https://doi.org/10.35848/1882-0786/ac3809>
- [5] Z. Guo, J. Yin, Y. Bin, D. Zhu, K. Shi, G. Wang, K. Cao, and W. Zho, Proceedings of the IEEE, **109**(8), 1398 (2021). <https://doi.org/10.1109/JPROC.2021.3084997>
- [6] S.J. Pearton, M.E. Overberg, G.T. Thaler, C.R. Abernathy, J. Kim, F. Ren, and N. Theodoropoulou, Physica Status Solidi (a), **195**(1), 222 (2003). <https://doi.org/10.1002/pssa.200306283>
- [7] I. Ahmad, and B. Amin, Computational Materials Science, **68**, 55 (2013). <https://doi.org/10.1016/j.commatsci.2012.07.037>
- [8] Y. Yang, Y. Wang, M. Khalid, K. Gao, S. Prucnal, O.D. Gordan, and G. Salvan, IEEE Transactions on Magnetics, **50**(11), 1 (2014). <https://doi.org/10.1109/TMAG.2014.2322332>
- [9] A. Laref, Z. Hussain, S. Laref, J.T. Yang, Y.C. Xiong, and S.J. Luo, Journal of Physics and Chemistry of Solids, **115**, 355 (2018). <https://doi.org/10.1016/j.jpcs.2017.12.002>
- [10] Z. Young-Zhi, and H. Mei-Chun, Chinese Physics Letters, **21**(8), 1632 (2004). <https://doi.org/10.1088/0256-307X/21/8/061>
- [11] J. Mašek, J. Kudrnovský, F. Máca, J. Sinova, A.H. MacDonald, R.P. Campion, B.L. Gallagher, and T. Jungwirth, Physical Review B, **75**(4), 045202 (2007). <https://doi.org/10.1103/PhysRevB.75.045202>
- [12] W. Sukkabot, Chemical Physics, **523**, 57 (2019). <https://doi.org/10.1016/j.chemphys.2019.04.007>
- [13] K. Kaur, and S. Sharma, in: *Proceedings of the International Conference on integrated interdisciplinary. Innovations in Engineering*, (Panjab, India, 2020), pp. 1033.
- [14] P. Mahandevan, and A. Zunger, Applied Physics Letters, **85**(14), 2860 (2004). <https://doi.org/10.1063/1.1799245>
- [15] N. Benbouchi, E.A. Mohammed-Mounir, F.Z. Dahou, A. Bahnes, and A. Laref, Results in Physics, **24**, 104118 (2021). <https://doi.org/10.1016/j.rinp.2021.104118>
- [16] P. Blaha, K. Schwarz, G.K.H. Madsen, D. Kvasnicka, and J. Luitz, in: *WIEN2K. An Augmented Plane Wave Plus Local Orbitals Program for Calculating Crystal Properties*, edited by K. Schwarz (Techn. Universität Wien, Austria, 2001).
- [17] F. Tran, P. Blaha, K. Schwarz and P. Novák, Physical Review B, **74**(15), 155108 (2006). <https://doi.org/10.1103/PhysRevB.74.155108>
- [18] J.P. Perdew, K. Burke, and M. Ernzerhof, Physical Review Letters, **77**(18), 3865 (1996). <https://doi.org/10.1103/PhysRevLett.77.3865>
- [19] P. Novák, J. Kuneš, L. Chaput, and W.E. Pickett, Physica Status Solidi (b), **243**(3), 563 (2006). <https://doi.org/10.1002/pssb.200541371>
- [20] O.A. Vydrov, J. Heyd, A.V. Krukau, and G.E. Scuseria, The Journal of Chemical Physics, **125**(7) (2006). <https://doi.org/10.1063/1.2244560>
- [21] A.D. Becke, The Journal of Chemical Physics, **98**(2), 1372 (1993). <https://doi.org/10.1063/1.464304>
- [22] M. Ernzerhof, and G. E. Scuseria, The Journal of Chemical Physics, **110**(11), 5029 (1999). <https://doi.org/10.1063/1.478401>
- [23] C. Adamo, and V. Barone, The Journal of Chemical Physics, **110**(13), 6158 (1999). <https://doi.org/10.1063/1.478522>
- [24] A.H. Reshak, and M. Jamal, Journal of Alloys and Compounds, **555**, 362 (2013). <https://doi.org/10.1016/j.jallcom.2012.12.028>
- [25] F.D. Murnaghan, Proceeding of National Academy of Sciences, **30**(9), 244 (1944). <https://doi.org/10.1073/pnas.30.9.244>

- [26] K. Kaur, and A. Rani, Applied Physics A, **123**(12), 791 (2017). <https://doi.org/10.1007/s00339-017-1398-z>
- [27] B. Doumi, A. Mokaddem, A. Sayede, M. Boutab, A. Tadjer, and F. Dahmane, Journal of Superconductivity and Novel Magnetism, **28**, 3163 (2015). <https://doi.org/10.1007/S10948-015-3148-9>
- [28] H. Ullah, K. Inayat, S.A. Khan, S. Mohammad, A. Ali, Z.A. Alahmed, and A.H. Reshak, Journal of Magnetism and Magnetic Materials, **385**, 27 (2015). <https://doi.org/10.1016/j.jmmm.2015.02.069>
- [29] A. Djedid, B. Doumi, S. Méçabih, and B. Abbar, Journal of Materials Science, **48**, 6074 (2013). <https://doi.org/10.1007/s10853-013-7405-7>

ВПЛИВ ОБМІННОЇ ТА КОРЕЛЯЦІЙНОЇ ВЗАЄМОДІЇ НА СПІНОВУ ПОЛЯРИЗОВАНУ ЕЛЕКТРОННУ СТРУКТУРУ ТА МАГНІТНІ ВЛАСТИВОСТІ $Ga_{0.75}Mn_{0.25}P$ У СТРУКТУРІ ЦИНКОВОЇ ОБМАНКИ ВЗ

Нуреддін Бутелджа^a, Мохамед Белаббас^b, Рашид Талеб^c

^a *Лабораторія теоретичної фізики та фізики матеріалів (LTPM), Факультет точних наук та інформатики, Університет Хасіба Бенбуалі, Члефі, Алжир*





^b *Кафедра фізики, Факультет точних наук та інформатики, Університет Хасіба Бенбуалі, Члефі, Алжир*

^c *Лабораторія електротехніки та відновлюваної енергії (LGEER), Технологічний факультет, Університет Хасіба Бенбуалі, Члефі, Алжир*

Це дослідження зосереджено на вивченні впливу обмінних і кореляційних взаємодій на спін-поляризовану електронну структуру та магнітні властивості $Ga_{0.75}Mn_{0.25}P$ у фазі ВЗ Zinc Blende. Розрахунки першого принципу були виконані шляхом систематичної зміни значення обміну Хартрі-Фока (HF) (α) від 0 до 25% з використанням локального функціоналу точного обміну для обрахунку поведінки корельованих електронів. Електронні та магнітні властивості показують, що $Ga_{0.75}Mn_{0.25}P$ демонструє напівметалеву феромагнітну поведінку при різних значеннях HF-обміну. Крім того, зі збільшенням параметра фракції (α) ширина забороненої зони збільшується, що призводить до модифікацій у спін-поляризованих зонах структурах. Крім того, наші дослідження показують, що обмінні та кореляційні взаємодії викликають збільшення параметра решітки та об'єму сполуки. Крім того, ці взаємодії призводять до зменшення магнітних моментів атомів P і Ga, тоді як моменти Mn збільшуються. Ці висновки дають цінну інформацію про поведінку $Ga_{0.75}Mn_{0.25}P$ для потенційних застосувань в дизайні спінтронних пристроїв.

Ключові слова: ВЧ-обмін; корельовані електрони; $GaMnP$; магнітний матеріал; напівметалічний; спінтроніка

DFT STUDIES ON ELECTRONIC, ELASTIC, THERMOELECTRIC AND OPTICAL PROPERTIES OF NEW HALF-HEUSLER XRhZ (X = V, Nb AND Z = Si, Ge) SEMICONDUCTORS

Bendehiba Sid Ahmed^a, Besbes Anissa^a,  Djelti Radouan^{a*},  Najwa Al Bouzieh^b,  I. Kars Durukan^c
 Noureddine Amrane^b

^a Technology and Solids Properties Laboratory, University of Mostaganem (UMAB), Algeria

^b Physics Department, College of Science, United Arab Emirates University (UAEU), 15551, Al Ain, UAE

^c Department of Physics, Faculty of Science, Gazi University, 06500 Ankara, Turkey

*Corresponding Author e-mail: Radouane.djelti@univ-mosta.dz, djeltired@yahoo.fr

Received November 12, 2023; revised December 8, 2023; accepted December 20, 2023

Density functional theory is used to explore the physical properties of the new half-Heusler alloys XRhZ (X = V, Nb and Z = Si, Ge). The exchange-correlation effects were treated by the TB-mBJ potential. The four studied compounds are nonmagnetic semiconductor with an indirect band gap. The formation enthalpy, cohesive energy and phonon band structures demonstrated that these semiconductors are structurally and dynamically stable. It was predicted by the elastic study that the XRhZ compounds (X = V, Nb and Z = Si, Ge) have stable mechanical properties, they possess an anisotropic character and reveal the ductile nature with a B/G ratio >1.75. The optical results show an interesting photocatalytic potential for the NbRhSi and NbRhGe semiconductors, they exhibit a high absorption coefficient in the visible domain, which is around 112.10^4 cm^{-1} . For energies greater than 10 eV (UV domain), the refractive index is less than one. The thermoelectric results confirmed that the XRhZ (X=V, Nb and Z=Si, Ge) compounds are very attractive for thermoelectric devices working in large temperature range including ambient temperature.

Keywords: Half-Heusler alloys; Semiconductor; Elastic properties; Seebeck coefficient; Merit factor; Absorption coefficient; Reflectivity

PACS: 71.20.-b, 72.15.Jf, 72.25.Ba, 73.50.L, 52.70.Kz

1. INTRODUCTION

Half-Heusler (HH) alloys have involved a remarkable interest over the past years due to their several properties in various technological domains, such as magnetic, optical, thermoelectric, piezoelectric, superconducting and topological properties [1-8]. The valence electron count (VEC) has always been found as responsible of the most physical and thermoelectrical properties [9-10]. The HH compounds with VEC of 18 are nonmagnetic semiconductors with fascinating optoelectronic properties due to their tunable band gap over broad energy range [11-12]. In addition, their smaller bandgap and high electrical conductivity and Seebeck coefficient make them effective in thermoelectric applications [13-14]. This type of material is composed by an X^{+n} ion occupying in a zinc blende YZ^{-n} sub-lattice and where the VEC linked with the YZ^{-n} sub-lattice is 18 ($d^{10}s^2p^6$) [15-16]. The valence electrons of the X atom are transferred to the Y and Z atoms, which are more electronegative, and thus acquire a closed shell configuration ($s^2p^6d^{10}$). P.K. Kamlesh et al., [17] explored by ab-initio calculations the optical possessions of AlNiX (X = P, As and Sb) HH, they confirm that the AlNiP and AlNiAs compounds are well suited for use as shields against high-energy of UV radiation due to their large reflectivity values in this area. Y.Wang et al., [18] give a theoretical analysis of transport properties of NbXGe (X = Rh, Ir) H.H materials, subject to network constraints. They have found that for a strain of -6%, the ZT value of NbRhGe has doubled by 50% compared with the unstrained case, so, they state that these materials are promising candidates for TE applications. D.M. Hoat [19] has investigated a series of HH compounds based on tantalum and having a VEC of 18, he noted that all the materials studied are indirect band gap semiconductor. The difference between the band gap values is due to the degree of overlap that exists between the Ta-5d and X-4d orbitals. Furthermore, the denser electronic states, close to the Fermi level (E_F), of TaRhSn and TaRhPb compounds strongly contributed to the thermoelectric performance characterized by high thermal power in the p region. The optical and thermoelectric study carried out by J. Wei and G. Wang [20] on the TaCoSn HH alloy showed a powerful light adsorption capacity in the visible zone, which is of 125.10^4 cm^{-1} . The results of transport properties show that TaCoSn exhibits an excellent thermoelectric performance characterized by a high Seebeck coefficient and merit factor. In an experimental study carried out by W. Silpawilawan et al., [21], the nanostructured $Nb_{0.9}Ti_{0.1}FeSb$ was synthesized by melt spinning followed by spark plasma sintering. An improvement of 20% in the ZT value was achieved, amelioration due to the reduction in thermal conductivity caused by this nanostructuring, which allow to effective phonon scattering. They declare that the NbFeSb remain one of the best p-type HH alloys in thermoelectric. Currently, the development of embedded systems engineering go through the search of the innovative (semiconductors, half-metallic) materials able to carry out actions in real time. For this it is necessary that these compounds will have high optical, thermoelectric and spintronic performances. It is in this perspective that we are going in this research to emphasize the thermoelectric and optical responses of four new semiconductors possessing 18 valence electrons.

Cite as: B.S. Ahmed, B. Anissa, D. Radouan, N. Al Bouzieh, I.K. Durukan, N. Amrane, East Eur. J. Phys. 1, 294 (2024), <https://doi.org/10.26565/2312-4334-2024-1-26>

© B.S. Ahmed, B. Anissa, D. Radouan, N. Al Bouzieh, I.K. Durukan, N. Amrane, 2024; CC BY 4.0 license

2. COMPUTATIONAL METHOD

In this work, all properties of the H.H compounds XRhZ ($X = V, Nb$ and $Z = Si, Ge$) have been studied with WIEN2k code [22] which is based on DFT calculations [23]. The computations were determined by full potential linearized augmented plane wave method [24]. Among the exchange-correlation functionals, the generalized gradient approximation (GGA) [25-26] and the Tran and Blaha modified Becke-Johnson method (TB-mBJ) [27] were retained for this study. The H.H have the C_{1b} crystal structure with the space group F-43m. The muffin tin radius (RMT) values of 2.5, 2.1 and 1.9 a.u were used for for X, Rh and Z elements. Other input data, such as k-point mesh (K_{MAX}), RMT*wave-vector, Gaussian parameter and the maximum angular momentum were selected to 14^*14^*14 [28], 7.0, 12 and 10 respectively. The value of -6.0 Ry is taken as the energy of the interval between the core and valence states and the energy convergence criterion of 10^{-4} Ry is adopted for the self-consistent field calculations. The electron transport properties are determined under a fine mesh of $46 \times 46 \times 46$ [29] by the semi-classical Boltzmann transport equation (BTE) as given in the BoltzTraP code [30]. The optical responses of our new compounds were determined by the complex dielectric function $\epsilon(\omega)$ as given from the Kramer–Kronig relation [31-33].

3. RESULTS AND DISCUSSIONS

3.1 Structural properties and phase stability

The H.H compounds XRhZ ($X = V, Nb$ and $Z = Si, Ge$) crystallizes in the face centered cubic space group (F43m). The Silicon (Germanium) and Vanadium (Niobium) atoms are located at the octahedral 4b ($1/2, 1/2, 1/2$) and 4a ($0, 0, 0$) Wyckoff positions, while the Rhodium element occupies tetrahedral position 4c ($1/4, 1/4, 1/4$). The unit cell structure of the XRhZ compound plotted using Vesta 4.5 software [34] is shown in Figure 1. We can observe that the arrangement contains three interpenetrating ordered fcc sublattices which are occupied by X, Rh and Z atoms respectively. The covalent nature of the [XZ] sublattice is emphasized as a zinc blende sublattice, while the Rh and Z atoms form a rock salt structure.

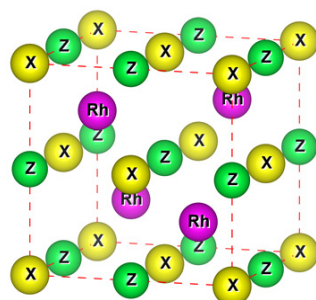


Figure 1. Crystalline structure of XRhZ ($X = V, Nb$ and $Z = Si, Ge$)

The NaCl-type substructure consisting of atoms with large electronegativity difference implies strong ionic bonding character, while the ZnS-type substructure, which involves strong covalent character, consists of atoms having a smaller difference in electronegativity [35]. Table 1 gives the structural parameters of VRhSi, VRhGe, NbRhSi and NbRhGe H.H. compounds calculated by using the GGA approximation in the ferromagnetic and nonmagnetic states. The main parameters are the bulk modulus B , its pressure derivative B' , the equilibrium lattice constant a_0 , cohesive energy E_{coh} , formation energy ΔH_f and ground state energy E_{min} . For the four alloys, the γ -phase is energetically more stable than α and β phases, in addition this most stable state, was found to be nonmagnetic. The calculated lattice parameters values are 5.71 Å, 5.80 Å, 5.91 Å and 5.97 Å respectively for VRhSi, VRhGe, NbRhSi and NbRhGe compounds. These values are in perfect harmony with those of other semiconducting H.H alloys with VEC of 18, let's quote TaCoSn (5.94 Å) [36], NbIrGe (6.02 Å) [18], HfCoSb (6.04 Å) [37].

The experimental synthesis of the H.H compounds XRhZ ($X = V, Nb$ and $Z = Si, Ge$) compounds is only possible if the formation energy value ΔH_f calculated according to relation (1) is negative [38].

$$\Delta H_f = E_{XYZ}^{tot} - (E_X^{bulk} + E_Y^{bulk} + E_Z^{bulk}). \quad (1)$$

Where E^{bulk} is the energy per atom of constituent atoms in bulk and E_{XYZ}^{tot} is the total energy of primitive cell. Negative values of the formation energy obtained for all the four H.H, confirms that the synthesis of these compounds remain possible. To predict the stability of the H.H alloys XRhZ ($X = V, Nb$ and $Z = Si, Ge$), we have calculated according to the relation (2) the corresponding cohesion energies [39].

$$E_{coh} = E_{XYZ}^{tot} - (E_X^{iso} + E_Y^{iso} + E_Z^{iso}). \quad (2)$$

Where E^{iso} is the isolated atom energy. The negative cohesive energies achieved justify that our four H.H are structurally stable. The calculation of phonon dispersion in the first Brillouin zone along the high-symmetry points is given for the studied compounds thanks to the Phono3py code [40]. The phonon band structures of NbRhGe compound is already given in previous study conducted by Y.Wang [18]. The absence of imaginary phonon frequency in whole Brillouin zone (Fig. 2) confirms the dynamical stability of our semiconductor's compounds in their ground states.

Table 1. Calculated structural equilibrium lattice constant a (Å), pressure derivatives B' , ground state energies E_{min} (Ry), formation energy ΔH_f (Ry) and cohesive energy E_{coh} (Ry)

Alloys	State	Type	a	B'	E_{min}	E_{coh}	ΔH_f
VRhSi	FM	α	5.72	3.91	-12049.276632	-1.4227	-0.199
	NM		5.72	3.09	-12049.276687		
	FM	β	5.69	4.09	-12049.302767		
	NM		5.70	3.01	-12049.303182		
	FM	γ	5.73	3.86	-12049.366754		
	NM		5.71	4.49	-12049.367117		
VRhGe	FM	α	5.81	5.87	-15667.350805	-1.2878	-0.844
	NM		5.81	5.20	-15667.350475		
	FM	β	5.79	6.56	-15667.341261		
	NM		5.81	6.41	-15667.341583		
	FM	γ	5.80	6.77	-15667.410282		
	NM		5.80	6.03	-15667.422243		
NbRhSi	FM	α	6.01	4.40	-17791.550849	-1.4905	-0.237
	NM		6.01	4.27	-17791.551936		
	FM	β	5.87	4.31	-17791.605674		
	NM		5.88	4.30	-17791.606164		
	FM	γ	5.92	4.72	-17791.690152		
	NM		5.91	5.21	-17791.692559		
NbRhGe	FM	α	6.09	6.01	-21409.636669	-1.3619	-0.868
	NM		6.09	5.98	-21409.636659		
	FM	β	5.97	5.30	-21409.652489		
	NM		5.97	5.34	-21409.652959		
	FM	γ	5.98	5.75	-21409.754550		
	NM		5.97	4.26	-21409.754950		
Phase α :			X (1/4, 1/4, 1/4)	Y (1/2, 1/2, 1/2)	Z (0, 0, 0)		
Phase β :			X (1/2, 1/2, 1/2)	Y (0, 0, 0)	Z (1/4, 1/4, 1/4)		
Phase γ :			X (0, 0, 0)	Y (1/4, 1/4, 1/4)	Z (1/2, 1/2, 1/2)		

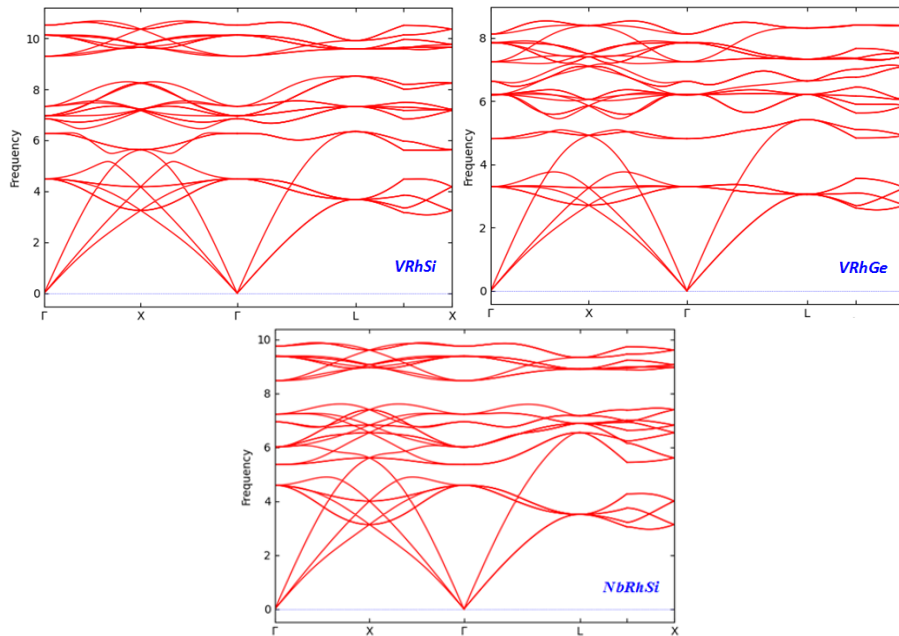


Figure 2. The phonon band structures of (a) VRhSi, (b) VRhGe and (c) NbRhSi

The acoustic modes exhibit the high dispersions, which means that they contribute well to the heat transport while the optical modes contribute little to the heat transport due to their weak dispersion. For the VRhSi and VRhGe, we see an overlap of acoustic and optical branches near X and L points thus indicating the strong phonon–phonon scattering [41].

3.2 Electronic properties

The magnetic performance of ternary H.H is estimated by the Slater-Pauling equation [42].

$$M_t = (18 - Z_t) \quad (3)$$

Z_t and M_t denote respectively the total number of valence electrons in the unit cell and the total magnetic moment. The explicit valence electrons for the XRhZ ($X=V, Nb$ and $Z=Si, Ge$) primal cell are V: [Ar] 3d³ 4s², Nb: [Kr] 3d⁴ 5s¹, Rh: [Kr] 4d⁸ 5s¹, Si: [Ne] 3s²3p² and Ge: [Ar] 3d¹⁰ 4s² 4p². At first sight and according to the relation (3), the four compounds studied in this research do not exhibit magnetism, because they all have 18 electrons in their valence shell. The calculation of their total magnetic moment shows that these compounds are not magnetic ($M_t = 0 \mu_B$), thus confirming the result already predicted by the optimization. The electronic band structures (EBS) of VRhSi, NbRhSi, VRhGe and NbRhGe H.H alloys was carried out at the equilibrium lattice parameters by TB-mBJ approach.

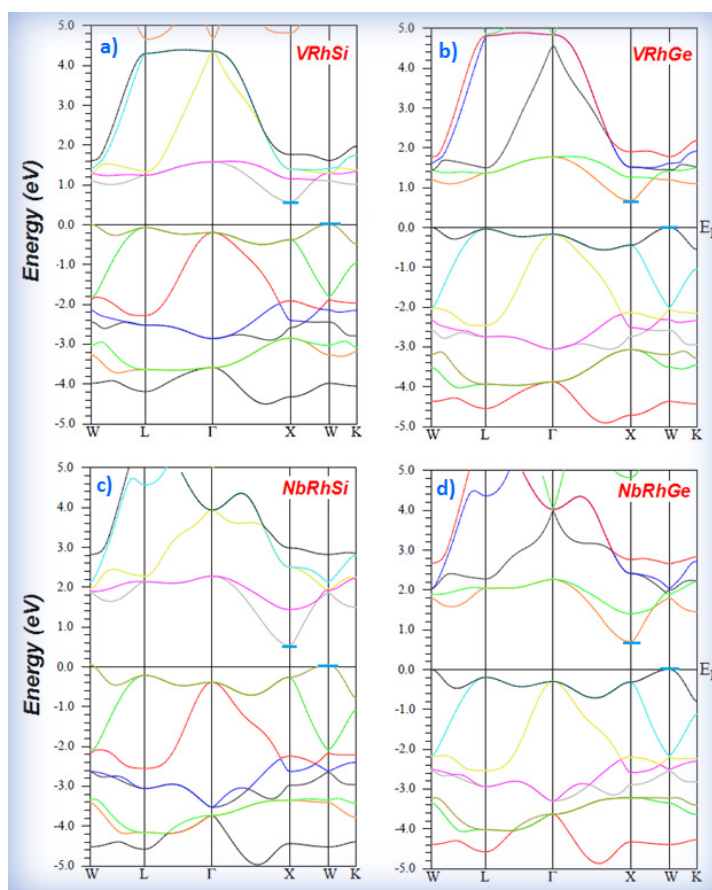


Figure 3. Band structures of (a) VRhSi, (b) NbRhSi, (c) VRhGe, (d) NbRhGe

The EBS diagrams (**Fig. 3a-d**) reveal for the studied compounds, that the top of valence band is located at W symmetry point while the bottom of conduction band is located at X-symmetry point. All the materials exhibit semiconductor nature with narrow indirect band gap of 0.59, 0.68, 0.51 and 0.71 eV for VRhSi, NbRhSi, VRhGe and NbRhGe respectively. These findings are in good adequacy with other fundamental results obtained for H.H semiconductors having the same X atom that our alloys, let us quote the NbIrGe (0.63 eV) [18], VRuSb (0.64 eV) [16], NaScSi (0.61 eV) [43]. We can observe from the BS plots that the L and Γ are the points for the valence bands convergence and that the distribution of these bands is mainly due to the heavy hybridization of the d states of the X (V, Nb) and Z (Si, Ge) atoms. The energy difference between the W and L points for the NbRhSi and NbRhGe compounds is around 0,16 and 0.18 eV while for the VRhSi and VRhGe compounds this difference is negligible. The four compounds show a triple band degeneracy at Γ point while L point show a double band degeneracy. This degeneracy of the valence band at the E_F constitutes an index of a good thermoelectric performance of the studied materials. To better comprehend the band diagrams of XRhZ ($X=V, Nb$ and $Z=Si, Ge$) compounds, we have computed using the TB-mBJ method their total (TDOS) and partial densities of states (PDOS). Based on the TDOS/PDOS spectra (**Fig. 4a-d**), we can notice that the four H.H alloys, show almost similar profile in valence and conduction band. For the VRhSi/VRhGe compound, the valence band maximum (VBM) is composed of V-3d states, Rh-4d states and a small dispersion of Si-3p (Ge-3p) states, while the conduction band minimum (CBM) is mainly constituted of V-3d states.

For the NbRhSi and NbRhGe compounds, the strong contribution below E_F comes from the Nb-4d state while the states above E_F are mainly due to the Nb-4d and Rh-4d states and to a small contribution of the Si-3p (Ge-3p) states. The p-type doping could have the capacity to contain more charge carriers than n-type doping [44] since around the Fermi level, the TDOS of the valence band is larger than that of the conduction band. From the PDOS plots, one can conclude for the four materials, that the X-d states and Rh-d states give the main contribution to conductivity, while the Ge-p and Ge-s states have no influence on transport properties.

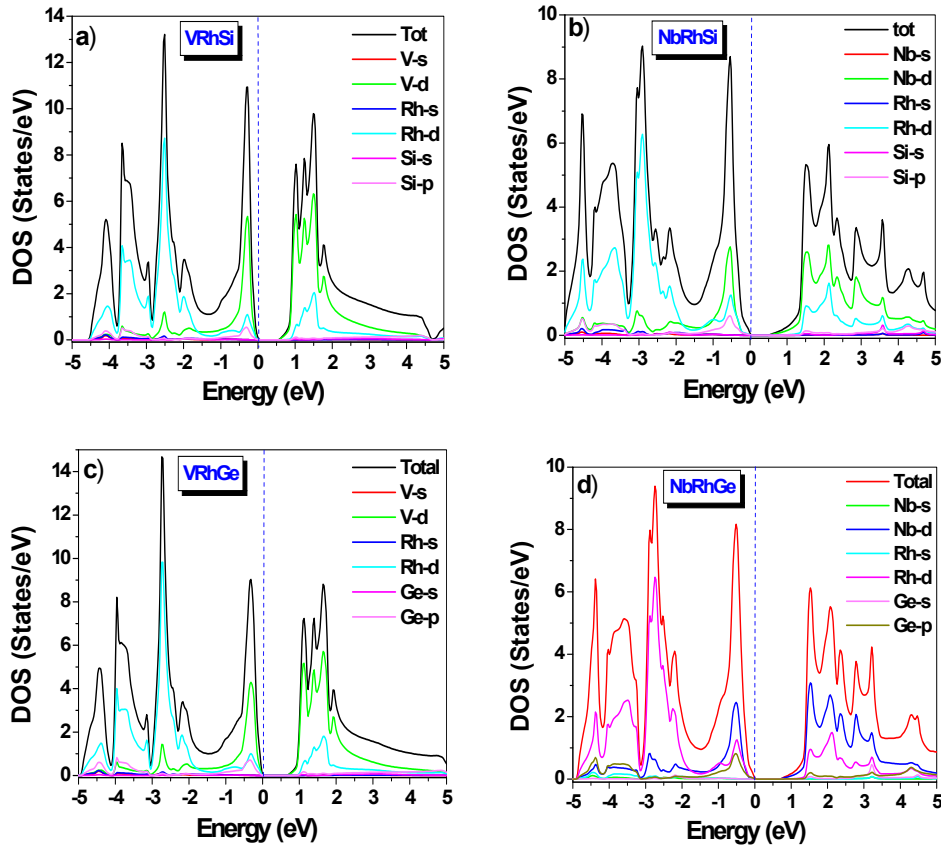


Figure 4. Total and partial density of states (TDOS / PDOS) of (a) VRhSi, (b) NbRhSi, (c) VRhGe, (d) NbRhGe.

3.3 Elastic properties

Examining the mechanical stability of H.H alloys XRhZ (X = V, Nb and Z = Si, Ge) requires the knowledge of the three elastic constants C_{11} , C_{12} , C_{44} [45]. These constants allow to estimated according to the equations (4) to (8), the bulk modulus B, the shear modulus G, Young's modulus E, Poisson's ratio ν and the elastic anisotropy factor A [46].

$$B = \frac{1}{3}(C_{11} + 2C_{12}), \quad (4)$$

$$G = \frac{C_{11} - C_{12} + 3C_{44}}{5}, \quad (5)$$

$$E = \frac{9BG}{3B + G}, \quad (6)$$

$$\nu = \frac{3B - E}{6B}, \quad (7)$$

$$A = \frac{2C_{44}}{C_{11} - C_{12}}. \quad (8)$$

From Table 2, which gives the independent elastic constants, we can conclude that at zero pressure, the H.H compounds XRhZ (X = V, Rh and Z = Si, Ge) are mechanically stable due to the fact that they satisfy all of Born's elastic stability criteria [47] ($C_{11} - C_{12} > 0$); ($C_{11} + 2C_{12} > 0$); ($C_{11} > 0$); ($C_{44} > 0$) and ($C_{12} < B < C_{11}$). For the alloys treated in this research, the condition $C_{11} > C_{22} > C_{33}$ was established, this confirms that XRhZ (X = V, Rh and Z = Si, Ge) alloys are most tough to the unidirectional compression than shear deformation. Compared to the three other H.H, the VRhGe show a low value of bulk modulus (B) which mean that this material is easy to compress. The shear modulus (G) describes the resistance of the material against permanent deformation due to a shear stress. Based on our calculations, NbRhSi has higher Shear modulus (65.22 GPa), so a higher hardness among other alloys, while the VRhSi has the lowest hardness (52.21 GPa). The ability of a material to resist changes in its length when subjected to longitudinal compression is defined by Young's modulus (E). Based on our calculations, NbRhSi has the highest Young modulus (167.26 GPa) so a highest stiffness and VRhSi has the lowest stiffness among the four studied alloys. According to the obtained values of G and E, the NbRhSi compound can be classified as a high rigidity hard material. The range of values found for shear moduli and Young's moduli is in agreement with those of several HH compounds cited in the literature [48-50].

Table 2. The computed elastic constants C_{ij} (GPa), bulk modulus B (GPa), Shear modulus G (GPa), Young's modulus E (GPa), Poisson's ratio (ν), anisotropic factor A , and Pugh's ratio (B/G) of VRhZ (Z=C, Si, Ge) half-Heusler materials

	C_{11}	C_{12}	C_{44}	B	G	E	ν	A	B/G
VRhSi	147.47	102.06	66.84	112.15	52.21	135	0.30	2.21	2.14
VRhGe	133.30	80.19	75.12	97.90	55.69	140	0.26	2.83	1.76
NbRhSi	176.39	109.98	82.34	127.92	65.22	167	0.28	2.08	1.96
NbRhGe	173.21	104.61	78.27	127.47	60.68	157	0.29	2.28	2.10

Poisson's ratio (ν) values obtained are located between 0.26 and 0.30, which confirms according to Haines et al. [51] the presence of covalent and metallic bonding ($\nu < 0.33$). The VRhSi, VRhGe, NbRhSi and NbRhGe compounds present an anisotropy coefficient (A) different from unity (Table 2), which confirms their anisotropic mechanical behavior. The risk of micro cracking within these compounds is minimal given that their degree of anisotropy is low. Other important characteristics, the ductility and fragility which are an intrinsic property of materials and which requires their determination in order to position material for a given application. According to Pugh's criterion [52], the material behaves in brittle manner when B/G is lower than 1.75 and as ductile manner for B/G higher than 1.75. For the present investigation based on first principles calculations, we noted that the four studied compounds show B/G values greater than 1.75, suggesting the ductility of these HH.

3.4 Thermoelectric properties

The thermoelectric properties such as the Seebeck coefficient (S), thermal conductivity (κ/τ), electrical conductivity (σ/τ), and Merit factor (ZT) are calculated using the BoltzTraP code. All these properties are studied as a function of chemical potential change (μ). The change of (μ) can influences the stability of the materials during doping even if the electronic band remains unchanged [53-54]. In addition, these properties will be given versus temperature for chemical potential equal to Fermi energy. The most remarkable thermoelectric properties given by equations (9 to 12) all derive from the semi-classical Boltzmann transport equation [55-56].

$$\sigma_{\alpha\beta}(\mathbf{T}, \mu) = \frac{1}{\Omega} \int \sigma_{\alpha\beta}(\epsilon) [-\partial f_{\mu}(\mathbf{T}, \epsilon)] d\epsilon, \quad (9)$$

$$\kappa_{\alpha\beta}(\mathbf{T}, \mu) = \frac{1}{e^2 \mathbf{T} \Omega} \int \sigma_{\alpha\beta} \epsilon (\epsilon - \mu)^2 \frac{\partial f_{\mu}(\mathbf{T}, \epsilon)}{d\epsilon}, \quad (10)$$

$$S = \frac{e}{\mathbf{T} \sigma} \int \sigma_{\alpha\beta}(\epsilon) (\epsilon - \mu) \left[\frac{-\partial f_{\mu}(\mathbf{T}, \epsilon)}{\partial \epsilon} \right], \quad (11)$$

$$ZT = \frac{S^2 \sigma \mathbf{T}}{\kappa}. \quad (12)$$

Where σ , μ , Ω , f , κ , S and ZT denotes respectively electrical conductivity, chemical potential, unit-cell volume, Fermi-Dirac distribution function, thermal conductivity, Seebeck coefficient and merit factor.

The knowledge of the temperature effect on thermoelectric properties is a crucial key for identifying the reliability of compounds in thermoelectric applications. The variation of Seebeck coefficient which provides us the insight of the type of charge carriers in XRhZ (X=V,Nb and Z=Si,Ge) compounds, have been drawn versus temperature (Fig. 5a). In all considered temperature range, the sign of S is positive, thus meaning that the holes are the majority charge carriers. For VRhGe H.H, the S value increases to its utmost value of $270 \mu V \cdot K^{-1}$ at 300 K then decrease to achieve $221 \mu V \cdot K^{-1}$ at 1200 K, while for the NbRhGe compound, S increases up to a maximum value of $261 \mu V \cdot K^{-1}$ at 900 K and then decreases weakly to reach $254 \mu V \cdot K^{-1}$ at 1200 K.

For the VRhSi alloy, the value of S goes from $240 \mu V \cdot K^{-1}$ at 300K to $269 \mu V \cdot K^{-1}$ at 700K then drops again to $240 \mu V \cdot K^{-1}$ at 1200K. The utmost value of " S " for the NbRhSi alloy is observed at 900 K it is of $262 \mu V \cdot K^{-1}$. Around room temperature, " S " shows a large positive value of about $270 \mu V/K$, $240 \mu V/K$ and $225 \mu V/K$ respectively for VRhGe, NbRhSi/VRhSi and NbRhGe. The trend of Seebeck coefficient with respect to chemical potential (μ), has been displayed in Fig. 6a and Fig. 7a. At room temperature, the peaks of S are obtained at μ values included between -0.03 to 0.01 eV for VRhGe/NbRhGe and between -0.02 to 0.01 eV for VRhSi/NbRhSi compound. Beyond these range of μ , S tends to zero. With rising in the temperature, the maximum value decreases, it goes from $1205 \mu V/K$ at 300K to $473 \mu V/K$ at 900K for VRhGe/NbRhGe and from $853 \mu V/K$ at 300K to $384 \mu V/K$ at 900K respectively for VRhSi/NbRhSi compounds. The optimal values of S occur on the negative side of μ . Above the room temperature, S gradually decreases with the rise in temperature; this is due to jumping of electron and hopping of holes around the localized states in the vicinity of E_F [57] which will generates a rise in the thermal energy. Comparatively to VRhSi and NbRhSi compounds, the VRhGe and NbRhGe H.H are well suitable for thermoelectric devices working around 300 K, since their maximum Seebeck values are reached at 300 K.

From Fig. 5b which give the evolution of electrical conductivity (σ/τ) versus temperature, we can see that σ/τ increases as temperature increases, suggesting the semiconducting nature of XRhZ (X=V,Nb and Z=Si,Ge) compounds. For all the studied compounds, the σ/τ value is almost similar up to room temperature, above 300 K a strong increase is

observed for the VRhGe compound. The lowest values of σ/τ are obtained at 100 K, they are around $6 \times 10^{17} (\Omega\text{ms})^{-1}$, while the maximum values are obtained at 1200 K they're from $4.61 \times 10^{19} (\Omega\text{ms})^{-1}$ for VRhGe and around $3 \times 10^{19} (\Omega\text{ms})^{-1}$ for VRhSi, NbRhGe and NbRhSi. The effect of chemical potential (μ) on the electrical conductivity (σ/τ) of the H.H compounds XRhZ ($X = V, Nb$ and $Z = Si, Ge$) is drawn in Fig. 6b and Fig. 7b.

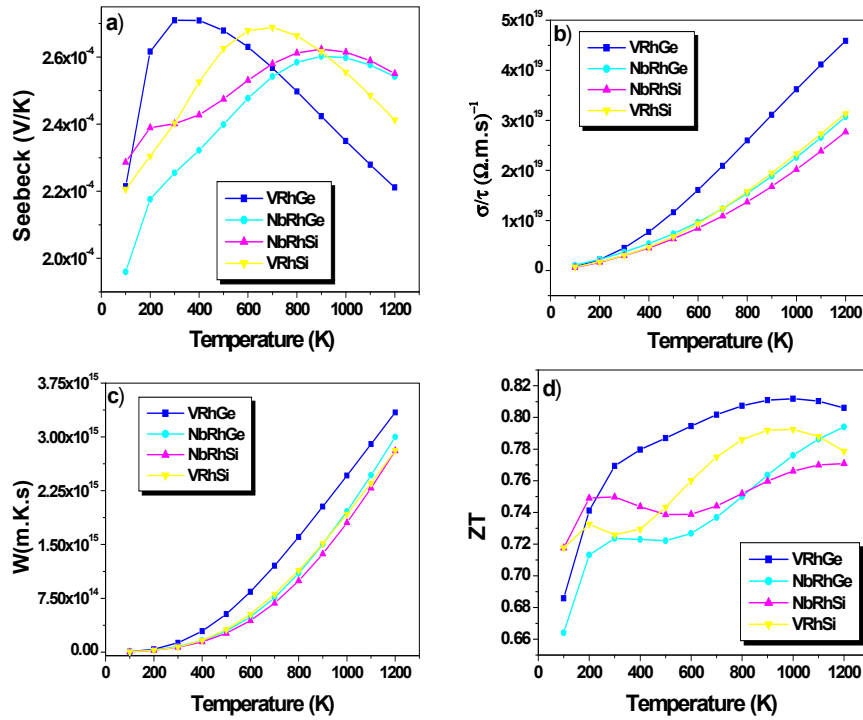


Figure 5. Evolution versus temperature of (a) Seebeck coefficient, (b) electrical conductivity, (c) thermal conductivity and (d) Merit factor of XRhZ ($X = V, Nb$ and $Z = Si, Ge$).

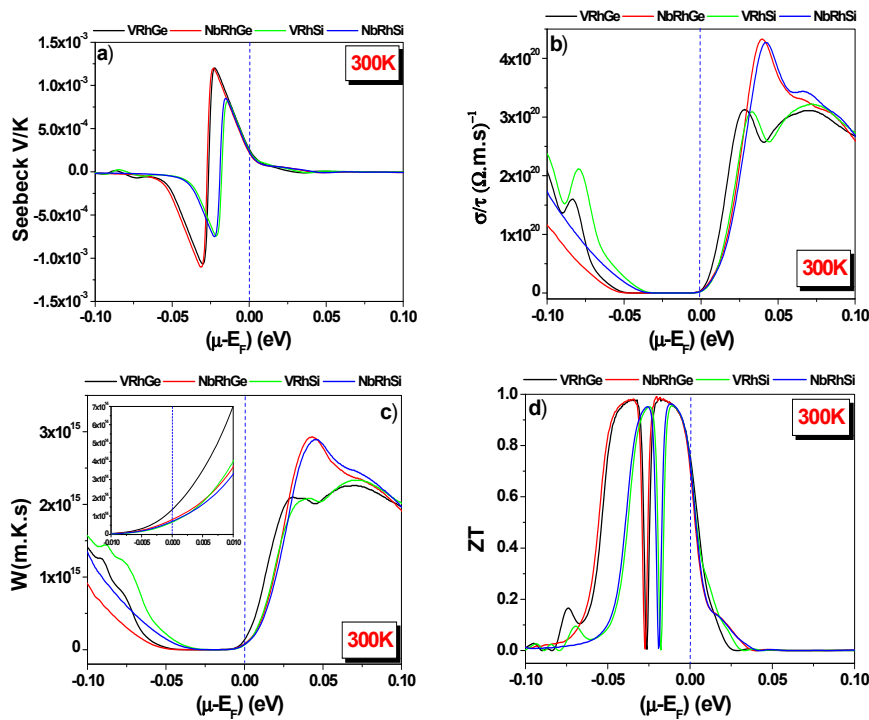


Figure 6. Evolution versus chemical potential of (a) Seebeck coefficient, (b) electrical conductivity, (c) thermal conductivity and (d) Merit factor of XRhZ ($X = V, Nb$ and $Z = Si, Ge$). ($T = 300\text{K}$)

Comparatively to the p-type region, the electrons in n-type region show at room temperature dominance with maximum peak intensity of $3.12 \times 10^{20} (\Omega\text{m}\cdot\text{s})^{-1}$ / $4.32 \times 10^{20} (\Omega\text{m}\cdot\text{s})^{-1}$ occurring at -0.028 eV / (-0.039 eV) respectively for NbRhSi/NbRhGe and VRhSi/VRhGe compounds. Almost the same result is obtained at 900K. For the temperatures

of 300 and 900 K, we notice that the profiles of σ/τ do not show any major change, the curves are almost confused except for a few small differences. The high values of σ/τ recorded for the four H.H denote the low losses by Joule effect; this is explained by the difference between the effective masses of electrons (conduction band) which are heavier than the effective masses of holes (valence band). From Fig. 5c, which depict the compoment of electronic thermal conductivity (κ_e/τ) as function of temperature, one can notice that κ_e/τ increases almost linearly with temperature. At ambient temperature the κ_e/τ is of 1.29×10^{14} for VRhGe and around 7.80×10^{13} for the other three compounds. For the materials studied in this paper, the lowest values of κ/τ are obtained at 100 K, while the maximum values are obtained at 1200 K. At the same chemical potential, the gap between the values of κ_e/τ increase as temperature increase, but with a gradient of less importance than that of the electrical conductivity σ/τ case. According to the Fig. 6c and Fig. 7c, which illustrates the thermal conductivity κ_e/τ given versus chemical potential μ (eV), we can reveal the clear amplification of κ_e/τ when the temperature increases. The κ_e/τ is higher for the p-type (electrons) than for the n-type (holes). At ambient temperature and for $\mu = E_F$, the κ_e/τ value is of $1,34 \times 10^{14}$ W/m.K.s for VRhGe and around $7,50 \times 10^{13}$ W/m.K.s for the other three compounds. The values of κ/τ are larger for $\mu > 0$ than for $\mu < 0$. At room temperature, the VRhSi and the VRhGe compounds exhibit a low thermal conductivity peak, which mean that these two H.H can provide high thermal efficiency. The high merit factor (ZT) values obtained constitute a strong index of the high thermoelectric performance of these materials. In fact, this parameter highly depends on the temperature, thermal conductivity (κ/τ), electrical conductivity (σ/τ) and Seebeck coefficient (S). Fig. 5d gives the evolution of merit factor (ZT) versus tempeprature at $\mu = E_F$. Electrons nearby the E_F play an essential role in the transport properties. ZT value of the VRhGe alloy remain the best among the four studied compounds, it increase from 0.68 at 100 K to its utmost value of 0.81 at 1000 K while at room temperature its value is of 0.77. Beyond 200 K, all the compounds have a ZT value that is greater than 0.71. From Fig. 6d and Fig. 7d, which give the change of ZT regarding the chemical potential, one can see that the values of ZT are lower in the p-type region than in the n-type region and as the temperature tends toward 300K, the utmost value of ZT progressively increases. At room temperature, the ZT values is around the unity, which makes the XRhZ (X=V,Nb and Z=Si,Ge) compounds very attractive for thermoelectric devices working at room temperature. We have identified in the literature several H.H semiconductors, which are classified as a good thermoelectric material and which exhibit the almost same values of ZT than our studied alloys, let's quote TiIrAs, TiIrSb [58].

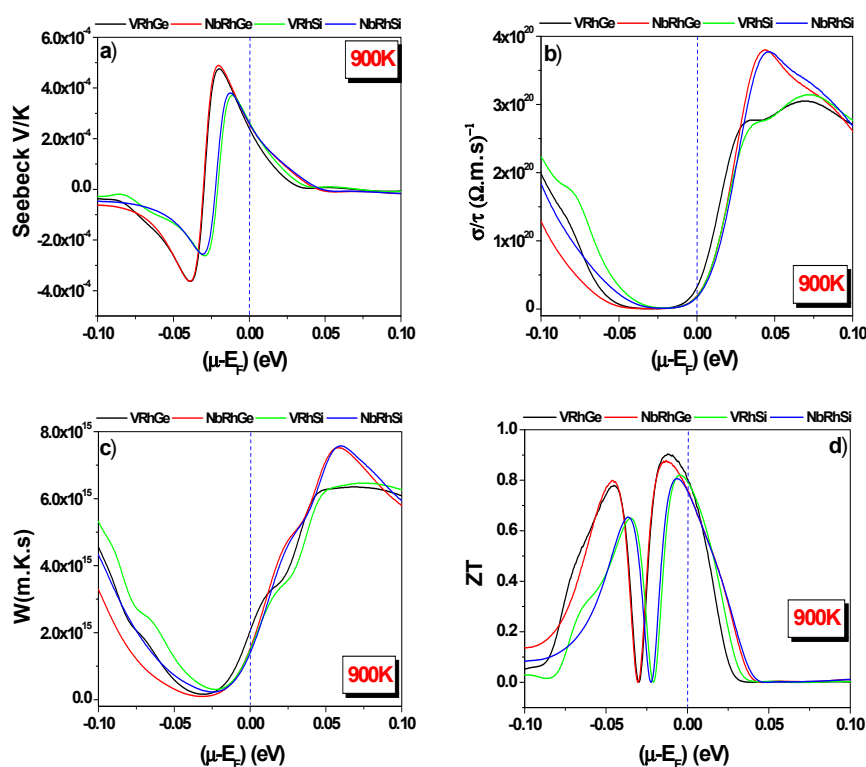


Figure 7. Evolution versus chemical potential of (a) Seebeck coefficient, (b) electrical conductivity, (c) thermal conductivity and (d) Merit factor of $XRhZ$ ($X = V, Nb$ and $Z = Si, Ge$). ($T = 900$ K)

3.5 Optical properties

Even though the semiconductor compound is known to be a very good material for optical applications, its optical study is considered necessary, because this type of material can lose its semiconductor characteristic at very low frequency and become metallic as it can also acquire the behavior of an insulator at very high frequency [59]. The majority of the optical characteristics come from the dielectric complex function $\epsilon(\omega)$ (eq.13) [33].

$$\boldsymbol{\varepsilon}(\boldsymbol{\omega}) = \boldsymbol{\varepsilon}_1(\boldsymbol{\omega}) + i\boldsymbol{\varepsilon}_2(\boldsymbol{\omega}) \quad (13)$$

$\boldsymbol{\varepsilon}_1(\boldsymbol{\omega})$ describes the dispersion of electromagnetic radiation whereas $\boldsymbol{\varepsilon}_2(\boldsymbol{\omega})$ represents the optical absorption of the material.

The imaginary part of the dielectric function $\boldsymbol{\varepsilon}_2(\boldsymbol{\omega})$ comes from the EBS computations with the help of the following relation

$$\boldsymbol{\varepsilon}_2(\boldsymbol{\omega}) = \left(\frac{4\pi^2 e^2}{m^2 \omega^2}\right) \sum_{i,j} \int \langle i|M|j\rangle^2 f_i(1-f_j)\delta(E_j-E_i-\boldsymbol{\omega})d^3k. \quad (14)$$

Where $\boldsymbol{\omega}$, e , m and M denote respectively the photon frequency, electron charge, electron mass and dipole matrix. E_j designates the final state electron energy, E_i the initial state electron energy and f_i the Fermi occupation factor of the single-particle state i .

Thanks to the Kramer's Kronig relations [60-61], the real part of the dielectric function $\boldsymbol{\varepsilon}_1(\boldsymbol{\omega})$ is deduce from the imaginary part of the same function $\boldsymbol{\varepsilon}_2(\boldsymbol{\omega})$.

$$\boldsymbol{\varepsilon}_1(\boldsymbol{\omega}) = 1 + \frac{2}{\pi} P \int_0^\infty \frac{\omega' \boldsymbol{\varepsilon}_2(\omega')}{\omega'^2 - \omega^2} d\omega'. \quad (15)$$

Where P represents the principal Cauchy value. Additional optical quantities can be also deduced from the calculated values of the imaginary and real parts of the dielectric function [62], the most sought after among them are the reflectivity $R(\boldsymbol{\omega})$, the refractive index $n(\boldsymbol{\omega})$ and the absorption coefficient $a(\boldsymbol{\omega})$. The crystallographic structures of the studied compounds are cubic; hence, the optical properties will be isotropic. In order to reach sensible accuracy on all probable electronic transitions, a dense mesh is considered necessary. A k-point mesh of 31*31*31 was adopted in this part of optical calculation. The various optical properties examined using the TB-mBJ method are plotted in the near infrared (NIR), visible (Vis) and ultraviolet (UV) domains.

$$R(\boldsymbol{\omega}) = \left| \frac{\sqrt{\boldsymbol{\varepsilon}(\boldsymbol{\omega})} - 1}{\sqrt{\boldsymbol{\varepsilon}(\boldsymbol{\omega})} + 1} \right|^2 \quad (16)$$

$$n(\boldsymbol{\omega}) = \left[\frac{\sqrt{\boldsymbol{\varepsilon}_1^2(\boldsymbol{\omega}) + \boldsymbol{\varepsilon}_2^2(\boldsymbol{\omega})} + \boldsymbol{\varepsilon}_1(\boldsymbol{\omega})}{2} \right]^{1/2} \quad (17)$$

$$a(\boldsymbol{\omega}) = \frac{\sqrt{2\boldsymbol{\omega}}}{c} \left(\sqrt{\boldsymbol{\varepsilon}_1^2(\boldsymbol{\omega}) + \boldsymbol{\varepsilon}_2^2(\boldsymbol{\omega})} - \boldsymbol{\varepsilon}_1(\boldsymbol{\omega}) \right)^{1/2} \quad (18)$$

The graphical plot of Fig. 8a gives the real part of dielectric function $\boldsymbol{\varepsilon}_1(\boldsymbol{\omega})$; part, which defines the extent a material, may be polarized. Comparatively to the visible and infrared regions, the H.H compounds XRhZ (X = V, Nb and Z = Si, Ge) react highly to the ultraviolet-light excitations; many peaks are detectable in this domain. The negative values of $\boldsymbol{\varepsilon}_1(\boldsymbol{\omega})$ mean that the material entirely reflects the incident radiation while the positive values mean that the photons move across the material. For the VRhGe compound, the negative values of $\boldsymbol{\varepsilon}_1(\boldsymbol{\omega})$, recorded between 1.97 and 2.40 eV (visible region) can be explained by the metallic character characterized by the reflection of incident radiation. The same observation was found for the VRhSi, NbRhGe and NbRhSi compounds in the energy ranges between 1.83 to 2.23 eV / (2.62 to 3.05 eV) / (2.65 to 3.21 eV) respectively. Beyond 12.90 eV, the four compounds show values of real part $\boldsymbol{\varepsilon}_1(\boldsymbol{\omega})$ fluctuating around zero. The static dielectric constant $\boldsymbol{\varepsilon}_1(\mathbf{0})$ (dielectric function for zero photon energy) which is inversely proportional to the band gap [63] was found respectively equal to 190.11, 178.77, 23.62 and 22.88 eV for the VRhSi, VRhGe, NbRhSi and NbRhGe compounds. The transition between the occupied and unoccupied states is mostly insured by the imaginary part of dielectric constant $\boldsymbol{\varepsilon}_2(\boldsymbol{\omega})$ [64]. From Fig. 8b, we can see that $\boldsymbol{\varepsilon}_2(\boldsymbol{\omega})$ curve of VRhSi/VRhGe has three main peaks located at 0.24eV, 1.90eV and 3.98eV, while $\boldsymbol{\varepsilon}_2(\boldsymbol{\omega})$ curve of NbRhSi/NbRhGe exhibits two main peaks positioned around 2.43eV and 4.92eV. According to the band structure plot of VRhSi/VRhGe (Fig.3a-b), the three highest peaks of $\boldsymbol{\varepsilon}_2(\boldsymbol{\omega})$ correspond to the indirect interband transitions between W-X, L-X and Γ -X states. The two highest peaks for the NbRhSi/NbRhGe, compound correspond to the indirect interband transitions between W-X and L-X states (Fig.3c-d). We can noticed that above 8.8 eV, the optical activity of the four compounds considerably decreases. Fig. 8c, illustrates versus photon energy the evolution of absorption coefficient $a(\boldsymbol{\omega})$. For the four compounds, we can observe from 0 to 50 eV that there are no regions, where the compounds are optically transparent to radiation ($a(\boldsymbol{\omega}) = 0$). The values of $a(\boldsymbol{\omega})$ start from 0 eV and reaches in the ultraviolet region their maximums of 371.48 at 40.14eV (VRhSi/VRhGe) and 314.42 at 33.26 eV (NbRhSi/NbRhGe). Due to these high absorption values, these compounds may be beneficial to absorb harmful UV rays. In the visible region, the maximum values of $a(\boldsymbol{\omega})$ is about 112.84 cm⁻¹ for NbRhSi/NbRhGe, and about 84.26 cm⁻¹ for VRhSi/VRhGe. These values are larger to those reported for many H.H semiconductors

compounds such as LiCaX (X=N, P and As) [65], ZrRhSb [66], XScZ (X = Li, Na; Z = C, Si, Ge) [67], RbScSn [68] and SiLiX (X = Ca and Sr) [69]. The evolution of light reflection $R(\omega)$ versus photonic energy is illustrated in Fig. 8d.

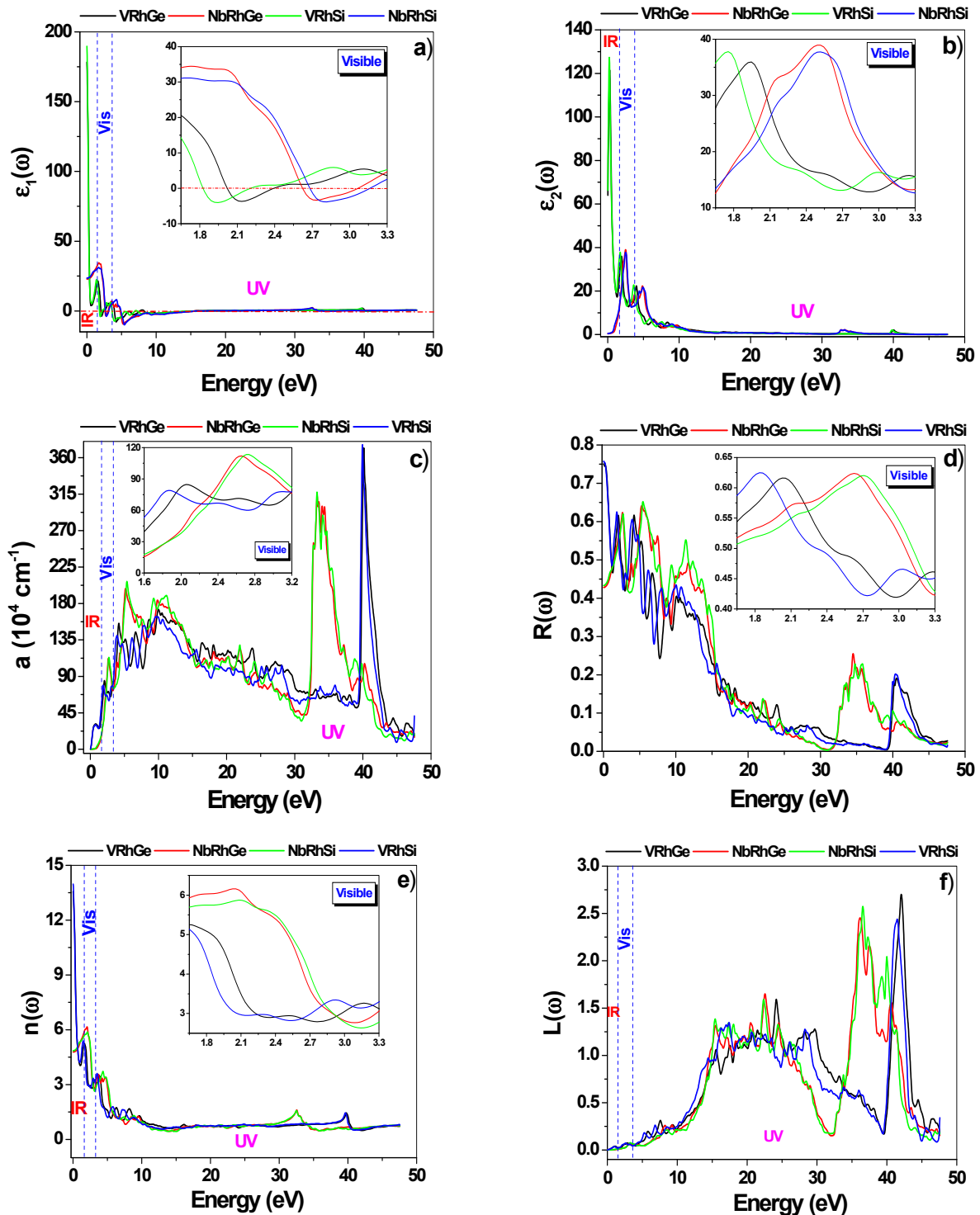


Figure 8. Illustration of (a) real $\varepsilon_1(\omega)$ and (b) imaginary $\varepsilon_2(\omega)$ component of dielectric function, (c) absorption coefficient $a(\omega)$, (d) reflectivity $R(\omega)$, (e) refractive index $n(\omega)$, and (f) electron energy loss $L(\omega)$ for $XRhZ$ ($X=V, Nb$ and $Z=Si, Ge$)

We can see that at zero energy, $R(0)$ is relatively high for VRhSi /VRhGe its value is of 75% while that of NbRhGe/NbRhGe is of 43%. Over low energies, $R(\omega)$ oscillates and the highest value for the VRhGe is obtained in the visible domain (62 %), while the utmost value for the NbRhGe which is of 64 % has registered in the UV domain. A value of R around 66% is observed in the UV domain for the alloys containing silicon (VRhSi and NbRhSi). The high-infrared reflectivity of approximately 75% makes VRhSi/VRhGe compounds ideal materials for use as high-performance heat shields. Fig. 8e shows the variation of refractive index versus phonon energy for the four

compounds studied in this research. We clearly notice that the $n(\omega)$ shape is similar to that of $\epsilon_1(\omega)$. For zero photon energy, the refractive index of VRhSi/VRhGe is significantly higher than, those of NbRhSi/NbRhGe. In addition, the real part of the dielectric constant $\epsilon_1(\mathbf{0})$ and the refractive index $n(\mathbf{0})$ are obey to the equation $\epsilon_1(\mathbf{0}) = n^2(\mathbf{0})$ [70]. For the VRhSi/VRhGe compounds, the refractive index $n(\omega)$ starts rapidly to decrease before reached 1eV, then increases to attain its utmost value of 5.30 at 1.60 eV. While for the NbRhSi/NbRhGe compounds, a slight increase is noted between 0.14-1.96eV, beyond this range we observed a decrease of $n(\omega)$ values to stabilize around 0.7. We notice that it is in the visible range that the utmost values of $n(\omega)$ occur. Fig. 8f, gives us the loss function energy $L(\omega)$; it can be seen that the prominent peaks of $L(\omega)$ for all four compounds are located in the high-frequency UV domain going from 15 eV to 42.0 eV. These peaks match to the fast decrease of the reflectivity $R(\omega)$. Also, the different peaks of $L(\omega)$ are directly related to the plasma resonance, in other words, to the state of electron vibrations in the valence band. In the infrared region and visible region, all the compounds exhibit a very weak energy loss.

CONCLUSIONS

In this manuscript, the structural, electronic, elastic, thermoelectric and optical behavior of ternary half-Heuslers XRhZ (X = V, Nb and Z = Si, Ge) in cubic phase have been studied and discussed using DFT methods. For all studied compounds, the structural optimization confirms that the NM state is more stable than the FM state, while the EBS and DOS graphs reveal non-magnetic semiconductor behavior. The negative values found for the formation enthalpy and cohesive energy are strong clues of the thermodynamic stability and possible structural synthesizability of these HH. The phonon band structures of XRhZ compounds show no imaginary frequency and testify to the dynamic stability of its semiconductors in the nonmagnetic γ phase. The elastic properties results showed that the four semiconductors are stable mechanically. They possess a low anisotropy degree therefore a minimal risk of micro cracking and they also revealed a ductile nature. The optical performances was studied in the energetic domain, ranging from 0 eV up to 50 eV. The high reflectivity greater than 60%, detected in the visible and UV areas as well as the high peaks of the absorption coefficient obtained in the same zones, allow using these alloys as UV filters, UV-visible photodetector, or as an effective shield in these domains. The increase in thermoelectric power generally passes through the decrease in thermal conductivity. For temperatures greater than 300K, the substitution of the germanium atom by the silicon atom (lighter atom) leads in a considerable reduction in thermal conductivity, reduction of 38% at 600K and 26% at 900K. With a merit factor values greater than 0.73 in wide temperature domain, all these compounds can be considered as alternative green energy sources and also for energy conversion.

ORCID

© Djelti Radouan, <https://orcid.org/0000-0002-0762-5818>; © Najwa Al Bouzieh, <https://orcid.org/0000-0003-4603-9982>
© I. Kars Durukan, <https://orcid.org/0000-0001-5697-0530>; © Noureddine Amrane, <https://orcid.org/0000-0003-0555-5315>

REFERENCES

- [1] C. Fu, T. Zhu, Y. Liu, et al., "Band engineering of high-performance p-type FeNbSb based half-Heusler thermoelectric materials for figure of merit $zT > 1$," *Energy Environ. Sci.* **8**, 216-220 (2015). <https://doi.org/10.1039/C4EE03042G>
- [2] G.T. Wang, and J.H. Wei, "Topological phase transition in half-Heusler compounds HfIrX (X = As, Sb, Bi)," *Comput. Mater. Sci.* **124**, 311 (2016). <https://doi.org/10.1016/j.commatsci.2016.08.005>
- [3] S. Singh, S.W. D'Souza, J. Nayak, et al., "Effect of platinum substitution on the structural and magnetic properties of Ni₂MnGa ferromagnetic shape memory alloy," *Phys. Rev. B Condens. Matter*, **93**, 134102 (2016). <https://doi.org/10.1103/PhysRevB.93.134102>
- [4] A. Besbes, R. Djelti, B. Bestani, and O. Akel, "First-principles study of structural, electronic, thermodynamic, and thermoelectric properties of a new ternary half-Heusler alloy PdZrGe," *Chinese Journal of Physics* **56**, 2926-2936 (2018). <https://doi.org/10.1016/j.cjph.2018.09.027>
- [5] A. Roy, J.W. Bennett, K.M. Rabe, and D. Vanderbilt, "Half-Heusler semiconductors as piezoelectrics," *Phys. Rev. Lett.* **109**, 037602 (2012). <https://doi.org/10.1103/PhysRevLett.109.037602>
- [6] Y. Gupta, M.M. Sinha, and S.S. Verma, "Investigations of mechanical and thermoelectric properties of AlNiP novel half-Heusler alloy," *Mater. Chem. Phys.* **265**, 124518 (2021). <https://doi.org/10.1016/j.matchemphys.2021.124518>
- [7] J. Nagura, T.M. Ashani, P.O. Adebambo, F. Ayedun, and G.A. Adebayo, "Thermoelectric and mechanical properties of XHfSn (X = Ni, Pd and Pt) semiconducting half-Heusler alloys: a first-principles study," *Comput. Condens. Matter*, **26**, e00539 (2021). <https://doi.org/10.1016/j.cocom.2021.e00539>
- [8] Vikram, J. Kangsabanik, Enamullah, and A. Alam, "Bismuth based half-Heusler alloys with giant thermoelectric figures of merit," *J. Mater. Chem. A*, **5**, 6131-6139 (2017). <https://doi.org/10.1039/C7TA00920H>
- [9] C.H. Hordequin, E. Lelievre-Berna, and J. Pierre, "Magnetization density in the half-metallic ferromagnet NiMnSb," *Phys. B*, **234-236**, 602-604 (1997). [https://doi.org/10.1016/S0921-4526\(96\)01207-0](https://doi.org/10.1016/S0921-4526(96)01207-0)
- [10] J. Tobola, J. Pierre, S. Kaprzyk, R.V. Skolozdra, and M.A. Kouacou, "Crossover from semiconductor to magnetic metal in semi-Heusler phases as a function of valence electron concentration," *J. Phys.: Condens. Matter*, **10**, 1013 (1998). <https://doi.org/10.1088/0953-8984/10/5/011>
- [11] K. Kaczmarek, J. Pierre, J. Beille, J. Tobola, R.V. Skolozdra, and G.A. Melnik, "Physical properties of the weak itinerant ferromagnet CoVSb and related semi-Heusler compounds," *J. Magn. Magn. Mater.* **187**, 210 (1998). [https://doi.org/10.1016/S0304-8853\(98\)00125-5](https://doi.org/10.1016/S0304-8853(98)00125-5)
- [12] S. Anand, K. Xia, I.V. Hegde, U. Aydemir, V. Kocovski, T. Zhu, C. Wolverton, and G.J. Snyder, "A valence balanced rule for discovery of 18-electron half-Heuslers with defects," *Energy Environ. Sci.* **11**(6), 1480-1488 (2018). <https://doi.org/10.1039/C8EE00306H>

- [13] J. Yang, H. Li, T. Wu, W. Zhang, L. Chen, and J. Yang, "Evaluation of half-Heusler compounds as thermoelectric materials based on the calculated electrical transport properties," *Adv. Funct. Mater.* **18**(19), 2880–2888 (2008). <https://doi.org/10.1002/adfm.200701369>
- [14] K. Bartholomé, B. Balke, D. Zuckermann, M. Köhne, M. Müller, K. Tarantik, and J. König, "Thermoelectric modules based on half-Heusler materials produced in large quantities," *J. Electronic Mater.* **43**(6), 1775–1781 (2014). <https://doi.org/10.1007/s11664-013-2863-x>
- [15] O.M. Abid, S. Menouer, A. Yakoubi, H. Khachai, S.B. Omran, G. Murtaza, D. Prakash, et al., "Structural, electronic, elastic, thermoelectric and thermodynamic properties of the NbMSb half heusler (M=Fe, Ru, Os) compounds with first principle calculations," *Superlattices Microstruct.* **93**, 171–185 (2016). <https://doi.org/10.1016/j.spmi.2016.01.001>
- [16] K. Bencherif, A. Yakoubi, N. Della, O.M. Abid, H. Khachai, R. Ahmed, R. Khenata, et al., "First principles investigation of the elastic, optoelectronic and thermal properties of XRuSb:(X= V, Nb, Ta) semi-Heusler compounds using the mBJ exchange potential," *J. Electron. Mater.* **45**, 3479–3490 (2016). <https://doi.org/10.1007/s11664-016-4488-3>
- [17] P.K. Kamlesh, R. Agrawal, U. Rani, and A.S. Verma, "Comprehensive ab-initio calculations of AlNiX (X = P, As and Sb) half-Heusler compounds: Stabilities and applications as green energy resources," *Materials Chemistry and Physics*, **275**, 125233 (2022). <https://doi.org/10.1016/j.matchemphys.2021.125233>
- [18] Y. Wang, J. Li, J. Wang, F. He, X. Xu, Y. Liu, and F. Yin, "Prediction of NbXGe (X = Rh, Ir) half-Heusler semiconducting compounds with promising thermoelectric property using 18-electron rule," *Applied Physics A*, **128**, 44 (2022). <https://doi.org/10.1007/s00339-021-05193-2>
- [19] D.M. Hoat, "Electronic structure and thermoelectric properties of Ta-based half-Heusler compounds with 18 valence electrons," *Computational Materials Science*, **159**, 470–477 (2019). <https://doi.org/10.1016/j.commatsci.2018.12.039>
- [20] J. Wei, and G. Wang, "Thermoelectric and optical properties of half-Heusler compound TaCoSn: A first-principle study," *Journal of Alloys and Compounds*, **757**, 118–123 (2018). <https://doi.org/10.1016/j.jallcom.2018.05.037>
- [21] W. Silpawilawan, Sora-at Tanuslip, Y. Ohishi, H. Muta, and K. Kurosaki, "Enhancement of thermoelectric figure of merit of p-type Nb_{0.9}Ti_{0.1}FeSb half-Heusler compound by nanostructuring," *Phys. status solidi a*, **217**(23), 2000419 (2020). <https://doi.org/10.1002/pssa.202000419>
- [22] P. Blaha, et al., WIEN2K, in: *An Augmented Plane Wave+ Local Orbitals Program for Calculating Crystal Properties*, edited by K. Schwarz, (Vienna University of Technology, Austria, 2001).
- [23] P. Hohenberg, and W. Kohn, "Inhomogeneous Electron Gas," *Phys. Rev.* **136**(3B), B864 (1964). <https://doi.org/10.1103/PhysRev.136.B864>
- [24] D. Singh, *Planewaves, Pseudopotentials and the LAPW Method*, (Kluwer Academic Publishers, Boston, Dordrecht, London, 1994).
- [25] J.P. Perdew, K. Burke, and M. Ernzerhof, "Generalized gradient approximation made simple," *Phys. Rev. Lett.* **77**(18), 3865 (1996). <https://doi.org/10.1103/PhysRevLett.77.3865>
- [26] Z. Wu, and R.E. Cohen, "More accurate generalized gradient approximation for solids," *Phys. Rev. B*, **73**, 235116 (2006). <https://doi.org/10.1103/PhysRevB.73.235116>
- [27] F. Tran, and P. Blaha, "Accurate Band Gaps of Semiconductors and Insulators with a Semilocal Exchange-Correlation Potential," *J. Phys. Rev. Lett.* **102**, 226401 (2009). <https://doi.org/10.1103/PhysRevLett.102.226401>
- [28] H.J. Monkhorst, and J.D. Pack, "Special points for Brillouin-zone integrations," *Phys. Rev. B*, **13**, 5188 (1976). <https://doi.org/10.1103/PhysRevB.13.5188>
- [29] P. Allen, "Boltzmann Theory and Resistivity of Metals," in: *Kluwer International Series in Engineering and Computer Science*, (1996), pp. 219–250. https://doi.org/10.1007/978-1-4613-0461-6_17
- [30] G.K. Madsen, D.J. Singh, "BoltzTraP. A code for calculating band-structure dependent quantities," *Comput. Phys. Commun.* **175**(1), 67–71 (2006). <https://doi.org/10.1016/j.cpc.2006.03.007>
- [31] S. Adachi, *Properties of Semiconductor Alloys: Group-IV, III-V and II-VI Semiconductors*, (John Wiley & Sons, 2009). <https://doi.org/10.1002/9780470744383>
- [32] J. Sun, H.T. Wang, and N.B. Ming, "Optical properties of heterodiamond B₂CN using first-principles calculations," *Appl. Phys. Lett.* **84**, 4544 (2004). <https://doi.org/10.1063/1.1758781>
- [33] J.M. Hu, S.P. Huang, Z. Xie, H. Hu, and W.D. Cheng, "First-principles study of the elastic and optical properties of the pseudocubic Si₃As₄, Ge₃As₄ and Sn₃As₄," *J. Phys.: Condens. Matter*, **19**, 496215 (2007). <https://doi.org/10.1088/0953-8984/19/49/496215>
- [34] K. Momma, and F. Izumi, "VESTA 3 for three-dimensional visualization of crystal, volumetric and morphology data," *J. Appl. Crystallogr.* **44**, 1272–1276 (2011). <https://doi.org/10.1107/S0021889811038970>
- [35] T. Graf, C. Felser, and S. Parkin, "Simple rules for the understanding of Heusler compounds," *Prog. Solid State Chem.* **39**, 1–50 (2011). <https://doi.org/10.1016/j.progsolidstchem.2011.02.001>
- [36] P.O. Adebambo, R.O. Agbaoye, A.A. Musari, B.I. Adetunji, and G.A. Adebayo, "Band structure, thermoelectric properties, effective mass and electronic fitness function of two newly discovered 18 valence electrons stable half-Heusler TaX(X=Co,Ir)Sn semiconductors: A density functional theory approach," *Solid State Sciences*, **100**, 106096 (2020). <https://doi.org/10.1016/j.solidstsciences.2019.106096>
- [37] C. Coban, Y.O. Ciftci, and K. Colakoglu, "Structural, electronic, elastic, optical, and vibrational properties of HfX₂Sb (X = Co, Rh, Ru) half-Heusler compounds: an ab initio study," *Indian J. Phys.* **90**(11), 1233–1241 (2016). <https://doi.org/10.1007/s12648-016-0873-2>
- [38] A. Amudhavalli, R. Rajeswarapalanichamy, and K. Iyakutti, "Half-metallic ferromagnetism in Ni based half Heusler alloys," *Comput. Mater. Sci.* **148**, 87–103 (2018). <https://doi.org/10.1016/j.commatsci.2018.02.026>
- [39] G.K. Gueorguiev, J. Neidhardt, S. Stafström, and L. Hultman, "First-principles calculations on the role of CN precursors for the formation of fullerene-like carbon nitride," *Chem. Phys. Lett.* **401**, 288 (2005). <https://doi.org/10.1016/j.cplett.2004.11.060>
- [40] A. Togo, and I. Tanaka, "First principles phonon calculations in materials science," *Scripta Mater.* **108**, 1–5 (2015). <https://doi.org/10.1016/j.scriptamat.2015.07.021>
- [41] M. Hong, Y. Wang, T. Feng, et al., "Strong Phonon–Phonon Interactions Securing Extraordinary Thermoelectric Ge_{1-x}Sb_xTe with Zn-Alloying-Induced Band Alignment," *J. Am. Chem. Soc.* **141**(4), 1742–1748 (2019). <https://doi.org/10.1021/jacs.8b12624>



- [42] I. Galanakis, P. Mavropoulos, and P.H. Dederichs, "Electronic structure and Slater–Pauling behaviour in half-metallic Heusler alloys calculated from first principles," *J. Phys. D: Appl. Phys.* **39**, 765–775 (2006). <https://doi.org/10.1088/0022-3727/39/5/S01>
- [43] I.K. Durukan, and Y.O. Ciftci, "First-principles calculations of vibrational and optical properties of half-Heusler NaScSi," *Indian J. Phys.* **95**(11), 2303 (2020). <https://doi.org/10.1007/s12648-020-01887-0>
- [44] J.K. Satyam, and S.M. Saini, "Narrow gap electronic structure and thermoelectric performance of p-type ErMSb (M = Ni, Pd) half Heusler compounds," *Physica B*, **631**, 413709 (2022). <https://doi.org/10.1016/j.physb.2022.413709>
- [45] J. Hornstra, and W. Bartels, "Determination of the lattice constant of epitaxial layers of III–V compounds," *J. Cryst. Growth*, **44**, 513–517 (1978). [https://doi.org/10.1016/0022-0248\(78\)90292-0](https://doi.org/10.1016/0022-0248(78)90292-0)
- [46] S. Wang, and H. Ye, "First-principles study on elastic properties and phase stability of III–V compounds," *Phys. Status Solidi*, **240**, 45 (2003). <https://doi.org/10.1002/pssb.200301861>
- [47] M. Born, and K. Huang, *Dynamics Theory of Crystal Lattices*, (Oxford University Press, 1954).
- [48] A. Iyigor, S. Al, and N. Arikan, "Density functional theory investigation on structural, mechanical, electronic and vibrational properties of Heusler alloys AlXIr_2 (X = Co, Cr, Cu, Fe and Zn)," *Chemical Physics Letters*, **806**, 140052 (2022). <https://doi.org/10.1016/j.cplett.2022.140052>
- [49] D. Kalita, M. Ram, N. Limbu, R. Kalita, and A. Saxena, "Prediction of some physical properties in new half Heusler alloy NbAgSi," *Journal of Solid State Chemistry*, **310**, 122999 (2022). <https://doi.org/10.1016/j.jssc.2022.122999>
- [50] J.-J. Shi, T. Song, P.-T. Qi, X.-Y. Wang, Z.-J. Liu, and X.-W. Sun, "Structural stabilities and half-metallicity properties of the OsTiVIn and OsZrVIn quaternary Heusler alloys under high pressure," *Journal of Magnetism and Magnetic Materials*, **566**, 170316 (2023). <https://doi.org/10.1016/j.jmmm.2022.170316>
- [51] J. Haines, J.M. Leger, and G. Bocquillon, "Synthesis and Design of Superhard Materials," *Annu. Rev. Mater. Res.* **31**, 1 (2001). <https://doi.org/10.1146/annurev.matsci.31.1.1>
- [52] S. Pugh, "XCII. Relations between the elastic moduli and the plastic properties of polycrystalline pure metals," *London, Edinburgh, and Dublin philosophical magazine and journal of science*, **45**, 823 (1954). <https://doi.org/10.1080/14786440808520496>
- [53] S. Ahmad, S.D. Mahanti, K. Hoang, and M.G. Kanatzidis, "Ab initio studies of the electronic structure of defects in PbTe," *Phys. Rev. B*, **74**, 155205 (2006). <https://doi.org/10.1103/PhysRevB.74.155205>
- [54] V. Kumar, and D.R. Roy, "Structure, bonding, stability, electronic, thermodynamic and thermoelectric properties of six different phases of indium nitride," *J. Mater. Sci.* **53**, 8302–8313 (2018). <https://doi.org/10.1007/s10853-018-2176-9>
- [55] A.H. Reshak, "Thermoelectric properties of fully hydrogenated graphene: semi-classical Boltzmann theory," *J. Appl. Phys.* **117**, 225104 (2015). <https://doi.org/10.1063/1.4922426>
- [56] A.H. Reshak, S.A. Khan, and S. Auluck, "Thermoelectric properties of a single graphene sheet and its derivatives," *J. Mater. Chem. C*, **2**, 2346–2352 (2014). <https://doi.org/10.1039/C3TC32260B>
- [57] J.A. Abraham, R. Sharma, S. Ahmad, and A. Dey, "DFT investigation on the electronic, optical and thermoelectric properties of novel half-Heusler compounds ScAuX (X = Si, Ge, Sn, Pb) for energy harvesting technologies," *Eur. Phys. J. Plus*, **136**, 109 (2021). <https://doi.org/10.1140/epjp/s13360-021-02021-7>
- [58] S. Chibani, O. Arbouche, M. Zemouli, K. Amara, Y. Benallou, Y. Azzaz, B. Belgoumene, et al., "Ab Initio Prediction of the Structural, Electronic, Elastic, and Thermoelectric Properties of Half-Heusler Ternary Compounds TiIrX (X = As and Sb)," *Journal of electronic materials*, **47**, 196–204 (2018). <https://doi.org/10.1007/s11664-017-5761-9>
- [59] M.S. Dresselhaus, *Optical properties of solids*, (New York, Academic Press, 1966).
- [60] G. Marius, *The Physics of Semiconductors: Kramers-kronig Relations*, (Springer, Berlin Heidelberg, 2010). pp. 775–776. https://doi.org/10.1007/978-3-642-13884-3_26
- [61] C. Ambrosch-Draxl, and J.O. Sofo, "Linear optical properties of solids within the full potential linearized augmented plane wave method," *Comput. Phys. Commun.* **175**, 1–14 (2006). <https://doi.org/10.1016/j.cpc.2006.03.005>
- [62] M. Irfan, M.A. Kamran, S. Azam, M.W. Iqbal, T. Alharbi, A. Majid, S.B. Omran, et al., "Electronic structure and optical properties of TaNO: an ab initio study," *J. Mol. Graph. Model.* **92**, 296–302 (2019). <https://doi.org/10.1016/j.jmglm.2019.08.006>
- [63] D.R. Penn, "Wave-Number-Dependent Dielectric Function of Semiconductors," *Phys. Rev.* **128**, 2093–2097 (1962). <https://doi.org/10.1103/PhysRev.128.2093>
- [64] M. Gajdoš, K. Hummer, G. Kresse, and J. Furthmüller, "Linear optical properties in the projector-augmented wave methodology," *Phys. Rev. B*, **73**, 045112 (2006). <https://doi.org/10.1103/PhysRevB.73.045112>
- [65] A. Azouaoui, A. Hourmatallah, N. Benzakour, and K. Bouslykhane, "First-principles study of optoelectronic and thermoelectric properties of LiCaX (X=N, P and As) half-Heusler semiconductors," *Journal of Solid State Chemistry*, **310**, 123020 (2022). <https://doi.org/10.1016/j.jssc.2022.123020>
- [66] F. Benzoudji, O.M. Abid, T. Seddik, A. Yakoubi, R. Khenata, H. Meradji, G. Uğur, et al., "Insight into the structural, elastic, electronic, thermoelectric, thermodynamic and optical properties of MRhSb (M = Ti, Zr, Hf) half-Heuslers from ab initio calculations," *Chinese Journal of Physics*, **59**, 434–448 (2019). <https://doi.org/10.1016/j.cjph.2019.04.009>
- [67] P.K. Kamlesh, R. Gautam, S. Kumari, and A.S. Verma, "Investigation of inherent properties of XScZ (X = Li, Na, K; Z = C, Si, Ge) half-Heusler compounds: Appropriate for photovoltaic and thermoelectric applications," *Physica B*, **615**, 412536 (2021). <https://doi.org/10.1016/j.physb.2020.412536>
- [68] A. Besbes, R. Djelti, and I.K. Durukan, "Study of structural, electronic, elastic, optical and thermoelectric properties of half-Heusler compound RbScSn : A TB-mBJ DFT study," *Optical and Quantum Electronics*, **54**, 372 (2022). <https://doi.org/10.1007/s11082-022-03780-y>
- [69] R. Djelti, A. Besbes, and B. Bestani, "Investigation of electronic, optical, and thermoelectric properties of new d^0 half-metallic half-Heusler alloys SiLiX (X = Ca and Sr)," *Emergent Materials*, **5**, 1097–1108 (2022). <https://doi.org/10.1007/s42247-021-00256-9>
- [70] D. Poelman, and P.F. Smet, "Methods for the determination of the optical constants of thin films from single transmission measurements: a critical review," *J. Phys. D Appl. Phys.* **36**, 1850 (2003). <https://doi.org/10.1088/0022-3727/36/15/316>

**ДОСЛІДЖЕННЯ ЕЛЕКТРОННИХ, ПРУЖНИХ, ТЕРМОЕЛЕКТРИЧНИХ ТА ОПТИЧНИХ ВЛАСТИВОСТЕЙ
НОВИХ НАПІВГЕЙСЛЕРОВИХ XRhZ ($X = \text{V}, \text{Nb}$ ТА $Z = \text{Si}, \text{Ge}$) НАПІВПРОВІДНИКІВ МЕТОДОМ DFT**Сід Ахмед Бендехіба^a, Бесбес Анісса^a, Джелгі Радуан^a, Найва Аль Бузіс^b, І. Карс Дурукан^cНуреддін Амране^b^a *Лабораторія технологій і властивостей твердих тіл, Університет Мостаганем (UMAB) – Алжир*^b *Фізичний факультет, Науковий коледж, Університет Об'єднаних Арабських Еміратів (UAEU), 15551, Аль-Айн, ОАЕ*^c *Кафедра фізики, Факультет природничих наук, Університет Газі, 06500 Анкара, Туреччина*

Теорія функціонала густини була використана для дослідження фізичних властивостей нових напівгейслерових сплавів XRhZ ($X = \text{V}, \text{Nb}$ і $Z = \text{Si}, \text{Ge}$). Обмінно-кореляційні ефекти обробляли потенціалом ТВ-mBJ. Чотири досліджувані сполуки є немагнітними напівпровідниками з непрямою забороненою зоною. Ентальпія утворення, енергія когезії та фононні зонні структури показали, що ці напівпровідники є структурно та динамічно стабільними. Пружним дослідженням було передбачено, що сполуки XRhZ ($X = \text{V}, \text{Nb}$ і $Z = \text{Si}, \text{Ge}$) мають стабільні механічні властивості, вони мають анізотропний характер і виявляють пластичну природу з відношенням $B/G > 1,75$. Оптичні результати демонструють цікавий фотокаталітичний потенціал для напівпровідників NbRhSi та NbRhGe , вони демонструють високий коефіцієнт поглинання у видимій області, який становить близько $112,104 \text{ см}^{-1}$. Для енергій понад 10 еВ (УФ-домен) показник заломлення менше одиниці. Термоелектричні результати підтвердили, що сполуки XRhZ ($X=\text{V}, \text{Nb}$ і $Z=\text{Si}, \text{Ge}$) дуже привабливі для термоелектричних пристроїв, що працюють у широкому діапазоні температур, включаючи температуру навколишнього середовища.

Ключові слова: *напівгейслерові сплави; напівпровідник; еластичні властивості; коефіцієнт Зеєбека; фактор заслуг; коефіцієнт поглинання; відбивна здатність*

EFFECT OF GADOLINIUM CONTENT ON MAGNETIC AND STRUCTURAL CHARACTERISTICS OF NFGO NANO-PARTICLES

Sara Durga Bhavani^{a,c},  K. Vijaya Kumar^{b*}, A.T. Raghavender^c, J. Arout Chelvane^d,
 B. Purna Chandra Rao^{e*}

^a Department of Chemistry, Government Degree College Rajendranagar, Rangareddy District - 501218, Telangana, India

^b Department of Physics, JNTUH University College of Engineering Jagtial, Nachupally (Kondagattu), Jagtial District 505501, Telangana, India

^c Department of Physics, International School of Technology and Sciences for Women, Rajamahendravaram, East Godavari - 533 294, Andhra Pradesh, India

^d Advanced Magnetic Group, Defence Metallurgical Research Laboratory, Kanchanbagh, Hyderabad-500 058, Telangana, India

^e Department of Chemistry, Gandhi Institute of Technology and Management, Hyderabad-502 329, Telangana, India

*Corresponding Author e-mail: kvkphd@gmail.com; pbhavnar@gitam.edu

Received November 5, 2023; revised December 7, 2023; accepted December 11, 2023

Sol gel auto-combustion was used to create gadolinium doped nickel ferrite nano-particles, which have chemical composition $\text{NiFe}_{2-x}\text{Gd}_x\text{O}_4$ ($x = 0.00, 0.010, 0.15, 0.20$ & 0.25). The investigation focused on how the composition of Gd^{+3} affected the magnetic properties and structural parameters. Magnetic properties were investigated using VSM technique, structural properties were determined using XRD and SEM techniques. XRD graphs verified the establishment of the spinel ferrite phase. With an increase in Gd composition, the crystallite size and lattice parameter increased from 21.0288 to 27.04125 nm and 8.3325 to 8.3367Å, respectively. It was also evident how the composition of Gd^{+3} affected the estimation of bond-angles and lengths in tetrahedral and octahedral structures. SEM micrographs showed that all of the grains had a small amount of agglomeration and that all of the synthesized compositions were homogenous. The range of 140.5–176.2 nm was found to be the average grain size. Using VSM at 300K, magnetic parameters like coercivity, residual magnetization, and saturation magnetization were computed. Until the composition was 0.20, the saturation magnetization and residual magnetization dropped from 30.28 emu/g to 15.35 emu/g and 5.07 emu/g to 3.65 emu/g, respectively. After that, they increased to 34.40 emu/g and 6.52 emu/g, respectively. Until composition 0.20, coercivity was raised from 154 to 261 Oe; after that, it was lowered to 233 Oe.

Keywords: Gadolinium doped nickel ferrite nano-particles; Sol gel auto-combustion; XRD; SEM and magnetic properties

PACS: 75.50.Gg, 61.05.cp, 61.05.cp, 68.37.Hk, 75.75.Fk

INTRODUCTION

The applications of spinel ferrite nano-particles in current context include drug delivery, photocatalysis, telecommunications, electronics, and electrical devices like transformer cores, permanent magnets, magnetic refrigeration, magnetic recording media, gas sensors, and microwave absorbers, among others [1-5]. Spinel ferrite is generally represented by the formula AB_2O_4 , where the B-site is referred to as octahedral at the center of the octahedron and the A-site is referred to as tetrahedral since it is positioned at the center of the tetrahedron and contains oxygen-ions at each corner. The big oxygen-ions are arranged in a face-centered cubic configuration with space between them occupied by metal-ions [6-7]. The inverse spinel structure of nickel ferrite, one of the ferrites that has been the subject of extensive research as a magnetic nanomaterial, shows that trivalent Fe^{+3} ions occupy both [A] and [B] sites whereas divalent Ni^{+2} ions occupy the octahedral [B] sites [8-9]. Researchers have employed a variety of methods to analyze the structural; electrical; optical; and magnetic properties; of their ferrite nano-particles in order to determine the impact of doping elements and manufacturing methods [10–12]. Their characteristics can be changed by doping them with rare earth elements in a cubic spinel ferrite structure [13-14]. Due to its half-filled $4f^7$ electronic configuration, gadolinium is a magnetically active high spin rare earth metal. The properties of the ferrites can be affected by a small amount of Gd doping. Since rare earth ions have high spin-orbit coupling and unpaired (4f) electrons, it is known that Fe-Fe exchanges in ferrites are caused by the spin coupling of (3d) electrons, which affects the structural, electrical, optical, and magnetic properties. Better magnetic and electrical properties result from rare earth ion interaction with Fe, or 3d-4f coupling, when these ions occupy ferrite lattice positions [15–16]. Furthermore, studies on the doping of ions in CoFe_2O_4 nano-particles have been published, and the results indicate that the characteristics of ferrites vary significantly [13]. There are few studies on Gd-doped nickel ferrites nano-particles in the literature that has been released [17–18], with the exception of those that concentrate on the composite materials' magnetic characteristics. Consequently, the composition of Gd^{+3} affects structural characteristics and magnetic properties in the current work, which is synthesized using the Sol gel (auto-combustion) process.

II. EXPERIMENTAL

According to Figure.1 [19–21], sol gel (auto-combustion) process was used to create $\text{NiFe}_{2-x}\text{Gd}_x\text{O}_4$ ($x = 0.00, 0.010, 0.15, 0.20$ & 0.25) ferrite nano-particles.

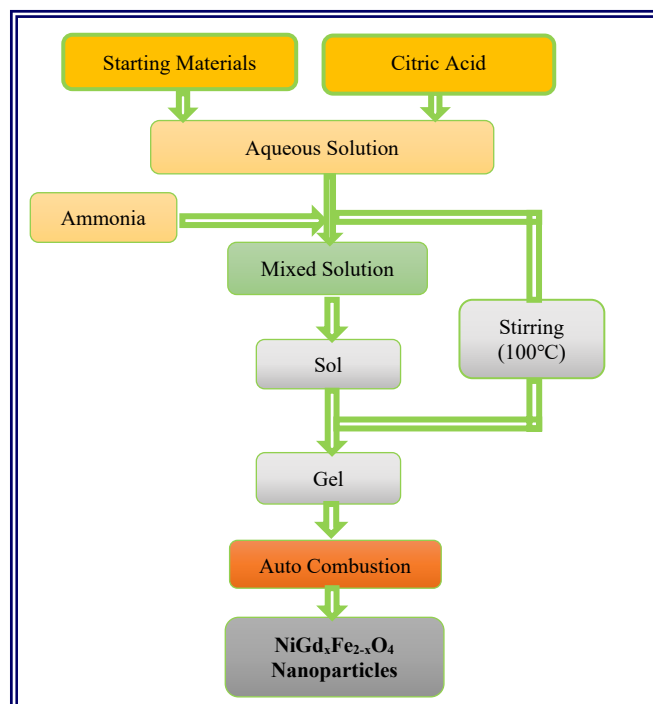


Figure 1. Flowchart of synthesis of $\text{NiFe}_{2-x}\text{Gd}_x\text{O}_4$ ($x = 0.00, 0.05, 0.10, 0.15, 0.20$ & 0.25) ferrite nano-particles

The precursor materials included ammonia, citric acid, ferric and gadolinium nitrates were AR graded. De-ionized water was used to dissolve the precursor materials in a stoichiometric ratio to create a transparent solution. The solution containing Ni^{+2} , Gd^{+3} , and Fe^{+3} ions was chelated by adding citric acid to the organized aqueous solution. Citric acid and total moles of nitrate ions were combined in 1:3 molar ratio. The attained solution was neutralized with ammonia in an appropriate amount to maintain a pH of 7. A hot plate was then used to heat the neutralized solution to approximately 100°C while stirring continuously. A thick gel was seen a few hours later. A loose powder [22–23] remained after the temperature was raised to 200°C , which started the ignition process and caused the generated gel to burn completely through auto-combustion. It was annealed for eight hours at 700°C and was known as "as-prepared powder."

Using a Phillips expert X-ray diffractometer, the XRD patterns for $\text{NiFe}_{2-x}\text{Gd}_x\text{O}_4$ ($x = 0.00, 0.010, 0.15, 0.20$ & 0.25) ferrite nano-particles were obtained. The $\text{NiFe}_{2-x}\text{Gd}_x\text{O}_4$ ($x = 0.00, 0.010, 0.15, 0.20$ & 0.25) ferrite nano-particles' microstructural morphology was examined using a ZEISS EVO-18 SEM. VSM were used to measure the magnetic properties at 300 K and a maximum applied magnetic field (15 kOe).

RESULTS AND DISCUSSIONS

Figure 2 displays XRD patterns of $\text{NiFe}_{2-x}\text{Gd}_x\text{O}_4$ ($x = 0.00, 0.10, 0.15, 0.20, 0.25$) ferrite nano-particles that were annealed for eight hours at 700°C [25]. Single-phase; cubic spinel structure; and $\text{Fd}\bar{3}\text{m}$ space-group; are indicated by XRD patterns. Because of nano-crystalline pattern of the prepared compositions, XRD data showed that XRD peaks grew wider with increasing Gd doping content. The variance in ionic-radius of Ni (0.74 \AA) and Gd (0.94 \AA) could be cause of slight shift in peak position observed with increase in Gd^{+3} composition. Various structural parameters were computed from XRD patterns using standard relations listed below.

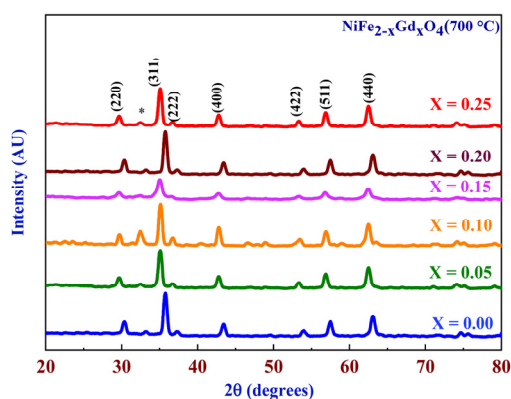


Figure 2. XRD pattern of $\text{NiFe}_{2-x}\text{Gd}_x\text{O}_4$ ($x = 0.00, 0.05, 0.10, 0.15, 0.20$ & 0.25) ferrite nano-particles annealed at 700°C [K.V. Kumar et al, (2023), Eur. Chem. Bull. 2023,12(4) 10479-1048]

The crystallite-size (D) of $\text{NiFe}_{2-x}\text{Gd}_x\text{O}_4$ ($x = 0.00, 0.010, 0.15, 0.20$ & 0.25) ferrite nano-particles was calculated for present XRD patterns using the Scherrer's formula [25]:

$$D = \frac{0.94\lambda}{\beta \cos\theta} \tag{1}$$

where, θ -diffraction angle, λ -wavelength (Co $K\alpha$ radiation), β -FWHM and D -crystallite size.

Using 2θ -values, interplanar spacing & lattice parameter of $\text{NiFe}_{2-x}\text{Gd}_x\text{O}_4$ ($x = 0.00, 0.010, 0.15, 0.20$ & 0.25) ferrite nano-particles was calculated with the following formula [26]:

$$a = \frac{d}{\sqrt{h^2+k^2+l^2}} \tag{2}$$

Crystallite size and lattice parameter were observed to increase with Gd^{+3} composition and were obtained in the range of 21.0288 to 27.04125 nm and 8.3325 to 8.3367Å respectively are tabulated in Table 1 and shown their variation with Gd composition in Figure 3. The improved values of lattice parameter confirmed the entrance of Gd^{+3} ions into the structure [27-28].

Table 1. Average Crystallite size, Lattice parameter and average interplanar spacing & average grain size of $\text{NiFe}_{2-x}\text{Gd}_x\text{O}_4$ ($x = 0.00, 0.05, 0.10, 0.15, 0.20$ & 0.25) ferrite nano-particles annealed at 700°C.

Gd Composition	Average Crystallite Size (nm)	Lattice parameter (Å)	Average Interplanar spacing (Å)	Average Grain size (nm)
0.0	21.02875	8.3325	2.17625	140.5
0.05	22.45000	8.3326	2.20625	145
0.10	25.06000	8.3327	2.20625	159.1
0.15	26.68375	8.3329	2.20500	153.33
0.20	27.04125	8.3333	2.20750	154.2
0.25	27.37250	8.3367	2.18875	176.2

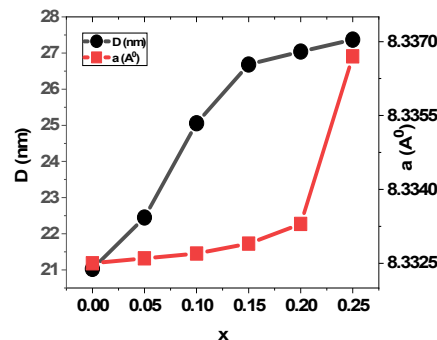


Figure 3. Variation of crystallite size (D) and lattice constant (a) for $\text{NiFe}_{2-x}\text{Gd}_x\text{O}_4$ ($x = 0.00, 0.05, 0.10, 0.15, 0.20$ & 0.25) ferrite nano-particles annealed at 700°C

Three different kinds of magnetic-interactions between the cations could be possible via intermediate oxygen-ions through the super-exchange mechanism because the metal-ions occupy at two different lattice sites in the spinel structure: A-A interaction, B-B interaction, and A-B interaction. The angles between cations dispersed over two sites and the distances between cations and oxygen determine an amount of interaction energy between relating cations. In order to investigate how the composition of Gd^{+3} affected the structural characteristics of the ferrite nanoparticles, as illustrated in Figure 4 [29].

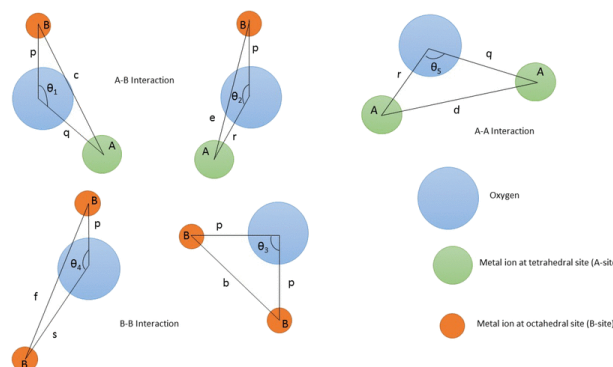


Figure 4. Ion pair configuration in spinel ferrite with bond lengths and bond angles [Raghvendra Singh Yadav et al., 2018, Journal of Materials Science: Materials in Electronics, 29, 15878-15893]

The bond-lengths between the cations at the tetrahedral and octahedral sites designated as b, c, d, e, and f were estimated. The subsequent formulas (3-7) [30] can be used to assess these:

$$b = \sqrt{2} \left(\frac{a}{4}\right) \quad (3)$$

$$c = \sqrt{11} \left(\frac{a}{8}\right) \quad (4)$$

$$d = \sqrt{3} \left(\frac{a}{4}\right) \quad (5)$$

$$e = \sqrt{3} \left(\frac{3a}{8}\right) \quad (6)$$

$$f = \sqrt{6} \left(\frac{a}{4}\right) \quad (7)$$

The bond lengths of the ferrite nano-particles between metal-ions and oxygen at various sites are denoted by the following equations (8-11) [30] and are represented as p, q, r, and s (bond-lengths between cation-anion) in Figure-4 [29]:

$$p = a \left(\frac{5}{8} - u\right) \quad (8)$$

$$q = a\sqrt{3} \left(u - \frac{1}{4}\right) \quad (9)$$

$$r = a\sqrt{11} \left(u - \frac{1}{8}\right) \quad (10)$$

$$s = a\sqrt{3} \left(\frac{u}{3} + \frac{1}{8}\right) \quad (11)$$

Equations (12-16) [31] can be used to determine the bond-angles between cations (oxygen-ions) and cation-anion (metal-ions) of the ferrite nano-particles, which are represented as θ_1 , θ_2 , θ_3 , θ_4 and θ_5 . The same was depicted in Figure-4 [28]:

$$\theta_1 = \cos^{-1} \left(\frac{p^2+q^2-c^2}{2pq}\right) \quad (12)$$

$$\theta_2 = \cos^{-1} \left(\frac{p^2+r^2-e^2}{2pr}\right) \quad (13)$$

$$\theta_3 = \cos^{-1} \left(\frac{2p^2-b^2}{2p^2}\right) \quad (14)$$

$$\theta_4 = \cos^{-1} \left(\frac{p^2+s^2-f^2}{2ps}\right) \quad (15)$$

$$\theta_5 = \cos^{-1} \left(\frac{p^2+q^2-d^2}{2rq}\right) \quad (16)$$

Tables 2, 3 & 4 contains a tabulation of all bond-length values and bond-angle values between cations and cation-anions. It was discovered that the Gd^{+3} composition increased the interatomic distance between the cations at two distinct sites (A & B) and the cation-anion. The greater ionic radius of Gd^{+3} ions is the cause of this variation. A-B and B-B interactions were found strengthened, as indicated by the increased bond-angles θ_1 , θ_2 , θ_3 , θ_4 and θ_5 [32-33].

Table 2. Variation of bond lengths between cations situated in $NiFe_{2-x}Gd_xO_4$ ($x = 0.00, 0.05, 0.10, 0.15, 0.20$ & 0.25) ferrite nano-particles annealed at $700^\circ C$

Gd Composition	b (Å)	c (Å)	d (Å)	e (Å)	f (Å)
0.0	2.945984	3.454472	3.608078	5.412118	5.102593
0.05	2.946019	3.454513	3.608122	5.412182	5.102655
0.10	2.946054	3.454555	3.608165	5.412247	5.102716
0.15	2.946125	3.454638	3.608252	5.412377	5.102838
0.20	2.946266	3.454804	3.608425	5.412637	5.103083
0.25	2.947469	3.456213	3.609897	5.414845	5.105165

Table 3. Variation of bond lengths between cation-anion situated in $NiFe_{2-x}Gd_xO_4$ ($x = 0.00, 0.05, 0.10, 0.15, 0.20$ & 0.25) ferrite nano-particles annealed at $700^\circ C$

Gd Composition	p (Å)	q (Å)	r (Å)	s (Å)
0.0	2.083125	1.804039	6.908944	3.6080783
0.05	2.08315	1.804061	6.9090269	3.6081216
0.10	2.083175	1.804082	6.9091098	3.6081649
0.15	2.083225	1.804126	6.9092757	3.6082515
0.20	2.083325	1.804212	6.9096073	3.6084247
0.25	2.084175	1.804948	6.9124265	3.609897

The morphological study of all the compositions was done by SEM. Micrographs of all Gd doped nickel ferrite compositions are shown in Figure 5, Numerous voids and pores are visible in non-uniform agglomerated fragments [15]. It was observed that every grain was dispersed randomly and had non-uniform sizes [16]. The average grain size was found increased with Gd^{+3} composition and it was observed in the range of 140.5-176.2 nm, tabulated in Table 1.

Table 4. Variation of bond angles between cations and cation-anion situated in $\text{NiFe}_{2-x}\text{Gd}_x\text{O}_4$ ($x=0.00, 0.05, 0.10, 0.15, 0.20$ & 0.25) ferrite nano-particles annealed at 700°C

Gd Composition	θ_1	θ_2	θ_3	θ_4	θ_5
0.0	125.2644	128.7162	91.4562	125.2644	88.4764
0.05	125.2662	128.7421	91.51876	125.6989	88.48011
0.10	125.2714	128.7622	91.51945	126.0281	88.4827
0.15	125.2732	128.7713	91.56347	126.2492	88.48441
0.20	125.2754	128.7784	91.58002	126.3602	88.48526
0.25	125.2734	128.7862	91.58176	126.6956	88.48781

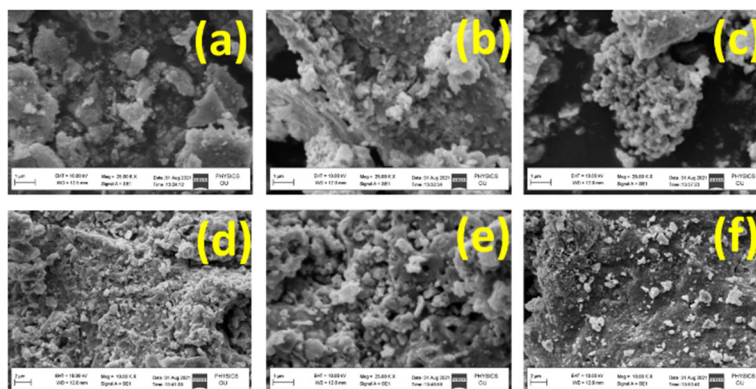


Figure 5. SEM images of $\text{NiFe}_{2-x}\text{Gd}_x\text{O}_4$ ($x = 0.00, 0.05, 0.10, 0.15, 0.20$ & 0.25) ferrite nano-particles annealed at 700°C

At room temperature, the magnetic properties of $\text{NiFe}_{2-x}\text{Gd}_x\text{O}_4$ ($x = 0.00, 0.010, 0.15, 0.20$ & 0.25) ferrite nano-particles were examined using a VSM. The synthesis method, grain size, cation doping, cation re-distribution, and other factors are major determinants of the magnetic properties of ferrite nano-particles [34]. Ferrite nano-particles' magnetic properties are mostly influenced by the $\text{Fe}^{+3}\text{-Fe}^{+3}$ interaction and the spin coupling of their third-dimensional electrons. When Gd^{+3} enters the Fe lattice, according to the cation distribution, the $\text{Gd}^{+3}\text{-Fe}^{+3}$ interaction happens with 3d-4f electrons spin coupling, and hence Gd^{+3} ions will replace Fe^{+3} ions in octahedral [B] site. Figure 6 illustrates the hysteresis of $\text{NiFe}_{2-x}\text{Gd}_x\text{O}_4$ ($x = 0.00, 0.05, 0.10, 0.15, 0.20$ & 0.25) ferrite nano-particles annealed at 700°C . The derived parameters such as saturation magnetization, remanent magnetization and coercivity are tabulated in Table 5.

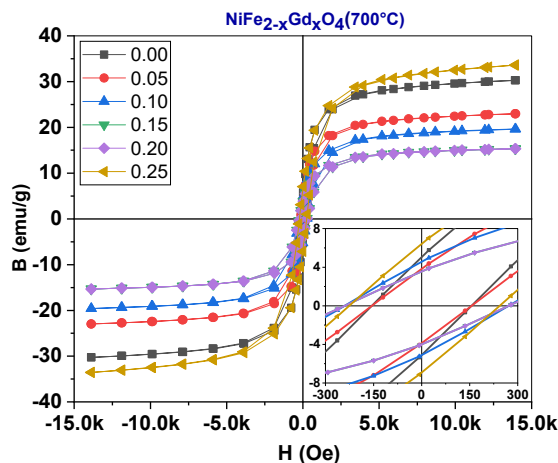


Figure 6. Hysteresis loops of $\text{NiFe}_{2-x}\text{Gd}_x\text{O}_4$ ($x = 0.00, 0.05, 0.10, 0.15, 0.20$ & 0.25) ferrite nano-particles annealed at 700°C

Table 5. Coercivity H_c (Oe), residual magnetization M_r (emu/g) and saturation magnetization M_s (emu/g) of $\text{NiFe}_{2-x}\text{Gd}_x\text{O}_4$ ($x = 0.00, 0.05, 0.10, 0.15, 0.20$ & 0.25) ferrite nano-particles annealed at 700°C

Gd Composition	H_c (Oe)	M_r (emu/g)	M_s (emu/g)
0.0	154	5.07	30.28
0.05	156	3.82	27.95
0.10	257	4.54	19.73
0.15	261	3.65	15.35
0.20	261	3.65	15.35
0.25	233	6.52	34.40

In general, Gd^{+3} ions have a magnetic moment of 7.9 BM whereas Fe^{+3} ions have magnetic moment 5 BM. Observing the Gd^{+3} and Fe^{+3} ions magnetic moments, the magnetization for all the compositions was supposed to increase Gd^{+3} composition in nickel ferrites. But it is clearly observed from Table-5 that M_s values and M_r values were decreased from 30.28 to 15.35 emu/g and 5.07 to 3.65 emu/g respectively. The coercivity was increased from 154 Oe to 261 Oe and the magnetization change may be due to Gd^{+3} - Fe^{+3} interactions. Figure-7 illustrate the variation of coercivity (H_c) and saturation magnetization (M_s) for $NiFe_{2-x}Gd_xO_4$ ($x = 0.00, 0.05, 0.10, 0.15, 0.20$ & 0.25) ferrite nano-particles annealed at $700^\circ C$.

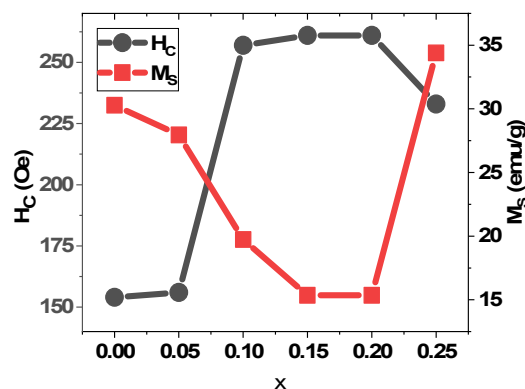


Figure 7. Variation of coercivity (H_c) and saturation magnetization (M_s) for $NiFe_{2-x}Gd_xO_4$ ($x = 0.00, 0.05, 0.10, 0.15, 0.20$ & 0.25) ferrite nano-particles annealed at $700^\circ C$

The strength of the spin-orbital coupling in ferrite materials limits their magnetic anisotropy. Presence of larger magnetic anisotropy in the ferrites results in the larger coercivity. Doping of Gd^{+3} ions in the nickel ferrites has resulted in the increase of coercivity which makes these ferrite compositions magnetically hard. Similar kind of results were observed for Tb^{+3} doped cobalt ferrites [35-36]. Presence of Gd^{+3} ions weaken the super-exchange interactions in nickel ferrites [37-38].

CONCLUSION

Sol gel auto-combustion was used to create $NiFe_{2-x}Gd_xO_4$ ($x = 0.00, 0.010, 0.15, 0.20$ & 0.25), ferrite nano-particles that were then annealed for eight hours at $700^\circ C$. The increased ionic radii of rare earth ions (Gd^{+3}) are responsible for the structural parameters, such as crystallite size and lattice parameter, which increased from 21.0288 to 27.04125 nm and 8.3325 to 8.3367Å, respectively, with Gd^{+3} composition. Estimates of the tetrahedral, octahedral, and bond-angles also demonstrated significant variation with the Gd^{+3} composition. The average grain size, which ranged from 140.5 to 176.2 nm, was found to increase with Gd composition. The composition of Gd resulted in a decrease in both saturation and residual magnetization. Gd content increases the coercivity and gives ferrite nano-particles their magnetic hardness.

ORCID

©K. Vijaya Kumar, <https://orcid.org/0000-0001-6160-8632>; ©B. Purna Chandra Rao, <https://orcid.org/0000-0001-7266-3338>

REFERENCES

- [1] X. Li, J. Wei, K.E. Aifantis, Y. Fun, Q. Feng, F.-Z. Cui, and F. Watari, Journal of Biomedical Materials Research Part A, **104**(5), 1285 (2016). <http://dx.doi.org/10.1002/jbm.a.35654>
- [2] K.K. Kefeni, T.A. Msagati, T.T. Nkambule, and B.B. Mamba, Mater. Sci. Eng. C: Mater. Biol. Appl. **107**, 110314 (2020). <https://doi.org/10.1016/j.msec.2019.110314>
- [3] K.K. Kefeni, and B.B. Mamba, Sustainable Materials and Technologies, **23**, e00140 (2020). <https://doi.org/10.1016/j.susmat.2019.e00140>
- [4] M.I. Hussain, M. Xia, X.N. Ren, K. Akhtar, A. Nawaz, S.K. Sharma, and Y. Javed, in: *Magnetic Nanoheterostructures*, (Springer, Cham, 2020), pp. 243-265.
- [5] P.B. Kharat, B.S. Sandeep, P.K. Pankaj, and K.M. Jadhav, ACS omega, **5**(36), 23378 (2020). <https://doi.org/10.1021/acsomega.0c03332>
- [6] L.B. Tahar, M. Artus, S. Ammar, L.S. Smiri, F. Herbst, M.-J. Vaulay, V. Richard, et al., J. Magn. Magn. Mater. **320**, 3242 (2008). <https://doi.org/10.1016/j.jmmm.2008.06.031>
- [7] M.M. Rashad, R.M. Mohamed, and H. El-Shall, J. Mat. Proc. Tech. **198**(1-3), 139146 (2008). <https://doi.org/10.1016/j.jmatprotec.2007.07.012>
- [8] S.B. Narang, and K. Pubby, Journal of Magnetism and Magnetic Materials, **519**, 167163 (2020), <https://doi.org/10.1016/j.jmmm.2020.167163>
- [9] K.V. Kumar, Advances in Materials Physics and Chemistry, **12**(3), 33 (2022). <https://doi.org/10.4236/ampc.2022.123003>
- [10] V.A. Bharati, S.R. Patade, S. Bajaj, R. Parlikar, A.P. Keche, and V.V. Sondur, Journal of Physics: Conference Series, **1644**, (1), 0120005 (2020). <https://doi.org/10.1088/17426596/1644/1/012005>
- [11] N. Soltani, A.B. Syuhada, W.M.M. Yunus, E. Saion, and A. Bahrami, Solid State Comm. **192**, 15 (2014). <http://dx.doi.org/10.1016/j.ssc.2014.05.002>
- [12] K.V. Kumar, R. Sridhar, and D. Ravinder, International Journal of Nano-particle Research, **2**(6), (2018). <https://doi.org/10.28933/ijnr-2018-01-0302>
- [13] V.S. Puli, S. Adireddy, and C.V. Ramana, J. Alloys and Comp. **644**, 470 (2015). <http://dx.doi.org/10.1016%2Fj.jallcom.2015.05.031>

- [14] M. Humayun, H. Ullah, M. Usman, A. Habibi-Yangjeh, A.A. Tahir, C. Wang, and W. Luo, *Journal of Energy Chemistry*, **66**, 314 (2022). <https://doi.org/10.1016/j.jechem.2021.08.023>
- [15] J. Jiang, L. Li, F. Xu, and Y. Xie, *Materials Science and Engineering: B*, **137**(1-3), 166 (2007). <http://dx.doi.org/10.1016/j.mseb.2006.11.014>
- [16] J. Jing, L. Liangchao, and X. Feng, *Journal of Rare Earths*, **25**(1), 79 (2007). [https://doi.org/10.1016/S1002-0721\(07\)60049-0](https://doi.org/10.1016/S1002-0721(07)60049-0)
- [17] N.C. Sena, T.J. Castro, V.K. Garg, A.C. Oliveira, P.C. Morais, S.W. da Silva, **43**(5), 4042 (2017). <https://doi.org/10.1016/j.ceramint.2016.11.155>
- [18] Z.K. Heiba, M.B. Mohamed, L. Arda, and N. Dogan, *Journal of Magnetism and Magnetic Materials*, **391**, 195 (2015). <https://doi.org/10.1016/j.jmmm.2015.05.003>
- [19] K.R. Krishna, K.V. Kumar, and R. Dachehalli, *Advances in Materials Physics and Chemistry*, **2**, 185 (2012). <http://dx.doi.org/10.4236/ampc.2012.23028>
- [20] K.V. Kumar, and S.D. Bhavani, *Science of Sintering*, **54**(4), 457 (2022). <https://doi.org/10.2298/SOS2204457K>
- [21] A.T. Raghavender, N. Biliškov, and Z. Skoko, *Materials Letters*, **65**(4), 677 (2011). <https://doi.org/10.1016/j.matlet.2010.11.071>
- [22] L.J. Berchmans, R.K. Selvan, and C.O. Augustin, *Materials Letters*, **58**, 1928 (2004). <http://dx.doi.org/10.1016/j.matlet.2003.12.008>
- [23] Z. Yue, J. Zhou, L. Li, X. Wang, and Z. Gui, *Materials Science and Engineering: B*, **86**, 64 (2001). [https://doi.org/10.1016/S0921-5107\(01\)00660-2](https://doi.org/10.1016/S0921-5107(01)00660-2)
- [24] V.K. Katrapally, and S.D. Bhavani, *Phase Transitions*, **95**(11), 770 (2022). <https://doi.org/10.1080/01411594.2022.2117622>
- [25] S.D. Bhavani, A.T. Raghavender, K.V. Kumar, and B.P.C. Rao, *Eur. Chem. Bull.* **12**(Special Issue 4), 10479 (2023). <https://doi.org/10.31838/ecb/2023.12.si4.0572023.22/04/202>
- [26] V. Patil, S.E. Shirsath, S. More, S. Shukla, and K. Jadhav, *Journal of Alloys and Compounds*, **488**, 199 (2009). <https://doi.org/10.1016/j.jallcom.2009.08.078>
- [27] M. Kumari, and M.C. Bhatnagar, *AIP Conference Proceedings*, **2220**(1), 110042 (2020). <http://dx.doi.org/10.1063/5.0002231>
- [28] M.A. Yousuf, M.M. Baig, N.F. Al-Khali, M.A. Khan, M.F. Aly Aboud, I. Shakir, and M.F. Warsi, *Ceram. Int.* **45**, 10936 (2019). <http://dx.doi.org/10.1016/j.ceramint.2019.02.174>
- [29] T. Ahmad, S. Khatoon, K. Coolahan, and S. Lofland, *Journal of Materials Research*, **28**, 1245 (2013). <https://doi.org/10.1557/jmr.2013.69>
- [30] R.S. Yadav, I. Kuritka, J. Vilcakova, J. Havlica, L. Kalina, P. Urbanek, M. Machovsky, et al., *Journal of Materials Science: Materials in Electronics*, **29**, 15878 (2018). <https://doi.org/10.1007/s10854-018-9674-z>
- [31] P.P. Naik, R.B. Tangsali, S.S. Meena, and S.M. Yusuf, *Mater. Chem. Phys.* **191**, 215 (2017). <https://doi.org/10.1016/j.matchemphys.2017.01.032>
- [32] Z. Yan, and J. Luo, *J. Alloys Compd.* **695**, 1185 (2017). <https://doi.org/10.1016/j.jallcom.2016.08.333>
- [33] Z. Karimi, Y. Mohammedi, H. Shokrollahi, Sh.Kh. Asl, Gh. Yousefi, and L. Karimi, *J. Magn. Magn. Mater.* **361**, 150 (2014). <https://doi.org/10.1016/j.jmmm.2014.01.016>
- [34] Z.K. Heiba, M.B. Mohamed, L. Arda, and N. Dogan, *Journal of Magnetism and Magnetic Materials*, **391**, 195 (2015). <https://doi.org/10.1016/j.jmmm.2015.05.003>
- [35] M.A. Dar, and D. Varshney, *J. Magn. Magn. Mater.* **436**, 101 (2017). <https://doi.org/10.1016/j.jmmm.2017.04.046>
- [36] T. Sodaee, A. Ghasemi, and E. Paimozd, *Materials Physics and Mechanics*, **17**, 11 (2013). https://www.ipme.ru/e-journals/MPM/no_11713/MPM117_03_sodaee.pdf
- [37] T. Sodaee, A. Ghasemi, E. Paimozd, A. Paesano, and A. Morisako, *Journal of electronic materials*, **42**, 2771 (2013). <https://link.springer.com/article/10.1007/s11664-013-2656-2#citeas>
- [38] K.K. Bamzai, G. Kour, B. Kaur, M. Arora, and R.P. Pant, *Journal of magnetism and magnetic materials*, **345**, 255 (2013). <https://doi.org/10.1016/j.jmmm.2013.07.002>
- [39] M.L. Kahn, and Z.J. Zhang, *Applied Physics Letters*, **78**(23), 3651 (2001). <https://doi.org/10.1063/1.1377621>

ВПЛИВ ВМІСТУ ГАДОЛІНІЮ НА МАГНІТНІ ТА СТРУКТУРНІ ХАРАКТЕРИСТИКИ НАНОЧАСТИНОК NFGO

Сара Дурга Бхавані^{a,c}, К. Віджая Кумар^{b*}, А.Т. Рагхавендер^c, Дж. Арут Челвейн^d, Б. Пурна Чандра Рао^{e*}

^a Факультет хімії, державний коледж Раджсендрангар, округ Рангаредді - 501218, Телангана, Індія

^b Факультет фізики, JNTUH Університетський інженерний коледж Джагтіал, Начупаллі (Кондагату),
Округ Джагтіал 505501, Телангана, Індія

^c Факультет фізики, Міжнародна школа технологій і наук для жінок, Раджамахендраварам,
Східний Годаварі -533 294, Андхра-Прадеш, Індія

^d Магнітна група, Лабораторія оборонних металургійних досліджень, Канчанбаг, Хайдарабад-500058, Телангана, Індія

^e Департамент хімії, Інститут технології та менеджменту Ганді, Хайдарабад-502 329, Телангана, Індія

Для створення наночастинок фериту нікелю, легованого гадолінієм, які мають хімічний склад $\text{NiFe}_{2-x}\text{Gd}_x\text{O}_4$ ($x = 0,00, 0,010, 0,15, 0,20$ і $0,25$) було використано золь-гель автоспалювання. Дослідження було зосереджено на тому, як склад Gd^{+3} вплинув на магнітні властивості та структурні параметри. Магнітні властивості досліджували методом VSM, структурні властивості визначали методами XRD та SEM. XRD-графіки підтвердили встановлення шпінельної феритової фази. Зі збільшенням складу Gd розмір кристалітів і параметр ґратки збільшилися з 21,0288 до 27,04125 нм і 8,3325 до 8,3367 Å відповідно. Було також очевидно, як склад Gd^{+3} вплинув на оцінку зв'язкових кутів і довжин у тетраедричних і октаедричних структурах. Мікрофотографії SEM показали, що всі зерна мали невелику кількість агломерації і що всі синтезовані композиції були однорідними. Встановлено, що діапазон 140,5–176,2 нм є середнім розміром зерна. Використовуючи VSM при 300K, були обчислені такі магнітні параметри, як коерцитивна сила, залишкова намагніченість і намагніченість насичення. Поки склад не становив 0,20, намагніченість насичення та залишкова намагніченість падали з 30,28 emu/g до 15,35 emu/g і з 5,07 emu/g до 3,65 emu/g відповідно. Після цього вони зросли до 34,40 emu/g і 6,52 emu/g відповідно. До складу 0,20 коерцитивна сила була підвищена з 154 до 261 Oe; після цього його знизили до 233 E.

Ключові слова: наночастинок фериту нікелю, леговані гадолінієм; золь-гель автоспалювання; XRD; SEM і магнітні властивості

EFFECT OF BIOSYNTHESIZED SILVER NANOPARTICLES ON THE OPTICAL, STRUCTURAL, AND MORPHOLOGICAL PROPERTIES OF TiO₂ NANOCRYSTALS

Jamila Tasiu^a, Muhammad Y. Onimisi^b,  Abubakar S. Yusuf^c,  Eli Danladi^{d*}, Nicholas N. Tasié^e

^a Department of Physics, Kaduna State University, Kaduna, Nigeria

^b Department of Physics, Nigerian Defence Academy, Kaduna, Nigeria

^c Department of Physics, Federal University of Technology, P.M.B 65, Minna, Nigeria State, Nigeria

^d Department of Physics, Federal University of Health Sciences, Otukpo, Benue State, Nigeria

^e Department of Physics, Rivers State University, Port Harcourt, Rivers State, Nigeria

*Corresponding Author e-mail: danladielibako@gmail.com

Received October 28, 2023; revised December 6, 2023; accepted December 8, 2023

The development of efficient metal doped semiconductors for Photovoltaic applications has gained a lot of research attention. In this present paper, pure and silver nanoparticles (AgNPs)-modified TiO₂ nanocrystals (NCs) with different amount of AgNPs (say 50, 100, 150, 200, and 250 μL) were achieved and the effects of AgNPs on the TiO₂ NCs were explored systematically. The optical, structural and morphological properties were probed using UV-visible spectrophotometer, X-ray diffraction (XRD), and scanning electron microscope (SEM). The results of the optical studies showed a characteristic peak of TiO₂ and the redshifting of the peak position was observed by introducing AgNPs. The synergetic effects from AgNPs and TiO₂ results to diminished band gap. The XRD result confirmed the formation of a tetragonal anatase TiO₂ phase with a decrease in crystallite size with increasing AgNPs content. The SEM images show enhanced nucleation and film growth with presence of shining surface which can be seen to contribute to good photon management by enhancing light scattering. The unadulterated TiO₂ and AgNPs-modified TiO₂ have spherical morphology and uniform size distribution ranging from 20 to 30 nm. This study established the view that surface modification of TiO₂ with AgNPs is a viable approach towards achieving an efficient light photocatalyst.

Keywords: AgNPs; TiO₂; Nanocomposites; LSPR Effect; Photocatalyst

PACS: 61.05.C-, 78.20.-e, 68.37.-d, 81.07.-b, 88.40.H-, 87.64.Ee

1. INTRODUCTION

Titanium dioxide (TiO₂) is a highly studied semiconductor due to its optoelectronic nature and high chemical stability [1] and has been proven to be one of the materials that have found applications in sensors, antireflective coatings, electrochromic devices, solar energy conversion [2] etc. Nanocrystalline TiO₂ is classified as one of the successful nanomaterials applied for photocatalytic and photoelectrochemical [3]. One of the disadvantages of TiO₂ is its wide band gap (for anatase phase is $E_g = 3.2$ eV, for rutile is 3.0 eV) that have made the absorption coefficient limited for applications in the visible region of the electromagnetic spectrum. As a result, altering the band gap of TiO₂ to render it photosensitive in the visible-light region of electromagnetic spectrum with low electron-hole recombination is considered a viable alternative in photocatalysis [4].

One of the path-way to improving the photocatalytic properties is incorporation of noble metal nanoparticles, such as Pt, Ag, Pd, Au, and alloys which can display plasmonic effect in TiO₂ matrix. This will render it active in visible light harvesting and charge carrier separation simultaneously without sacrificing its crystal quality [5,6].

When noble metals come in contact with TiO₂, they behave as electron reservoir suppressing the recombination rate and significantly enhance carrier life time [4]. Among the noble metals, silver nanoparticles (Ag NPs) have displayed some extra ordinary properties that makes it attractive for application in different catalyst. Amongst these properties are; unique physical, chemical, electronic, and optical properties [4,7,8]. Introducing AgNPs in the TiO₂ environment also results to increase in photocatalytic efficiency by interfacial charge transfer that takes place through Ti-Ag-O phase and the presence of oxygen vacancies [4,9]. During sunlight visible interaction with the AgNPs, surface plasmon resonance effect is displayed which drive the electron from AgNPs to TiO₂ or the vice versa and in turn enhance light harvesting due to frequency matching [10,11].

Different methods of fabricating Ag doped TiO₂ have been demonstrated. For instance, some studies have utilized a chemical reduction method to introduce Ag⁺ into TiO₂ NPs [9,12]. Photo reduction method was used by Yang et al. [13] to introduce silver nitrate (AgNO₃) into TiO₂ NPs under UV light. In another study by Zhou et al. [14], they fabricated Ag/Ag-doped TiO₂ using modified sol-hydrothermal method in the presence of NaOH as additive. Daniel et al. [1] used successive ionic layer absorption and reaction to introduce AgNPs in TiO₂. Although in the reported works, chemical route was utilized to fabricate Ag doped TiO₂ NCs.

In our present work, we reported the biosynthesis of AgNPs and its effect on TiO₂ nanocrystal. The effect of the Ag nanoparticles on the optical, structural, and morphological was explored in a systematic way. The results showed that on introducing different amount of AgNPs through spin coating, the band optical properties of TiO₂ matrix were enhanced resulting to diminished bandgap of TiO₂ which presents good prospects for photocatalytic activity and photovoltaic

applications. This entire paper is presented in four sections. After the introduction section is the materials and method section, which offers a full description related to the synthesis and fabrication techniques. Section 3, includes the results and discussion. The conclusion section includes a summary of the findings.

2. MATERIALS AND METHODS

2.1. Materials

Ti-Nanoxide (T/SP36) was purchased from solaronix, Methanol (99.8%), Silver nitrate (99%), the commercial titanium dioxide (99.5%), Degussa P25, Sodium hydroxide (98.5%), were supplied by Sigma Aldrich. All the chemicals were of analytical grade and used as received without any further purification.

2.2. Preparation of Titanium dioxide

The Titanium Nanoxide T/SP 36 was diluted in absolute ethanol in the ratio 1:3 respectively to obtain the required composition. The prepared TiO₂ solution was sealed with aluminum foil to prevent it from absorbing moisture.

2.2. Preparation of biosynthesized AgNPs

The silver nanoparticle (AgNPs) was made in a green synthetic way using soluble starch as a reducing agent. In a typical one-step synthesis protocol, 0.5 g of soluble starch was added to 50 mL of deionized water and gently heated under continues stirring on hotplate at 100°C for 30 minutes. Later 0.01 M, 50 mL of AgNO₃ was added to the mixture and continued boiling at 90°C for 6 hours on hotplate with stirring. The colour of the silver nitrate solution changed from colourless to brownish yellow which indicate the formation of AgNPs. The obtained AgNPs were purified through repeated centrifugation at 11500 rpm for 20 minutes. AgNPs were collected and redispersed in deionized water.

2.3. Quantitation of the biosynthesized AgNPs

The concentration of AgNPs was estimated from concentration of AgNO₃ solution (0.01 M, 50 mL) following a procedure earlier described by Kalishwaralal et al. [15], and Rani et al. [16]

Step 1: Average number of atoms per nanoparticle (N):

From the synthesis we assumed that 100% of the silver atoms were converted into AgNPs

$$N = \frac{\pi \rho D^3}{6M} N_A$$

Where $\pi=3.142$, ρ is the density of the face-centered cubic crystalline structure of silver (i.e., 10.5g/cm³) [16], D is the average diameter of AgNPs (18 nm), M is the atomic mass of silver (107.86 g), and N_A is the number of the atoms per mole (Avogadro's number = 6.023×10^{23}). Therefore;

$$N = \frac{3.142 \times 10.5 \times (1.8 \times 10^{-6})^3 \times 6.023 \times 10^{23}}{6 \times 107.8}$$

$$N = 179166$$

Step 2: Molar concentration of AgNPs solution:

$$C = \frac{N_T}{NVN_A}$$

Where N_T = product of the molarity of AgNO₃ and atoms present in one mole, N = number of atoms per nanoparticle (as calculated in step 1), and V is the volume of solution. Therefore;

$$C = \frac{0.01 \times 6.023 \times 10^{23}}{179166 \times 0.05 \times 6.023 \times 10^{23}}$$

$$C = 1.12 \times 10^{-6} \text{ M.L}^{-1} = 1120 \text{ nM}$$

2.4. Deposition of TiO₂ Layer

The TiO₂ liquid paste was spin-coated on the substrate using modified centrifuge machine at 3000 rpm for 15 seconds. The deposited TiO₂ was dried at 150°C for 5 minutes and then annealed at 450°C for 30 minutes.

2.5 Silver nanoparticles deposition on TiO₂

Green synthesized metallic silver nanoparticles (AgNPs) was sputtered onto the surface of spin coated TiO₂ films by spin coating technique at room temperature. The silver content on the surface of the TiO₂ was varied by drop-casting 50, 100, 150, 200, and 250 μL . Immediately after the Ag deposition onto TiO₂, the films are annealed at 150°C for 5 minutes.

2.6 Films characterization

2.6.1 UV-vis spectrophotometer

UV-vis spectroscopy was performed to predict the charge transfer possibility between the acceptor and donor using Axiom Medicals (UV752 UV-Vis-NIR spectrophotometer) by scanning the absorption maxima of the mixture at wavelengths between 200–1200 nm.

2.6.2 X-ray diffraction (XRD)

The crystal structure of the nanoparticle films was performed on X-ray diffraction (Rigaku D, Max 2500) recorded in the 2 theta range from 10° to 70° and equipped with $CuK\alpha$ radiation ($\alpha = 1.54 \text{ \AA}$). The spectral data were operated at 40 kV and a current of 40 mA.

2.6.3. Scanning Electron Microscope (SEM)

Scanning Electron Microscope (SEM) was used to study the surface morphologies using JEOL (JSM-7600F) at a 20 kV acceleration voltage.

3. RESULTS AND DISCUSSION

3.1 Optical study

Figure 1a shows the curve of the absorbance against wavelength for pure TiO_2 and TiO_2 modified with different μL of AgNPs.

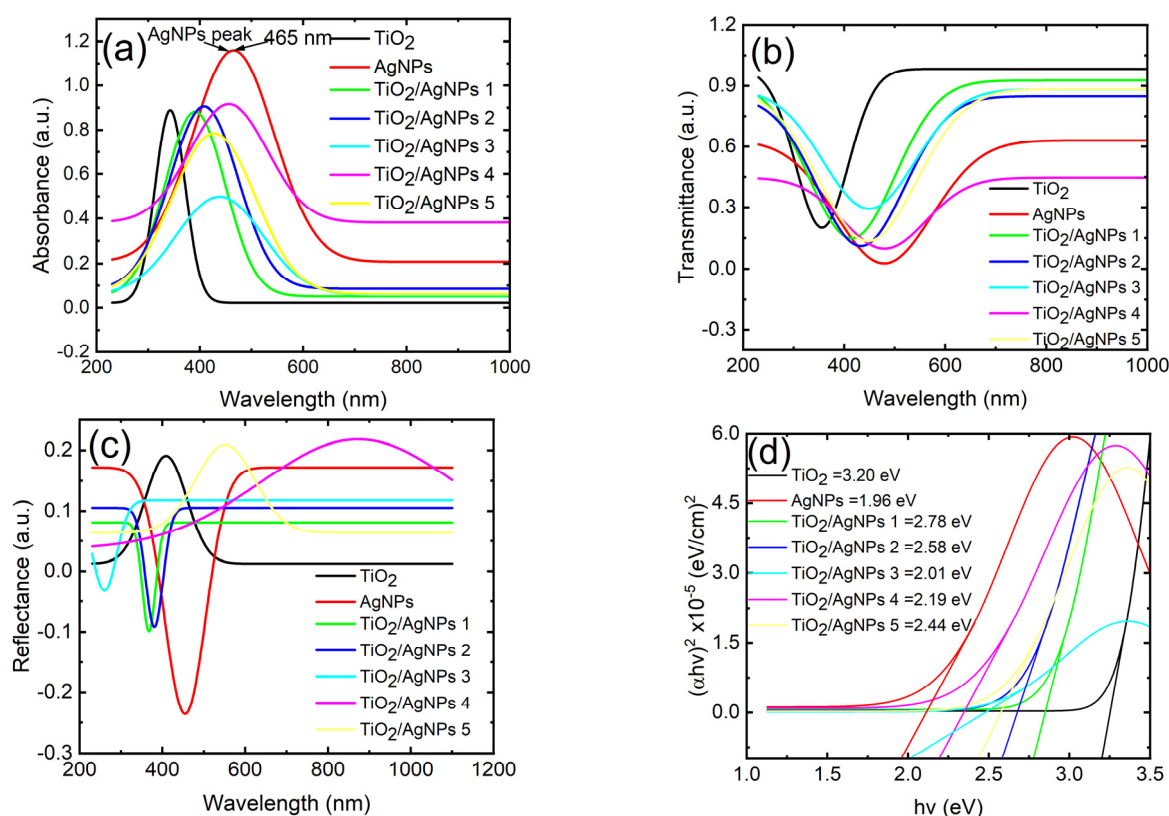


Figure 1. (a) Absorbance of TiO_2 , AgNPs, $TiO_2/AgNPs_1$, $TiO_2/AgNPs_2$, $TiO_2/AgNPs_3$, $TiO_2/AgNPs_4$, and $TiO_2/AgNPs_5$, (b) Transmittance of TiO_2 , AgNPs, $TiO_2/AgNPs_1$, $TiO_2/AgNPs_2$, $TiO_2/AgNPs_3$, $TiO_2/AgNPs_4$, and $TiO_2/AgNPs_5$, (c) Reflectance of TiO_2 , AgNPs, $TiO_2/AgNPs_1$, $TiO_2/AgNPs_2$, $TiO_2/AgNPs_3$, $TiO_2/AgNPs_4$, and $TiO_2/AgNPs_5$, (d) Band gap energy of TiO_2 , AgNPs, $TiO_2/AgNPs_1$, $TiO_2/AgNPs_2$, $TiO_2/AgNPs_3$, $TiO_2/AgNPs_4$, and $TiO_2/AgNPs_5$

Where AgNPs₁=50 μL , AgNPs₂=100 μL , AgNPs₃=150 μL , AgNPs₄=200 μL , and AgNPs₅=250 μL

As it is seen from all the spectra, the curves modified with AgNPs show improved absorption in the visible range of the electromagnetic (em) spectrum. The titanium dioxide did not display any visible or near infrared peak, however an absorption peak between 278–405 nm in ultraviolet region with maximum peak at 341 nm was observed. This peak can be attributed to strong interaction between O 2p to Ti 3d charges [4]. As a result of the observed peak at the UV region, there is need to modify TiO_2 to make it active at the visible and near IR region.

On close inspection of the spectrum, the AgNPs shows a broad band with a visible peak observed at 465 nm which correspond to the plasmonic absorption of AgNPs [3,17–20]. The surface plasmon resonance effect is due to the mutual oscillation of conduction electrons which are in resonance with the light wave. The sample containing AgNPs is depicted to show a redshift in visible light matching which is attributed to surface plasmon resonance effect.

The TiO₂/AgNPs1 film shows a peak at 395 while the TiO₂/AgNPs2 film shows a further shift to 407 nm. On increasing the AgNPs drops to 3 and 4, we observed a redshift in the spectra with absorption peak of 440 nm and 460 nm. Further increase to 5 drops results to a blue shift in optical absorption which is attributed to photodegradation due to higher surface adsorption.

The optical transmittance of the samples is shown in Figure 1b which was obtained from equation 1.

$$T = 10^{-A} \tag{1}$$

where T is transmittance and A is absorbance.

As seen from the curve, at wavelengths between 400 to 1000 nm, all samples with AgNPs have lower transmittance than the sample without AgNPs. This differences in transmittance is attributed to the fact that the refractive index of TiO₂ is being more dispersive than those of AgNPs modified samples [21]. All the samples display high transparency in the visible region and near IR region with a sharp fall noticed at lower wavelength. The higher transmittance observed in pure TiO₂ than the AgNPs modified TiO₂ shows that, the introduction of AgNPs on TiO₂ increase the porosity of the film. We can attribute the possible reason of decrease in optical film density with increase in AgNPs content to this reason. The disparities in the transmittance of the film can be seen to arise mainly from the presence of different amount of AgNPs (50, 100, 150, 200, and 250 μL) introduced which results in inconsistencies in surface morphology, crystal size, and transmittance to light scattering [3,22].

The optical reflectance of pure TiO₂ and TiO₂ modified with different μL of AgNPs shown in Figure 1c were obtained from equation 2.

$$R = 1 - (A + T). \tag{2}$$

Where R is the reflectance, A is the absorbance and T is the transmittance

As depicted in the figure, all the films were seen to be reflective.

The reflectance was characterized with a peak and a valley. The presence of AgNPs with different content results to increase in porosity of the films which also causes a decrease in reflectance. This redshifting indicates that multiple light can scatter due to the pores as a result of introduction of AgNPs. This clearly means that, the unadulterated TiO₂ film shows a smaller porosity which enhances light reflectivity.

The optical band gap (E_g) was determined using the Tauc method which is a graph that expresses a relationship between $(\alpha hv)^2$ and hv . The extrapolation of the linear part (αhv) to zero point provides the band gap value.

The E_g were estimated utilizing the Tauc curve $(\alpha hv)^{1/r} = A[hv - E_g]$, where α = absorption coefficient, v = incident photon frequency, E_g = bandgap, h = plank constant and A = constant, respectively. In the Tauc equation above, the value of r depends on optical absorption. For example, the transitions $1/2$ is known as direct allowed and 2 is known as indirect allowed, respectively, while the transitions 3 is known as direct forbidden and $3/2$ as indirect forbidden, respectively [23].

The band gap energy of the TiO₂ without AgNPs was 3.20 eV (see Figure 1d). Similar results have been reported by other researchers [1,3,24]. Upon incorporation of different μL of AgNPs, the band gaps were reduced to be 2.78, 2.58, 2.01, 2.19 and 2.44 eV for TiO₂, TiO₂/AgNPs1, TiO₂/AgNPs2, TiO₂/AgNPs3, TiO₂/AgNPs4 and TiO₂/AgNPs5 as depicted in Figure 1d. The AgNPs band gap is 1.95 eV. The reduced bandgap is as a result of increase in grain size due to increase in AgNPs content. This reduction has simply established the phenomenon of quantum size effects, in which the bigger the particle size, the smaller the bandgap [3,25].

3.2. Structural study

XRD patterns were studied to illustrate the structure and phase composition of the as synthesized nano materials. Figure 2a shows the XRD pattern of TiO₂ and TiO₂ modified with various μL of AgNPs and spin coated.

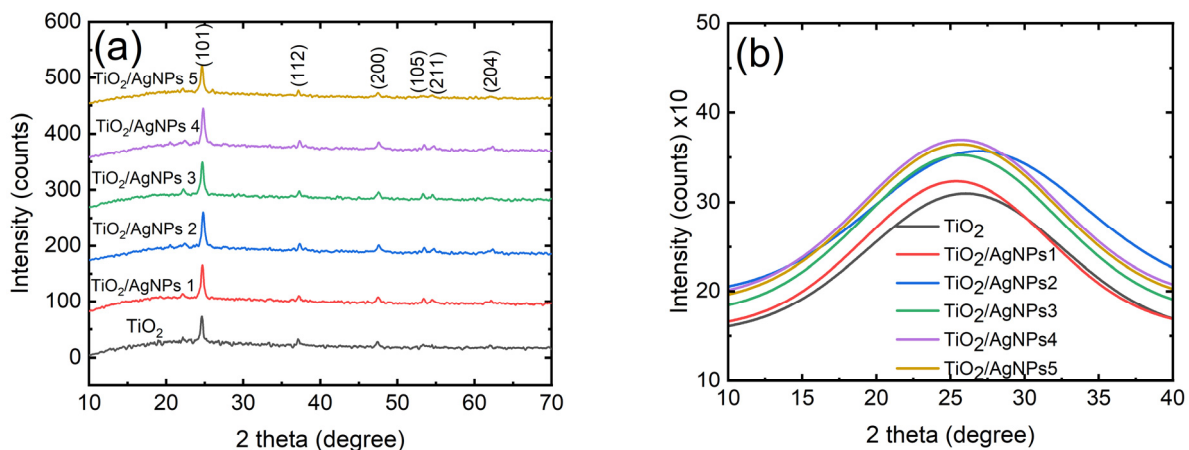


Figure 2. (a) – XRD pattern of TiO₂, and TiO₂ with different content of AgNPs; (b) – Gaussian fitted peaks for the most pronounced plane (101)

The creation of a tetragonal anatase TiO₂ phase was confirmed by all peaks in the pattern. The significant peaks at 24.59°, 37.22°, 47.88°, 53.42°, 54.53°, 62.21°, and 67.40°, which correspond to the planes (101), (112), (200), (105), (211), (204), and (116), respectively, are clearly visible. The peaks and planes exhibit great agreement with standard JCPDS card No. 89-4921 and also agrees with the findings reported by Danladi et al. [3] and Manju & Jawhar [26]. Anatase titania has been generated inevitably in all the films coated with the biosynthesized AgNPs, as evidenced by the absence of extra peaks due to AgNPs or comparable phases in the XRD plot. This only suggests that the addition of AgNPs improves the crystallinity of the film. AgNPs are introduced as a synthetic antenna, which alters the diffraction peak intensity and somewhat broadens the dominating peaks.

The peaks intensities increase with increasing drops of AgNPs except the film with 250 µL of AgNPs where the intensity is lower and this difference can be attributed to faster agglomeration rate of silver nanoparticles. We can see that, in relation to the AgNPs content increase, the high-intensity peak (101) position is somewhat pushed marginally into the higher angle position. To support our claim, the Gaussian fitted peaks for the most pronounced plane (101) are presented in Figure 2b.

The crystallite sizes (D) of all the pure and AgNPs modified films were estimated using equation 3 which is called the Debye–Scherrer equation [27]. All the parameters obtained are as shown in Table 1.

$$\text{Crystallite size } D = \frac{k\lambda}{\beta \cos\theta} \quad (3)$$

Table 1. Structural Parameters of TiO₂ and TiO₂ coated with 50, 100, 150, 200, and 250 µL of biosynthesized AgNPs.

2θ (degree)	hkl	Crystallite size (nm)					
		TiO ₂	TiO ₂ /AgNPs1	TiO ₂ /AgNPs2	TiO ₂ /AgNPs3	TiO ₂ /AgNPs4	TiO ₂ /AgNPs5
23.46	101	3.87	5.02	4.69	4.28	4.27	4.54
37.36	112	11.94	9.92	10.74	10.95	10.46	9.57
47.13	200	10.41	11.39	6.51	8.19	7.47	8.68
53.36	105	42.82	38.63	24.97	28.11	17.45	32.97
54.38	211	8.22	30.38	41.28	12.24	22.89	17.37
61.08	204	19.51	2.43	10.99	45.18	11.32	35.45
67.92	116	5.49	12.39	5.49	5.34	9.71	3.11

3.3 Morphological Study

The morphological characteristics of the prepared films were studied using SEM micrographs.

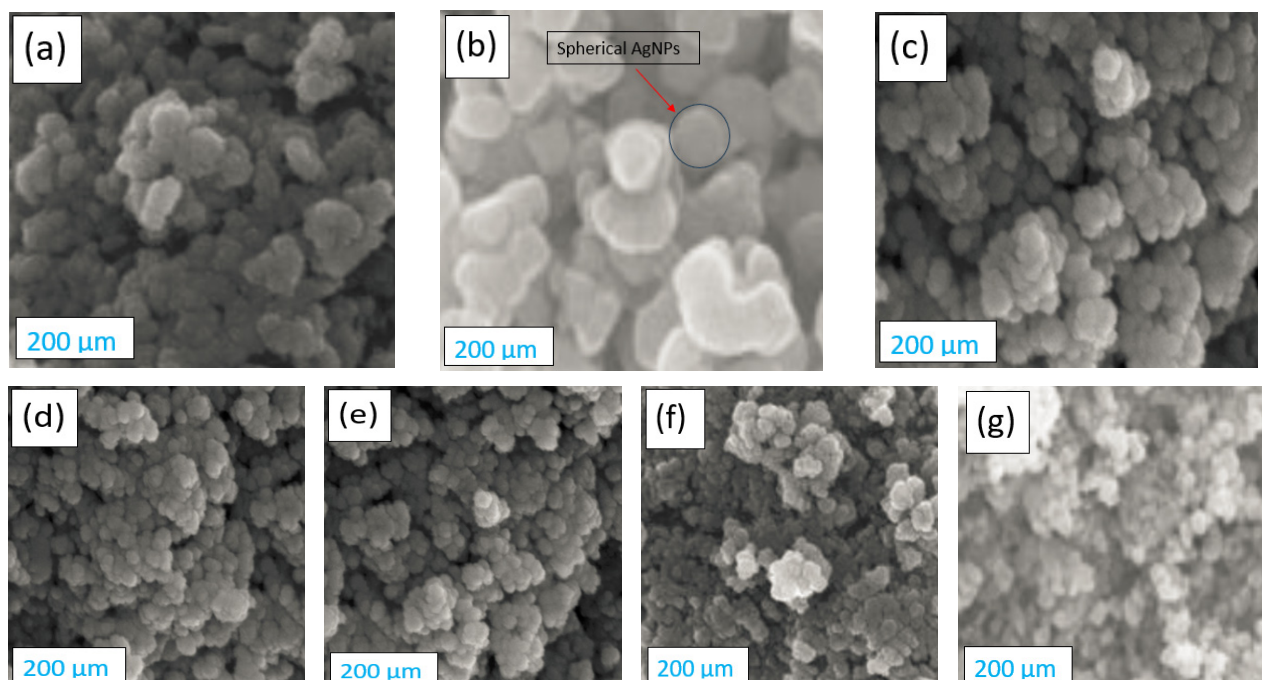


Figure 3. SEM images of (a) pure TiO₂, (b) Biosynthesized AgNPs, (c) TiO₂ with 50 µL of AgNPs, (d) TiO₂ with 100 µL of AgNPs, (e) TiO₂ with 150 µL of AgNPs, (f) TiO₂ with 200 µL of AgNPs and (g) TiO₂ with 250 µL of AgNPs

Figure 3a shows the SEM image of pure TiO₂, Figure 3b shows the SEM image of AgNPs, Figure 3c shows the SEM image of TiO₂/AgNPs1, Figure 3d shows the SEM image of TiO₂/AgNPs2, Figure 3e shows the SEM micrograph of TiO₂/AgNPs3, Figure 3f shows the SEM micrograph of TiO₂/AgNPs4 and Figure 3g shows the SEM micrograph of TiO₂/AgNPs5. The morphological structures of the films show well-densified surface which has spherical porosity. This

spherical porosity is an indication of the film to allow proper infiltration of the AgNPs into the space for good surface interaction. From the XRD data from Scherrer's formula and the SEM micrographs pattern, the sizes are in the nanoscale with the silver nanoparticles having average diameter of 18 nm.

Interestingly, the anchored Ag nanoparticles on the surface of TiO₂ is seen for the samples with Ag nanoparticles modification (Figure 3c-g) which further affirms the successful attachment of Ag nanoparticles on the surface of nanocrystalline TiO₂. As it is seen clearly, the micrographs with AgNPs show a shiny surface which display enhanced catalytic properties that can improve scattering of light and minimize recombination effect. The size of the AgNPs is controlled in our study by varying the μ L of AgNPs added in the TiO₂ nanocrystal. The size of the particle is increased with decreasing μ L of the AgNPs content added. This shows that the presence of AgNPs initiate nucleation with much film coverage. These different amount of AgNPs were utilized as light scattering layer in the modified films. From the structure, a greater aggregation was shown in the SEM image with 250 μ L of AgNPs which shows more islands formation and will subsequently results to less attachment at specific site of the titania. This by indication can lessen the catalytic effect and reduce the nucleation site that will give room for crystal film growth. We can relate this assertion with the XRD result of the film with 250 μ L of AgNPs where the intensity is lower due to faster agglomeration rate of silver nanoparticles.

4. CONCLUSION

In this study, pure TiO₂ and TiO₂ modified with AgNPs different μ L were successfully prepared and there optical, structural and morphological properties were probed using UV-visible spectrophotometer, X-ray diffraction (XRD), and scanning electron microscope (SEM). The optical properties detect surface plasmon resonance effect occurring at 465 nm which is the characteristic of surface plasmon resonance (SPR) of silver nanoparticles. The Ag incorporated TiO₂ films show a narrowed band gap and the Ag doping enhances the absorption of visible light due to plasmonic effect. XRD analysis reveals that the silver is crystallized in metallic state, and Ag nanoparticles are successfully formed in titanium dioxide matrix without indication of existence of Ag phases. As it is seen clearly, the micrographs with AgNPs show a shiny surface which display enhanced catalytic properties that can improve scattering of light and minimize recombination effect. This study established the view that deformation of TiO₂ with AgNPs is a good means towards achieving an efficient photocatalyst for photovoltaic application.

Conflict of interest. Authors have declared that there was no conflict of interest.

Funding. This article did not receive any funding support.

ORCID

©Eli Danladi, <https://orcid.org/0000-0001-5109-4690>; ©Abubakar S. Yusuf, <https://orcid.org/0000-0001-8181-9728>

REFERENCES

- [1] D. Thomas, E. Danladi, M.T. Ekwu, P.M. Gyuk, M.O. Abdulmalik, and I.O. Echi, *East European Journal of Physics*, **4**, 118 (2022). <https://doi.org/10.26565/2312-4334-2022-4-11>
- [2] T. Ivanova, A. Harizanova, T. Koutzarova, and B. Vertruyen, *Optical Materials*, **36**, 207 (2013). <https://doi.org/10.1016/j.optmat.2013.08.030>
- [3] E. Danladi, A. Ichoja, E. D. Onoja, D. S. Adepehin, E. E. Onwoke, O. M. Ekwu, and D. O. Alfred, *Materials Research Innovations*, **27**, 521 (2023). <https://doi.org/10.1080/14328917.2023.2204585>
- [4] F. Ahmed, M. B. Kanoun, C. Awada, C. Jonin, and P. F. Brevet, *Crystals*, **11**, 1488 (2021). <https://doi.org/10.3390/cryst11121488>
- [5] K. Wilke, and H. Breuer, *Journal of Photochemistry and Photobiology A*, **121**, 49 (1999). [https://doi.org/10.1016/S1010-6030\(98\)00452-3](https://doi.org/10.1016/S1010-6030(98)00452-3)
- [6] S. W. Verbruggen, M. Keulemans, M. Filippousi, D. Flahaut, G. V. Tendeloo, S. Lacombe, J. A. Martens, and S. Lenaerts, *Applied Catalysis B: Environmental*, **156–157**, 116 (2014). <https://doi.org/10.1016/j.apcatb.2014.03.027>
- [7] H. Zhang, C. Liang, J. Liu, Z. Tian, G. Wang, and W. Cai, *Langmuir*, **28**, 3938 (2012). <https://doi.org/10.1021/la2043526>
- [8] A. Subrahmanyam, K. Biju, P. Rajesh, K. J. Kumar, and M. R. Kiran, *Solar Energy Materials and Solar Cells*, **101**, 241 (2012). <https://doi.org/10.1016/j.solmat.2012.01.023>
- [9] D. Gogoi, A. Namdeo, A. K. Golder, and N. R. Peela, *International Journal of Hydrogen Energy*, **45**, 2729 (2020). <https://doi.org/10.1016/j.ijhydene.2019.11.127>
- [10] P. Wang, B. Huang, Y. Dai, and M.H. Whangbo, *Physical Chemistry Chemical Physics*, **14**, 9813 (2012). <https://doi.org/10.1039/C2CP40823F>
- [11] M. L. De Souza, D. P. dos Santos, and P. Corio, *RSC Advances*, **8**, 28753 (2018). <https://doi.org/10.1039/C8RA03919D>
- [12] Z. V. Quiñones-Jurado, M. Waldo-Mendoza, H. M. Aguilera-Bandin, E. G. Villabona-Leal, E. Cervantes-Gonzalez, and E. Pérez, *Materials Sciences and Applications*, **5**, 895 (2014). <http://dx.doi.org/10.4236/msa.2014.512091>
- [13] L. Yang, Q. Sang, J. Du, M. Yang, X. Li, Y. Shen, X. Han, X. Jiang, and B. Zhao, *Physical Chemistry Chemical Physics*, **20**, 15149 (2018). <https://doi.org/10.1039/C8CP01680A>
- [14] L. Zhou, J. Zhou, W. Lai, X. Yang, J. Meng, L. Su, C. Gu, T. Jiang, E. Y. B. Pun, and L. Shao, *Nature Communications*, **11**, 1785 (2020). <https://doi.org/10.1038/s41467-020-15484-6>
- [15] K. Kalishwaralal, S. BarathManiKanth, S.R.K. Pandian, V. Deepak, and S. Gurunathan, *Colloids Surfaces B Biointerfaces*, **79**, 340 (2010). <https://doi.org/10.1016/j.colsurfb.2010.04.014>
- [16] P. Rania, V. Kumar, P.P. Singh, A.S. Matharu, W. Zhang, K.H. Kimf, J. Singh, and M. Rawat, *Environment International*, **143**, 105924 (2020). <https://doi.org/10.1016/j.envint.2020.105924>
- [17] V. Katta, and R. Dubey, *Materialstoday: Proceedings*, **45**, 794 (2021). <https://doi.org/10.1016/j.matpr.2020.02.809>

- [18] M.G. González-Pedroza, A.R.T. Benítez, S.A. Navarro-Marchal, E. Martínez-Martínez, J.A. Marchal, H. Boulaiz, and R.A. Morales-Luckie, *Scientific Reports*, **13**, 790 (2023). <https://doi.org/10.1038/s41598-022-26818-3>
- [19] M. Madani, S. Hosny, D. M. Alshangiti, N. Nady, S. A. Alkhursani, H. Alkhalidi, S. A. Al-Gahtany, M. M. Ghobashy, and G. A. Gaber, *Nanotechnology Reviews*, **11**, 731 (2022). <https://doi.org/10.1515/ntrev-2022-0034>
- [20] Y. Khane, K. Benouis, S. Albukhaty, G. M. Sulaiman, M. M. Abomughaid, A. Al Ali, D. Aouf, F. Fenniche, S. Khane, W. Chaibi, A. Henni, H. D. Bouras, and N. Dizge, *Nanomaterials*, **12**, 2013 (2022). <https://doi.org/10.3390/nano12122013>
- [21] Y. M. Yeh, Y. S. Wang, and J. H. Li, *Optics Express*, **19**, A80 (2011). <https://doi.org/10.1364/OE.19.000A80>
- [22] P. Malliga, J. Pandiaraja, N. Prithivikumar, and K. Neyvasagam, *IOSR Journal of Applied Physics*, **6**, 22 (2014). <http://dx.doi.org/10.9790/4861-06112228>
- [23] F. Arjmand, Z. Golshani, S.J. Fatemi, S. Maghsoudi, A. Naeimi, and S.M.A. Hosseini, *Journal of Materials Research and Technology*, **18**, 1922 (2022). <https://doi.org/10.1016/j.jmrt.2022.03.088>
- [24] E. Danladi, M.Y. Onimisi, S. Garba, P.M. Gyuk, T. Jamila, and H.P. Boduku, *IOP Conference Series: Material Science and Engineering*, **805**, 012005 (2020). <https://doi.org/10.1088/1757-899X/805/1/012005>
- [25] M. Oztas, *Chinese Physics Letters*, **25**, 4090 (2008). <https://doi.org/10.1088/0256-307X/25/11/069>
- [26] J. Manju, and S. M. J. Jawhar, *Journal of Materials Research*, **33**, 1534 (2018). <https://doi.org/10.1557/jmr.2018.155>
- [27] A. Patterson, *Physical Review*, **56**, 978 (1939). <https://doi.org/10.1103/PhysRev.56.978>

ВПЛИВ БІОСИНТЕЗОВАНИХ НАНОЧАСТИНОК СРІБЛА НА ОПТИЧНІ, СТРУКТУРНІ ТА МОРФОЛОГІЧНІ ВЛАСТИВОСТІ НАНОКРИСТАЛІВ TiO₂

Джаміла Тасю^a, Мухаммад Й. Онімісі^b, Абубакар С. Юсуф^c, Елі Данладі^d, Ніколас Н. Тасі^e

^a Кафедра фізики, Університет штату Кадуна, Кадуна, Нігерія

^b Кафедра фізики Нігерійської оборонної академії, Кадуна, Нігерія

^c Факультет фізики, Федеральний технологічний університет, Р.М.В 65, Мінна, штат Нігерія, Нігерія

^d Факультет фізики, Федеральний університет наук про здоров'я, Отукно, штат Бенуе, Нігерія

^e Факультет фізики, Університет штату Ріверс, Порт-Гаркорт, штат Ріверс, Нігерія

Розробка ефективних легованих металом напівпровідників для фотоелектричних застосувань привернула велику увагу дослідників. У цьому документі було отримано чисті та модифіковані наночастинки срібла (AgNP) нанокристали TiO₂ (NC) з різною кількістю AgNP (скажімо; 1, 2, 3, 4 та 5 крапель), а також вплив AgNP на TiO₂ NCs. досліджено систематично. Оптичні, структурні та морфологічні властивості досліджували за допомогою УФ-видимого спектрофотометра, рентгенівської дифракції (XRD) та скануючого електронного мікроскопа (SEM). Результати оптичних досліджень показали характерний пік TiO₂, а червоне зміщення положення піку спостерігалось при введенні AgNPs. Синергетичний ефект від AgNP і TiO₂ призводить до зменшення забороненої зони. Результат XRD підтвердив утворення фази тетрагонального анатазу TiO₂ із зменшенням розміру кристалітів зі збільшенням вмісту AgNPs. Зображення SEM показують посилене зародження та ріст плівки з наявністю блискучої поверхні, яка, як видно, сприяє хорошему управлінню фотонами за рахунок посилення розсіювання світла. Чистий TiO₂ і модифікований AgNPs TiO₂ мають сферичну морфологію та рівномірний розподіл розмірів від 20 до 30 нм. Це дослідження встановило точку зору, що модифікація поверхні TiO₂ за допомогою AgNP є життєздатним підходом до досягнення ефективного світлового фотокаталізатора.

Ключові слова: AgNPs; TiO₂; нанокмозити; ефект LSPR; фотокаталізатор